

Silesian University of Technology
Faculty of Mechanical Engineering
Department of Fundamentals of Machinery Design

Doctoral dissertation

Electric car battery leakage detection system

MSc, Eng. Grzegorz Wójcik

Dissertation advisor:
PhD, DSc, Eng. Piotr Przystałka, Associate Professor

Industry supervisor:
PhD, Eng. Wojciech Sebzda

Gliwice, 2023

Contents

List of used acronyms and symbols	ii
1 Introduction	1
1.1 Research background and motivation	5
1.2 Scientific problem, research and implementation tasks	6
1.3 Aim	7
1.4 Scope	7
1.5 Acknowledgments	9
2 Selected issues of battery pack systems	10
2.1 System overview	10
2.2 Battery pack faults	16
2.2.1 Internal faults	16
2.2.2 External faults	18
2.2.3 Liquid leakage and intrusion faults	18
2.3 Battery fault diagnosis	21
2.4 Patent search results	26
2.5 Conclusions	29
3 Introduction to polymer optical fiber sensors	31
3.1 Sensing techniques	32
3.1.1 Intensity-based sensing	32
3.1.2 Wavelength-based sensing	33
3.2 Refractive index sensors	34
3.3 Applications in the automotive industry	37
3.3.1 Pedestrian protection system	37
3.3.2 Jam protection for car windows	39
3.4 Applications in aerial industries	40
3.5 Conclusions	42
4 Optical liquid detection system	43
4.1 System description	43
4.1.1 Functional requirements	45
4.1.2 Non-functional requirements	46
4.2 System implementation	47
4.2.1 ECU development	47
4.2.2 Communication protocol	49
4.2.3 System assembly	52
4.3 Experimental study on refractive index sensors	52
4.4 Summary	64

5	Fault detection methods	65
5.1	Fault detection method using LSTM neural networks	66
5.2	Fault detection method using autoencoder neural networks	68
5.3	Recurrent neural networks	69
5.3.1	Long Short-Term Memory	70
5.3.2	Gated Recurrent Units	71
5.3.3	Autoencoders	72
5.4	Model performance indicators	74
5.5	Fault detection performance indicators	76
5.6	Summary	77
6	Verification study	78
6.1	Verification plan	78
6.2	Preliminary study under laboratory conditions	79
6.2.1	Test rig	79
6.2.2	Data acquisition under laboratory conditions	81
6.2.3	Elaboration of fault detection schemes for laboratory conditions	85
6.2.4	Fault detection results for experiments under laboratory conditions	88
6.3	Comprehensive tests under road conditions	92
6.3.1	Test rig for experiments in road conditions	92
6.3.2	Data acquisition under road conditions	95
6.3.3	Elaboration of fault detection approach for road conditions	100
6.3.4	Fault detection results for experiments under road conditions	105
6.4	Summary	109
7	Dissertation summary	111
7.1	Main conclusions	112
7.2	Future works	114
7.3	Implementation in the industry	115
	Bibliography	117
	Abstract	127
	Streszczenie	128
	Appendices	129
A	Elementary terms and definitions	130
B	Tables	132
C	Preliminary study under laboratory conditions - datasets	133
D	Comprehensive tests under road conditions - datasets	145
E	Used hardware and software	163
F	Schematics	165

List of used acronyms

Vehicle and Battery Technology

BCU	Battery Control Unit
BEV	Battery Electric Vehicles
BMS	Battery Management Systems
BTM	Battery Thermal Management
BJB	Battery Junction Box
CSC	Cell Supervision Circuit
EV	Electric Vehicle
HEV	Hybrid Electric Vehicles
ICE	Internal Combustion Engine
LIB	Lithium-Ion Battery
OVC	Overcharge
OVD	Overdischarge
PCM	Phase Change Material
PHEV	Plug-In Hybrid Electric Vehicles
REESS	Rechargeable Energy Storage System
SC	Short-Circuit
SEI	Solid Electrolyte Interphase
SOC	State of Charge
SOH	State of Health

Machine Learning and Artificial Intelligence

ANN	Artificial Neural Network
BPNN	Back-Propagation Neural Network
CNN	Convolutional Neural Network
ELM	Extreme Learning Machine
FFNN	Feed-Forward Neural Network
GPR	Gaussian Process Regression
GRU	Gated Recurrent Units
LSTM	Long Short-Term Memory
LR	Logistic Regression
ML	Machine Learning
RAE	Recurrent Autoencoders
RF	Random Forest
RBFN	Radial Basis Neural Network
RNN	Recurrent Neural Networks
SVM	Support Vector Machine
TDNN	Time Delay Neural Network
WNN	Wavelet Neural Network

Fiber Optics and Sensor Technology

EW	Evanescant Waves
FBG	Fiber Bragg Gratings
GOF	Glass Optic Fiber
LPG	Long Period Grating
MOST	Media Oriented Systems Transport
OLDS	Optical Liquid Detection System
OTDR	Optical Time Domain Reflection
POF	Plastic Optic Fiber
POFBG	POF Bragg Grating

Automotive Electronics and Systems

ASIL	Automotive Safety Integrity Level
CRC	Cyclic Redundancy Check
ECU	Electronics Control Unit
EMI	Electromagnetic Interference
ESD	Electrostatic Discharge
IMU	Inertial Measurement Unit
LIN	Local Interconnect Network
MCU	Microcontroller Unit
PCB	Printed Circuit Board
RI	Refraction Index

Metrics

AIC	Akaike's Information Criterion
BIC	Bayesian Information Criterion
MAE	Mean Absolute Error
MSE	Mean Squared Error
nRMSE	Normalized Root Mean Squared Error
PHI	Hannan-Quinn's Criterion
RMSE	Root Mean Squared Error

Other Acronyms

GTR	Global Technical Regulation
IIR	Infinite Impulse Response
OEM	Original Equipment Manufacturer
SHM	Structural Health Monitoring

List of used symbols

Machine learning and Artificial Intelligence

D, $\mathbf{d}(k)$	disturbance signal array
F, $\mathbf{f}(k)$	fault signal array
R, $\mathbf{r}(k)$	residual signal array
S, $\mathbf{s}(k)$	diagnostic signal array
U, $\mathbf{u}(k), \mathbf{x}_t$	input signal array
Y, $\mathbf{y}(k)$	output signal array
$f(k)$	fault signal
$r(k)$	residual signal
$s(k)$	diagnostic signal
$u(k)$	input signal
$y(k)$	output signal
$y_m(k)$	model-calculated output signal
$y_e(k)$	model-calculated error signal
$\bar{r}_1(k), \bar{r}_2(k)$	moving average signal
n_1, n_2	moving average window size
p	fixed fault threshold
$p^\pm(k)$	adaptive fault threshold
\bar{r}	mean
σ_r	standard deviation
t_α	significance level
P	threshold crossing indicator level
m_f	threshold crossing indicator time window
W	weights matrix
IW, LW	input, output weights matrix
R	recurrent weight matrix
b	bias matrix
f¹	non-linear activation function
σ_g, σ_c	activation function
\tilde{H}_t	candidate activation
g_t	cell candidate
c_t, h_t, z_t	cell, hidden, current states
f_t, i_t, o_t	forget, input, output gates
r_t, H_t	reset, update gates

Performance indicators

n_s	number of outputs
N_G	cardinality of testing datasets
L_G	testing dataset
y_{ij}	j-th output of the model observed for the i-th input
\hat{y}_{ij}	predicted value of the j-th output of the model
h	number of model parameters

Q_c	selected quality measure of the process dynamics
r_{fd}	false detection rate
r_{td}	true detection rate
t_{dt}	detection delay time

Optical liquid detection system

S_{TX}	transmitted POF sensor signal
S_{RX}	received POF sensor signal
S_{norm}	received POF sensor sensor signal (normalized)
S_{ref}	reference POF sensor signal measurement
A_x, A_y, A_z	accelerations measured along x, y, and z axes respectively
A	resultant acceleration
R_{T_int}	variable resistance of internal thermistor
R_{T_ext}	variable resistance of external thermistor
T_{int}	internal temperature
T_{ext}	external temperature
β_{0_int}	internal thermistor coefficient
β_{0_ext}	external thermistor coefficient
$k_{solution}$	POF sensor measurement
k_{water}	POF sensor measurement (when exposed to water)
k_{norm}	POF sensor measurement (normalized)
k_{avg}	POF sensor measurement (averaged)
S	POF sensor sensitivity

Operators

\odot	element-wise multiplication of vectors
$card$	cardinality

General denotation concept

x, X	(bold) 1D and n D arrays, $n > 1$
x, X	(regular italics) scalar
x_n	(numerical subscript) x indexed by n
x^n, x_n	(superscript or non-numerical subscript) context-dependent annotation

1. Introduction

Over the last decade, electromobility has been growing rapidly. From 2013 to 2018, the global stock of electric passenger cars increased from 0.3M to over 5M, with a 2.1M increase just in 2018. This has quintupled in just four years up to over 25M by the end of 2022. By means of electric passenger cars, Battery Electric Vehicles (BEVs), as well as Plug-in Hybrid Electric Vehicles (PHEVs), are taken into account, excluding Hybrid Electric Vehicles (HEVs) - that cannot be plugged into the charger. In 2022, more than half of the fleet (i.e. 53%) was located in the People's Republic of China (hereafter, China), which is the leader in the electric car market share, followed by Europe (30%) and the US (8%) as shown in Fig. 1.1.

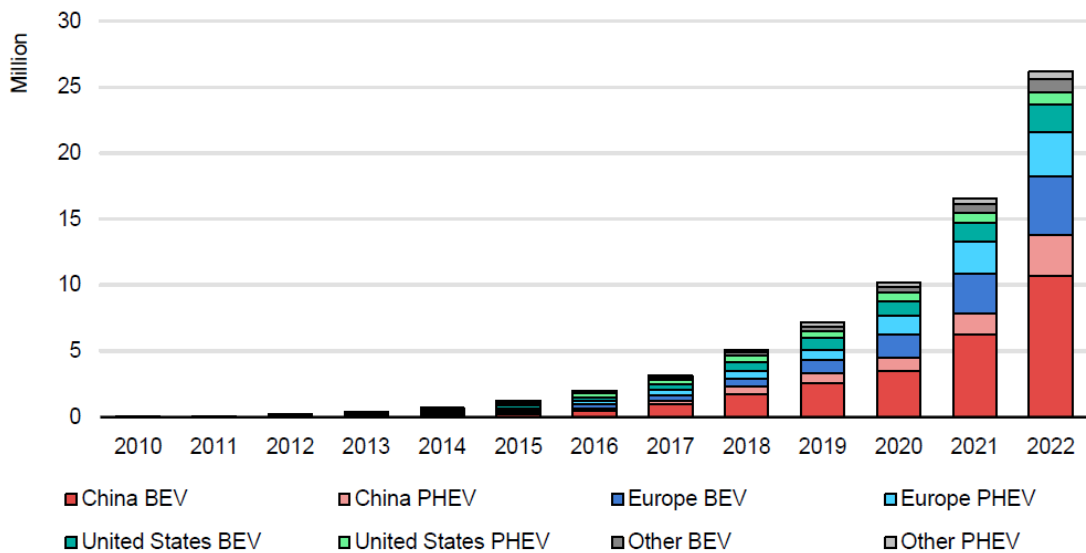


Fig. 1.1. Passenger electric car stock in main markets 2010-2022 [1]

The data gathered and analyzed by the International Energy Agency clearly indicate that the trend of new car sales is growing each year (Fig. 1.2). Globally, more than two-thirds of electric car sales in 2022 were BEVs. However the ratio between BEV sales to PHEV sales varies for each country.

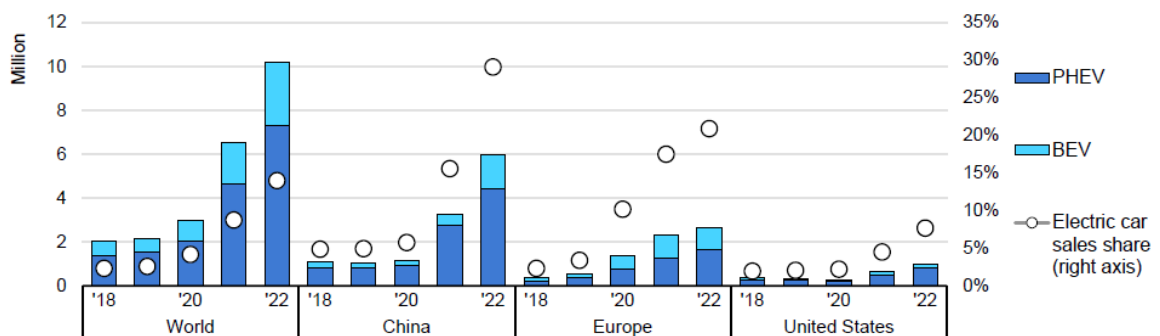


Fig. 1.2. Global electric car sales and market share, 2016-2022 [1]

Sales of electric vehicles in China have been dominated by BEVs since 2013. For the US, BEVs are also the majority of new electric cars, although the PHEV to BEV ratio was higher in the early 2010s. The non-consistent trends in the US's electric vehicles market share could be related to the popularity of the Tesla Model 3, which was introduced at the turn on 2016/2017. Exponential growth and the records have been hit despite the COVID-19 outbreak and electronic component shortages. With relation to the global car market, electric car sales accounted for 10% - four times as much as they did in 2019 [1–3]. Likewise, the average size of BEVs battery has been increasing over the years (with just a 14% increase in 2019). This trend is expected to continue, reaching an average battery size of 70-80 kWh, allowing BEVs to achieve 350-400 km of the average driving range by 2030. Driven by increased electrification, the global EV battery capacity (for all transport modes combined) is estimated to increase from around 170 GWh per year in 2020 up to 1.5 TWh (Stated Policies Scenario) or 3 TWh (Sustainable Development Scenario) by 2030. These projections account for the share of BEVs and PHEVs in overall EV sales (Fig. 1.1). EVs other than cars would account for only 11% of overall battery demand in 2030 [4].

According to the International Energy Agency's report, Lithium-Ion Batteries (LIBs) are to dominate the EV market for the next decade [4]. Technology is well established, (i.e. proven to be manufacturable with large-scale applications) and its long-term characteristics has been specified. To date, significant investments in the manufacturing and supply chains were made. This can be a barrier to alternate technologies. Nevertheless, the Technology Readiness Level (TRL) of alternative battery technologies is still in a lower range - none have yet been used in real-life conditions in commercial vehicle applications, as shown in Fig. 1.3 (0 = worse than Li-Ion battery; 1 = comparable to Li-Ion; 2 = improvement compared to Li-Ion; 3 = major improvement relative to Li-Ion).

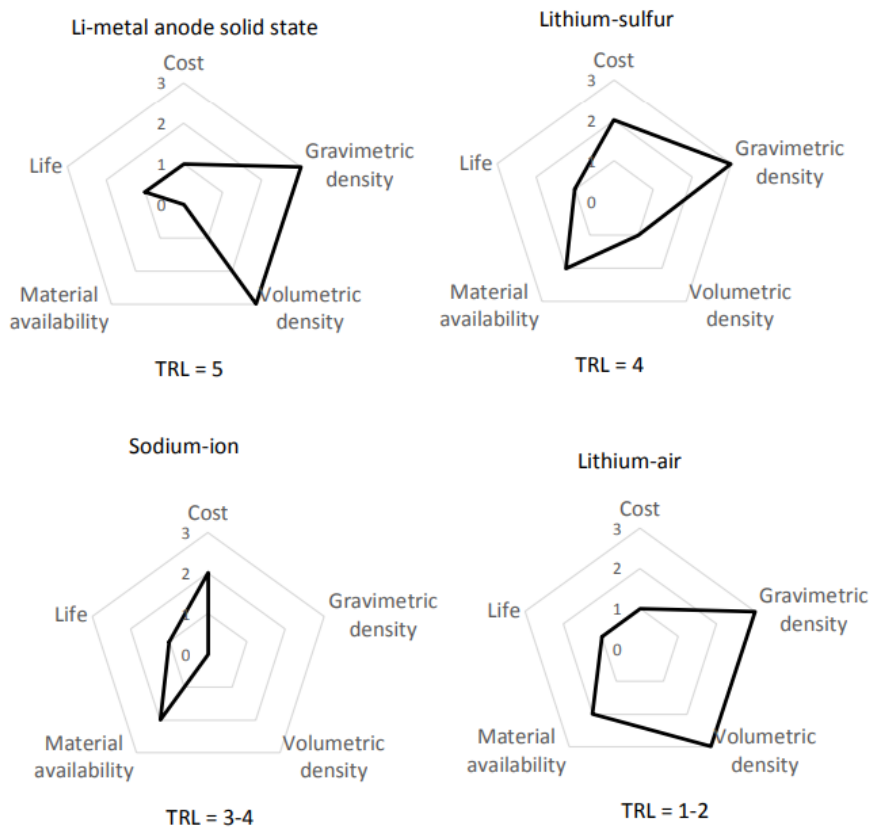


Fig. 1.3. Relative advantages of post lithium-ion battery technologies [4]

Although lithium-ion batteries have gone through many modifications to serve as long-service devices, their lifespan significantly depends on environmental conditions and operation modes. High charging and discharging currents shorten their service life, especially when in too low or too high ambient temperatures [5]. They are required to operate within a specified temperature range (-20°C - $+60^{\circ}\text{C}$) to not be damaged. In order to optimize the EV battery's performance even further, the cell's temperature should be close to $+20^{\circ}\text{C}$ [6]. Because of that, modern battery packs utilize Battery Management System (BMS) and Battery Thermal Management (BTM) circuits to prevent the battery cells from damaging or aging too quickly, e.g., by cell balancing, charge management, thermal management, state of charge (SOC), and state of health (SOH) estimations [7]. Due to differences in ambient temperatures that EVs are exposed to in different parts of the World, the battery packs shall be designed to handle both low and high operating temperatures. Recent simulations also show, that depending on the ambient temperature and trip length, the range of the EV could be improved by actively heating the battery pack during the trip or even by pre-conditioning it (heating it before the start of the trip) [8]. A 3D model of one of the most modern BEV, the Porsche Taycan (together with a cross-section of its battery pack system), was shown in Fig. 1.4. This is the first series production vehicle that employs an 800 V battery pack system [9], which complexity was illustrated in the figure. In this case, 33 battery modules (12 battery cells per module) with a total capacity of 93.4 kWh were employed. Such battery pack requires complex cooling mechanisms and efficiency-optimized architecture to minimize power losses dissipated in the system. Moreover, because the battery pack is also the chassis of such BEV, it has to be carefully designed to provide mechanical integrity, adhesives, sealants, and thermal interfaces during EV's lifespan.



Fig. 1.4. Porsche Taycan and 3D model of its battery pack [10]

Car electrification causes the emergence of new technologies or the adaptation of currently used technologies to new requirements. The change of the Internal Combustion Engines (ICE) for the sake of electric motors and high-density battery packs is a source of new problems that have to be solved. Among these, the most severe problems are reported to be thermal runaway and thermal propagation events [7]. The observed rise in demand for lithium-ion battery packs has coincided with infrequent but high-profile fire incidents, which have gained significant attention (beyond the regional level). Despite having a lower incident frequency than vehicles with combustion engines, such incidents have resulted in the loss of confidence among customers regarding the safety of electromobility and increased risk of property damage and personal injury. These occurrences have necessitated extensive recall and inspection campaigns, either on a proactive basis or as mandated by the government, and have caused financial and reputational harm to the manufacturers. According to [11], to reduce risks associated with fire incidents, different approaches have been identified in the recent literature, including:

- increasing the thermal stability of cells by alternative active materials or additives,
- decreasing the heat transfer from cell to cell (e.g., by utilizing a more efficient battery thermal management systems),

- mechanisms of early battery fault detection to provide warning and evacuation time.

Possible causes of thermal propagation events are so severe, that the Global Technical Regulation (GTR) on the Electric Vehicle Safety proposed a regulatory framework with a thermal propagation test procedure (that may cover cell, module, pack, and vehicle level) to ensure occupant safety in a vehicle if thermal runaway occurs in the battery pack system [12]. During such test, the thermal propagation is triggered by a single-cell thermal runaway due to an internal short circuit (internal and external short circuits have been described in Section 2.2). GTR specifies that a warning signal must be reported to the vehicle occupants at least 5 minutes prior to the thermal propagation event.

Because the short-circuit can be caused by a conductive liquid (such as contaminated water) in the case of a battery pack system any undesirable liquid is a threat to the battery cells and should be reported immediately. Current solutions (Dräxlmaier Group’s internal reports and [13]) utilize electronic circuits, which operating principle, mostly, is based on a resistance change when their electrodes are immersed in a conductive liquid. This type of sensor provides the basic functionality of liquid detection, as the sensor reports a warning in case of liquid presence. It does not provide any information about the type of liquid itself. The datasheet for one of the commercial products states that due to the electrolysis of liquid and sensor, it is not suggested to use this sensor for more than 1 hour in liquid. Furthermore, this sensor has to be replaced each time a water intrusion warning is reported to the vehicle [13]. Based on the author’s experience, utilizing this type of sensor inside a battery pack system requires isolation or additional protection of the power supply and communication lines between the BMS (low voltage) and the battery (high voltage) in order to protect the BMS from hazardous events that could be conducted via the sensor and its harness.

Usually, electric vehicles (BEVs) utilize 400 V battery packs, but there are also new designs with 800 V structures [14]. Battery packs of such vehicles can be discharged with currents in the order of hundreds of amperes upon car acceleration or charged with similar currents upon fast charging. Due to the non-ideal parameters of components of the system, currents of this magnitude lead to excessive heat generation of the individual cells, which results in decreased performance of the battery packs. The need for higher performance pushes new Battery Thermal Management (BTM) designs, among which fully submerged LIB packs can be distinguished (Fig. 1.5).

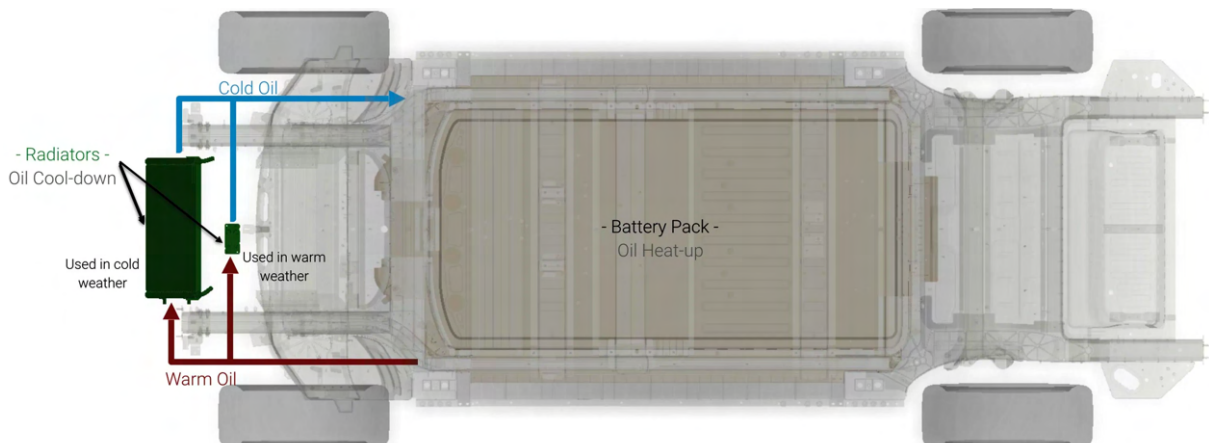


Fig. 1.5. FF91’s immersion-cooled battery pack [15]

Such systems present heat removal capabilities two orders of magnitude higher than air cooling, and the ability to homogenize temperature distributions [16] but can be susceptible to coolant (dielectric fluid, usually mineral oil) leakage or/and water intrusion. The first decreases

the battery's thermal performance, while the second can cause short circuits, corrosion, and changes parameters of the cooling medium. Although complex in design, this type of battery thermal management has been already applied to McLaren Speedtail, Mercedes AMG GT 63 S E Performance, and Faraday Future FF91 vehicles [15, 17, 18].

The following dissertation focuses on researching and evaluating faults occurring in immersion-cooled battery packs and developing a leak detection system for such energy-storage devices. To reduce drawbacks and the risks of hazardous events associated with the aforementioned electrical sensors (being exposed to high voltages), polymer optical fiber sensors have been researched, developed, and applied. Additionally, such a system required additional extensive verification tests to evaluate its performance.

1.1 Research background and motivation

Dräxlmaier Group [10] is an automotive supplier of, among many other components, complete e-mobility packages. From the charging sockets, through the wiring harnesses and high-voltage switch boxes, to the battery pack systems. As an example, Dräxlmaier engineers designed a complete 800 V battery pack system for the electric Porsche Taycan [19]. The production plant was established in Sachsenheim, Germany, and started in 2019. The whole design process required various competencies and consisted of:

- development (electronic and mechanical systems),
- simulation engineering (cooling systems, crash simulations),
- prototyping the construction,
- testing (high voltage tests, battery power tests at extreme temperatures, EMC and stress tests).

Author's internal proof-of-concepts research at Dräxlmaier Group regarding fluid sensing techniques has shown that there are other ways of detecting liquids, which could be implemented in the EV battery packs. The most practical solution would be the one that does not need isolation between high voltage and low voltage systems as it would improve safety and bring cost reductions. Studies have shown that optical sensing (based on the law of refraction) could detect a liquid intrusion as well as the type of fluid (whether it is air, water, or oil). This kind of sensor would be useful, especially for fully immersed batteries, where both types of faults (liquid leakage and intrusion) could be detected. Furthermore, the lack of direct contact between electronics and liquid increases the system's reliability compared to other solutions. However, because polymer optical fiber sensors are not common for automotive use, there are concerns about their performance under automotive conditions. Wide operating temperature (-40°C - $+85^{\circ}\text{C}$), vibrations, and long lifetime (10-20 years) are only some of the possible issues.

Another challenge is to develop advanced methods dedicated to the processing of measurement data obtained with this type of sensor in order to achieve the symptoms of the above-mentioned faults. In such a context, advancements in artificial intelligence and machine learning offer promising prospects for enhancing the diagnostic processes within EV battery packs. In particular, the development and application of a model-based fault detection approach with the use of computational intelligence can significantly improve the efficiency and accuracy of formulated liquid intrusion and leakage detection algorithms. Such model-based fault detection methods rely on a process model that accurately represents the normal operation of the system. Through continuous monitoring and comparison of real-time operational data against this model, the algorithms can detect deviations that would signal potential anomalies and faults. However, implementing AI and model-based fault detection in an automotive environment does come with its unique challenges. The algorithm must be robust against harsh automotive conditions, similar to the polymer optical fiber sensors. Moreover, the long lifetime of vehicles implies

that the algorithm should not only be robust but also adaptable to the aforementioned issues, including long-term changes in the system's operation due to aging.

1.2 Scientific problem, research and implementation tasks

The growing demand for high-performance battery packs pushes car manufacturers to elevate the charging and discharging currents of battery cells with even higher currents than before. Because of that, battery thermal management systems are being redefined to ensure safe conditions for battery cells, and to reduce aging effects. However, the battery packs are still prone to various faults, including faults occurring on a battery pack or module level (such as sensor, cell connection and cooling system faults) or faults occurring on an individual battery cell level (such as overcharge, overdischarge, short-circuits, etc.) [7]. Even small faults can initiate a chain reaction that can ultimately lead to explosion [20].

Although significant research has been conducted in understanding and mitigating various types of faults, one area that is still underexplored - constituting a research gap - is the detection and prevention of liquid leakage and intrusion faults. Primarily driven by industry demand, these types of faults may severely impair battery performance [21] and safety [22, 23], yet have not received as much academic attention as other faults. Taking into account the results of research on the state of the art, it can be concluded that additional prevention mechanisms are needed to increase safety and to warn the system of hazardous events occurring inside battery packs. Such mechanisms need to operate inside high voltage areas that are susceptible to electromagnetic interference and electrostatic discharges which could harm main battery management system drivers. A different approach shall be considered to ensure safe system monitoring. Such an approach can be done using optical signals instead of electrical signals inside hazardous areas, although it shall be investigated whether such a system can handle automotive conditions. Based on these requirements and limitations, the following research tasks were identified:

- Investigate the faults of lithium-ion battery packs, especially faults caused by liquid leakage and liquid intrusion.
- Carry out a literature review on polymer optical fiber sensors, their sensing techniques and fabrication technologies, as well as on fault detection approaches for battery pack systems.
- Prototype a fault detection system based on the proposed and fabricated polymer optical fiber sensor capable of monitoring liquid intrusion and liquid leakage.
- Develop model-based liquid leakage and liquid intrusion detection methods employing artificial intelligence techniques such as shallow and deep neural networks.
- Develop components as well as dedicated test rigs suitable for each verification study.
- Develop a diagnostic research plan and carry out comprehensive experiments to collect the data necessary for verification and validation of the system in laboratory as well as in road conditions.
- Perform experimental research on deep neural models involving the search for optimal hyperparameters.
- Draw conclusions that can be used to increase the technology readiness level of the system.

The detection system for liquid leakage and intrusion, which forms the core subject of the following dissertation, is intended for integration within an EV's battery pack system. In line with this goal, a set of implementation tasks has been planned. These tasks involve:

- The conceptualization, assembly, prototyping, and evaluation of the mechatronic system deployed in the context of this dissertation, which included, but were not limited to, battery module housing, battery module cover, component mountings, power supply circuits, microcontroller-based systems, and electro-optical circuits.

- The development of embedded software for microcontrollers, employing languages such as C/C++, as well as software for data visualization using Python and MATLAB. This also included the design and implementation of fault detection algorithms with the use of the C-code generation functionality of MATLAB software.
- The fabrication and subsequent performance analysis of polymer optical fiber sensors.
- The formulation of functional and non-functional requirements, in compliance with the expectations of potential customer and automotive standards (such as ISO 10605, ISO 11452, or customer-specific norms).
- The preparation and submission of two UK patent applications [24, 25] related to the developed technologies.
- Progress updates to departmental directors within the Dräxlmaier Group.

1.3 Aim

The aim of the doctoral dissertation is to develop an innovative electric car battery leak detection system, which is seen as a liquid leakage and intrusion detection system for immersion-cooled electric vehicle lithium-ion battery packs, using evanescent wave absorption polymer optical fiber sensors and fault detection algorithms based on shallow and deep neural networks. The liquid leakage or intrusion can be a result of e.g., the damaged battery housing or heat exchanger. Driven by industry demand, such a liquid leakage and intrusion detection system is aimed to be employed inside a battery pack system with an immersive-cooling approach. Therefore, it should be robust enough to handle automotive conditions.

1.4 Scope

The thesis focuses on the liquid leakage and intrusion detection system, in particular for immersion - cooled battery packs of electrical vehicles. To increase the safety of such battery packs, the system utilizes polymer optical fiber sensors instead of traditional electrical sensors inside the high-voltage area, therefore reducing the exposure of low-voltage and sensitive driving circuits to the high-voltage on a battery module level. The dissertation addresses many issues in the field of mechanical engineering, including the faults associated with the long-term operation of such battery packs, the development of a system useful for collecting large datasets under road conditions, the formal description of model-based fault detection methods based on computational intelligence techniques (such as shallow and deep neural networks), and also diagnostic experiments.

Chapter 1 lays the foundational background relevant to the dissertation, emphasizing the exponential growth in electromobility witnessed globally over the past 12 years. The chapter describes the motivation behind the research together with the significance and relevance of addressing battery pack faults in electric vehicles. Furthermore, the chapter presents the raised scientific problems, offering a clear context and setting the direction for the following chapters.

Chapter 2 describes the concept of electric vehicle battery pack systems. It begins by providing a comprehensive overview, discussing the pros and cons of various cell chemistries and shapes for the automotive industry. This is followed by the description of different battery thermal management systems, guiding the reader towards an immersive cooling approach, relevant to the following dissertation. The chapter presents the limitations of the lithium-ion battery cells that are currently the most popular choice for car manufacturers. Based on those, results of the research on faults associated with battery packs are provided, highlighting the liquid leakage and liquid intrusion faults. The overview dives further and explores state-of-the-art fault diagnosis

algorithms used by the battery pack systems for different purposes. Especially, the algorithms benefiting from the use of computational intelligence and machine learning. Lastly, the patent search results on battery packs and their solutions for detecting liquid leakage and liquid intrusion are presented. The thorough overview of the chapter is summarized with conclusions relevant to the dissertation.

Chapter 3 describes the fundamental principles of polymer optical fiber sensing techniques, taking into account intensity-based and wavelength-based sensing approaches, potentially suitable for the automotive industry. To distinguish different types of fluids, the research focuses on refractive index sensors and considers their manufacturing techniques. Furthermore, the chapter presents the application of polymer optical fiber sensors in the automotive industry, such as a pedestrian protection system and a jam protection system. Because of the limited number of applications found for the industry of interest, the research was extended for a more demanding, aerial industry. Similarly as in the previous chapter, the most important conclusions are presented.

Chapter 4 introduces the concept of an optical liquid detection system in the context of electric vehicles' battery packs. It provides not only the theoretical background by means of architecture and requirements (functional and non-functional) but also describes the system implementation process and experimental studies on refractive index sensors. The described implementation process consists of, but is not limited to, the development of electronic control unit, and communication protocol. Moreover, it presents the assembled system. The experimental studies on refractive index sensors highlight the fabrication procedure, results of sensor characterization, and climatic chamber tests. The chapter is summarized with the most important remarks.

Chapter 5 provides a theoretical background for the author's fault detection methods that are proposed to be employed by the optical liquid detection system. This chapter delves into recurrent neural networks, with a particular focus on Long Short-Term Memory (LSTM), Gated Recurrent Units (GRU), and Recurrent Autoencoders (RAE). It outlines the devised LSTM-based and RAE GRU-based techniques and lists a number of model performance indicators that were utilized to assess the efficacy of the models. The chapter also presents indicators useful for the evaluation of the proposed fault detection methods.

Chapter 6 outlines the verification study on the developed optical liquid detection system, as well as the extensive validation tests of the introduced fault detection methods. The first part focuses on the performance of the fault detection method using LSTM neural networks (verified under laboratory conditions) and provides relevant conclusions. The second part highlights the performance of the fault detection method using autoencoder neural networks which was verified under road conditions. The application of each method is described in detail, providing a step-by-step overview of phases such as data acquisition, model preparation, parameter selection, and results evaluation. The proposed methods have been tested offline using pre-recorded datasets from the corresponding environment.

The final chapter of this study summarizes the research findings, presenting a thorough analysis of the most important contributions of this doctoral dissertation and main conclusions. Furthermore, a set of future works is provided to highlight potential directions and emphasize the multidisciplinary nature of the research. Finally, a brief description of the implementation in the industry and achieved milestones is provided.

Appendix A contains definitions of selected terms related to battery pack systems and fault diagnosis which are important for the thesis.

Appendix B is a table of refractive indices for different weight-to-weight concentrations (%) of water and sucrose.

Appendix C presents a complete set of visualized results for the preliminary study under laboratory conditions throughout every considered system state.

Appendix D presents a complete set of visualized results for the comprehensive tests under road conditions throughout every considered system state.

Appendix E highlights the list of used hardware and software.

Appendix F contains block schematics of the developed Electronics Control Unit.

1.5 Acknowledgments

This research described in the thesis was financed by the Ministry of Education and Science of Poland under grant No DWD/33/33/2019. The dissertation is the result of four years of intense work, marked by persistent observation of industry trends. Neither the object of research nor the idea of solving this scientific problem would have come into being without the help and support of many people, especially the authorities and research staff of the Silesian University of Technology. The journey involved numerous interdisciplinary workshops with people of different fields of expertise. These workshops not only facilitated the exchange of ideas and knowledge but also fostered collaborations that greatly enriched the scope and depth of this research. I would like to offer my special thanks to the industry supervisor Ph.D. Eng. Wojciech Sebzda and other people at Dräxlmaier, especially Ph.D. Eng. Marek Sznura, Gerd Vogler, and Michael Steckel for their unwavering support and belief in the project. This significantly improved the quality of the described solution.

Furthermore, I would like to express my sincere gratitude to my dissertation advisor Ph.D. D.Sc. Eng. Piotr Przystałka, Associate Professor, for the insightful comments, suggestions, and critical assessment of my work. Maintaining a rigorous scientific approach was instrumental in shaping my own approach to research. I am thankful for your mentorship, which has significantly enriched my academic journey.

I would also like to thank my family, especially my fiancée Eryka, for her support, patience, and understanding, especially in the period of writing my doctoral thesis. To my beloved grandfather, Stanisław, whose unending support and pride in my academic journey were a constant source of motivation and encouragement. Although he could not see this dissertation to its completion, his presence has been felt every step of the way. This dissertation is dedicated to his memory.

2. Selected issues of battery pack systems

Automotive systems must fulfill conformance with different automotive standards. In terms of safety, electrical/electronic (E/E) systems must meet ISO26262 (Road Vehicles Functional Safety Standard). This standard was defined by the International Organization for Standardization (ISO) in 2011. A detailed description of ISO26262 is far beyond the scope of this dissertation, but some of the basic terms and aspects of this standard shall be explained. The standard addresses possible hazards that may be caused by the malfunctioning behavior of E/E safety-related systems. This includes the interaction of systems but excludes hazards related to electric shock, fire, smoke, heat, and radiation [26]. The Automotive Safety Integrity Level (ASIL) specifies the item's necessary safety requirements to avoid unreasonable risk due to malfunction. ASIL is determined by three impact factors: severity, probability, and controllability. There are four ASILs identified by ISO 26262: A, B, C, and D. ASIL A represents the lowest degree and ASIL D represents the highest degree of automotive hazard. ASIL level is given based on e.g., sensor redundancy or prevention mechanisms. Because of that, it was essential to investigate:

- common architectures of battery packs (electrical and mechanical),
- sensors and datasets that are being used by battery management systems,
- faults, failures, and malfunctions that may occur to the battery system during its lifespan,
- fault diagnosis methods that are used for fault detection and isolation.

This chapter provides an overview of battery pack systems architecture and investigates threats associated with different kinds of faults. To emphasize the differences in threats for different architectures of such energy storage devices, an overview of battery thermal management strategies was provided as well. Although Original Equipment Manufacturers (OEMs) tend not to share their technological advances and proprietary algorithms, this chapter also tries to investigate the state-of-the-art battery pack fault detection and diagnosis algorithms, in particular, the ones that have employed artificial intelligence and machine learning techniques.

2.1 System overview

As shown before, Lithium-Ion batteries (LIB) are most likely to dominate the EV market for the next decade. This is mainly because of their attractive properties such as: high specific energy, specific power, efficiency, moderate cycle life and lack of memory effect [2, 27]. Among the disadvantages of the LIBs, they do have a high technology feasibility cost and require complex safety and monitoring systems, called battery management systems [28].

Fundamentally, batteries are a storage medium made up of two electrodes in an electrolyte. This electrolyte provides a medium for the exchange of ions which produce electricity. Individual cell design can come in several different forms and shapes (Fig. 2.1). Although cylindrical cells provide higher mechanical strength and $\sim 20\%$ higher volumetric energy densities (in the case of the 18650 cell form factor) than their prismatic and pouch counterparts, some OEMs decide to use the non-cylindrical cells. This is mainly due to higher degrees of design freedom of the prismatic and pouch cells, which is associated with smaller dead volumes (on the module level) [29].

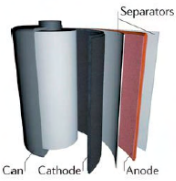
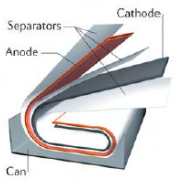
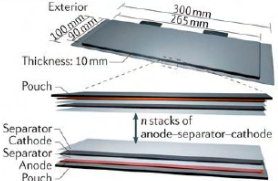
Shape	Cylindrical	Prismatic	Pouch
Diagram			
Electrode Arrangement	Wound	Wound	Stacked
Mechanical Strength	++	+	-
Heat Management	-	+	+
Specific Energy	+	+	++
Energy Density	+	++	+

Fig. 2.1. Cell designs and relative strengths and weaknesses [29]

Lithium-ion batteries consist of two types: lithium-ion-liquid (aqueous, organic) and lithium-ion-solid (polymer, ceramic) with liquid-ion type preferable for electric vehicles [30]. Figure 2.2 represents a graphical comparison (the larger the colored area the better solution) of different lithium-ion battery types (LiCoO₂ - Lithium Cobalt Oxide, LMO - Lithium Manganese Oxide, LFP - Lithium Iron Phosphate, NMC - Lithium Nickel Manganese Cobalt Oxide, NCA - Lithium Nickel Cobalt Aluminum Oxide, LTO - Lithium Titanate) from the following perspectives (outer hexagons are the most desirable):

- specific energy (capacity) - how much energy a battery holds per unit weight (relates to a vehicle's driving range),
- cost - technology feasibility and required safety systems such as a BMS,
- life span - battery longevity and cycle count,
- performance - a condition of the battery when driving under extreme conditions,
- safety - causes of e.g. thermal runaway, aging,
- specific power - indicates potential vehicle acceleration (ability to provide high current on demand).

As reported by [27], LMO, NCA, NMC and LFP technologies have been successfully adopted in electric vehicles by carmakers such as Tesla, BMW, BYD, Chevrolet, Mercedes Benz-Daimler, Volkswagen, Nissan. An interesting point is that Tesla is mainly using NCA technology, while other automakers use LFP, NMC, LMO, or blended NMC and LMO technologies. NMC battery technology is expected to increase its market share from 26% to 41% by 2025, owing to its higher energy density than LFP. Although LiCoO₂-based chemistry has been applied for EVs such as Tesla Roadster and Smart Fortwo, due to safety issues caused by the technology's intrinsic structural instability upon overcharging and limited availability of cobalt, this type of lithium-ion battery pack has been identified as difficult and expensive in its application in the automotive industry [28].

Electric vehicles store energy in battery packs. They are commonly designed as pack-module-cell structures (Fig. 2.3). Depending on the power and capacity requirements, the number of cells and modules varies. Cells and modules can be connected in series, in parallel or combined. Parallel connections increase the battery's capacity and amperage ratings, whilst series connection increases the overall voltage rating. The international norm ISO 6469-3 distinguishes two voltage classes, called low voltage (voltage class A) and high voltage (voltage class B) [31]. To carry out work in this high voltage range, specific training and certificates are necessary [32].

It is important to differentiate between terms such as battery cell, battery module, and battery pack. Battery cells are basic components, which voltage varies from 3 V to 4.2 V in

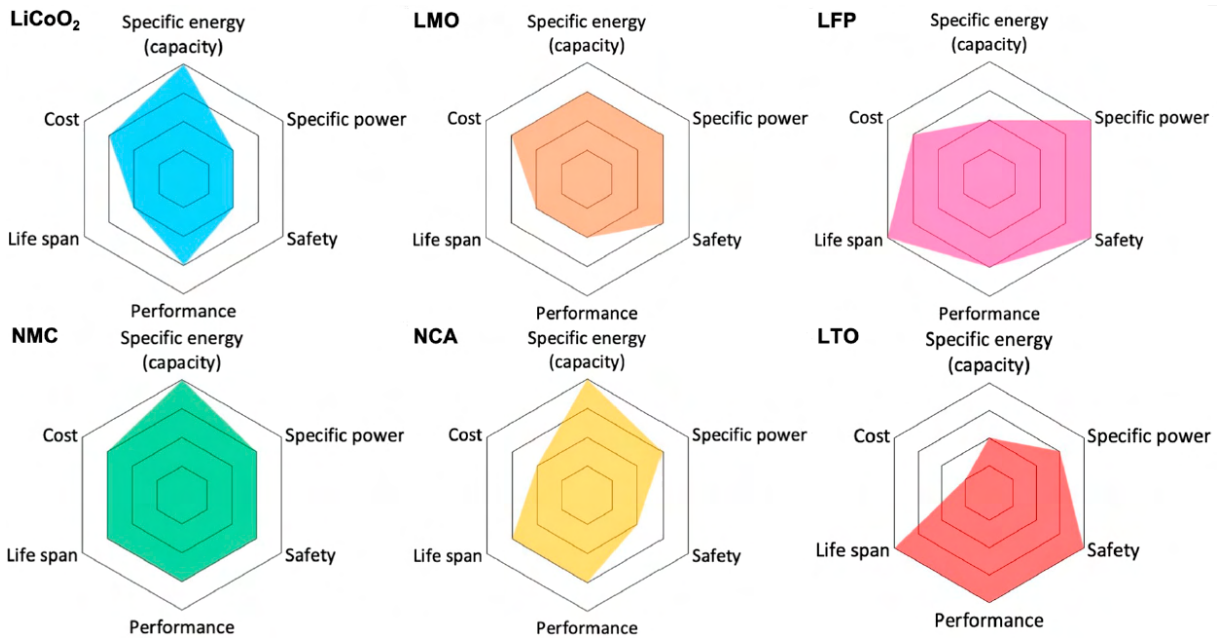


Fig. 2.2. Comparison of different lithium-ion battery types [28]

the case of li-ion chemistries. Battery modules are collections of series-connected cells. They are typically designed to meet low voltage ratings. In such cases, they can be handled without cost-intensive safety measures during production and transport. Battery packs are collections of battery modules, connected in series and/or in parallel, with up to 1000V in order to meet high voltage ratings.

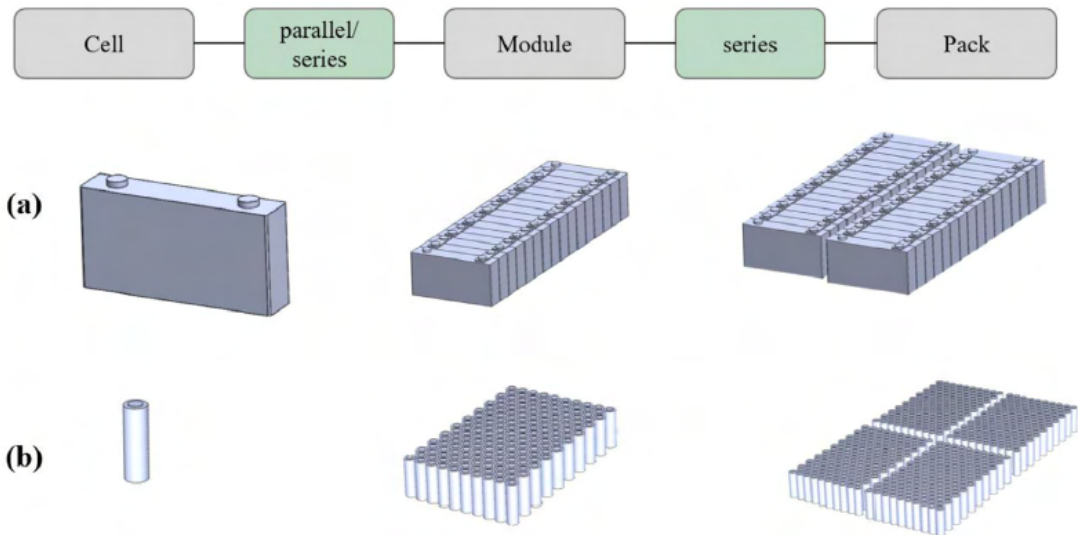


Fig. 2.3. Overview of battery packs indicating two constructions with (a) cylindrical and (b) prismatic cells [33]

As mentioned before, EV batteries consist of a large number of individual battery cells that are interconnected electrically and mechanically. As an example, a Tesla Model S 85kWh battery pack consists of 16 modules with 6 groups in series (groups contain 74 cells). This provides a 344V nominal voltage and a total number of 7104 li-ion Panasonic 18650A NCA cells [34]. Audi

R8 e-tron 90.2kWh battery pack consists of 52 modules of 144 cells each. This gives 7488 cells in total and 385V nominal voltage [35].

Connection topologies significantly influence the battery pack characteristics in terms of its performance, capacity, and lifetime. One of the aspects determining the LIB's performance is its Battery Thermal Management. Factors influencing lithium-ion cell's thermal behavior are extremely complex and were overviewed thoroughly by [36–38]. The essential conclusions are that for LIB pack's performance, temperature range and variation are the two critical, influential parameters. The desired temperature range of the traction battery is between $+15^{\circ}\text{C}$ and $+35^{\circ}\text{C}$. At the single cell's level, three important processes can be distinguished: heat generation, heat transport, and heat dissipation. These processes dominate the battery temperature. Having said that, it is clear that BTM is one of the key factors regarding traction battery design. There are various cooling strategies, such as air-based, liquid-based (direct and indirect), and Phase Change Material (PCM) based (Fig. 2.4). Each strategy is a trade-off between: ease of use, adaptability, heat transfer efficiency, maintenance, life, first cost and annual cost, etc [39]. Air-based cooling is said to be the easiest in use, but the temperature distribution of individual battery cells is the most uneven. Direct liquid cooling strategies (immersion cooling) present heat removal capabilities two orders of magnitude higher than air cooling, and the ability to homogenize temperature distributions [16].

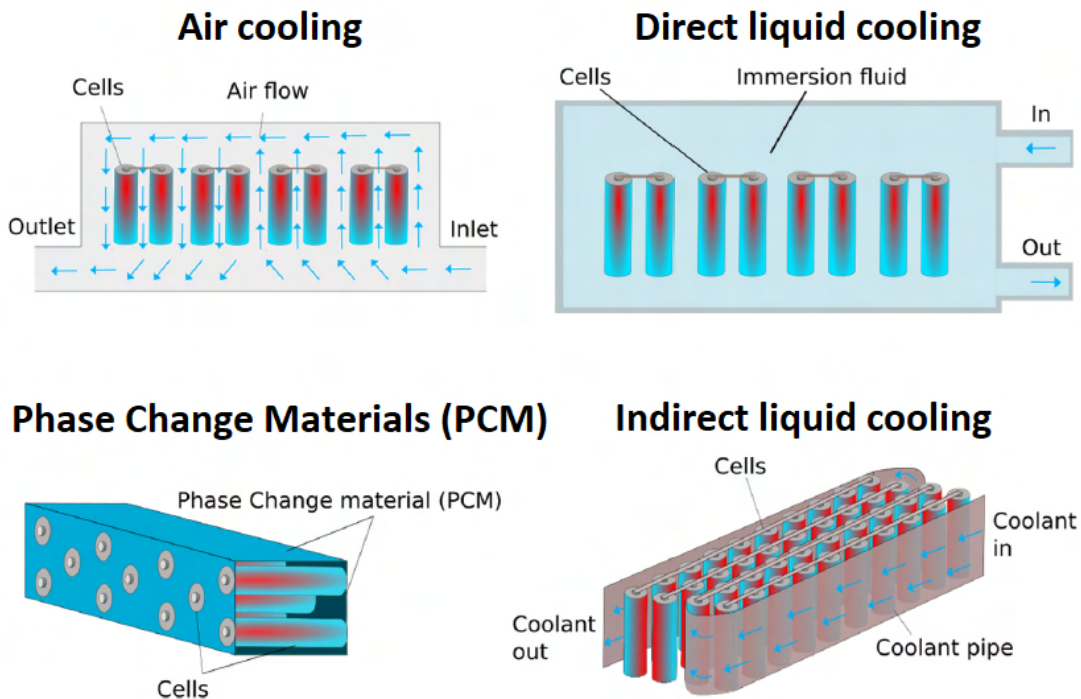


Fig. 2.4. Different battery thermal management system strategies [16]

LIB cell characteristics are sensitive to operating temperature. When they are operated at temperatures above 50°C , especially at high SOCs, their recoverable power and capacity can be reduced significantly. This is due to increased ohmic resistance, as well as lithium loss from increased growth of the Solid Electrolyte Interphase (SEI) on the negative electrode (from reacting with the electrolyte). The capacity may also be reduced if it is cycled at temperatures significantly below -10°C . The non-uniform temperature distribution causes hotter cells to be capable of discharging or charging faster than the colder cells, which negatively impacts the battery pack's lifespan and capacitance. This is one of the reasons why electrical cell balancing

(either passive or active) is important when it comes to LIB battery design, and why lithium-ion secondary cells shall operate within a specific safety operating window as shown in Fig. 2.5.

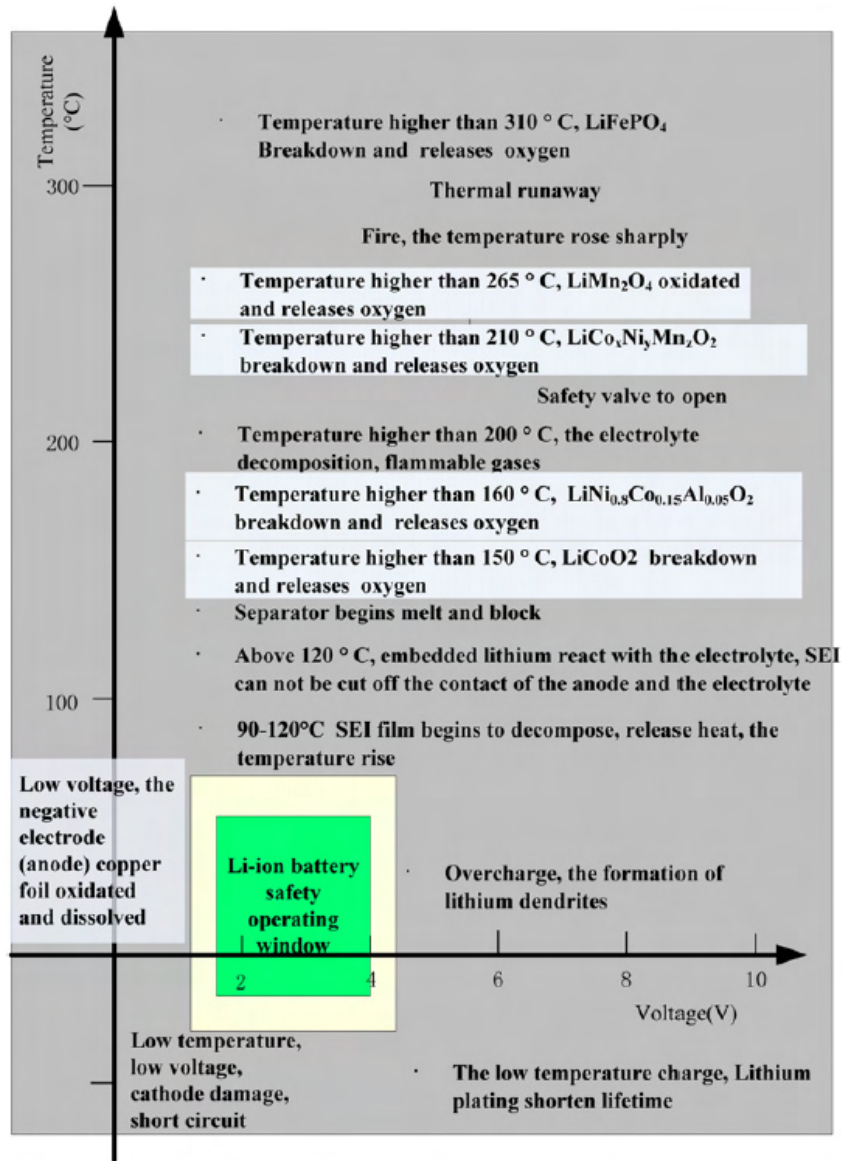


Fig. 2.5. Safety operating window for lithium-ion secondary cells [20]

Figure 2.6 presents a simplified block diagram of the electric vehicle's battery pack. As described in Section 2.1, the battery pack system embodies multiple battery modules. They consist of multiple secondary cells connected in series and parallel to meet the design requirements. They also comprise Cell Supervision Circuits (CSC) which monitor modules' temperature, current, etc. Besides those devices, the battery pack also consists of a battery management system, a switch-box (also known as a Battery Junction Box, BJB), a battery thermal management system, and a housing/interface section.

The battery management system is a device that has to interface with a number of other onboard systems. It has to work in real-time, in rapidly changing charging and discharging conditions, under high electromagnetic fields, as the vehicle accelerates and brakes, and it has to work in a harsh, uncontrolled environment. The battery management systems become more and more complex (by means of both firmware and hardware) and are at the point, where a single

ASIC is not enough and the BMS itself is based on single or multi-core microcontrollers that meet ASIL-D requirements. This device is also responsible for majority of the fault detection and diagnosis processes, as it is equipped with the highest computational capabilities among the whole battery pack system [32, 40–42]. Among many functions, the main responsibilities of the BMS are:

- providing mechanisms in case of uncontrolled conditions, emergency (fail safe mechanisms),
- monitoring the conditions of individual cells/battery modules (SoC, SoH),
- estimating the range possible with the remaining SoC,
- managing the two-stage charging to limit inrush currents,
- maintaining all of the cells/modules within their operating limits (undervoltage, overvoltage, undertemperature, overtemperature, overcharge, overdischarge, short circuit),
- compensating any cell imbalances by actively or passively managing their state of charge,
- executing fault detection and diagnosis algorithms,
- recording battery usage and abuse (log book),
- communication with other vehicle systems.

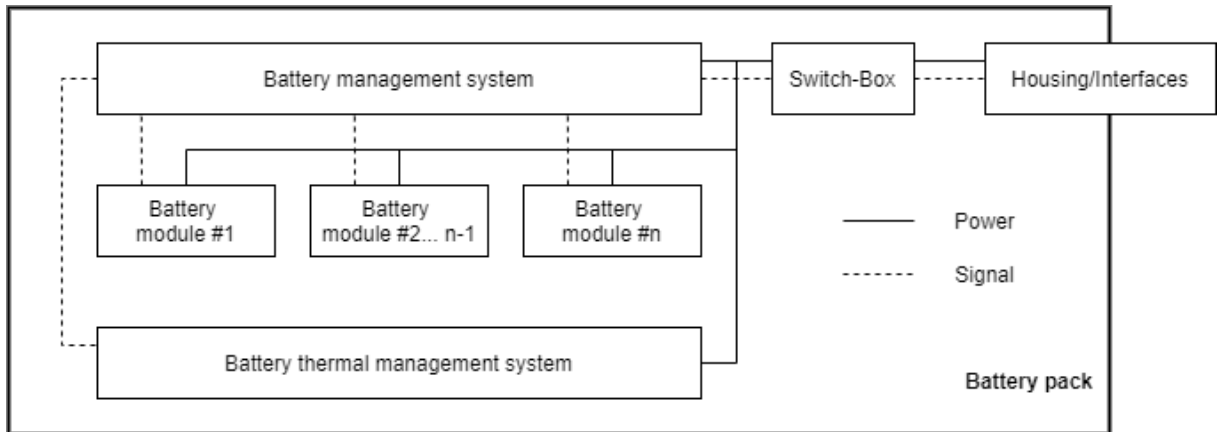


Fig. 2.6. Simplified block diagram of the electric vehicle’s battery pack

Switch-box performs a critical role in the system, as it is responsible for the instantaneous shutdown of high-voltage electric currents in case of traffic accidents and malfunctions. Since an instantaneous shutdown of such currents is not an easy task to do electronically, the BJBS tend to use pyrotechnic fuses instead (Tesla, Porsche). This component is also responsible for high current measurements (in the order of hundreds of amperes) as well as pre-charging the system using contactors. During the pre-charging phase, the inrush current is limited by an additional resistance. This prevents the electronics from being damaged by a high voltage spike [43].

Battery thermal management system is one of the key components when it comes to the battery pack design, as it is responsible for heating or cooling the cells to maintain their temperature within the safety operating window (Fig. 2.5). Depending on the LIB design, various thermal management strategies may be used, such as air, liquid, or PCM based (Fig. 2.4).

Lastly, the battery pack’s housing and structure have to be safe enough in case of a crash. Its design is very complex and consists of crash protection and tightness, casting integration, connections to the car body, and battery thermal management-related components. Despite its complexity, the design has to incorporate mechanisms for future maintenance. All of that has to be achieved with a reasonable weight.

An exemplary battery pack system is shown in Fig. 2.7, where majority of the aforementioned components can be distinguished.

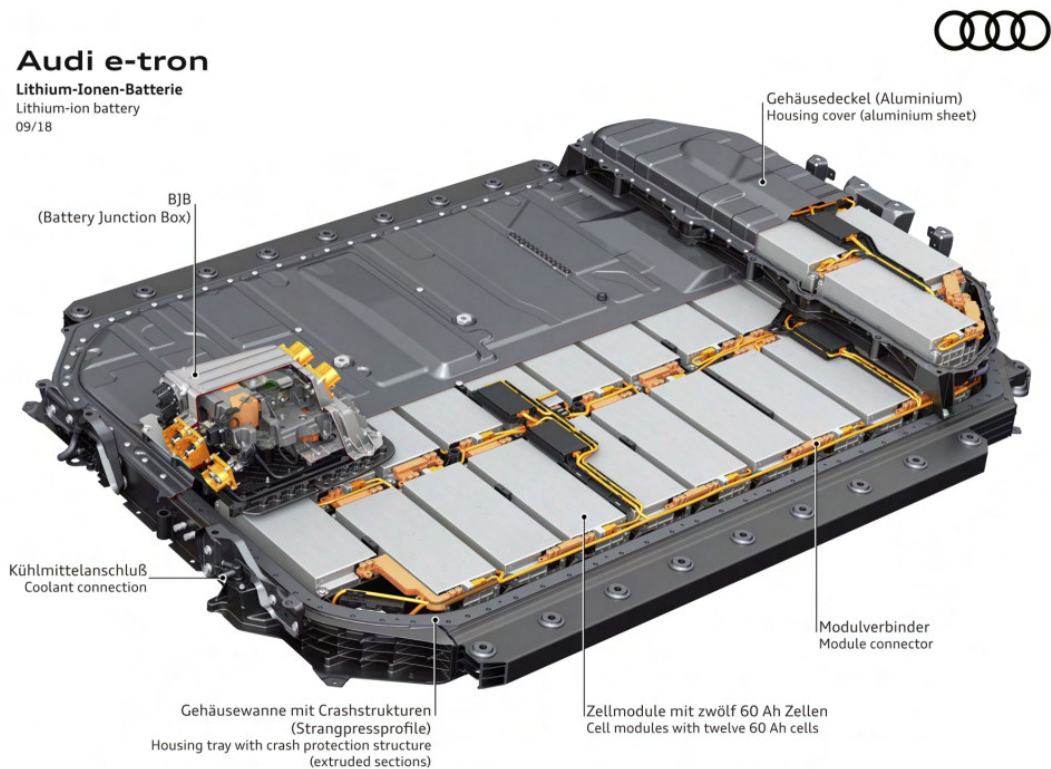


Fig. 2.7. Battery pack of the 2019 Audi e-tron [44]

2.2 Battery pack faults

Lithium-ion battery packs are known as devices of high power and energy densities and low self-discharge performance. However, their lifetime is highly dependent on environmental conditions and operation modes. Faults usually come from extreme operating conditions, manufacturing flaws, or battery aging. A key component in monitoring battery health and safety is the battery management system, which role was described in the previous section.

A thorough review, performed by [7], lists multiple factors that affect LIB operation, such as collision and shock, vibration, deformation, metallic lithium plating, formation of a solid electrolyte interphase, formation of dendrite, etc. These factors may lead to multiple faults of the battery pack system and ultimately to a system failure. Battery pack faults were categorized into external and internal (Fig. 2.8). External faults include faults of sensors (such as voltage, current, temperature), cell connection, and cooling system. Internal faults consist of overcharge, overdischarge, internal and external short circuits, overheating, accelerated degradation, and thermal runaway.

2.2.1 Internal faults

As it was described in Chapter 2.1, battery packs are commonly designed as pack-module-cell structures. Internal faults are the faults occurring to battery cells. Internal faults can be identified as deviations from the cell's characteristics properties, both electric and mechanical. Such deviations may be observed as voltage drop, SOC change, temperature rise, increase in internal resistance, swelling. All of listed internal faults do affect battery operation, but accelerated degradation and thermal runaway were found to be the most dangerous to users.

Overcharge (OVC) is a fault that can be caused due to the capacity variation of interconnected battery cells, incorrect voltage and current measurement, inaccurate BMS SOC esti-

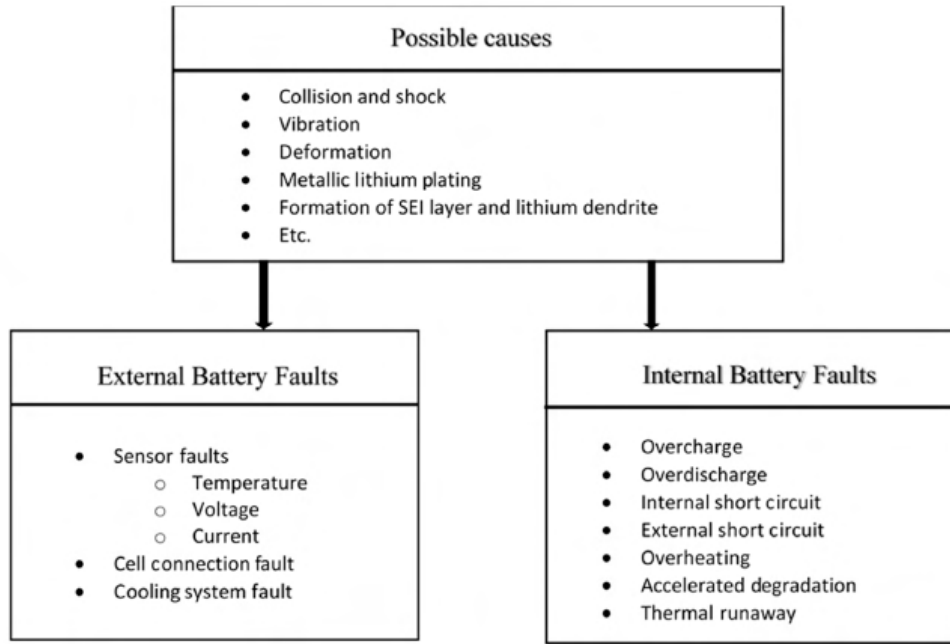


Fig. 2.8. Internal and external Lithium-ion (Li-ion) battery faults and their causes [7]

mation, or simply by a broken charging unit. Overcharging Lithium-Ion battery cells leads to electrochemical reactions between cell's components and the loss of active materials. OVC may lead to more severe faults, such as accelerated degradation and thermal runaway. Before overcharging, the surface temperature of the battery increases notably. This results in a thick SEI layer and may cause an internal short circuit inside the battery cell. Furthermore, for sealed batteries OVC may cause a buildup of gases that leads to burst [45]. Similarly to overcharge, overdischarge (OVD) can be caused by inappropriate voltage and current sensing, SOC estimation. Electrochemical impedance spectroscopy studies have found that during battery cell's OVD, the the impedance of the anode is much smaller than that of the cathode, i.e. the SEI change on the anode is much larger than the cathode. This results in capacity loss and current collection corrosion. OVD affects cell's lifetime, thermal stability, and for lithium polymer cells, it may cause considerable swelling [45, 46].

Short circuit (SC) can occur internally and externally. Internal SC occurs when there is the insulating separator layer between the cell's electrodes fails. This can be caused by high temperatures, cell deformation, formation of dendrite, compressive shock. When internal SC occurs, there is a release of large amount of heat and flammable gases, which causes a thermal runaway [47]. External SC occurs when battery cell tabs are connected electrically by low resistance path. Such low resistance path can be electrolyte that is leaked from cell swelling due to gas generation (caused e.g. by OVC). It can also be caused due to water immersion and battery structure deformation [48].

When it comes to battery cell overheating, it can be caused by excessive discharging and charging currents. This includes external and internal short circuits as well. Overheating accelerates the degradation of the cathode and leads to SEI layer growth on the anode and to capacity loss. Cell overheating can be also the source of gas bubbles and pressure build-up, causing the battery to swell and possible explode. When the overheating cannot escape as rapidly as it is formed, a runaway reaction takes place [7, 49].

Accelerated degradation is a common characteristic in most batteries. It is an abnormal condition which can cause severe problems for LIB packs. Aging and self-discharging mechanisms, higher frequency of cycle, SOC change, voltage rates are among the reasons of accelerated degra-

dation, which can be accelerated even further due to elevated temperatures [50]. Accelerated degradation is one of the major issues for automotive battery packs, as it shortens their lifetime and according to [51], this fault can also lead to surface layer formation and contact deterioration, which results in electrode and material disintegration, and loss of lithium. These phenomena can result in penetration of the separator and cause an internal short circuit and, ultimately, a thermal runaway.

Thermal runaway can be caused by all of the above internal battery faults, as well as by operating the battery cells under excessive temperatures and currents. A violent reaction of thermal runaway can be caused if temperature reaches the melting point of the metallic lithium. According to [52], the probability of thermal runaway increases with the number of charging and discharging cycles. This fault is the most severe that can occur in a LIB pack. It results in a cascade of events, starting from significant increase in pressure and temperature of the cell, ending with destruction of the container and the release of large amount of flammable and toxic gases [53, 54].

2.2.2 External faults

External faults are the faults which occur at the battery module or pack level. They may influence BMS functionality and cause internal faults the battery cells. Battery pack utilizes various sensors to ensure battery safety and performance. Voltage, current, temperature, liquid, and other sensing devices may protect cells from internal faults described in Section 2.2.1 or identify the fault in time. Lack of reliable sensor readings or damaged sensor can accelerate the degradation process, and impede the BMS functions due to incorrect state estimation, and cause other internal battery faults [55]. Vibration, collision, electrolyte leakage, loose battery terminals, corrosion are among the factors causing sensors to fail [56].

Cell connection faults are related to poor electrical connection between terminals of the cells. Vibrations may cause the terminals to become loose, or the terminals may corrode over time. This fault causes the resistance of the connection to increase significantly, which leads to cell imbalance due to uneven currents, as well as lowered cell efficiency and it is overheating due to excessive power dissipation. This type of fault is simple to detect, yet when unresolved, it may lead to severe consequences as loose connection may cause an external short circuit or thermal runaway[57].

The cooling systems transfers the heat away from the battery pack and ensures that the cells operate in the optimal temperature range, as described in the Chapter 2.1. Faults of the cooling system occur when the cooling motor or fan fail to operate, when sensors of the cooling system fail, or simply due to a broken fuse. Since a failure of the cooling system may result in overheating of battery cells or modules, this type of fault is one of the most sever. It may ultimately lead to a thermal runaway [38, 46].

2.2.3 Liquid leakage and intrusion faults

Although significant academic attention has been put to the most severe faults (such as thermal runaway and accelerated degradation), the number and variety of smaller faults and possible root causes strongly depend on the architecture of the designed battery pack system. Because of that, there are still areas that seem to be unexplored, especially when it comes to modern, immersive-cooled battery packs, which are considered a novelty in the automotive industry as described in Chapter 1. The knowledge about their typical faults and, most importantly, access to their examination, is very limited due to the relatively small number of manufactured vehicles. Examples of such unexplored areas have already been identified by the industry as faults associated with liquid leakage and liquid intrusion. Liquid leakage can be caused e.g., by a damaged battery pack structure or damaged or worn sealings. Water intrusion can be caused

by a damaged heat exchanger or condensed water. Such faults could be detected by an electric car battery leakage detection system, which is the subject of this dissertation. It is important to note that for the following dissertation, leakage detection is understood not only as liquid leakage detection but also as water intrusion detection.

In the context of electrical vehicles' battery packs, liquid leakage fault can cause different threats, depending on the battery pack's architecture. In any case, the leaks are mostly associated with battery thermal management systems, where the coolant is used to keep the battery within its temperature safety operating window. One exception is the air cooling approach, where no liquid coolant is used. When it comes to LIB packs with indirect liquid cooling approach, leakage of the coolant can result in severe consequences, especially if the used coolant is electrically conductive. Such scenario has already been the case for the Victorian Big Battery fire in July 2021 in Australia, during its testing phase. The Victorian Big Battery is a 300-Megawatt grid-scale battery storage system that consists of 212 Tesla Megapacks (lithium-ion battery stationary energy storage systems). As reported by [58], the origin of the fire was a leak within the liquid cooling system of Megapack-1, that caused arcing in the power electronics of the Megapack's battery modules. This resulted in heating of the battery module's lithium-ion cells that led to a propagating thermal runaway event and the fire, that lasted for six hours and damaged two Tesla Megapacks in total. Although the aforementioned lithium-ion battery failure did not occur in any EV, it presents the risks associated with the coolant leakage for the very similar lithium-ion battery packs of electrical vehicles.



Fig. 2.9. Tesla Megapack on fire at Victorian Big Battery, Australia [59]

For LIB packs with direct-liquid cooling approach, the coolant leakage may result in different, less severe faults. In such case, since the electronics and battery cells are submerged in the coolant, the coolant itself must be electrically non-conductive. The contact between the electricity and non-conductive liquid is the main feature of this battery thermal management system approach, which improves the thermal performance. For such battery pack systems, the coolant leakage results in the decreased performance of the battery module, and the coolant may leak from those modules to the dry areas of the battery pack system, providing no short-circuit associated risks. However, this decreased performance may lead to battery module overheating, uneven aging of individual battery cells, and inaccurate cell parameters estimation. As the cool-

ing system fails to provide adequate cooling, such fault may lead to decreased battery lifetime, and even further failure propagation into the thermal runaway [7, 60].

Similarly as for liquid leakage, the threats associated with liquid intrusion depend on the architecture of the designed battery pack system. Although the designs utilizing an immersive cooling approaches significantly reduce the risks and effects of thermal runaway (immersion liquids can act as fire suppressants) [16], water intrusion still can pose significant threats to the operation and safety of the battery pack. In some extreme cases, especially for battery packs with air cooling or indirect liquid cooling BTM, battery packs might catch fire and such situations have already taken place e.g., due to heavy rain (Fig. 2.10b) or flood (Fig. 2.10b).

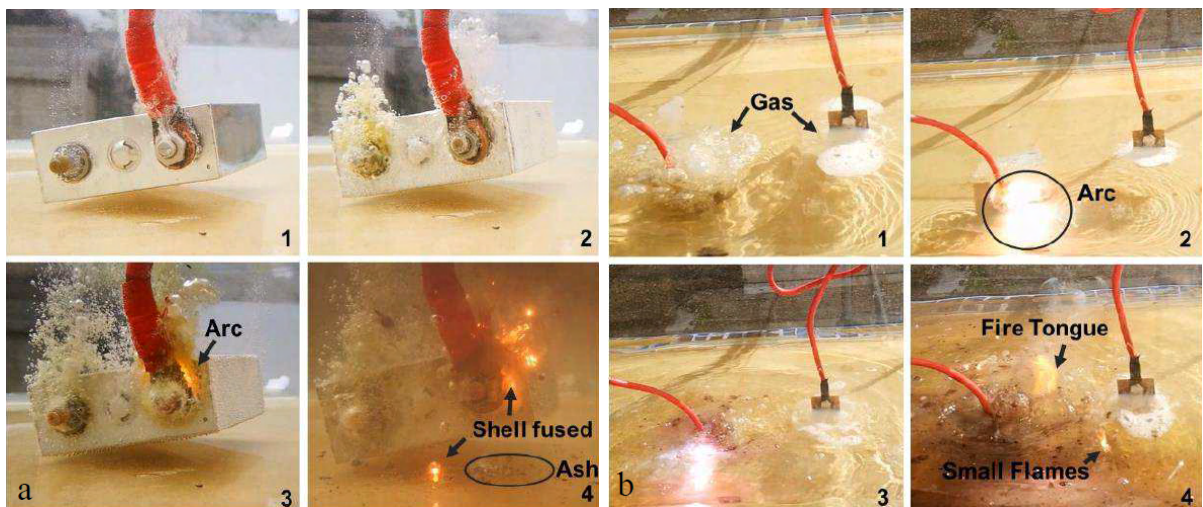


(a) 2018/09 Guangzhou China, EV caught fire due to soaking in heavy rain

(b) 2016/07 Nanjing China, EV-buses caught fire due to pack (IP54) immersion in flooding water

Fig. 2.10. Battery pack fires due to water intrusion [61]

One of the threats resulting from water intrusion is electrolysis. The presence of water within the battery system can facilitate a chemical reaction which splits the water into its constituent hydrogen and oxygen atoms. This is potentially dangerous as the build-up of these gases can create pressure within the sealed battery pack system, leading to possible rupture. Moreover, the recombination of these gases, especially in the presence of a spark or heat, can result in a violent reaction, leading to fires or explosions (Fig. 2.11).



(a) Reaction process of single cell under water

(b) Phenomena above water

Fig. 2.11. Effects of submerging lithium-ion battery cells in water [62]

An experiment carried out by [62] investigated the effects of immersing lithium-ion battery cells in water. Although cells were fully immersed (meaning that mentioned situation was not a typical incipient fault), this research has shown that electric arcs can be caused by gas breakdown due to severe electrolysis of battery cell terminals. In fact, the electrolysis was considered as the main factor leading to pack failure. This is because arc under water fused the cell poles and shells. Electrolyte leakage was evaporated and ignited (Fig. 2.11a), causing a flashing fire tongue and burning flames floating on water surface (Fig. 2.11b).

Another threats resulting from water intrusion is corrosion. The components of the battery pack system are typically made of metals that can oxidize when in contact with water, resulting in corrosion. Over time, this corrosion can degrade the materials and compromise the integrity of the system, leading to performance issues or even failure.

At low temperatures, water intrusion presents an additional risk of the potential for ice formation. When the intruded water freezes, it expands, which can exert significant pressure on the components of the battery module. This can lead to mechanical damage, including deformation or even rupture of the battery cells or other critical components. Furthermore, the ice can act as an insulator, impeding the proper functioning of the thermal management system and leading to uneven cooling or heating, which can accelerate degradation and lead to premature failure of the battery pack.

2.3 Battery fault diagnosis

As described in previous sections, battery faults may lead to potentially hazardous consequences. Risks associated with the operation of a LIB packs can be however minimized by safety functions of the BMS. To reduce the likelihood of fault occurrence and severity of faults, the BMS manages parameters such as the operating voltage, current, and temperature based on connected sensors with the aim to keep the cells within the safety operating window shown in Fig. 2.5. Lithium ion batteries are complex systems that undergo many different degradation mechanisms due to their electrochemical properties. Fault symptoms are even harder to be extracted because of hysteresis and inconsistency among cells [63]. For that reason, these safety measures are often not adequate and fault diagnostic algorithms are required for the BMS [7].

Any deviations of battery pack systems are monitored through sensors and state estimation, with the use of modeling or data analysis. Since there are many faults of different kind, various fault diagnostic methods need to cooperate to correctly detect and isolate a specific fault. Battery management systems have limited computing space and a specific, restricted time intended for the execution of each function. Due to a large number of battery cells, the diagnostic algorithms shall be designed with a trade-off between computational power, algorithm accuracy, and reliability.

Fault diagnosis includes fault detection, fault isolation, and fault identification [64]. For the automotive industry and lithium-ion battery packs, two main categories of fault diagnostic methods (model-based and non-model-based) were found in the literature as presented in Fig. 2.12. Model-based methods include state estimation, parameter estimation, parity space, and structural analysis. Non-model-based methods are divided into signal processing and knowledge-based methods.

Model-based methods use the relations between several measured variables to extract information on possible changes caused by faults. The relations are in the form of equations or if-then rules. Fault detection methods extract special features like parameters, state variables, residuals and compare them with their nominal values. By doing so, analytical symptoms can be generated. These symptoms are the basis for fault detection [65]. In the context of the automotive industry, model-based methods utilize models of a battery pack to generate residuals.

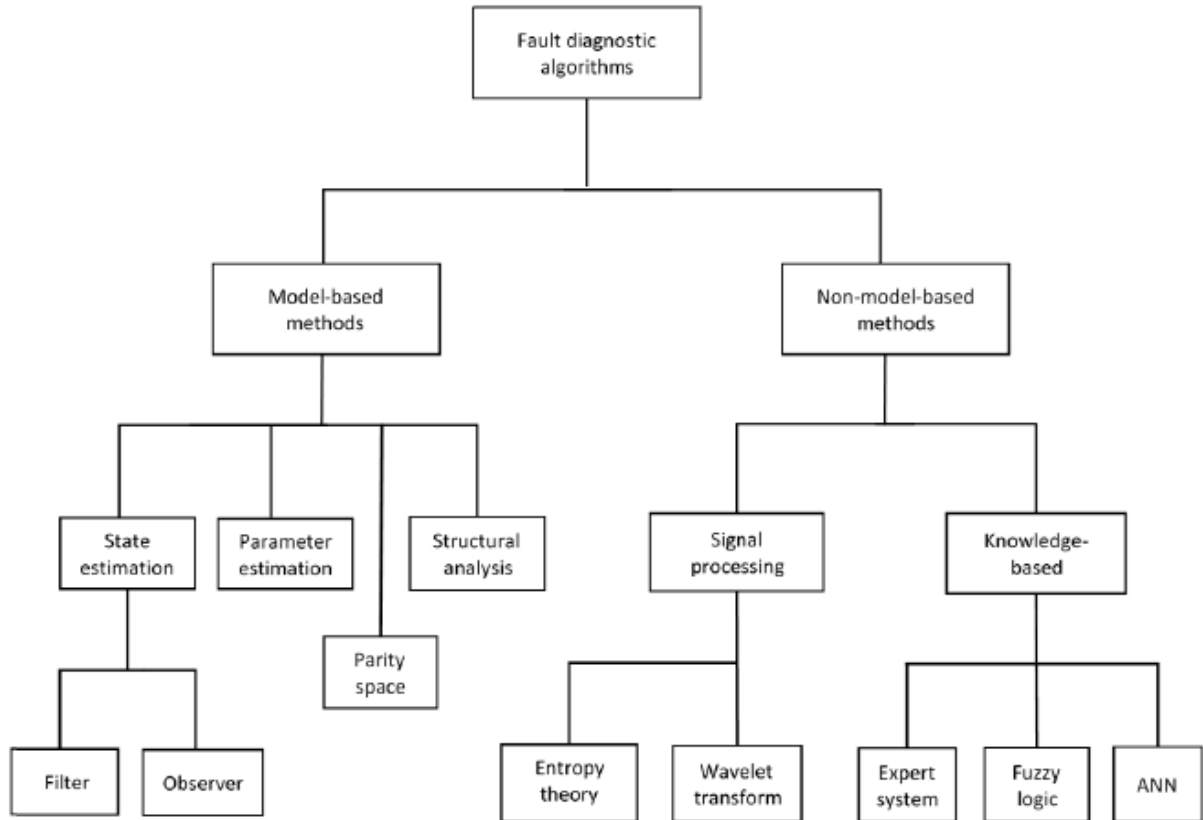


Fig. 2.12. The classification of Li-ion battery fault diagnostic algorithms [7]

Used models depend on the application and purpose. In general, models such as electrochemical, electrical, thermal, and combinations such as electro-thermal may be used. This kind of diagnosis is often used in fault diagnosis for its simplicity and cost-efficiency [7].

For a state estimation method, the system state is estimated from a model using filters or observers. Fault detection is based on residuals between estimated and measured values. For this method, Kalman filter was found to be the most popular and was used for the estimation of state of charge [66], fault detection and isolation of voltage and current sensors [67–70], fault detection of overcharge and overdischarge [71, 72], as well as for the detection of internal short circuit fault [73, 74]. Particle filter [75] has found its application in the detection of metallic lithium plating fault. Luenberger observer was used for the detection of cell connection [76] and thermal runaway [77]. Lyapunov-analysis-based nonlinear observer [78] and Partial-differential-equation-based observer [79] were used for monitoring thermal behaviour of battery cells, providing a cell overheating fault detection mechanism. Proportional integral observer [80], and Sliding mode observer [81] were the other algorithms used for fault detection, that were used for the detection of sensors faults, including current, voltage, and temperature sensing devices. Parameter estimation is used to determine the model parameters using filter algorithms. In this case, a fault is detected from the change in the estimated model parameter [56]. Parity space methods detect faults based on residuals generated from the input and output relationship between the model and the measurements. Only a few methods using parity space were found [82, 83]. Structural analysis is used to detect and isolate a fault using structural overdetermined part of the system model. This is possible without the accurate knowledge of battery parameters, but just depending on the structural information of battery dynamics.

Non-model based methods do not require difficult battery modeling and are based on signal processing or knowledge-based methods. This kind of methods, especially data-driven methods,

may predict battery behavior as it degrades and may aid the model development process [7]. Signal processing algorithms exhibit good dynamic performance but are sensitive to measurement noises and are not able to detect early faults reliably. Measured signals are transformed into fault parameters, such as entropy or correlation coefficient [84–86]. When an abnormality occurs for these parameters, the fault is detected. Knowledge-based approach includes expert systems [87], fuzzy logic [88], and artificial neural networks [89]. To detect a fault, this approach uses the knowledge obtained from observations or gathered data to set appropriate rules or train neural networks. Expert systems require in-depth knowledge of the diagnosed system. This knowledge is necessary to set effective rules for precise battery fault detection. Since not all battery faults are fully understood, this is a challenging task. There are more complex knowledge-based methods, such as machine learning (ML). ML-based techniques simplify the fault diagnosis by eliminating the steps of collecting the battery’s physical information and learning the nonlinear correlation between battery internal parameters and external measured parameters (such as operating current, terminal voltage and temperature). Because of that these methods present high accuracy and compatibility with a nonlinear systems, such as lithium-ion batteries. These methods require however a time-consuming training process and a large amount of data [7]. An extended classification of fault diagnostic algorithms was presented by [90]. Authors have added a more detailed classification of machine learning based techniques that have been successfully used in the BMS of lithium ion batteries. Figure 2.13 presents a classification based on learning approaches (supervised learning, unsupervised learning and reinforcement learning).

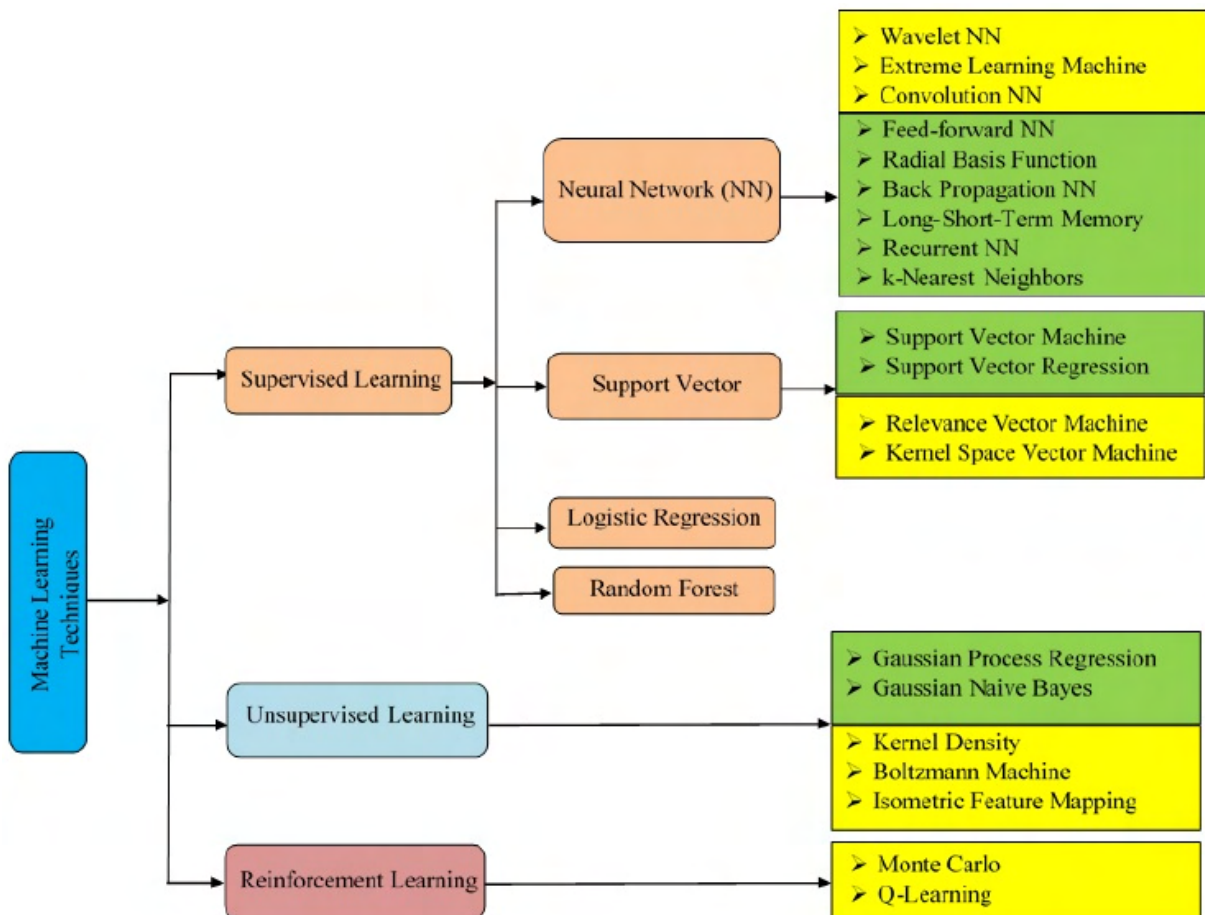


Fig. 2.13. Machine learning-based techniques used in BMS of lithium ion batteries [90]

Artificial Neural Networks (ANNs) are inspired by biological neural networks and are one of the most popular frameworks of machine learning algorithms. Models trained with ANNs frequently utilize supervised learning approaches. Thanks to their self-adaptability and learning abilities, no task-specific rules are needed prior to training and ANN is capable to capture the dynamics of a highly nonlinear systems, such as lithium ion battery. The operating principle is based on learning implicit rules from known pair of input and output data. Later on, the ANN is validated with test input and output data which are unknown to the model (the training is typically conducted offline). Differences between normal and abnormal conditions can be easily distinguished if ANN model was well-trained with sufficient amount of data. Several variants of artificial neural networks can be distinguished. They were divided into two subgroups:

- classic neural networks: wavelet neural network (WNN), back-propagation neural network (BPNN), radial basis function network (RBFN), feed-forward neural network (FFNN), extreme learning machine (ELM),
- modern neural networks (also known as deep neural networks): recurrent neural networks (RNNs), convolutional neural networks (CNNs).

BMS applications often use a combination of one of these techniques. One example is the application of an RNN-LSTM (which is a combination of RNN and LSTM) for voltage prediction and fault prognosis of the battery pack system [91]. Such technique allowed the authors to predict the voltage of one hundred individual battery cells and the whole battery pack with a mean relative error being approximately 0.0001. The authors have decided to trigger the fault detection based on a standard deviation of the predicted voltage, with a threshold set to 0.05 (± 0.15 V from the average voltage). Such an approach provided no false detections.

Random Forest (RF) classifier, similarly to ANN, is a supervised ML approach. It has been demonstrated that this method is capable of well approximating variables with nonlinear relationships and has high robustness performance against outliers. Research conducted by [92] presents a Random Forest regression-based estimation algorithm for online battery capacity estimation. The proposed technique learns the battery capacity dependency on the features that are extracted from the charging voltage and capacity measurements. RF regression is based only on signals, that are available onboard during typical battery operation, and collected raw data can be directly fed into the trained model without pre-processing. This results in a low computational cost. Experimental results have shown that the proposed technique is able to evaluate the health states of different batteries under varied cycling conditions with a root-mean-square error of less than 1.3%. Although the research is not focused on fault detection mechanisms, such estimation could be the base for the detection of internal faults such as overcharge, overdischarge, and accelerated degradation.

Support Vector Machine (SVM) has been recently introduced into the domain of intelligent fault diagnosis of LIBs. SVM aims to form different data clusters by constructing hyperplanes in high dimensional space in order to distinguish a different class of data while dealing with classification problems. The typical criteria for finding optimal separation boundaries are to maximize the distance between the hyperplane and the nearest data point of any cluster. This technique exhibits high accuracy and requires less training data when compared to ANNs, but the data preprocessing is time-consuming and complex. A study given by [93] presents a battery system intelligent fault diagnosis method based on SVM, where a fusion of the discrete cosine filtering method and grid search technique with SVM were used to diagnose the battery pack's connection fault of series connected lithium-ion cells. Despite highly satisfactory performance, the state identification was found to be very time-consuming. The minimum time requirement was around 167 s. Furthermore, the impact of cell aging and temperature variation on cell parameters was not considered. The reported fault diagnosis accuracy was 95% [90].

Logistic Regression (LR) is a statistical classification technique used to classify observed data based on pre-defined criteria. This technique has shown very good performance in linear and nonlinear regression. Similarly to GPR, not many researchers have employed this method for LIB system fault detection. Application of this technique can be found in the work of [94], where LR was used for fault diagnosis in a battery system based on Nickel-Metal Hydride (Ni-MH) battery cells, in particular overcharge and overdischarge faults. Such an approach was reported to provide a good performance of 96.4% by means of a true detection rate, with a single false-positive value among 28 Ni-Mh cells that were subjected to the fault diagnosis. The same research paper utilized a Gaussian Naive Bayes, which is based on Bayes' theorem and assumes that the features in the input data are independent and normally distributed. GNB exhibited high classification efficiency when dealing with battery cells that were either unbalanced or damaged. The underlying principle of the GNB-based classifier involved constructing a non-linear smooth curve that separates faulty and non-faulty cells based on the probability of event occurrences. This technique requires a lot of training data for such performance and was reported to provide the same performance as LR.

Unsupervised learning approaches identify hidden patterns and relationships in unlabeled datasets. In the context of BMS, the already implemented algorithms were based on Gaussian Process Regression (GPR). The main aims of this method are to cluster the data into groups by similarities, and to compress the data (by means of dimensionality reduction) while maintaining its structure and usefulness. GPR is a non-parametric, flexible technique that requires high computational complexity [90]. So far, only a few studies have used GPR for LIB fault detection, including work done by [95] for LIB SOH estimation of high accuracy, or research conducted by [96], where GPR was used for LIB degradation mode diagnosis.

Another unsupervised learning method that has been used for LIB pack's SOC estimation in combination with an LSTM neural network is Autoencoder. The autoencoder neural network was used to extract and reconstruct the training features for the LSTM network [97] because of its ability to learn the input features without corresponding output data. The authors have used the voltage and the current of the battery per second and the battery ambient temperature as inputs for the Autoencoder's NN to extract new features as input for the LSTM neural network. This method was not listed in Fig. 2.13, but on the basic level it is very similar in its functional form (although with different interpretation and training procedures) to Restricted Boltzmann Machines. More specifically, the deterministic function that maps from input to mean hidden representation is the same for both models [98]. SOC estimation using this approach was evaluated under three different temperatures, namely 0°C, 25°C, and 45°C with the mean absolute error of 0.71%, 0.66, and 0.71% respectively. Although not directly related to any fault detection algorithm, such estimation could be used for further evaluation for overcharge, overdischarge, and accelerated degradation faults.

The conducted research on fault diagnosis in the context of EV battery packs revealed that the main areas of interest are the areas associated with battery thermal behavior, sensor (voltage, current, temperature) performance, parameter (SOC, SOH) estimation, as well as the battery degradation assessment. No research directly related to the performance or fault detection of the cooling system has been found, showing a research gap in this context. Additionally, the research on machine learning techniques showed that a variety of techniques have already been employed by the scientific community for parameter estimation and fault detection mechanisms, where no prior difficult system modeling was required. This can be important, especially for the modern LIB packs with a direct liquid-cooling approach. Such systems have not been used on a large scale so far and knowledge about their architectures is very limited. Therefore, it would be justified to implement a machine learning technique for the designed and prototyped optical liquid detection system, feeding the neural networks with datasets collected for the real system under various conditions.

2.4 Patent search results

Patent research was another part of the prior-art review. Such a comprehensive review of existing patents is an integral part of the research process. The primary motivation for conducting such a patent search lies in its potential to reveal critical insights into the state of the art and the current trajectory of technological developments in the field under investigation - in this case, liquid detection mechanisms in battery packs for electric vehicles and the threats associated with liquids. Furthermore, such a patent overview can reveal gaps or opportunities within the existing technology landscape.

This search was conducted using the USPTO search engine [99] and summarized in Tab. 2.1. Column description:

- query - shows the search engine input phrase,
- records - presents total results that were returned,
- relevant - the number of patents that were found to be relevant to the topic of this dissertation.

The aim of the patent search was to explore existing solutions related to liquid leakage, and liquid intrusion detection, in particular for the automotive battery packs.

Tab. 2.1. Patent search results

Source	Query	Records	Relevant
USPTO Patent Full-Text and Image Database	"optical liquid detection"	4	1
	"liquid leakage detection"	48	4
	"liquid intrusion detection"	1	0
	"battery liquid intrusion"	0	0
	"traction battery" AND "intrusion"	21	1
	TTL/battery AND "liquid intrusion"	0	0
	TTL/"battery pack" AND intrusion	126	4

A number of patents were found that describe technical solutions of protecting the electric vehicle's battery packs from the intrusion of unwanted liquids, like water or coolant. Obtained records were divided into two sections: systems related to the prevention of liquid intrusion or leakage, and systems related to the detection of liquid intrusion or leakage.

For the systems used for protecting the electric vehicle's battery packs from the intrusion of unwanted liquids, like water or coolant, several records were found. Toyota's invention (US20140154531A1 [100]) describes a water escape mechanism and points out a problem of liquid intrusion. If a liquid like water, is condensed from moisture in the atmosphere (for reasons of day-night air temperature differences) and intrudes the battery control unit, it may cause a failure of the BCU. Mitsubishi has claimed a battery pack tray (US20140014428A1 [101]), which prevents rainwater intrusion. A fail-safe serviceable high voltage battery pack patent (US20110014501A1 [102]) consists of a gasket that protects the interior of the enclosure from rain, snow, moisture, and other possibly degrading matter. Tesla Motors' patents describe a method of controlling battery pack humidity (US8247097B1 [103]) and a battery pack dehumidifier (US20120315517A1 [104]) with an active reactivation system for absorbing/adsorbing water vapor. Ford's disclosure (US20170214016A1 [105]) details an electronics umbrella for preventing moisture, such as condensation, from infiltrating an electronics module housed inside the battery pack of an electrified vehicle.

Only a few patents focused on detecting unwanted, intruded, or leaked liquids were found. Bosch and Samsung have claimed a patent (US20120194004A1 [106]) for an automotive battery pack where the BCU cuts off electrical connection between the battery modules (by disconnecting

the sub-relays) when it is determined that the battery pack is damaged from an airbag impact, moisture, or impact sensor,

Volvo has been granted an application (US20190198946A1 [107]) of a damage detection and warning system of a battery pack, where optical sensor is used. It includes an optical fiber, an optical receiver and an optical emitter. The optical receiver is configured to detect an optical signal transmitted through the optical fiber, and the optical sensor is configured to detect an alteration of the optical signal being indicative of a deformation. This application is not aimed to detect a liquid leakage or intrusion detection in particular, but it utilizes fiber optic sensing devices inside an automobile's battery pack. Such technology and measurement technique is of concern for this dissertation, as it could be implemented for the optical liquid leakage and intrusion detection system.

IHI Inspection and Instrumentation Co Ltd has invented a liquid detector and liquid identifying system based on optical fibers (EP2604991A1 [108]), although without specifying whether the fibers are glass or polymer. The system is used for detecting any liquid leaked from the casing, where the optical fibers are located outside of the casing itself. The liquid detection is realized through bent optical fibers, which indicates that the intrinsic sensing technique is used there. According to the provided so-called identification table, depending on the bending radius different types of liquid can be detected: liquid with RI greater or equal to 1.33, liquid with RI greater than or equal to 1.44, and liquid with RI greater or equal to 1.50.

The invention claimed by (US5514920A [109]) is a fuel dispenser leak detector that is used for detecting the presence of a liquid in the base of a dispenser containment box and interrupting the supply of electrical power when such liquid is detected. Although it is not specified whether the invention utilized glass or polymer optical fiber cables, the sensing technique is based on extrinsic sensing because of the used prism-like transparent body. The optical probe itself is coupled to a light-emitting diode, a photosensitive transistor, and includes a light path with at least one total internal reflection surface. The device is used only for presence detection, not for detecting the type of liquid. It is to be positioned near the bottom of the containment box.

Microvast Power Systems has patented (US2013018352A1 [110]) a liquid leakage detection method, where the detection is aimed for electrolyte of battery cells. The application points out that a conventional way of detecting the liquid leakage is by using a gas detection. A battery box is a relatively hermetic space, where some gases are often formed and released when the electrolyte is leaked from the battery pack, and these gases can be detected by a gas detector. In such case, it represents that an accident of leakage occurs to the battery pack. This method is described as relatively expensive solution, which cannot deliver a good detection effect when the concentration of gases is relatively low. The leaked electrolyte is a flammable organic material, and is easy to ignite due to sparks or electrostatic discharges when being exposed to the air, which reduces the safety of the battery pack and endangers the vehicle.

For this application, a battery pack system comprising a plurality of individual batteries, an isolated liquid and a battery box containing the isolated liquid was presented. The battery cells are soaked in the isolated liquid, which is a fire-retardant and insulating liquid (one or both of silicone oil and transformer oil) that has a specific density smaller (0.95 kg/L) than electrolyte (1.5 kg/L) and is insoluble in the electrolyte. The box body is formed with an isolated liquid outlet and an isolated liquid inlet. A liquid separation device and a circulation pump are further disposed in the circulation passage. The liquid separation device is connected with a detection device. When the electrolyte is leaked from any of the battery cells, the isolated liquid mixed with the leaked electrolyte is detected by a detection component, in this case a conductivity sensor. The application describes a detection component as one or more of: a conductivity sensor, a PH sensor, a fluorion selective electrode and a liquid-level refraction sensor.

Toyoko Kagaku's invention (US20050162280A1 [111]) relates to a liquid leakage detecting system for detecting a leakage of an electrically conductive liquid (such as water, acid solution,

alkaline solution, etc.), and a leakage of a liquid having an insulating property (such as pure water, organic solution of an alcohol, benzene, etc.). This invention is not related to electric vehicles, nor automotive industry in general, but the detection system utilizes optical devices and extrinsic sensing techniques. In particular, the light is projected from a light source to an opaque filter, where the filter changes into a transparent state by absorbing a leaked liquid. Thanks to that, the liquid leakage can be accurately detected based on measuring the amount of a received light through the transmitting filter or from a reflecting light on the above filter. The light waves are guided to the filter using optical fibers.

Ali Reza et al have patented (JP2013250281A [112]) a leak detector using optical fiber. The apparatus comprises an optical fiber sensor for detecting leakage of fluid from a hose as quickly as possible and detecting a location and type of the leak. A fiber optic sensor may include an optical fiber and a fluid sensing material that causes a volume change upon contact with a particular fluid. Changes in the volume of the fluid sensitive material can cause optical fiber microbending. Preferably, the optical fiber is tied to the fluid sensitive material by a thread, such as a Kevlar. Due to the volume change of the material, the optical fiber can be pressed against the yarn, causing microbending in the fiber. Optical fiber microbends result in light loss due to attenuation, reducing the intensity of backscattered light from the expansion point. The Optical time domain reflection (OTDR) measurement emits a series of very short high power light pulses into the optical fiber. As the light travels along the length of the fiber, it is internally reflected and a small amount of light is backscattered to the source detector. This data is then collected and processed. If there is a leak in the internal hose carcass or the external hose carcass, oil or water enters the space between the two layers. This results in local microbends of the optical fiber as the petroleum or water passes through the porous protective sleeves and expands coating of the sensors. The microbends lead to an increased loss of detected backscattered light.

Kim Sung-kyu's invention (KR20210037459A [113]) presents a battery pack comprising a flexible printed circuit board (FPCB) for liquid sensing. Due to changes in external temperature and humidity, water condensation may occur inside the battery module. If it penetrates through the current-carrying part, a short circuit may occur and the battery module may be damaged. Provided circuit is capable of transmitting a liquid detection status signal to a BMS or an ECU of a vehicle. The aim of the invention is to utilize an FPCB inside a battery module to provide a battery module capable of monitoring the occurrence of condensation or penetration of moisture inside the battery module.

The patent search conducted for the dissertation yielded 200 inquiries, out of which 9 inventions were identified as relevant to the topic of the doctoral research. The majority of the inventions were primarily focused on waterproofing the mechanical construction of battery packs and moisture management. These inventions were linked to major car manufacturers, including Toyota, Mitsubishi, Tesla, and Ford. Only a minor portion of the examined inventions considered the detection of liquids in battery packs. A single patent (attributed to Volvo) was found that employs polymer optical fibers and an optical path. However, the primary application of this invention is to detect deformations in the mechanical structure of the battery system, not the presence of liquids. Nevertheless, such an application is important for the sake of this dissertation, as it proves the implementation of polymer optical fibers and intensity-based sensing in the context of electric vehicle battery packs. Thus, while there are patents addressing various aspects of moisture and fluid management in battery systems, there seems to be a noticeable gap in the patented solutions specifically targeting the detection of liquid intrusion using optical signals within EV battery pack systems.

As different liquid detection concepts have been considered throughout this dissertation, the noticed gap has been filled with two different patent applications. The first (optical liquid detection sensor device, publication no. GB2602001A [24], aimed for the detection of liquid presence, regardless of its type, that utilizes an extrinsic sensing technique (described in Section

3.1). The second and more complex that is subject of this dissertation (optical liquid detection system device, application no. GB2203308.8 [25], aimed to provide a fault-detection mechanism (liquid intrusion and liquid leakage), using an intrinsic sensing technique thanks to the polymer optical fiber sensing device. The system was described in Chapter 4. The sole authorship of both patents is attributed to the author of this dissertation, and they have been assigned to the Dräxlmaier Group.

2.5 Conclusions

Battery packs of electric vehicles have been deeply researched and described. An overview of battery thermal management systems has been provided, including the immersion-cooled battery packs, for which the liquid detection system of the following dissertation is being researched and developed. Scientists are concerned that the industry has paid too little attention to battery thermal management systems and the focus has been put on cutting costs and boosting the amount of energy of a single battery cell [114]. Although complex in design, it has been already applied to low-volume cars such as McLaren Speedtail, Mercedes AMG GT 63 S E Performance, and Faraday Future FF91 vehicles [15, 17, 18]. In the automotive industry, as the technology readiness level matures, one of the further steps is to implement new technology into low-volume cars before it reaches the high-volume ones. This is a good sign as the immersive cooling strategy is a promising technology that is reaching more attention among car manufacturers.

Internal and external faults of battery packs were described. Provided research lists accelerated degradation and a thermal runaway as the most severe faults that can occur. The following dissertation focuses on the detection of faults associated with liquid leakage and liquid intrusion. In the context of battery packs with a direct liquid cooling approach, such faults can cause degraded performance of the battery thermal management system, e.g. by causing coolant leakage or water intrusion. It is important to point out, that in the context of immersion cooling BTM, water intrusion is among the factors causing a short circuit and coolant leakage is among factors causing system overheating. Both faults may lead to failure propagation. The consequences of such cascaded events in a large LIB pack can be severe due to a release of large amounts of heat and flammable gases. As a result, a very dangerous situation for automotive battery packs occurs, i.e. the thermal runaway. Rapid increase of temperature and pressure increases the risk of combustion and explosion [20].

Fault diagnostic algorithms were classified into two main categories: model-based methods and non-model-based (also called model-free) methods. Model-based techniques often have low computational cost and fast detection time. They, however, depend on the accuracy of battery modeling. An accurate LIB battery model has not been fully developed yet, and the faults themselves were not fully understood due to the complex electrochemical properties of the lithium-ion battery cells. Non-model-based techniques do not rely on the battery model, but they require a time-consuming training process that needs a large amount of data. Several applications of ML methods in lithium-ion battery packs were also described. Provided review and reviews conducted by [7, 90] have revealed that many presented applications of model-based and non-model-based fault diagnostics for LIB are based either on simulation study or through an experimental test of a prototype system with a limited number of lithium-ion secondary cells. Due to that, further research is needed to verify developed fault detection techniques in the real-life LIB pack system, where factors such as hardware limitations, noise effects, environmental conditions, and cell aging play a significant role. ML-based techniques are highly dependent on the external parameters that are measured by sensors. Researchers often assumed either the sensor or battery is trouble-free, which may cause serious consequences in a real-life system. Adverse environmental conditions do influence not only battery performance, but the hardware as well. Taking these factors into account, the effective determination of fault threshold is to be

researched, since most of the studies use fixed threshold or double-threshold approaches, and the concept of adaptive threshold has not yet been deeply explored.

3. Introduction to polymer optical fiber sensors

Over the years, car safety, entertainment, and comfort have been significantly improved due to increasing number of electronic devices. Because of that, wiring harnesses were becoming more and more complex. These factors, among others, caused the total weight of the car to increase. Because each automotive manufacturer developed its own proprietary wiring standards, cost optimization for mass production was not as effective as it could be. In 2000, German auto manufacturer Daimler-Benz realized that the way to reduce costs was to develop and buy to a common standard, and its further analysis indicated that Plastic Optic Fibres (POF) ring networks would meet the needs of future automobiles. Six of the main automotive manufacturers (including BMW and Volkswagen) were convinced to join it in developing a standard called MOST (Media Oriented Systems Transport). The MOST Cooperation is responsible for the development and promotion of the MOST Technology. Not only specifies the optical interface and connector recommendations, but also releases the MOSTPlatform specification to the network and application interface (Fig 3.1) [115, 116].

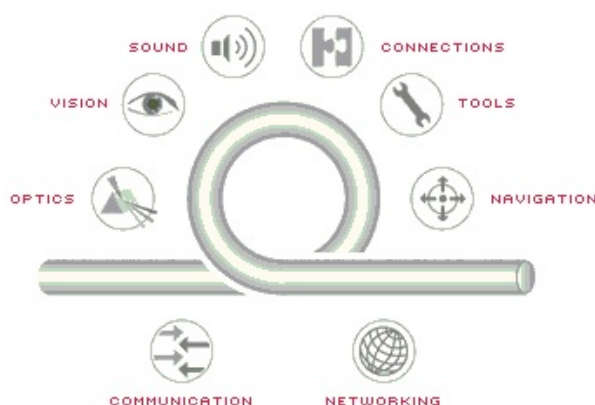


Fig. 3.1. Scope of the MOST Cooperation [116]

There is tremendous pressure from automakers on their suppliers to reduce prices. By developing a standard that is accepted by automobile manufacturers, suppliers can produce to the same standard and obtain economics of scale. This has a major impact on all sectors of the POF industry.

Electrical sensors represent the majority of sensor applications in the automotive industry. However, there are hazardous areas and factors within the car that can significantly increase the cost of using them:

- For high-voltage systems, there is usually a need to protect low-voltage signals (and their processing) from a high-voltage system. To achieve this, additional electrical components and isolation have to be used.
- For devices, where a strong electromagnetic field is being generated (i.e. where high currents are drawn, e.g. by inductive loads such as motors), the sensors need to have hardware filtering, or they need to use digital filtering that is done on a software level.

This is exactly the case for electrical vehicle's battery pack systems. The liquid leakage and intrusion detection system, being a part of this dissertation, can take advantage of using optical signals instead of electrical signals, especially in high-voltage and hazardous areas to mitigate those issues. Such areas usually exist on the battery pack level, between battery modules (which themselves usually are low-voltage areas). This chapter focuses on polymer optical fiber sensors, in particular, the sensing techniques, their manufacturing technologies, and applications in hazardous environments. Such research and drawn conclusions are later used as a base for the development of the optical liquid detection system, capable of detecting both liquid leakage and intrusion faults.

3.1 Sensing techniques

Optic fiber-based sensors (not only polymer) present several advantages over other sensing technologies, with the most important being immune to electromagnetic interference (EMI), compactness, lightweight, multiplexing capabilities, and higher sensitivity. When compared to silica optical fibers, POFs have higher flexibility to bending, higher sensitivity to strain, higher thermo-optic coefficients, and require fewer handling precautions (they do not produce sharp edges when broke). However, both Glass Optical Fibers (GOFs) and POFs can not be bent, such as traditional cables and wires, because the core (either silica or polymer) may break. For POFs, the operating temperature range is significantly narrower, which can limit their use in the vehicle. However, the transition from ICE vehicles to BEVs caused major changes in operating temperatures inside the vehicles. Because BEVs are powered by secondary cells, the operating temperature range is narrower, especially for lithium-ion battery packs. Their range fully covers the operating range of polymer optical fiber sensors [117].

Several parameters can be measured by exploiting the properties of light, depending on a sensing methodology. This includes refractive index, temperature, humidity, strain, pressure, bending, color, and turbidity. The scientific community managed to research and develop the following sensing techniques:

- variations of intensity,
- wavelengths shifts,
- interferometry pattern changes,
- plasmon resonance,
- polarimetry interaction.

To achieve the techniques mentioned above, the fiber itself may require morphological or chemical modifications, such as bending, polishing, etching, drilling, tapering, photopolymerization, thin film deposition, etc [115].

3.1.1 Intensity-based sensing

Measurements based on the variation of light intensity have a significant advantage (over other methodologies) through low-cost components. The simplest measurements of this kind can be done using a light source, a light detector, and an optical fiber. The light, transmitted by the source, is guided by the optical fiber. It then reacts with the environment, and as a result, a distorted light beam is received by the detector. Intensity-based sensing can be divided into the following categories:

- Extrinsic sensing (Fig. 3.2) - light leaves the POF into an external medium, interacts with it, and then is captured again by the POF. Extrinsic sensing is the easiest to use and is sometimes called an air-gap design. The intensity variation depends on the optical coupling between fibers and the environment (which property is to be measured).



Fig. 3.2. Extrinsic sensing methodology [118]

- Intrinsic sensing (Fig. 3.3) - light does not completely leave the fiber and tries to promote the interaction of its evanescent field with the external medium.

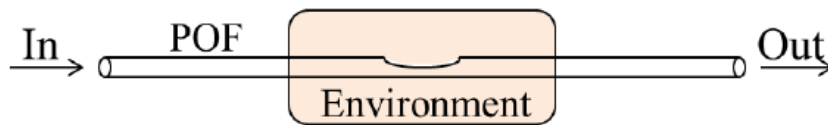


Fig. 3.3. Intrinsic sensing methodology [118]

Evanescent field of the optical fiber

The light travels through the fiber based on the principle of attenuated total reflection. It strikes the core-clad interface at an angle greater than the critical angle, resulting in total reflection of the propagating waves in the core. However, there will be some vibrations in the clad to prevent the violation of Maxwell's equations and associated boundary conditions. These electromagnetic vibrations are known as evanescent waves (EW).

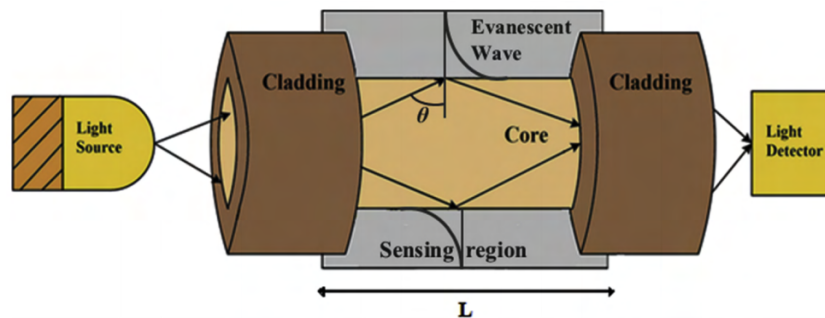


Fig. 3.4. Diagram of an evanescent wave-based fiber optic sensor [119]

EWs are the exponentially decaying electromagnetic fields in the optical fiber clad that correspond to radiative losses of the transmitting light through the optical fiber (Fig. 3.4). The exponentially decaying field has the ability to penetrate the medium placed in contact with the fiber. The interaction of evanescent wave with surrounding medium can be manipulated by modifying the fiber's cladding or the fiber's geometric structure itself (e.g. by polishing, tapering, etc.). This will lead to the change of critical angles of refraction and result in a variation of output power (i.e. the light intensity at the fiber's output).

3.1.2 Wavelength-based sensing

Wavelength-based sensing can be achieved by altering the refractive index of POF sensing area by ultraviolet or infra-red light exposure. This is usually done using phase mask or interferometric patterning methods for small grating pitch. Fiber Bragg Gratings (FBG) and long period grating

(LPG) are technologies that use this principle by creating a periodic refractive index change in the POF's core. The interaction between light and these periodic structures (Fig. 3.5) can be detected with high-resolution spectrum analyzers.

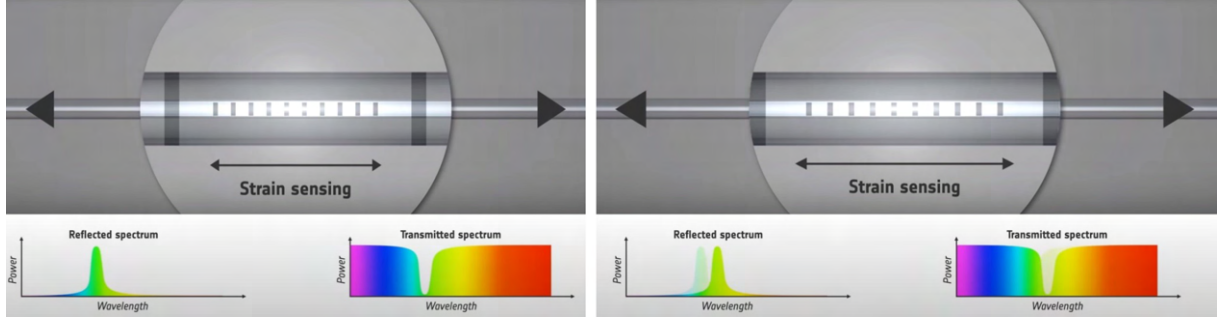


Fig. 3.5. Wavelength-based sensing principle [120]

The FBG preferentially reflects light with a wavelength λ_B determined by the Bragg condition [121]:

$$\lambda_B = 2n\Lambda, \quad (3.1)$$

where n is the effective index of the guided mode and Λ is the spatial period of the modulation. FBG sensing can be used e.g. for temperature, strain, deflection, pressure, and refractive index sensing because any of these perturbations applied to the fiber may change both the period and index of the grating leading to a shift in the reflected wavelength which can be determined by spectroscopic measurement of some kind [115, 122].

3.2 Refractive index sensors

Conducted research revealed that refractive index POF sensors can be fabricated using several techniques. Research given by [123] presents U-shaped (or U-bent) double side-polished POF sensors, which were experimentally demonstrated to have a sensitivity of 1541%/RIU within the RI range from 1.33 nD – 1.39 nD. These sensors are fabricated by rotating the POF around a steel cylinder, followed by a heat treatment which helps to obtain a small bend radius. After that, a grinding paper is used to symmetrically polish the bent POF. The final part is to reduce the roughness of the exposed area with fine grinding. Fabricated sensors are presented in Fig. 3.6. Authors have investigated the influence of the polishing angle, the polishing depth, the curvature radius, and the temperature on the sensor's performance. In comparison with the U-bent sensor that was not polished at all, any polishing results in the increased sensitivity. Authors have measured sensitivities for polishing angles from the range of 30° - 90°, and the highest sensitivity was obtained when the polishing angle was set to 60°. Polishing depth does influence the sensor's sensitivity - it monotonously increases when the polishing depth is lower than 400 μm . Further increasing the polishing depth results in decreased sensitivity. For the curvature radius, the sensitivity increases as the bending radius is decreasing, due to enhanced interaction between the light guided by the fiber and the external medium. The sensor's transmittance as a function of RI at temperatures in the range of 20°C - 50°C, with a 10°C step was measured. The sensor exhibits transmittance variation over this temperature range. As pointed out by the authors, this is caused not only by the thermo-optic effect and thermal expansion of the POF sensor structure but also by the thermo-optic effect of the measured liquid. The authors have compensated the

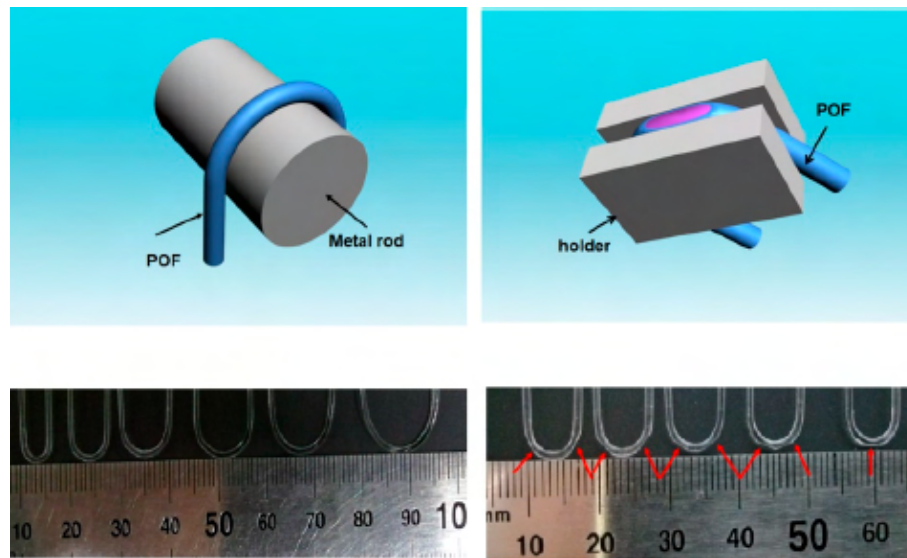


Fig. 3.6. Fabrication process and pictures of U-shaped double side-polished POF sensors [123]

variation of the measured liquid's refractive index due to the temperature change. After that, the POF probe showed almost linear variation with the temperature increment.

Another proposed RI POF sensor was fabricated by microdrilling a POF with a 0.7 mm diameter holes (Fig. 3.7). According to the authors, when the hole is filled with a liquid having lower refractive index than the POF (usually 1.49 nD), then the hole behaves as a concave lens. In such case, the fiber's transmittance increases in proportion to the refractive index. The authors have evaluated an analytical expression for the transmittance and compared the calculations with the experimental results. Both the equations and the experimental results indicate that the hole size does influence the sensor resolution. The higher the diameter of the drilled hole, the larger the sensor resolution. Since the hole size influences the ruggedness of the POF, a trade off has to be found to satisfy both aspects. The authors haven't characterized the sensor over a wide RI range. Instead, only 3 liquids of different RI were used: water ($n = 1.33$ nD), n-dodecane ($n = 1.42$ nD), and 99% glycerol ($n = 1.47$ nD). The fabricated sensor's response does however fit the exponential curve, similarly to results presented by other researchers. Furthermore, the difference between experimental and calculated results showed to be less than 6% [124].

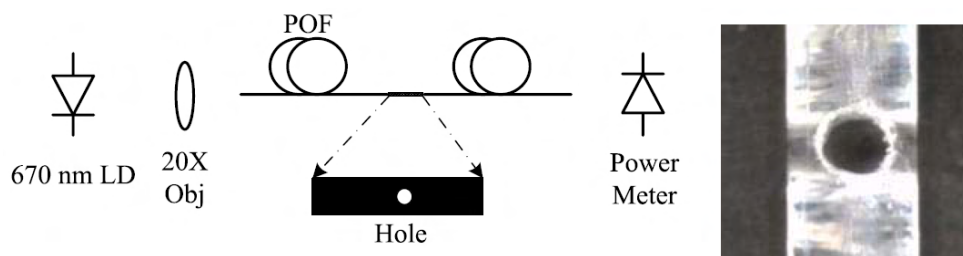


Fig. 3.7. Experimental setup for fabricating the POF refractive index sensor and measuring the transmittance. The photograph on the right shows a hole made in a POF [124]

A study by [125] shows a refractive index POF sensor fabricated by tapering methods. The fiber was fixed on an electrical translation stage on which a V-shaped groove was mounted. The tapering is done by pulling simultaneously both sides during the heating groove process. Authors have evaluated the sensor's characteristics for three different dominant light wavelengths, i.e. 532 nm, 633 nm, and 780 nm. The characterization was done using different sucrose solutions (with RI

in the range of 1.33 nD - 1.42 nD). Sensor sensitivity was found to be the highest for the 633 nm wavelength. Because of the tapering, the transmitted light power decreases as the refractive index of the external environment becomes larger. Researchers have observed that the sensor's linearity increases significantly when the diameter of the tapered region becomes smaller. Further experiments have shown that a double-tapered fiber performs better than a single-tapered POF. Its sensitivity was measured to be almost four times higher than for a single tapered RI POF sensor.

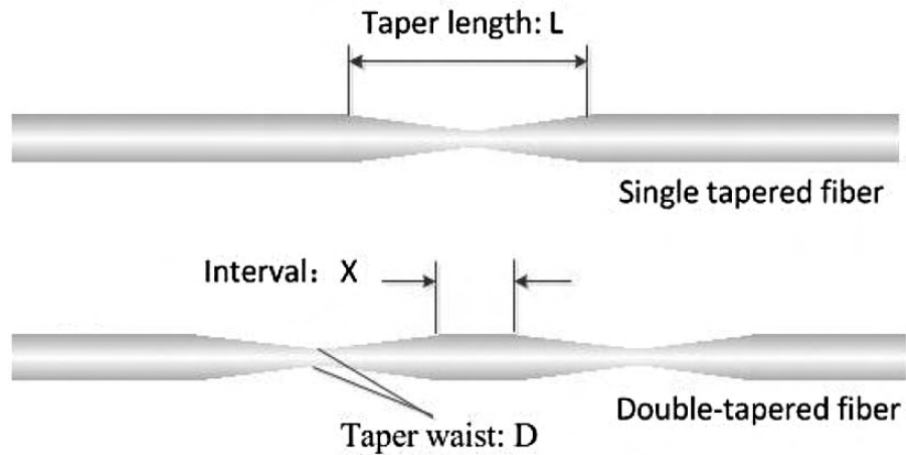


Fig. 3.8. Schematic of the single- and double-tapered fiber [125]

As presented by [126], a low-cost refractive index optical sensing system based on the variation of the transmitted light can be made using simple polishing methods. Authors have evaluated polishing procedures and investigated the relationship between the roughness of the sensing part, and the sensitivity of the sensor.

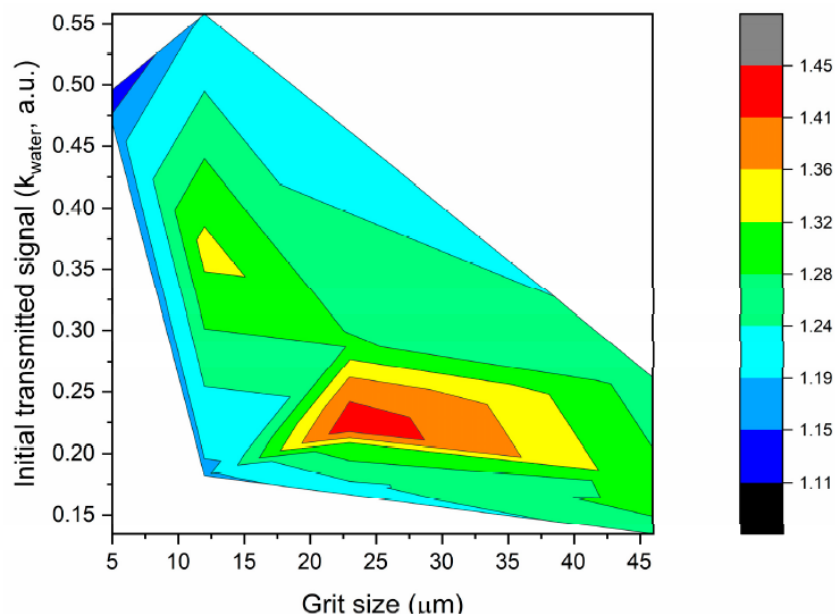


Fig. 3.9. Maximum response of the D-shaped POF sensors with the initial transmitted signal (k_{water}) and the grit size of the polishing [126]

The developed RI sensors are highly non-linear. The higher the refractive index of the external medium, the higher the sensitivity and lower the resolution of the sensors. Sensors present higher sensitivities when polished with sandpapers of lower gradations. Smoother surfaces allow for more light being transmitted, whereas rougher surfaces lead to more scattering losses, but up to a certain point. The best performances (by means of sensor sensitivity) were achieved after polishing the sensing region with P600 sandpaper (26 μm grit size) as presented in Fig. 3.9.

3.3 Applications in the automotive industry

Automotive systems have evolved from having a simple radio or CD player to having a variety of sophisticated entertainment and information systems that need to communicate and interact with each other and with a human user. As more and more digital communications connections are being utilized, increased demands on the architecture of the data connections as well as the transmission media are being made. Thanks to low weight, small cross-section and insensitivity to electromagnetic interferences, polymer optic fibers found their use in the automotive industry. The first comprehensive application of POF in data communication has been done in DaimlerChrysler vehicles (Europe, 1998). Nowadays, automotive systems are more feature-rich than many other A/V applications such as home Audio/Video (A/V) distribution, security A/V systems and industrial applications. MOST offers an optimized architecture for the real-time transport of audio, video, data and control. It is the backbone of modern infotainment systems [127]. This section presents the literature review of the POF-based sensing applications in the automotive industry.

3.3.1 Pedestrian protection system

Pedestrian protection systems are classified into two categories: passive systems (which only utilize structural measures, such as sufficient deformation room between the hood and engine, to cushion the impact) and active systems (that may trigger an action even prior to the impact). Siemens-VDO, in cooperation with the POF-AC Nürnberg, has developed a new sensor principle for detecting collisions with pedestrians [127]. The provided solution utilizes sensors to register the pedestrian's impact with the vehicle and then trigger protective measures [128], such as lifting the hood, by means of actuators as shown in Fig 3.10.



Fig. 3.10. Pedestrian protection system [127]

Siemens VDO's solution uses sensors to register the pedestrian's impact with the vehicle and then trigger protective measures, such as lifting the hood, by means of actuators. The solution uses a fibre optic cable as the sensor element, with a coupling element emitting the light pulses

to one end of the optical fibre and reading them out at the other end. The electronics system, also installed in the front end, analyzes the signal by means of the algorithms and triggers the actuation decision. This information is then forwarded to either a separate controller or a central control unit, such as the airbag control module, which subsequently triggers the actuators. Polymer fibers in which certain zones of the cladding have been modified to serve as sensing regions are called treatments. The treatment zones have been applied to the side of the fiber and are used for measuring the fiber's deflection. When the fiber is bent in the direction of the notches the coupling-out of light is diminished, when bent in the opposite direction the light emission is increased (Fig 3.11). Not only the degree of the bend can be determined, but also the direction.

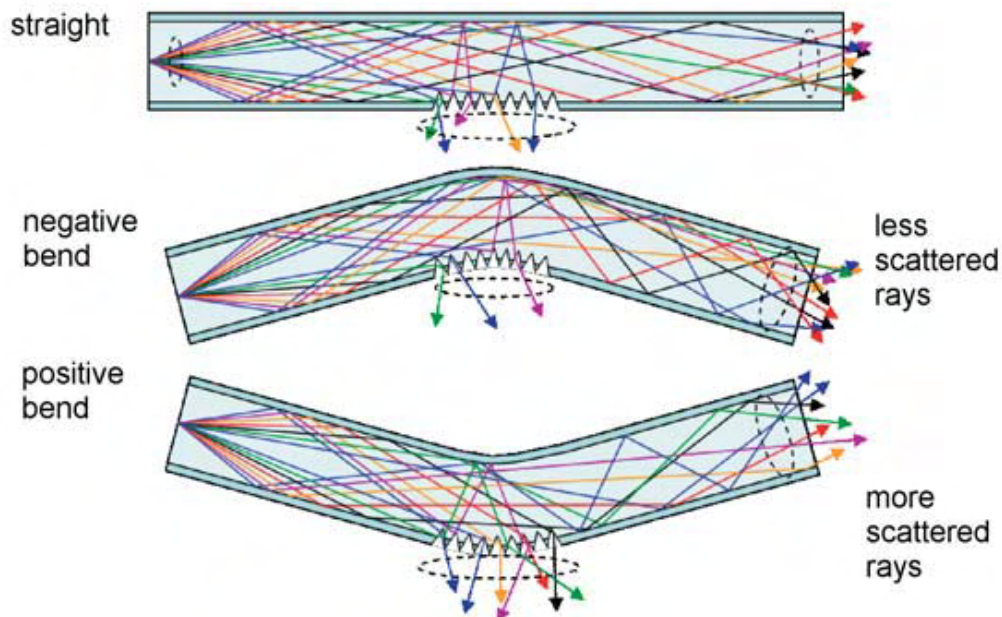


Fig. 3.11. Principle of the measurement of bending radius and direction [127]

According to [128], the sensor's characteristics is temperature dependent. The receiver receives different signal waveforms, since the front-end material becomes more elastic as temperature increases. For example, in test conditions of -40°C and $+85^{\circ}\text{C}$, the penetration depth of the leg impactor changes by up to 54%. Siemens VDO correlates the signal algorithm with the environmental conditions, to ensure that the actuators are not prematurely triggered in extremely hot conditions. The algorithm accounts for the temperature by means of three temperature classes (-40°C , room temperature and $+85^{\circ}\text{C}$).

Siemens VDO's pedestrian protection system consists of four POFs integrated into the ribbon and two additional strain relief elements. The laser-marked zones are positioned on the four fibres in a staggered pattern (Fig 3.12), so that the exact point of impact of an obstacle on the front end can be quickly localized. The 1.5×12 millimeter thin sensor runs in a loop across the front end. Nearly the entire width of the vehicle is covered by the staggered perforated zones. Only small nonsensitive sections are located on either end. One end of the loop leads into the light source, the other into the coupling element and electronic system. To close the cycle, the ribbon is deflected on a roll 30 millimetres in diameter on the other side of the vehicle.

Siemens VDO has patented both the sensor system for detecting the pedestrian collision in the front region of a motor vehicle (US20070162231A1), as well as the method for lasering the perforation of the sensor itself. According to [128], positioning the slits in a precisely geometrical and continuously reproducible manner requires expert know-how and is the key process

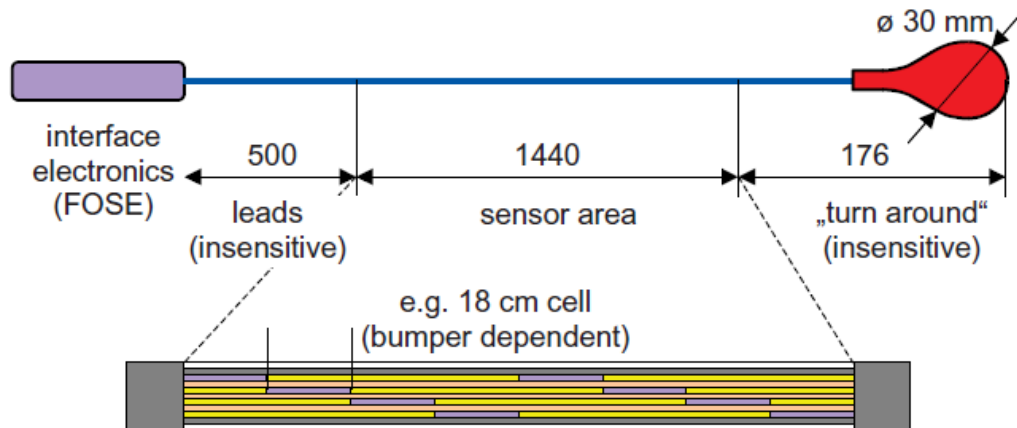


Fig. 3.12. Pedestrian protection system hardware setup [127]

of the entire production operation. The four-fibre conductor path unspools from a roll into the machining station, where it is cut at defined spots. These positions are then marked, re-sealed with a transparent filler and dried. In a second machining process, the ribbon is guided into an extruder and, together with the two strain relief elements, sheathed to form the finished sensor band. The sensor band is then cut into approx. 4-meter-long pieces for each vehicle, equipped with the coupling element, tested and finally connected to the electronic system.

3.3.2 Jam protection for car windows

In this case, a polymer optical fiber without the cladding serves as the sensitive element (anti-squeeze/presence sensor) in order to detect accidental closures of power-driven windows in personal vehicles. The sensor is based on microbend induced loss in the POF and relies on an all-polymer and flexible design that is favorable from the cost, safety, and mounting/packaging perspectives. The sensor utilizes the total internal reflection and evanescent wave absorption techniques. It consists of one flexible optical waveguide with a core similar to a normal plastic optical fiber. A sensing area is made of a light-absorptive layer in the optical cladding, which attenuation depends strongly on the local pressure (Fig. 3.13).

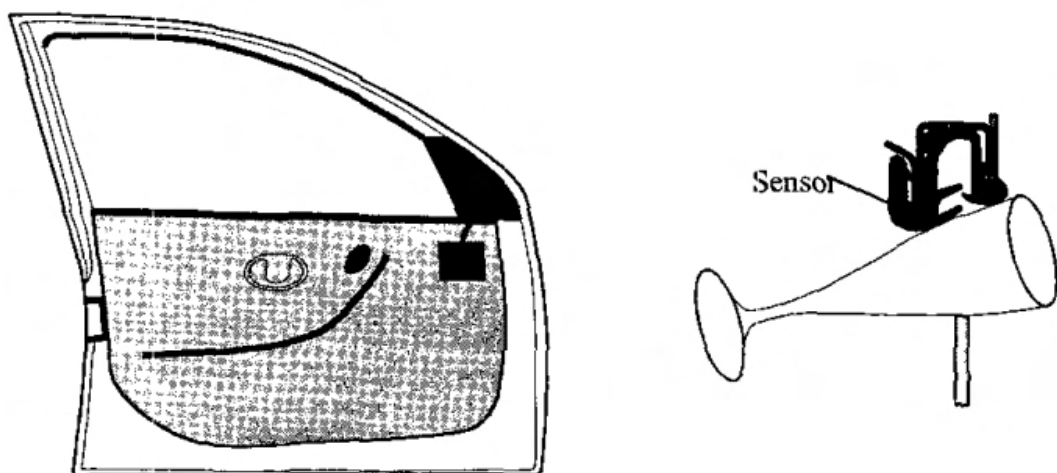


Fig. 3.13. Safety protection sensor for car windows [129]

Under pressure, the optical rays will be absorbed, resulting in a strong rise of the fiber optical attenuation. The life-span tests were performed at room and elevated temperatures (85°C). The results show that POF microbend sensors can easily reach and exceed 20 000 to 200 000 operational cycles. Further improvements are probably possible by additional optimization of the perturbation structure, and proper custom sensor fiber design. The presented sensor meets EU 2000/4/EC directive and FMVSS No. 118 requirements for passenger safety and can be readily applied as an anti-squeeze sensor in automotive applications. The presented experimental results show that when properly applied, POF can be used in relatively demanding applications, where the wear of the sensor is an important concern. While good mechanical durability is a known attribute of glass fibers, this work confirms a similar performance for polymer optical fibers [129].

3.4 Applications in aerial industries

For avionics industry, there is a need to reduce weight and improve safety of the aircraft's devices. As pointed out by [130], the consequent electrical wire damage is among major factors leading to airplane failures. Immunity to EMI is one of the substantial aspects which has promoted the migration of copper harnesses to optical fibre-based systems, following the "fly-by-light" concept. Modern aircrafts have higher operational needs motivated by the increase in safety-critical systems for flight and engine control, as well as non-safety-critical systems, such as structural and engine health monitoring systems, cabin environmental control systems, etc. According to researchers, they can be answered better in the optical domain. POF-based sensing have successfully been demonstrated for measuring temperature, discrete liquid-level, strain, vibrations.

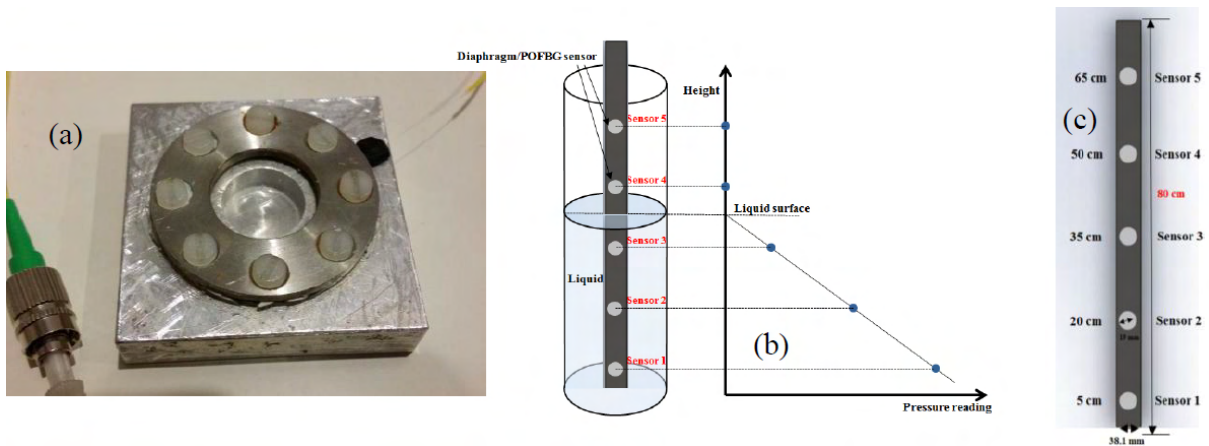


Fig. 3.14. (a) Design of the sensor system using a single POFBG. (b) Left: five discrete pressure sensors and determination of liquid level using linear regression. (c) Acrylic tube sensor arrangement [131]

The main disadvantage of an aircraft's electronic sensing solutions is the risk of explosion as the electrical current must be introduced into the flammable (or simply conducting) liquid. Optical fuel level monitoring for the aircraft's tank was presented by [131]. The pressure inside the tank is proportional to the density of the liquid multiplied by the depth and may be monitored by measuring via the deflection of a thin diaphragm exposed to the liquid on one side and ambient pressure on the other. The system utilizes a Polymer Optical Fiber Bragg Grating (POFGB) sensor attached to the surface of such a diaphragm. When the diaphragm deflects, the optical FBG sensor picks up an increasing strain. Authors have developed a multi-sensor

based system, which incorporates the idea of determining liquid level by measuring the pressure at the bottom of the liquid container. Their results demonstrate that the system has a highly linear response over the entire measurement region. The wavelength shift induced over the 75 cm measurement region was around 4.3 nm, leading to a mean sensitivity of 57.2 ± 0.4 pm/cm. (Fig. 3.14). They have fabricated a silica (9/125 μm) FBG sensor for a comparison. POFBG sensor presented sensitivity to water depth of 57 pm/cm, which was significantly higher than silica FBG sensor that presented sensitivity to water of 10.2 pm/cm.

Polymer Optical Fiber Bragg Grating (POFBG) sensors for detecting the water content in aviation fuel were developed by [131] (Fig. 3.15b).

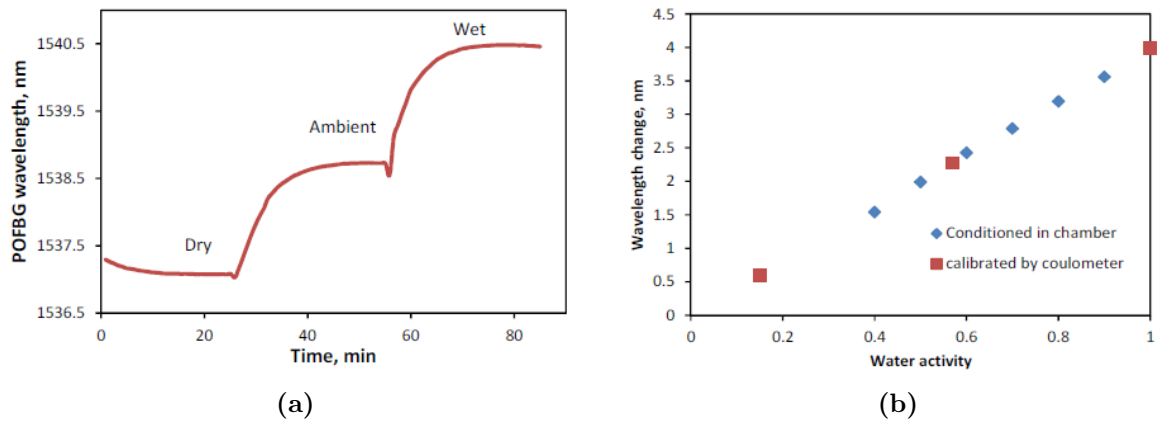


Fig. 3.15. (a) POFBG response of 3 calibrated fuel samples (b) POFBG wavelength change vs. water activity of fuel [131]

A critical situation occurs when the water content reaches the saturation point. If it's further exceeded, the free water becomes a destructive contaminant to almost all fuel applications. The free water will freeze at the low temperatures encountered in high-altitude flights, which may result in impeded fuel flow and plugged fuel filters. For the measurement of water activity in the fuel, the POFBG sensor was used. A PMMA based optical fiber grating sensor allows to detect very tiny amounts of water in fuels that have low water saturation point and potentially give early warning of the unsafe operation of a fuel system. This kind of sensors are wavelength-shift based. According to the results the sensitivity of water content detection in fuel using a POFBG can be estimated as 59 ± 3 pm/ppm for a grating at 1535 nm.

Structural Health Monitoring (SHM) is essential in aircraft transportation to reduce the time and costs related to maintenance. It also allows for continuous monitoring of the structures subjected to strain to prevent from exceeding their limits. According to the [130], POF based sensing stands out as ideal candidate for the strain measurement due to their relatively high Young's modulus. Figure 3.16 shows the schematic of POF-based sensor presented by [132] to measure an aircraft's flap elongation. The working principle relies on the comparison of the phase difference between two modulated light signals. The elongation of one of the POFs (POF1) leads to a phase shift in the signal, which can be measured by the corresponding photodetector (Receiver 1). It was reported that the sensors can be safely used in real-time conditions, with operating temperature up to 95°C . Experimental tests have shown high degree of repeatability and lack of hysteresis of the sensor signal observed in single movements and cyclical-type movements at different velocities.

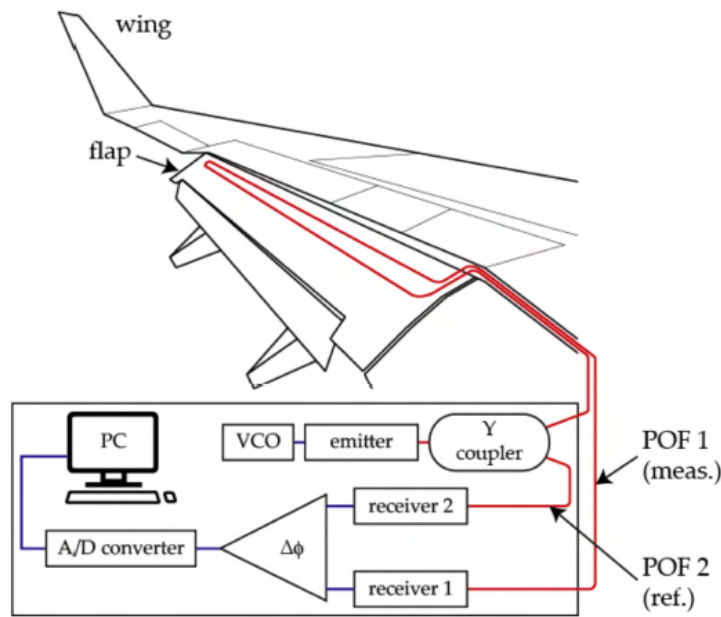


Fig. 3.16. Schematic of the POF elongation sensor to measure the elongation of an aircraft flap [130]

3.5 Conclusions

The conducted literature research shows that polymer optical fiber sensors have already been used in the automotive industry, e.g., for pedestrian protection systems and power window jam protection systems. Because the automotive industry is a type of industry where prototypes, new ideas, and emerging solutions are not published unless they are well protected or patented, not many applications or considerations of POF sensing applications were found. On the other hand, the avionics industry has also been researched due to the fact that this industry is even more demanding than the automotive industry. Here, more academic considerations of POF sensing were found. This proves that polymer optical fiber sensing is a point of interest even for such safety-critical and harsh environments. Based on the investigated sensing techniques, intensity-based sensing (in particular, evanescent wave absorption sensing) was selected as the technique that will be used by the liquid detection system. Research has shown that this technology can be simple in manufacturing, cost-effective, and capable of measuring the refractive index. The refractive index parameter can be used to distinguish different types of fluids, such as air (RI = 1.00 nD), water (RI = 1.33 nD), and oil (RI = 1.47 ÷ 1.48 nD). This would allow the system to monitor the state of the battery pack's coolant (e.g., mineral oil) by means of liquid intrusion (e.g., water) or coolant leakage.

4. Optical liquid detection system

It is important to differentiate between the battery pack system and the liquid leakage and/or intrusion detection system. The latter is the main goal of the presented dissertation and thereafter will be also called an Optical Liquid Detection System (OLDS, as per patent application GB2203308.8 [25]). Although full product development strongly exceeds the scope of this dissertation, the optical liquid detection system is meant to be an integral part of the battery pack system to provide measurements for the BMS. The following chapter presents the system's research and development results and is divided into three main parts. The first is system description, where architecture together with functional and non-functional requirements are described. The second is system implementation, which describes the developed electronic control module, communication protocol, and the assembled system. The third focuses on an experimental study on refractive index sensors. This comprehensive study highlights not only the fabrication process but also the resulting sensor's sensitivity with respect to the sensor fabrication procedure, the intensity of the light source, sensor reproducibility, and different operating temperatures. This chapter emphasizes the interdisciplinary activities that were performed in order to present to final versions of the iterative research and development process.

4.1 System description

Figure 4.1 presents a block diagram of the EV's battery pack (derived from Fig. 2.6), including the optical liquid detection system (OLDS). Although each component is subjected to a variety of faults, the optical liquid detection system is aimed at the detection of two of them, namely liquid intrusion and liquid leakage. The occurrence of such faults has been marked with red color in the aforementioned figure.

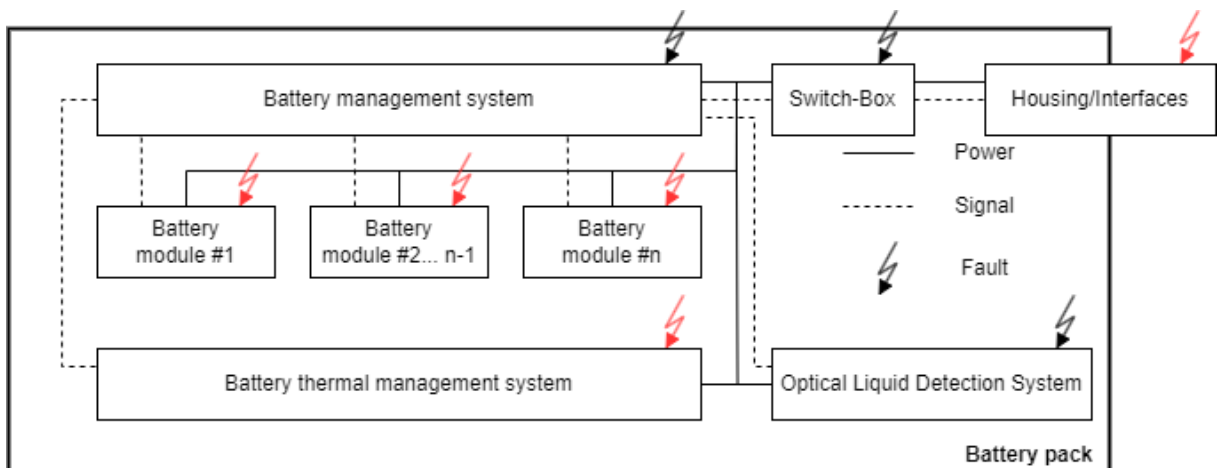


Fig. 4.1. Simplified block diagram of the electric vehicle's battery pack - with optical liquid detection system and faults

Because the battery packs of electrical vehicles are sizable, heavy, and expensive devices, the simulated battery pack system was meant to be significantly simplified for the development and validation phases. For a single battery module, a real battery module housing was used

(and equipped with the developed OLDS). The proposed, simplified system is shown in Fig. 4.2. Usually, a single battery module is a low-voltage device (the connection of multiple battery modules creates the high voltage area on a battery pack level). For the sake of this dissertation, areas called low voltage and high voltage can be distinguished. This is only for representative purposes, because due to safety reasons, no high voltage was present during the development, nor during the tests, and the system was supplied by a 12 V battery. Besides the battery unit, the low voltage area was occupied by a data recorder and an electronic control unit (ECU), which was connected to multiple polymer optical fiber sensors, and an external temperature sensor. Polymer optical fiber cables were guided from the low voltage area to the high voltage area, where sensing regions were placed and immersed in the coolant (oil) to monitor the state of the liquid. Besides polymer optical fiber sensors, a temperature sensor was placed in the high-voltage area as well. This sensor was used only for development purposes (to measure the temperature of the oil) and its data was not used by the developed fault detection algorithms.

Based on the presented block diagram, the development of the ECU (both hardware and software) and the polymer optical fiber sensors (design and fabrication) was in the scope of this dissertation. The data logger can be any suitable device that can be used for logging purposes. Although, polymer optical fiber sensors may have more than one sensing region, only one POF cable with one sensing region was employed.

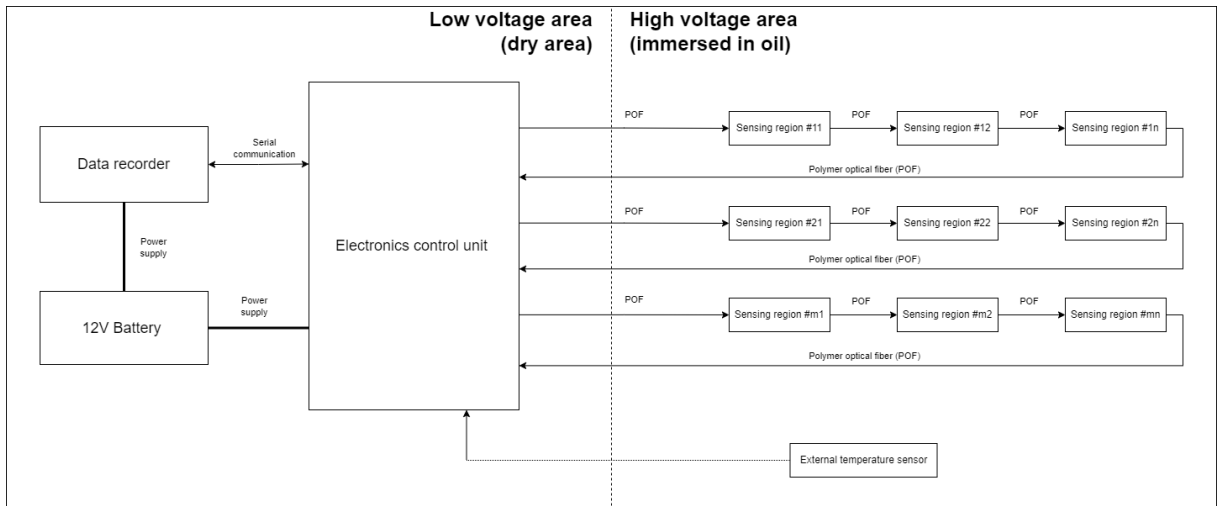


Fig. 4.2. Block diagram of a simplified battery module utilizing an optical liquid detection system

It was assumed that the purpose of the optical liquid detection system was to detect faults, in particular, either oil leakage or water intrusion (selected faults were described in detail in Section. 2.2.3). Different technical states considered in the dissertation were presented in Tab. 4.1. However, fault isolation and identification steps are beyond the scope of this dissertation.

Tab. 4.1. Considered technical states

State ID	State description
F0	Faultless state
F1	Oil leakage
F2	Water intrusion

The table includes the faultless state (F0) together with two fault states (F1, F2), where in the context of this particular, simplified battery pack system:

- Faultless state - corresponds to the battery pack system with the functionality and behavior within its specification and requirements.
- Oil leakage state - corresponds to the battery pack system with unpermitted deviations to the coolant level, e.g., due to damaged battery pack structure or sealings. In the initial phase, such a fault might cause abnormal performance of the battery thermal management system.
- Water intrusion state - corresponds to the battery pack system with intruded water, e.g. due to a damaged heat exchanger or condensed water. In the initial phase, such a fault might cause corrosion, short-circuits or damage other components with ice particles (when under low operating temperatures).

In order to detect relevant faults, the data processing concept has been formulated and presented in Fig. 4.3. The system acquires data from sensors such as POF sensors, 3-axis accelerometer, as well as internal and external thermistors. Based on collected datasets, the system monitors their values, and in case of any unpermitted deviation, the system is able to determine the presence of a fault and the period of occurrence. Through blocks with dashed lines the figure also shows that the system shall be able to determine the fault kind, location, time of detection, and fault ID. This is however beyond the scope of this dissertation. Additionally, according to the proposed fault detection methods (described in Chapter 5) not every sensor is necessary for a robust fault detection algorithm. However, such additional data were useful for the understanding of the system behavior.

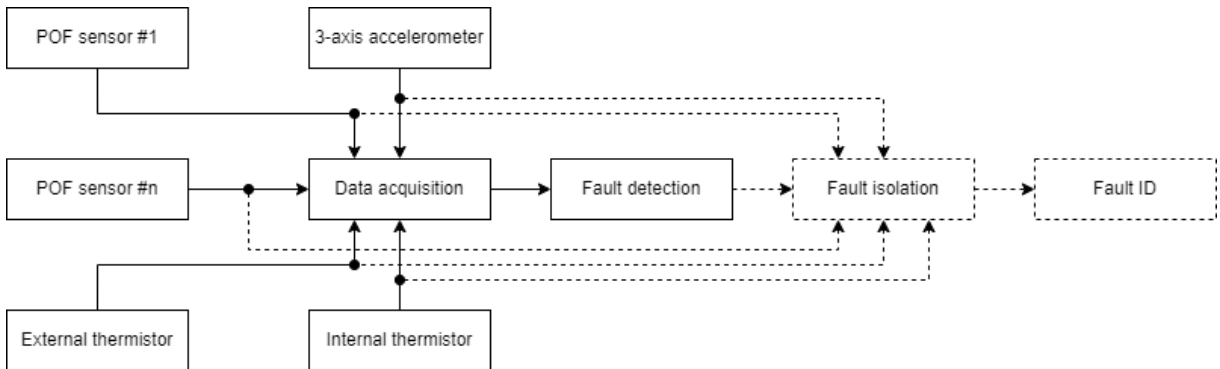


Fig. 4.3. Block diagram of the data processing

In the process of designing the mechatronics system for the OLDS, two categories of system requirements were established: functional and non-functional requirements. Both categories are crucial to a comprehensive system design process and allow for a holistic view of the system's needs and expectations. These two categories of requirements, though fundamentally different, are interconnected. Both are vital to ensure the OLDS not only fulfills its purpose of detecting liquid intrusion and leakage using polymer optical fiber sensors but also is robust and reliable enough to be integrated successfully into automotive applications. For the following dissertation, a set of generic functional and non-functional requirements was formulated, regardless of any particular Original Equipment Manufacturer's (OEM) standards. The requirements were formulated in cooperation with Dräxlmaier Group to ensure a common direction towards the implementation in the industry.

4.1.1 Functional requirements

Functional requirements are the primary and essential tasks that the system should perform - the core functionality that defines what the system is supposed to do. These requirements define the

interactions between the system and its environment, specifying calculations, technical details, data handling, and processing, and other specific functionalities. In the case of the OLDS, these functional requirements relate directly to its capacity to accurately detect liquid intrusion within EV battery packs. Given that, the OLDS:

1. shall be able to monitor its state through employed polymer optical fiber sensor measurements, including the faultless conditions, the water intrusion fault and the oil leakage fault,
2. shall be able to control the forward current of up to four polymer optical fiber transmitters (LED),
3. shall be able to measure the output signal of up to four optical fiber receivers (using photodiodes or phototransistors),
4. shall withstand a reversed polarity voltage up to 30 V at the main connector,
5. shall not electrically interfere or interrupt other devices,
6. shall be able to communicate with other devices,
7. shall be able to monitor the temperature inside the high-voltage area (external temperature measurement),
8. shall be able to monitor the temperature of the ECU itself (internal temperature measurement),
9. shall be able to monitor vibrations at the ECU level.

4.1.2 Non-functional requirements

While it is necessary that the system performs its primary function, it's equally important for it to operate reliably under real-world conditions. This leads to the non-functional requirements, which describe the system's behavior, characteristics, and performance standards. Non-functional requirements for the OLDS include resilience to environmental factors common in automotive applications such as wide operating temperature ranges, exposure to vibrations, and a long lifetime to match the vehicle's service life. They ensure the system's reliability, efficiency, and overall quality, enabling it to function effectively as a component of an automotive system, thus aligning with the broader standards of the automotive industry. The optical liquid detection system:

- shall present a fault detection time of at least 300 s,
- shall present a true detection rate of at least 80%,
- shall present a false detection rate of at most 2%,
- shall be fully operational under 9 V - 16 V input voltage range,
- shall be fully operational under an operating temperature range of -40°C - $+85^{\circ}\text{C}$ (including self-heating),
- shall have a start-up time of no longer than 5 seconds (including necessary calibration procedures),
- shall be able to distinguish fluid types of refractive indices in the range of 1.00 nD - 1.47 nD,
- shall present a Technology Readiness Level of 5 (Appendix A),
- shall communicate with other modules using a serial interface, for example, LIN bus,
- shall allow other devices, such as BMS to initiate a sensor calibration procedure,
- shall provide sensor measurements with the frequency of at least 50 Hz,
- shall allow other devices, such as BMS to request diagnostics data of the ECU.

4.2 System implementation

Thanks to Dräxlmaier Group's portfolio (that was briefly described in Section 1.1), it was possible to acquire a bottom part of the housing that is being used by a series production car, i.e., hybrid Mercedes AMG GT 63 S E Performance [18]. This battery pack is based on a single module that utilizes a direct-liquid cooling battery thermal management approach, where not only all battery cells but also the electronics are fully immersed in mineral oil. Internally named HPB80, the 6.1 kWh battery pack can deliver 94 hp of continuous power and 201 hp of peak power for up to ten seconds (Fig. 4.4a). The acquired part, presented in Fig. 4.4b, was used to build a technology demonstrator for an optical liquid detection system. Prototyping and testing phases performed with this part are considered more reliable. This is because the part is a single part made of casted aluminum alloy, that is able to operate under elevated temperatures without notable deformations. The housing is covered with a cover that was laser-cut from poly (methyl methacrylate).



Fig. 4.4. (a) HPB80 battery pack with immersive cooling [133] (b) Bottom part of the HPB80's battery pack housing

4.2.1 ECU development

A block diagram of the ECU that is a result of the functional and non-functional requirements described in Sections 4.1.1 and 4.1.2 is presented in Fig. 4.5. The ECU consists of a connector, a reverse polarity protection circuit, an ESD protection, an EMI filter, a DCDC converter, a microcontroller, current sources, photocurrent converters, four sets of POF connectors (receivers, transmitters), an inertial measurement unit (IMU), internal thermistor, and a connector for an external thermistor.

Reverse polarity protection circuit, electrostatic discharge protection (ESD), and electromagnetic interference (EMI) filters are used to improve the electrical safety of the ECU and other devices. DC/DC converter converts the input voltage to the level suitable for the microcontroller unit (MCU). The role of the MCU is to drive electro-optical circuits, perform measurements, communicate with the BMS or other devices, and perform diagnostics or share the measurement data with other devices. Current sources are used for setting a forward current of the transmitter (typically a red LED) inside the POF connector. Photocurrents generated by photodiodes have to be converted into a high-impedance voltage signal that can be measured by the microcontroller. POF connectors correspond to plastic housings with embedded transmitters (LEDs) or receivers (photodiodes). They are used to provide sufficient and reliable electro-optical coupling under road conditions. Furthermore, the block diagram presents that one internal thermistor is connected to the microcontroller, and the second, external, shall be connected via a provided connector. An internal measurement unit (IMU) is used for vibration measurements. The main

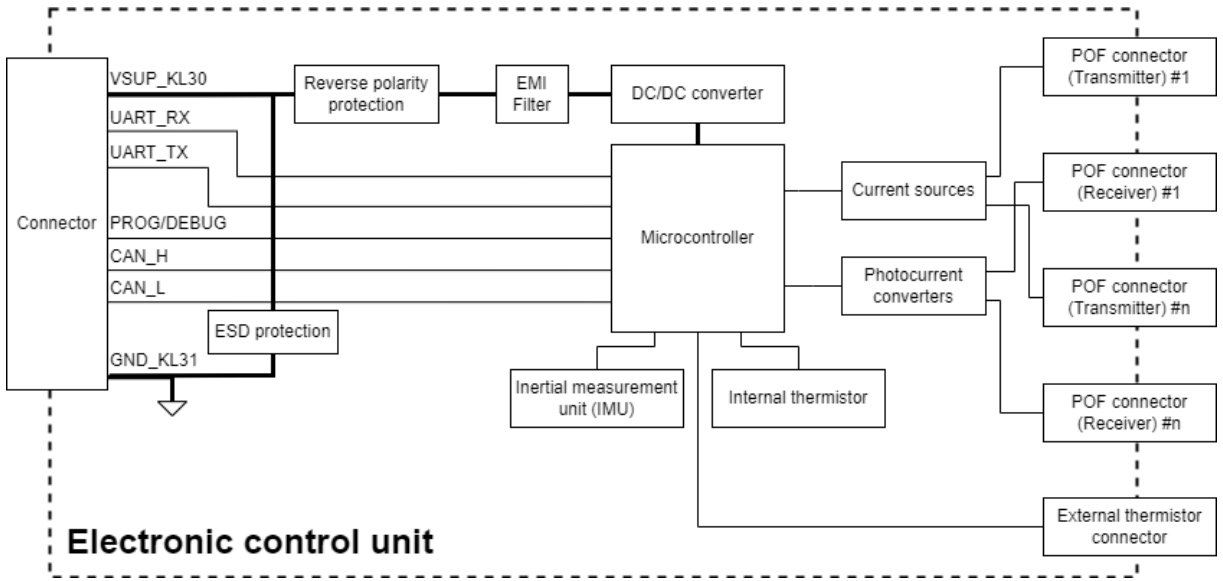


Fig. 4.5. Block diagram of the ECU

connector delivers the power supply, serial communication (UART, CAN), and an interface for programming and debugging. A block diagram of the electronics circuit that has been developed to fulfill the aforementioned requirements and assumptions is shown in Appendix. F. The designed PCB is presented in Fig. 4.6a, while the manufactured and assembled PCB is presented in Fig. 4.6b.

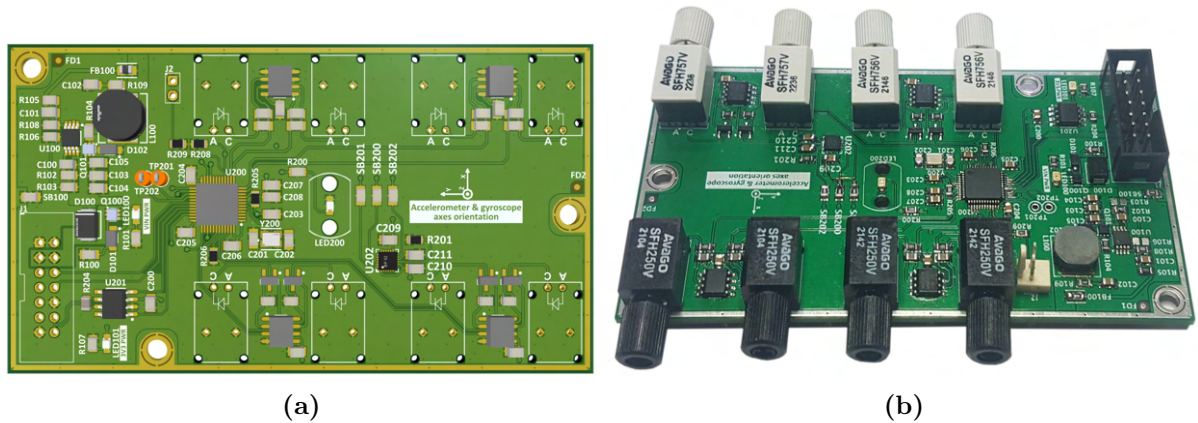


Fig. 4.6. (a) 3D-view of the designed ECU (b) Real image of the ECU

The ESD protection is provided by a bipolar TVS diode. The reverse-polarity protection is realized through a P-channel MOSFET. The device is turned on by applying a negative Gate Source voltage. By referring the Gate signal to the ground line, the device is fully turned on when the power is applied in the right polarity. For the first start-up, the intrinsic body diode of the MOSFET conducts, until the channel is switched on in parallel. The Zener diode clamps the Gate of the MOSFET to its Zener voltage and protects it against overvoltage. Under the reverse polarity, the MOSFET is switched off, because the Gate Source voltage for this case will be positive (voltage drop over the Zener diode). An additional Zener diode is used to increase the reverse-polarity protection voltage up to 35 V. The EMI filter is based on additional MLCC capacitors that reduce the unintentional energy carried out by the ECU to the car system, i.e. the conducted emissions. The DC/DC converter section utilizes a high-

efficiency P-channel MOSFET switching regulator controller that reduces the input voltage to 3.3 V. This voltage level is delivered to other parts of the ECU. For a microcontroller, an Arm® 32-bit Cortex®-M3 CPU core, STM32F103C8T6 is selected that can work with a maximum frequency of 72 MHz. POF transmitting and receiving connectors are realized by SFH757V and SFH250V respectively. Because POF sensors are based on the variation of light, it is important to deliver a constant light source. Although multiple factors may influence the light intensity (such as the temperature, forward current, and aging processes), constant current sources were developed to reduce the impact of at least one of the major factors. Receiving POF connectors (SFH250V) have embedded photodiodes. Because the generated photocurrents are in the range of a few microamperes (and the change in photocurrent caused by the light variation is in the range of hundreds of nanoamperes), an additional circuit was developed in order to not distort these high impedance signals through measuring circuits (such as ADC of the MCU). This was realized through transimpedance amplifiers. Such circuits have high-impedance inputs and are used for the current-to-voltage conversion, which allows the MCU to perform ADC measurements without influencing the high-impedance signals themselves. In total, four pairs of POF connectors are provided. For the inertial measurement unit, an MPU-9250 is selected. For both thermistors (internal and external), a 10 kΩ, with a 3455 K temperature coefficient and a resistance tolerance of 1% are selected.

4.2.2 Communication protocol

To visualize data collected by the ECU and to communicate with external devices (e.g., other embedded devices), the firmware of the ECU is supplied with a flexible communication protocol over a universal asynchronous receiver-transmitter (UART). The flexibility is achieved by having a variable payload size, where the ECU indicates how many payload bytes will be sent, and the receiving device parses every byte accordingly. The communication protocol is derived from the protocol used by an open-source SerialPLot application [134].

Tab. 4.2. Protocol architecture

Byte number	Byte description
1	Frame Start (first byte)
2	Frame Start (second byte)
3	Payload size (P)
4..P	Payload
P + 4	8-bit CRC of the Payload

The architecture of the communication protocol is described in Tab. 4.2. The frame starts with two starting bytes. This is followed by the size of the payload. To increase the protocol's robustness, an 8-bit CRC is generated out of the payload and sent as the last byte. The communication is programmed to work with a baud rate of 115200bps, 8-bit data, no parity, and 1 stop bit.

The protocol used for broadcasting all of the necessary measurements is described in Tab. 4.3. It is decided that 17 different `int16_t` fields are enough to cover all of the necessary data that shall be shared with other devices. To achieve that, the payload byte shall be set to 30 and shall use the little-endian sequence of bytes. The protocol is implemented on every embedded device used by the Optical Liquid Detection System (e.g., the ECU or data logger).

Tab. 4.3. Communication protocol used by the OLDS

Byte number	Field description	Base unit
1	0xAA	
2	0xBB	
3	30	
4, 5	Timestamp	seconds (s)
6, 7	1st POF sensor - TX signal	raw signal
8, 9	1st POF sensor - RX signal	raw signal
10, 11	1st POF sensor - RX signal (normalized)	percentage (%)
12, 13	2nd POF sensor - TX signal	raw signal
14, 15	2nd POF sensor - RX signal	raw signal
16, 17	Accelerometer - Ax	raw signal
18, 19	3rd POF sensor - TX signal	raw signal
20, 21	3rd POF sensor - RX signal	raw signal
22, 23	Accelerometer - Ay	raw signal
24, 25	4th POF sensor - TX signal	raw signal
26, 27	4th POF sensor - RX signal	raw signal
28, 29	Accelerometer - Az	raw signal
30, 31	Internal thermistor	millivolts (mV)
32, 33	External thermistor	millivolts (mV)
34, 35	Residual signal	raw signal
36, 37	Diagnostic signal	raw signal
38	8-bit CRC of the Payload	

The payload consists of:

- the timestamp (seconds) which starts once the system is powered on (the OLDS is not equipped with an RTC clock),
- transmitter's (TX) raw signal S_{TX} of a corresponding POF sensor. This value indicates whether the transmitter is turned OFF (value equal to 0) or ON (value equal to 1000),
- receiver's (RX) raw signal S_{RX} of a corresponding POF sensor. This value is a converted ADC measurement and it is treated as a raw signal of the returned light intensity,
- normalized receiver's (RX) signal S_{norm} of a corresponding POF sensor. When a calibration command is received by the ECU, the most recent ADC measurement is stored inside the flash memory as a reference S_{ref} . Since then, every further ADC measurement is according to the following equation:

$$S_{norm} = \frac{S_{RX}}{S_{ref}} \times 100\%. \quad (4.1)$$

Because the output values depend on how the system is assembled, such normalization can be used e.g., once the polymer optical fiber sensors are assembled inside the housing to achieve a common value for every sensor (starting with $S_{norm} = 100\%$ after the calibration).

- accelerometer's raw data, in the range of -32768 to 32767. The full-scale range of the accelerometer is programmed to ± 8 G, and to achieve acceleration units, the raw measurements can be converted using the following equations:

$$A_x = \frac{A_{RawX}}{4095}, A_y = \frac{A_{RawY}}{4095}, A_z = \frac{A_{RawZ}}{4095}, \quad (4.2)$$

- thermistor's output voltage (in millivolts to avoid the usage of floating point numbers) for the internal ($V_{T.int}$) and external ($V_{T.ext}$) thermistors. To obtain measurements in Celsius degrees, the first step is to convert the measured voltages into corresponding resistance values:

$$R_{T.int} = \frac{(V_{IN} \times R_{209}) - (V_{T.int} \times R_{209})}{V_{T.int}}, \quad (4.3)$$

$$R_{T.ext} = \frac{(V_{IN} \times R_{208}) - (V_{T.ext} \times R_{208})}{V_{T.ext}}, \quad (4.4)$$

where $V_{IN} = 3.30$ V, $R_{208} = R_{209} = 33$ k $\Omega \pm 1\%$.

Next, the obtained resistance values can be converted using a simplified B coefficient Steinhart-Hart equation [135]

$$\frac{1}{T_{int}} = \frac{1}{T_{0.int}} + \frac{1}{\beta_{0.int}} \times \ln \frac{R_{T.int}}{R_{T_{0.int}}}, \quad (4.5)$$

$$\frac{1}{T_{ext}} = \frac{1}{T_{0.ext}} + \frac{1}{\beta_{0.ext}} \times \ln \frac{R_{T.ext}}{R_{T_{0.ext}}}, \quad (4.6)$$

where $T_{0.int} = T_{0.ext} = 298.15$ K, and $\beta_{0.int} = \beta_{0.ext} = 3455$,

- calculated residual, as per chosen diagnostic method,
- generated diagnostic signal (as per chosen diagnostic method).

An additional set of messages can be also used to request particular actions from the ECU, including sensor calibration and data erasure. Such messages have different starting bytes and just one int8.t payload byte (Tab. 4.4) that indicates the ID of the requested action.

Tab. 4.4. Communication protocol used for action request

Byte number	Field description
1	0xBE
2	0xEF
3	1
4	action ID
5	8-bit CRC of the Payload

Depending on the given value of the payload, the following actions can be performed:

- 0xFF - the ECU will calibrate POF sensors as described above,
- 0xBE - the ECU will erase any previously stored calibration values.

4.2.3 System assembly

The optical liquid detection system was assembled in the lower section of the HPB80 battery pack housing, as presented in Fig. 4.7. This was conducted in strict accordance with the proposed system architecture, illustrated in Fig. 4.2. Two key elements of the system, namely the data recording device (1) and the electronic control unit (2), were placed within a dry, low-voltage area (3) of the system. The high-voltage region (4) was designed for complete immersion in oil, serving as the designated zone for fault injection experiments. This zone was occupied with a fabricated polymer optical fiber sensor (5) and an external thermistor (7), responsible for monitoring the temperature within the immersed environment. The routing of the POF cable and external thermistor from the high to low-voltage areas was carefully managed to maintain the integrity of the system. Given the original battery pack housing was not equipped with the necessary provisions for liquid sensing devices, additional mounting components were necessary. These were designed, 3D-printed using PET-G material, and subsequently incorporated into the system. These components play a critical role in preventing undesired movements of the POF cables that could potentially affect the sensor's performance. The housings incorporate small openings, strategically engineered to expose the polymer optical fiber cable and its sensing area (6) to the external medium, in this case, oil. As for the system's power requirements, a 12 V automotive battery was utilized. Given the spatial constraints within the battery pack housing, the power supply unit was located externally.

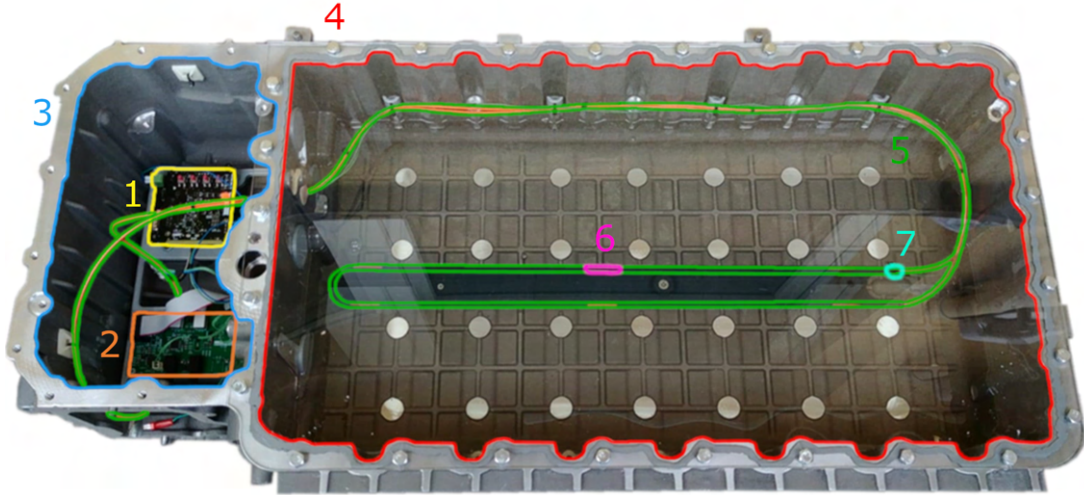


Fig. 4.7. OLDS assembly inside HPB80's housing

4.3 Experimental study on refractive index sensors

Based on the conducted research on polymer optical fiber sensors, the refractive index evanescent wave absorption sensing technique has been chosen and implemented in the optical liquid detection system. The concept of RI POF sensing inside an exemplary battery module with a direct liquid cooling approach as per patent application GB2203308.8 [25] is shown in Fig. 4.8. Under normal conditions, the battery cells, their connections, and the polymer optical fiber sensor are immersed in the coolant liquid (in this case an electrically non-conductive mineral or silicone oil). In such case, the RI POF sensor shall report the refractive index of the oil (that is susceptible to variation due to aging and ambient temperature). Based on the refractive index variation due to liquid intrusion or leakage, the fault detection algorithm should indicate a fault based on the provided POF sensor measurements.

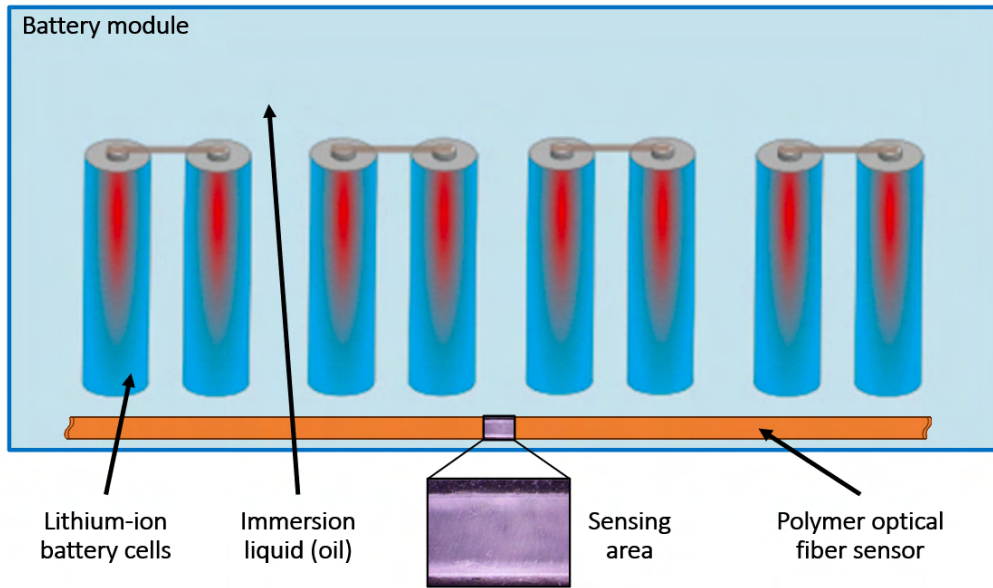


Fig. 4.8. Polymer optical fiber sensor placement

The research and development process of the refractive index evanescent wave absorption polymer optical fiber sensor has to take into account numerous factors for comprehensive evaluation and optimization. These considerations are critical to ensure that the sensor performs effectively and reliably under automotive conditions. Because of that, the following considerations are taken into account:

- Sensor sensitivity with respect to sensor fabrication procedure - the fabrication procedure can greatly affect the sensor's sensitivity due to potential variations in the fabrication process.
- Sensor sensitivity with respect to the intensity of the light source - the intensity of the light source directly influences the signal-to-noise ratio and the overall sensitivity of the optical sensor. Evaluating the sensor's response to different light intensities revealed whether a constant light source is needed for the operation of the optical liquid detection system and whether the intensity of the light source impacts the sensor performance.
- Sensor sensitivity with respect to the sensor reproducibility - reproducibility is a critical aspect of any sensor design. It refers to the ability to consistently reproduce the same output under identical conditions. Understanding the sensitivity of the sensor concerning its reproducibility is essential to ensure the reliability of its measurements and enhance its credibility.
- Sensor's output with respect to different operating temperatures - the operating temperature can significantly affect the sensor's performance due to potential changes in the optical properties of the sensor materials or the medium being sensed. This assessment is particularly crucial for applications where the sensor could be exposed to a wide range of operating temperatures, such as in automotive applications.

Investigating these aspects provides a thorough understanding of the sensor's performance characteristics, helps identify potential areas of improvement, and ultimately contributes to the design and development of a robust, reliable, and efficient optical liquid detection system. A summarized version of the research was described in [136].

The prototyped POF sensor is based on Mitsubishi GH4001 polymer optical fiber cable, where the EW absorption is enhanced by modifying the fiber structure, in this case by polishing

the sensing area of the POF. Automotive MOST polymer optical fibers differ in their construction in comparison with traditional POFs. They consist of a POF itself (made of a core and a cladding), an inner jacket (polyamide), and an outer jacket (soft polyamide) as shown in the Fig. 4.9. This makes the sensor fabrication process more difficult, as it is necessary to remove the outer as well as the inner jackets, prior to reaching the clad-core structure.

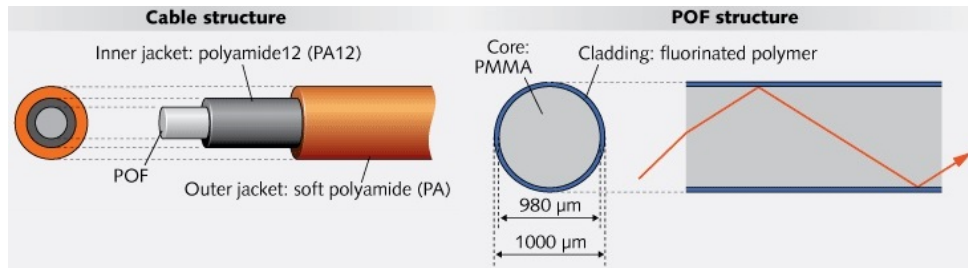


Fig. 4.9. Automotive MOST Polymer Optical Fiber [137]

Fabrication procedure

A starting point for the sensor fabrication research was formed on the results obtained by [126]. Two sets of POFs with lengths of 50 cm were prepared. For the polishing, a 3 cm long, middle areas of the POFs were selected. The fabrication procedure consists of a sequence of polishing, using sandpapers of different grit sizes in decreasing order. Smoother surfaces allow more light to be transmitted through the POF, whereas rougher surfaces lead to more scattering losses (which result in less light transmission through the POF).

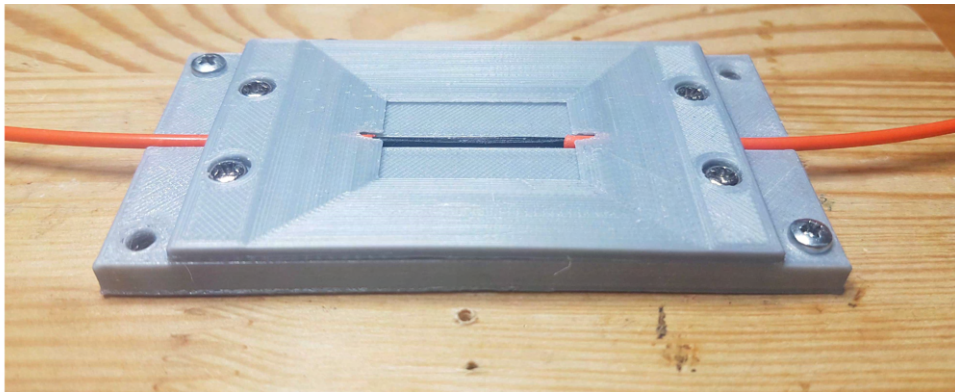


Fig. 4.10. A 3D printed platform used for a POF sensor fabrication

According to [126], the best sensor performance (by means of sensor sensitivity) shall be achieved when a balance between roughness (enhancing the interaction of light and the external medium) and transmission losses due to polishing is obtained. A custom polishing platform was designed and 3D printed (polyethylene terephthalate glycol) in order to mount and fix the position of the POF (Fig. 4.10). During the fabrication procedure, the POF is attached to the platform after removing the outer jacket, which is done carefully using a utility knife. After each polishing procedure, the sensing area is cleaned twice using distilled water. Later, microscopy images of the sensing region are taken, and the sensor is characterized by means of refractive index sensitivity. Figure 4.11 presents the microscopy images of the sensing region after each polishing stage. The bottom images present the sensing areas with the POF transmitter (red LED) turned ON. The polishing sequence starts with P80 ($\sim 195 \mu\text{m}$ grit size) that is used for

removing the inner jacket. This is followed by polishing with P220 ($\sim 65 \mu\text{m}$ grit size), and P400 ($\sim 38 \mu\text{m}$ grit size). The final polishing is done using P600 ($\sim 26 \mu\text{m}$ grit size) sandpaper.

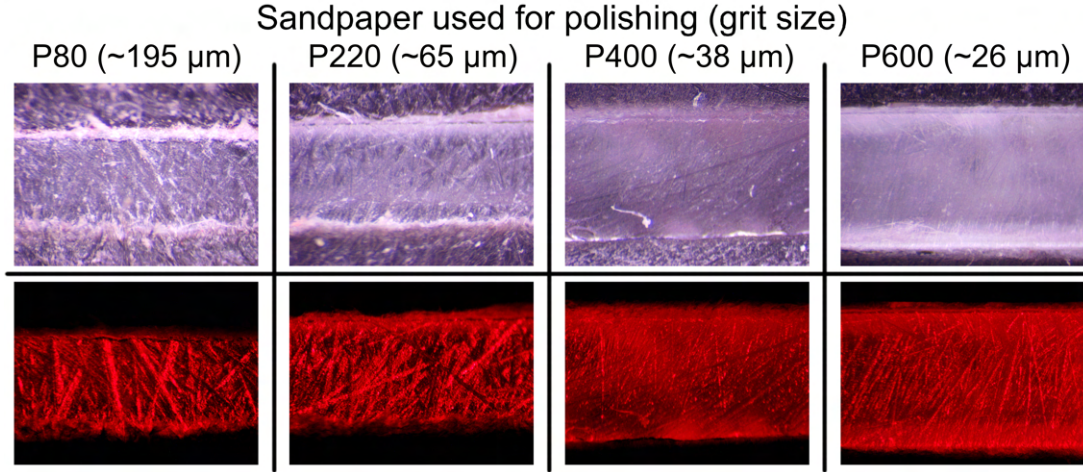


Fig. 4.11. Optical microscopy images of the sensing area after each polishing stage

Characteristics

The performance of fabricated sensors was evaluated by exposing the sensing areas to liquids of known refractive index values. Such characterization was done using solutions of distilled water and sucrose of different weight-to-weight (w/w) concentrations starting from 0% (distilled water) and ending at 50% with a step of 10%. Solutions were prepared according to Tab. B.1 using a magnetic stirrer at room temperature and verified with an external digital refractometer Kern ORF-R (measurement range: 1.3330 nD - 1.5400 nD, accuracy: 0.0005 nD[138]). Refractive indices of prepared solutions were listed in Tab. 4.5.

Tab. 4.5. Refractive index of prepared sucrose solutions

Measured refractive index [nD]	Estimated concentration [% w/w]
1.3324	0.00
1.3480	10.0
1.3614	19.0
1.3822	31.0
1.3992	40.0
1.4140	SL2672
1.4167	49.0
1.4776	Orlen Oil Trafo

Two different types of electrically non-conductive oils that can be used for immersion-cooled battery packs were placed in the table for reference. The first is Shell SL2672 oil, which refractive index was measured to be 1.4140 nD. It is within the range of 40%-50% w/w sucrose solutions. The second is Orlen Oil Trafo, which refractive index was measured to be 1.4776 nD and is significantly higher than the RI of the previous oil (which can indicate that this oil is of a different type).

Figure 4.12 presents the response of the fabricated refractive index sensors at consecutive stages of polishing procedure. Sensors were characterized using developed ECU (described in

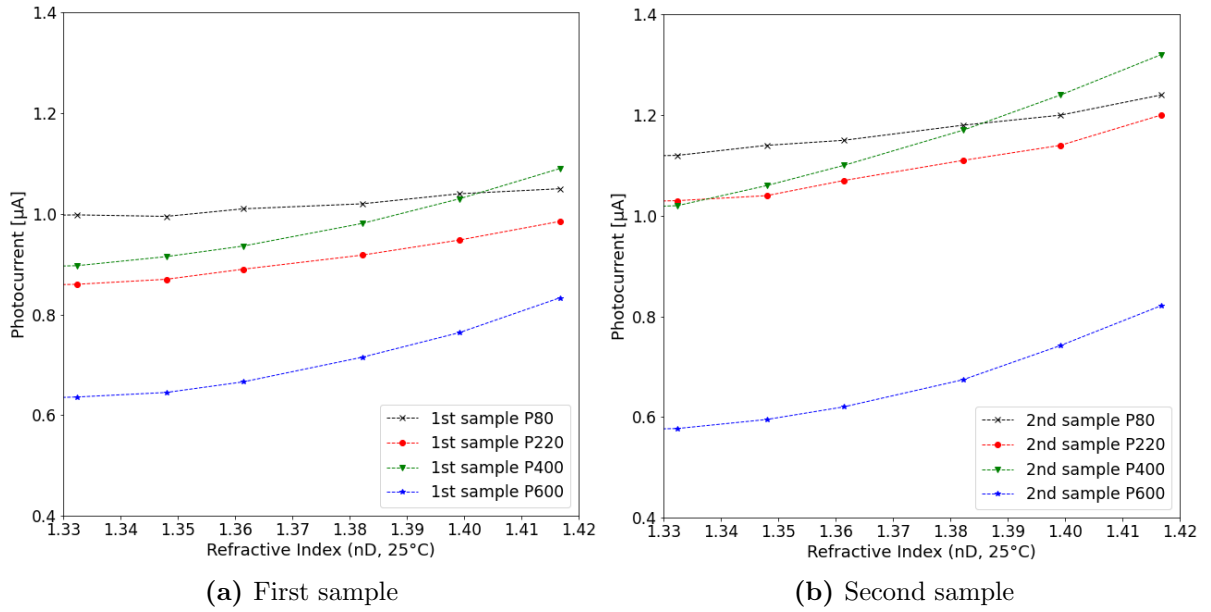


Fig. 4.12. Response of the fabricated sensors - photocurrent vs refractive index (transmitter's current 10 mA)

Section 4.2.1), with a transmitter's current set to 10 mA. Figure 4.12a and Fig. 4.12b show the first and the second fabricated sensor response respectively. The first polishing procedure was done using P80. At this stage, the change of fabricated sensors response is visible when exposed to liquids of different refractive indices, although the generated photocurrents have changed only by 0.050 µA for the first, and by 0.120 µA for the second sample. Decreasing the sensor's surface roughness by polishing with lower gradations results in a higher signal attenuation (less photocurrent generated by a receiver), but also with significantly higher change in the generated photocurrent due to exposing the sensor to liquids of higher refractive indices. After the last polishing procedure (P600) was done, the photocurrent generated for the liquid with RI of 1.3324 nD was measured to be 0.636 µA, and 0.833 µA for the liquid with RI of 1.4167 nD. The second fabricated sample presented a 0.577 µA for liquid with RI of 1.3324 nD, and 0.821 µA for liquid with RI of 1.4167 nD.

In order to make the obtained measurements more readable and easier for further data processing, the measurements can be normalized. The normalization (k_{norm}) is made by dividing measurements ($k_{solution}$), by a common reference measurement (k_{water}), as shown by the following equation:

$$k_{norm} = \frac{k_{solution}}{k_{water}}. \quad (4.7)$$

In this case, the reference measurement was done using distilled water, which refractive index was additionally measured and was equal to 1.3324. Although the optical transmission attenuation increases as roughness of the sensing area decreases, the normalized data sets (Fig. 4.13) clearly show that the sensor response to a refractive index change is more significant. The measurements (k_{norm}) of both samples also present that there is a difference between the first and second sample measurements. This is because these prototypes were among the first attempts and the sensor reproducibility is quite low. The difference between sensor measurements (after final polishing with P600) when immersed in 50% sucrose solution is 0.113129 arbitrary unit.

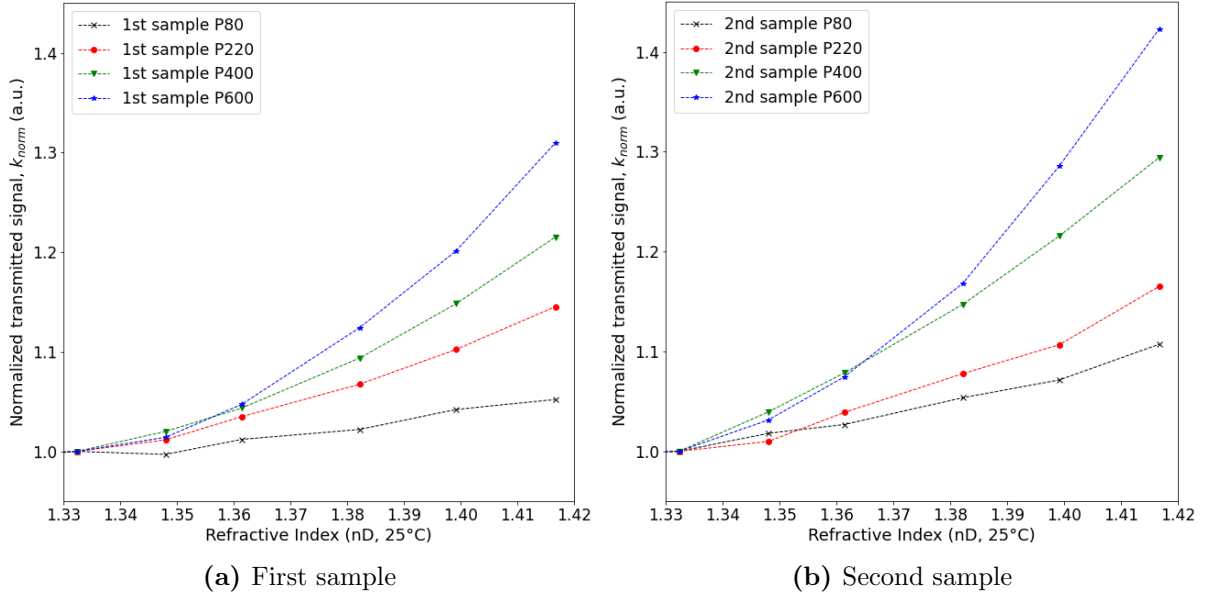


Fig. 4.13. Normalized response of the fabricated sensors (transmitter's current 10mA)

Sensor sensitivity is calculated according to:

$$S = \frac{\delta k_{norm}}{\delta RI}. \quad (4.8)$$

where the sensitivity S for each sensor is calculated individually (because only two samples were prepared at that time). That means a k_{norm} is used instead of k_{avg} .

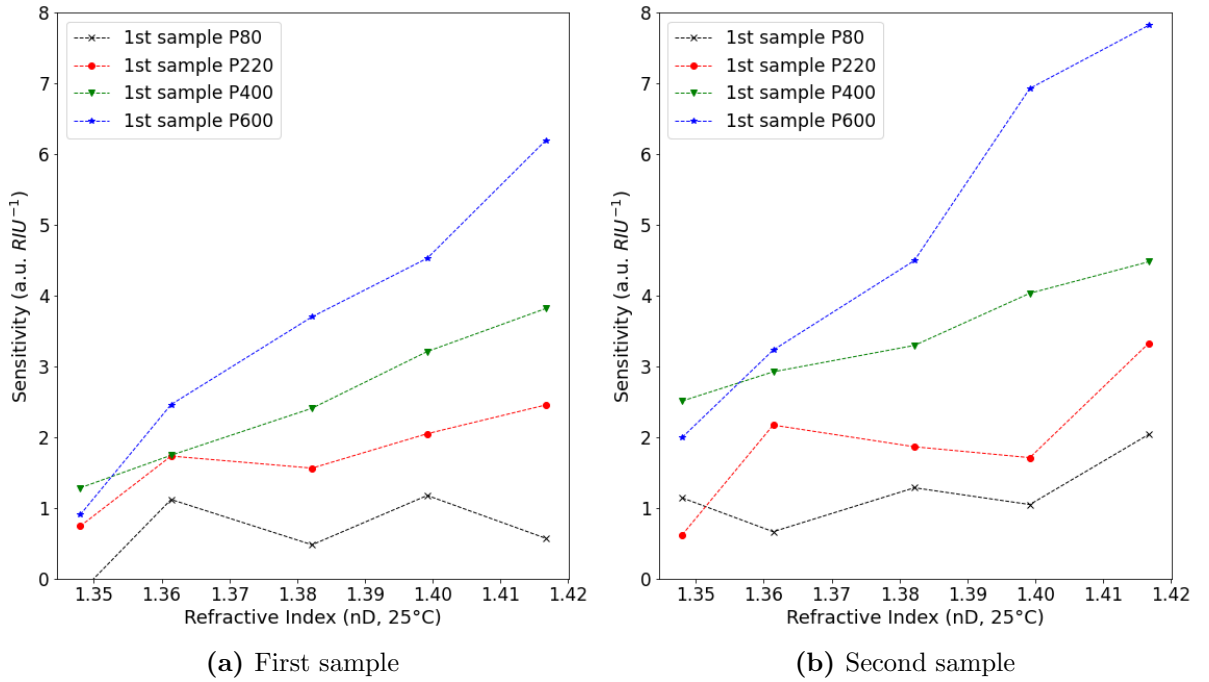


Fig. 4.14. Sensitivity of the fabricated sensors (transmitter's current 10mA)

Based on derived sensitivities (Fig. 4.14a and 4.14b) it was concluded that

- the final polishing yields the best results - because of the highest sensitivity,

- the sensor reproducibility has to be improved - because of notable differences among obtained sensor sensitivities (differences in sensor characteristics between the first and the second fabricated samples).

To investigate the influence of light intensity on the sensor's performance, measurements were performed for different forward currents (5 mA, 10 mA, 15 mA) for both samples. The datasets after normalization were presented in Fig. 4.15.

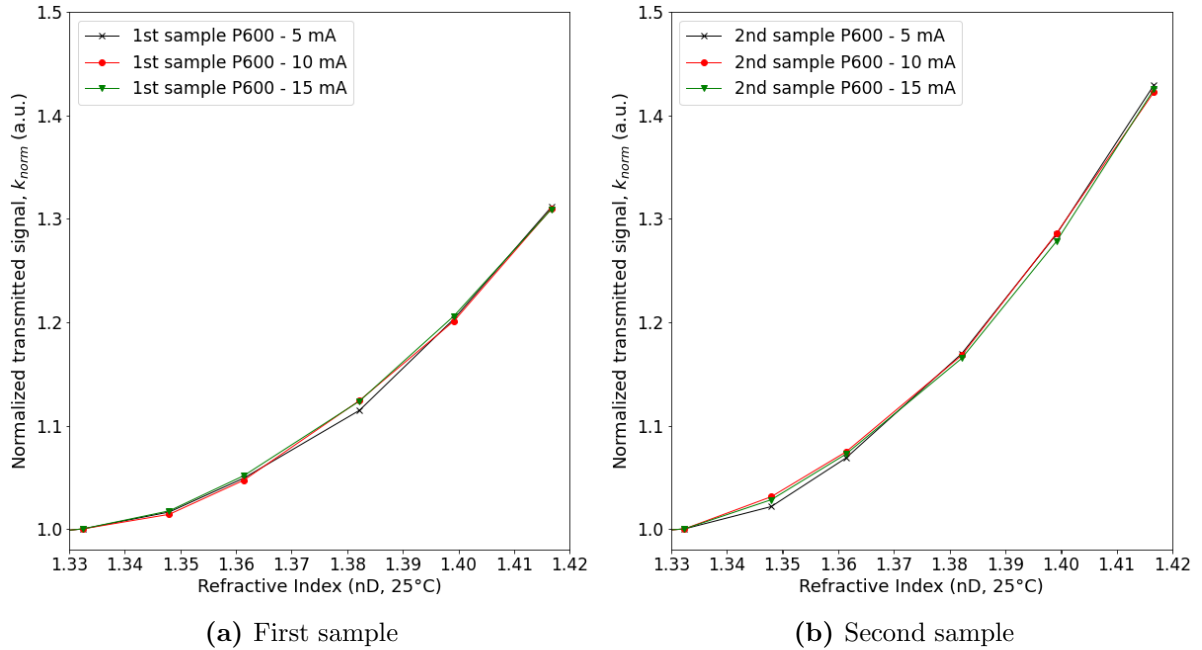


Fig. 4.15. Normalized response of the fabricated sensors for different transmitter's current

They do not include the influence of the light intensity on the output signal level. Raw measurements naturally show that the higher the light intensity, the higher the output signal voltage. By normalizing the data it was possible to compare results, which show that there is almost no correlation between increasing the transmitter's current intensity and obtaining better sensor performance.

Sensor reproducibility

A critical aspect of optimizing the performance and reliability of side-polished evanescent wave absorption polymer optical fiber (POF) sensors lies in understanding the impact of the quality of the cleaved POF end-faces. The quality of the cleave plays a significant role in shaping the light propagation and signal strength of the optical sensor. The cleave quality can be influenced by the cleaving tool used, and inconsistencies can lead to variances in sensor readings, affecting both their performance and reproducibility.

Therefore, to evaluate the correlation between cleave quality and sensor performance, a comprehensive investigation was conducted. In this context, the use of different cleaving tools and their impact on sensor performance was explored. The goal was to identify a cleaving tool or methodology that consistently produces high-quality cleaves and hence, improved sensor performance. The methodology of the experiment, as illustrated in Fig. 4.16, allowed to systematically investigate these relationships. The procedure was carefully designed to control other influencing factors, ensuring that any observed differences in sensor performance could be reliably attributed to the variation in cleave quality.

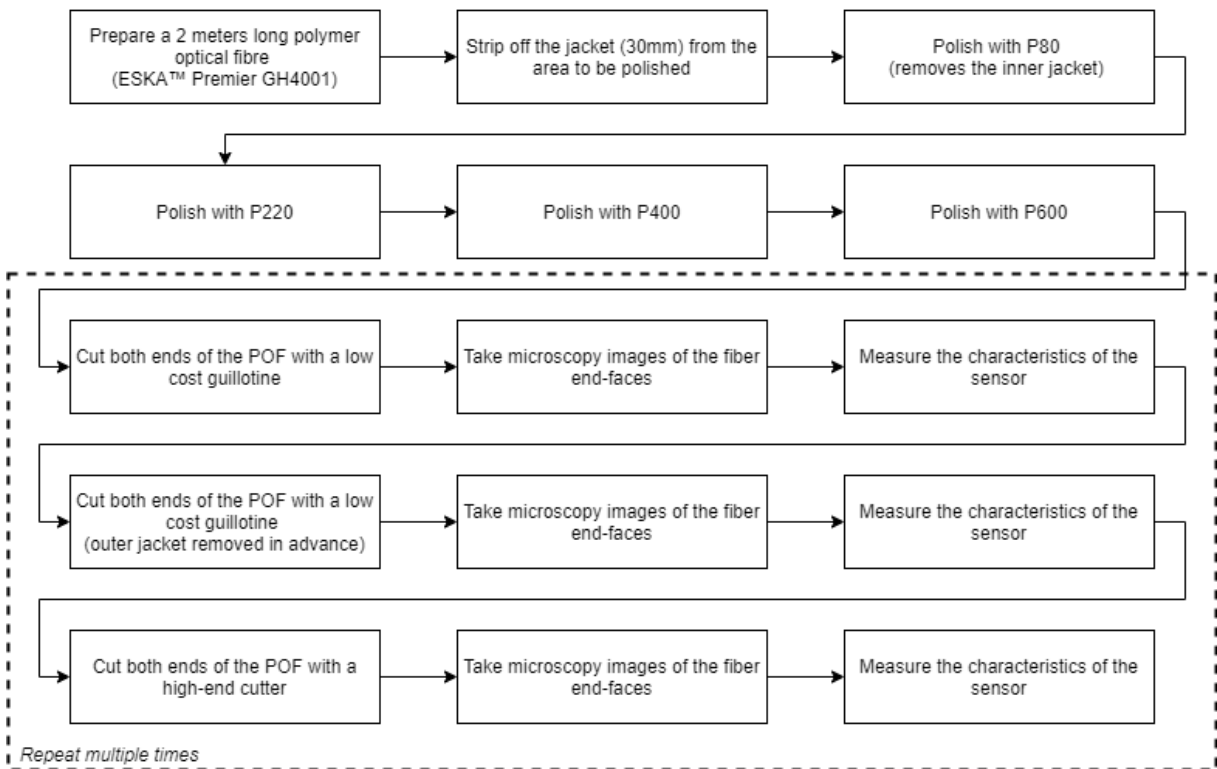


Fig. 4.16. Methodology of the experiment - the influence of POF end faces on sensor performance and reproducibility

For this experiment, two different cleaving tools were used. The sensor itself was fabricated out of two-meters long fiber optic cable (Mitsubishi GH4001). This was done only once and the same sensor was used throughout the experiment. The goal of this experiment was to obtain optical fiber end-faces with different qualities to investigate if the quality of the end-face does influence the sensing performance. For fiber cleaving, a low-cost tool, as well as a high-end one, were selected. The first tool is a low-cost guillotine. According to the manufacturer, the razor blade of this tool shall be used only several times. After that, this tool has to be changed because the blade gets worn out. This guillotine was used in two different scenarios, without and with stripping off the outer jacket of the fiber optic cable. For the second variant, cracks and deformations were found on the surface of the fiber's core due to the lack of an outer jacket. The second tool is a high-end cleaving tool with a razor blade that rotates after each cut. In other words, each new cut is done with a sharp edge of the razor blade. The rotating mechanism gets locked after a few hundred of cleaving when the rotating blade performs a full revolution. After the sensor was fabricated, both ends of the fiber were cleaved with a particular tool. Then, microscopy images of the end faces were taken and the sensor characteristics were measured (similarly as presented in previous sections). This procedure was repeated several times for every selected variant.

Figure 4.17 presents the quality of the polymer optical fiber after cleaving with a particular tool. Upper images present fiber surfaces after cleaving with a high-end tool, i.e. the RENNSTEIG 8002 004 3. Visual inspection shows that the surfaces do not have any deformations, nor cracks. The surfaces look smooth and only some small amount of polymer contamination may gather on the final part of the cleaving. The middle pictures represent the POF

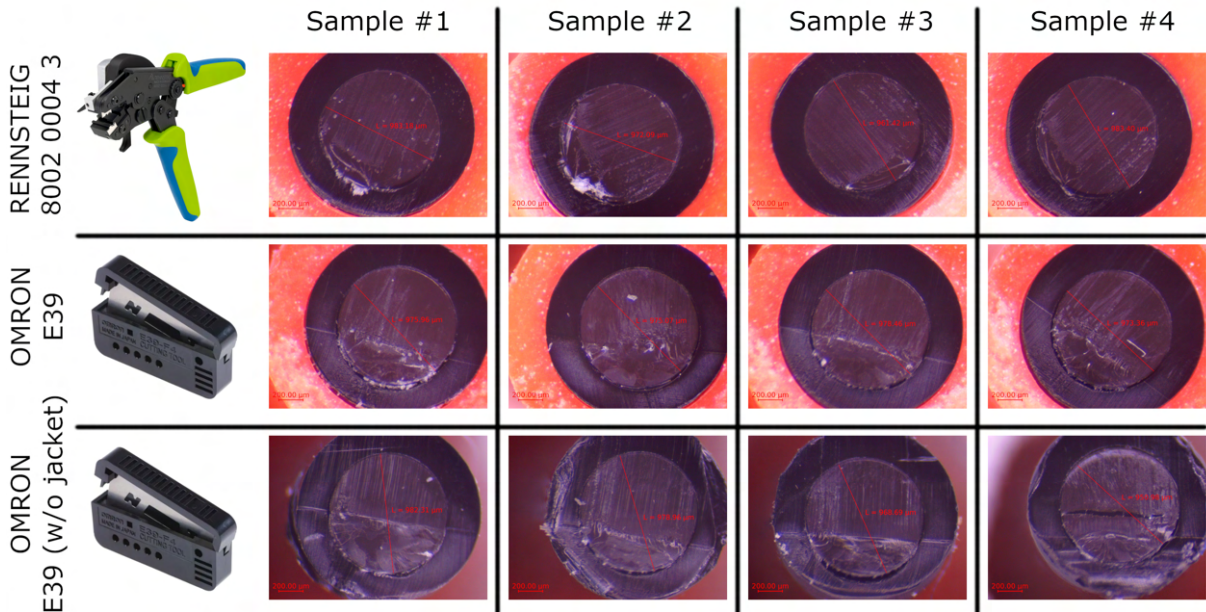


Fig. 4.17. Microscopy images of the POF end faces

surfaces cleaved with a low-cost guillotine, without stripping off the jacket. The surface of the end faces presents some artifacts, and it looks as if the cutting speed was not constant. The bottom images show end-faces of a guillotine cleaving without outer jacket. The fiber is deformed and looks, similarly as before, as if the cleaving speed was not constant. Furthermore, some cracks are visible. Its quality is very poor because the fiber was rather compressed than cleaved due to the lack of the outer jacket.

Figure 4.18 presents obtained characteristics for the fabricated sensor with both end-faces of the POF cleaved with different tools. All of the charts present generated photocurrent data in the upper row, normalized data in the middle row, and averaged normalized measurements with standard deviations in the lower row. The charts provide a comprehensive comparison of the sensor's performance for different cleaving tools utilized on the polymer optical fiber (POF). The impact of cleaving quality is visualized through three distinct scenarios.

In Fig. 4.18a, the POF's end-faces are cleaved with a high-end tool, delivering superior quality cuts. On the other hand, Fig. 4.18b represents the scenario where a low-end tool is employed, potentially affecting the quality of cleaves. Lastly, Fig. 4.18c illustrates the condition where the POF is cleaved with the low-end tool, with the outer jacket stripped off, providing a slightly modified context for comparison.

Each scenario is further divided into three sub-sections in the charts. The upper row presents raw data obtained directly from the experimental setup without any postprocessing. This data provides an unaltered look into the actual measurements and gives an idea of the inherent variability and noise present in the data. The middle row, in contrast, offers normalized data for each scenario. Normalization is an essential data post-processing step that adjusts the measurements to a standard scale. It allows for a fair comparison of the results across different tests by eliminating the influence of certain varying factors such as light intensity and slight variations in setup. Lastly, the lower row features the averaged normalized measurements along with their standard deviations. Averaging the measurements provides a single representative value for the set of observations, facilitating a straightforward comparison between different cleaving tools. Meanwhile, the standard deviation, a measure of data spread, provides insights into the consistency and reproducibility of the sensor readings under each scenario.

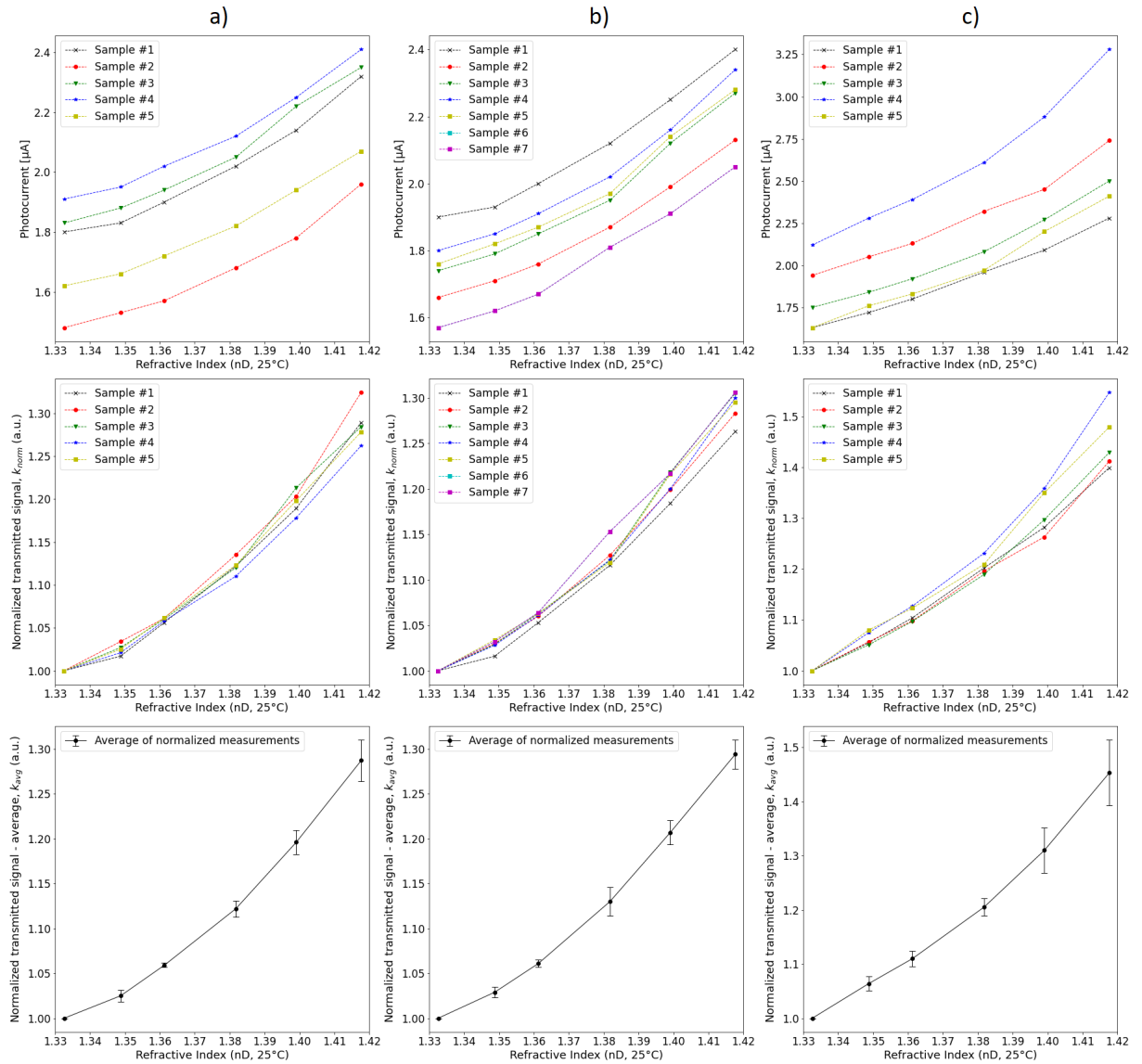


Fig. 4.18. Sensor characteristics: (a) RENNSTEIG 8002 004 3; (b) Omron E39-F4; (c) Omron E39-F4 (outer jacket removed)

Figure 4.19 presents the comparison between all three sets of measurements, including the normalized average transmitted signal (Fig. 4.19a) as well as average sensor sensitivity (Fig. 4.19b). Interestingly, the results show an unexpected trend in the context of sensor sensitivity. Contrary to what one might expect, the sensors cleaved with lower-end tools, leading to a less refined finish, exhibited a higher sensitivity. While this might be counter-intuitive, it underscores the complex interplay between the angle of incidence of light coupled from the POF transmitter and the cleaved end-face quality. The irregular surfaces of poorly cleaved ends might be causing a change in the light incidence angle, leading to higher sensitivity. However, this comes at the cost of decreased reproducibility, which is of significant concern for real-world applications.

Overall, these findings underscore the importance of the cleaving process in the design and fabrication of evanescent wave absorption polymer optical fiber sensors. They also highlight the need for further research to strike a balance between achieving high sensitivity and maintaining good reproducibility, a crucial requirement for practical implementations of these sensors.

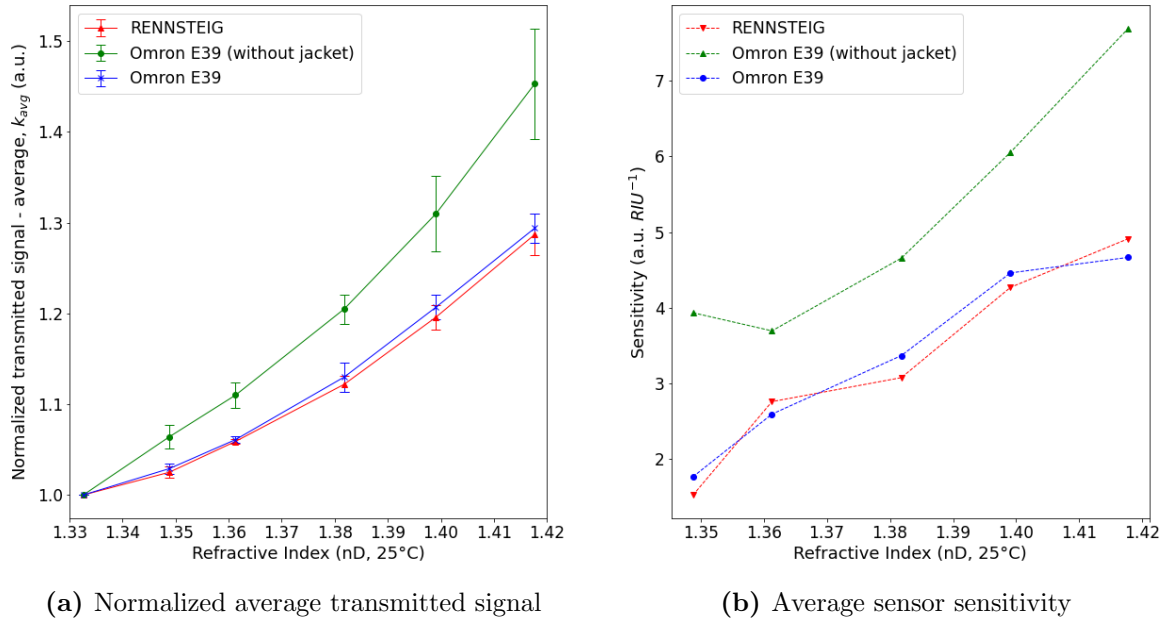


Fig. 4.19. Comparison of fabricated sensors cleaved with different cleaving tools

Climatic chamber tests

Temperature stress tests were performed using a climatic chamber (Fig. 4.20). During the test, the ECU was supplied by a bench power supply (with the output voltage set to 12 V) and connected to a PC to record the data. Inside the climatic chamber, the fabricated polymer optical fiber sensor and a polymer optical fiber cable were placed. The polymer optical fiber sensor's sensing area was immersed in oil (Orlen Oil Trafo, Tab. 4.5) inside an oil container. The ends of the optical fibers were guided outside the chamber and connected with the ECU through POF transmitters and receivers. The ECU had connected an external thermistor, which was used to monitor the temperature of the oil.

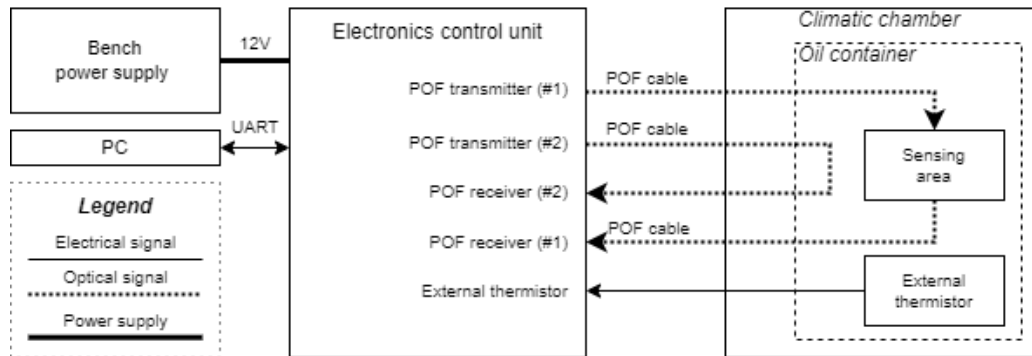


Fig. 4.20. Block diagram of a test rig used during climatic tests

The aim of this test was to record the behavior of the fabricated POF sensor and of the raw polymer optical fiber cable as the temperature might impact not only the optical signal attenuation but also the refractive index of the used oil. Furthermore, obtained results could be used to derive the hysteresis. A polymer optical fiber cable was used for a reference to compare the results. This reference POF cable, being subjected to the same temperature variations as the fabricated POF sensor but without the sensing areas, offers insight into the intrinsic

temperature-dependent behavior of the optical fiber material itself. By measuring the optical signal attenuation in the reference cable, it is possible to isolate and understand the fundamental changes that the polymer optical fiber undergoes due to temperature variations.

The test procedure started with setting the chamber's temperature to -40°C , and waiting until the thermistor's temperature reaches -30°C . After that, the temperature was set to 80°C and the testing script waited until the oil achieved 60°C . This temperature range fully covers the lithium-ion cell's safety operating window (shown in Fig. 2.5), i.e., the temperature range that could be expected inside the battery pack with an immersive liquid cooling approach, and the chamber's temperature does not exceed the polymer optical fiber cable operating temperature range. During the test, a PC was recording the data provided by the ECU, in particular:

- timestamp,
- measurements of polymer optical fiber connector receivers (the fabricated polymer optical fiber sensor and a reference polymer optical fiber cable),
- measurements of the external thermistor.

The recorded measurements are presented in Fig. 4.21. One complete temperature cycle test lasted 300 minutes on average. This is not only due to the large volume of the chamber but also due to the inertia of oil (approx. 1 liter). The chart presents the temperature of ECU (red), the temperature of oil (black), and raw measurements for POF sensor (blue) and POF cable (green). It can be observed that there is a significant variation in the light transmitted via fabricated polymer optical fiber sensor. The difference between signal at 20°C and 60°C ($\Delta T = 40\text{ K}$) is 11%. Notably higher variation was observed for lower temperatures. The difference between signal at 20°C and -30°C ($\Delta T = 50\text{ K}$) is almost 60%. On the other hand, the signal variation for a raw polymer optical fiber cable was recorded to be the range of $\pm 0.05\%$.

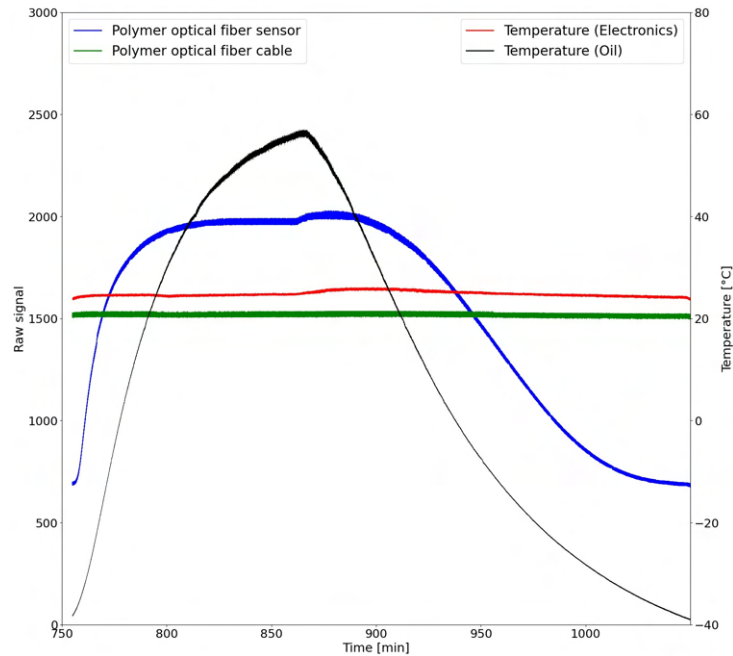


Fig. 4.21. Raw response vs oil temperature

During the performed tests, the speed of temperature change was not constant and differed for the heating and cooling processes. To provide a better overview of the temperature dependence of the recorded output signals, hysteresis were derived for the polymer optical fiber sensor and a raw optical fiber cable (Fig 4.22a).

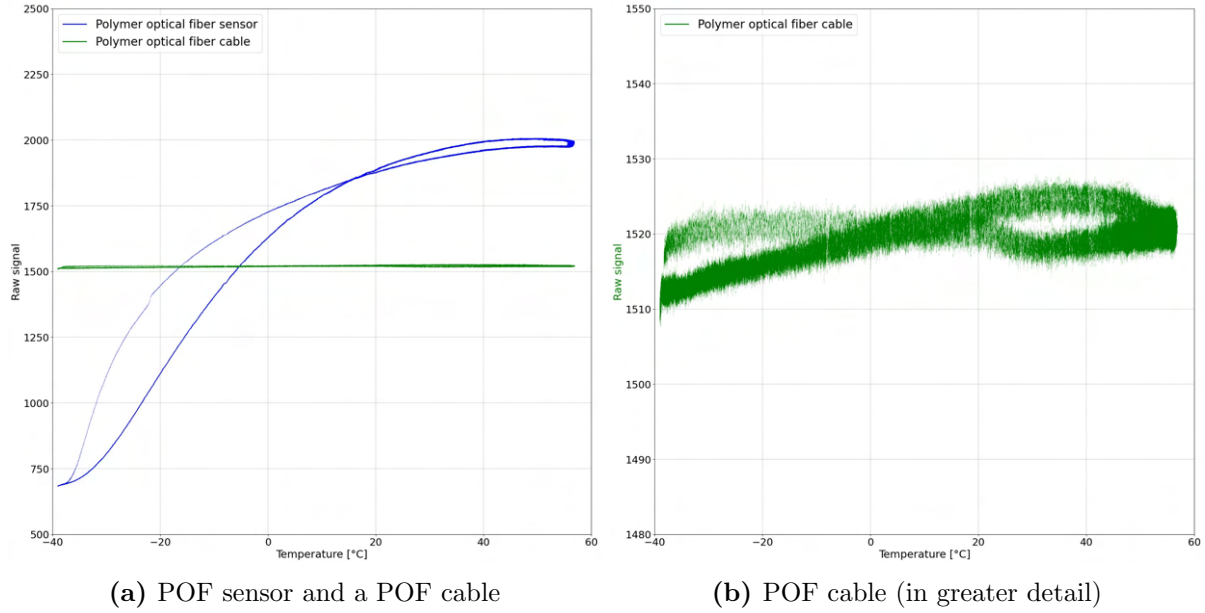


Fig. 4.22. Observed hysteresis

For the fabricated POF sensor, the output signal changes exponentially with temperature change. However, the change is not directly caused by the temperature, as the temperature also influences the density of the liquid and thus, its refractive index. According to the literature, the refractive index of oil (both mineral and silicone) is linearly dependent on the temperature [139, 140] and it decreases as the temperature increases due to the fact, that oil becomes less dense. According to the conducted research on POF sensor characteristics (Fig. 4.18), linear change in the refractive index would cause an exponential change of the output signal. This is exactly what can be observed in the derived hysteresis. Although in different orders of magnitude, the shape of hysteresis is similar for the raw polymer optical fibers and for the fabricated polymer optical fiber sensor.

4.4 Summary

This chapter thoroughly described the proposed optical liquid detection system, presenting the architecture, together with the formulated functional and non-functional requirements, where aspects such as fault detection time, true detection rate, and fault types were specified. Such aspects were tailored for a system that was supposed to be applied inside electric vehicles' battery packs, in particular, battery packs with the direct liquid-cooling approach. Later, the implementation process was presented. Although this was an iterative process, where more than 3 different hardware and software versions were designed and implemented, this chapter presented the final shape of the system capable of fulfilling the aforementioned requirements and architecture. The experimental research on the evanescent wave absorption polymer optical fiber refractive index sensor was documented, showcasing its fabrication procedure and performance measures when exposed to liquids of different refractive indices. Because the sensor was further to be operated in road conditions, tests under elevated temperatures (-40°C to $+60^{\circ}\text{C}$) were performed as well. Individual parts of the system were assembled, making such OLDS ready for the verification study, where liquid leakage and liquid intrusion faults were simulated under laboratory and road conditions.

5. Fault detection methods

Technical diagnostics is an interdisciplinary field of science, which deals mainly with recognizing the technical condition of the object (e.g., a machine, a device, a process) on the basis of selected information (both current and/or historical) about this object [141]. In the context of process diagnostics, the aim of the diagnosis itself is to monitor the current state of the diagnosed object. According to [65], the diagnosis can be done through different consecutive steps, including fault detection (determination of faults present in a system and time of detection), fault isolation (determination of kind, location, and period of occurrence of a fault by evaluating symptoms), and fault identification (determination of size and time-varying behavior of a fault).

Such steps can be taken using direct or indirect diagnosis approaches. For a direct diagnosis, the system's parameters or variables that directly relate to the potential fault or issue are monitored. These variables are usually clearly defined and can directly indicate the presence of a fault when they cross a certain threshold or behave irregularly. In the case of indirect diagnosis, parameters or variables that do not directly indicate a fault, but whose behavior changes when a fault occurs are monitored. This approach might sometimes require complex mathematical models or machine learning algorithms to interpret these changes and infer the presence of a fault.

The optoelectrical properties of the designed OLDS are subjected to various factors (especially under road conditions), e.g.:

- elevated temperatures causing changes in the refractive index of coolant oil (Fig. 4.21) and influencing LED-based light transmitters [142],
- aging effects for coolant oil [143] and LED-based light transmitters [144],
- vibrations influencing the optomechanical coupling between POF and a corresponding LED transmitter and/or photodiode receiver.

Therefore, the following dissertation addresses fault detection employing a model-based approach, where such factors are taken into consideration indirectly. A typical model-based fault detection approach is shown in Fig. 5.1.

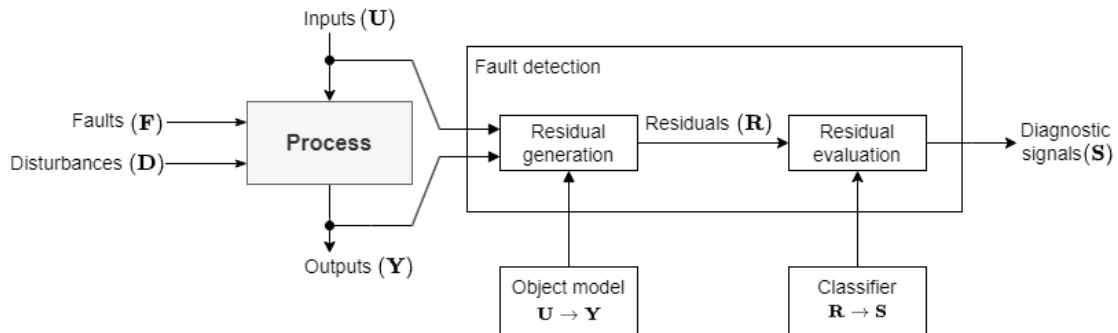


Fig. 5.1. Block diagram of a model-based fault detection approach [64]

The diagram presents input \mathbf{U} and output \mathbf{Y} signals that are fed to the fault detection block. This block generates residuals \mathbf{R} (typically being a difference between the observed and calculated output signals) and evaluates them. Based on the obtained results, diagnostic signal \mathbf{S} is updated.

This chapter describes the formulated model-based fault detection methods that are based on Recurrent Neural Networks (RNNs), useful in the context of this dissertation for learning long-term dependencies and varying system responses under different ambient conditions. In total, two different methods were proposed. The first - a fault detection method using Long Short-Term Memory (LSTM) neural networks (with two different residual evaluation approaches). This method was tested and verified using datasets acquired under laboratory conditions. On the basis of obtained results and conclusions drawn, the second method, namely a fault detection method using autoencoder neural networks was proposed. This method utilizes a slightly different approach than the approach presented in Fig. 5.1, as the employed autoencoder is only fed with output signals \mathbf{Y} . This method was tested and verified using the final version of the OLDS that was used to collect datasets under road conditions. To evaluate the performance of both schemas, a set of model and detection performance indicators were used. Such indicators were described in corresponding sections.

5.1 Fault detection method using LSTM neural networks

Two fault detection schemas based on the LSTM neural network are proposed. The aim of employing the LSTM neural network is to capture the time-series dependencies within the input and output data. This approach involves using an LSTM model to generate residuals for the evaluation process. The LSTM model is trained on data collected during normal operating conditions, and its output $y_m(k)$ is utilized to compute the residual signal $r(k)$ in comparison to the actual process output. This residual generation allows the LSTM-based method to account for temporal dependencies and potentially detect abnormal behavior in the system. Both techniques utilize the same residual generation methods but differ in the residual evaluation process. For the evaluation, two different schemas are proposed. The first is based on statistical analysis, and the second is based on the model error modeling methodology in which a feed-forward input-delay backpropagation network (TDNN) is applied [145].

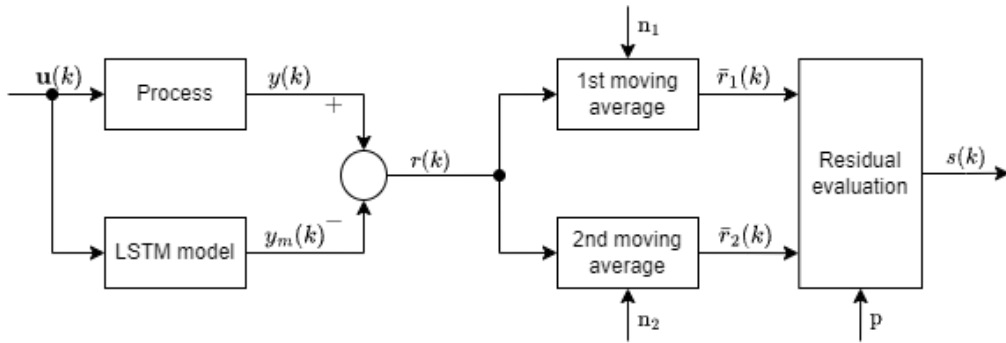


Fig. 5.2. Simple model-based fault detection scheme

The first approach's scheme is shown in Fig. 5.2. This is the typical model-based approach in which the model of a process is trained using the data collected for normal conditions. The residuals $r(k)$ are calculated according to the following formula:

$$r(k) = y(k) - y_m(k), \quad (5.1)$$

where $y(k)$ is the measured signal, $y_m(k)$ is the signal that is calculated using the LSTM model.

The binary diagnostic signal $s(k) \in \{0, 1\}$ is computed based on the absolute value of the difference between the two moving averages, according to the proposed equation:

$$s(k) = \begin{cases} 0 & \text{for } |\bar{r}_1(k) - \bar{r}_2(k)| \leq p \\ 1 & \text{otherwise} \end{cases}, \quad (5.2)$$

where $\bar{r}_1(k)$ and $\bar{r}_2(k)$ denote the first and second moving average window of the residual signal with different sample sizes (n_1, n_2) , p is the arbitrary threshold.

The second residual evaluation technique is a model-based approach using the model error modeling methodology proposed by [146]. This is adopted and extended to create a robust fault detection scheme. The scheme presented in Fig. 5.3 illustrates the main idea of the model-based approach with adaptive threshold evaluation of the residuals.

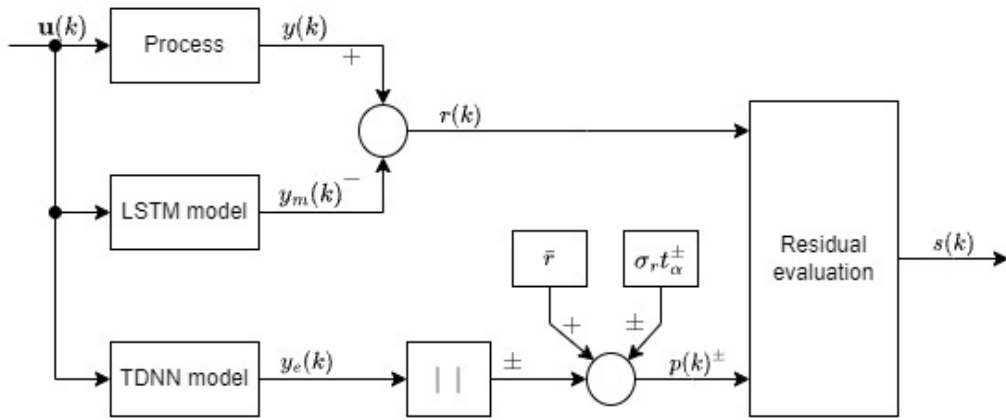


Fig. 5.3. Robust model-based fault detection scheme

In this approach, the model of the process is created using training and test data collected for fault-free operations of the system. The output of this model $y_m(k)$ is used to calculate a residual signal $r(k)$. The test dataset was also applied to prepare additional training and test data subsets needed to create a model of the residual (model error). The estimation of the residual signal $y_e(k)$ is then used to compute adaptive thresholds $p^\pm(k)$. In this way, it is possible to obtain a robust decision block of the fault detection scheme. The robustness of the fault detection algorithm to uncertainties of different natures without losing sensitivity to faults is performed by evaluating adaptive thresholds which are given in the following form:

$$p^\pm(k) = \bar{r} \pm t_\alpha^\pm \sigma_r \pm \left| \mathbf{LW} \mathbf{f}^1 \left(\mathbf{IW} \mathbf{u}'(k) + \mathbf{b}^1 \right) + \mathbf{b}^2 \right|, \quad (5.3)$$

where \bar{r} and σ_r represent the mean and standard deviation values of the residual (these statistics are calculated for the faultless condition), t_α^\pm denotes the critical value corresponding to a given significance level α . The second part of the Eq. (5.3) concerns the estimation of the residual behavior $y_e(k)$ and it becomes realized with the help of the TDNN model, where \mathbf{IW} is an input weight matrix, \mathbf{LW} is an output weight matrix, \mathbf{b}^1 , \mathbf{b}^2 are bias matrices, \mathbf{f}^1 is a non-linear activation function, $\mathbf{u}'(k) = [\mathbf{u}(k), \mathbf{u}(k-1), \mathbf{u}(k-2), \dots, \mathbf{u}(k-n)]^T$.

The binary diagnostic signal $s(k) \in \{0, 1\}$ is originated as a result of two-value evaluation of residuals and, therefore it can be computed according to the following rule:

$$s(k) = \begin{cases} 0 & \text{for } p^+(k) \geq r(k) \geq p^-(k) \\ 1 & \text{otherwise} \end{cases}. \quad (5.4)$$

5.2 Fault detection method using autoencoder neural networks

The next proposed method is based on the RAE-GRU (Recurrent Autoencoder with Gated Recurrent Unit) neural network, which is an alternative to the previously implemented LSTM-based fault detection approach. This method provides a more practical solution for real-time monitoring on low-cost embedded devices, and multiple of those are commonly used throughout the vehicle E/E systems [147]. Still, it offers reasonable performance in capturing time-series dependencies. The LSTM-based method, while effective, suffers from high computational complexity. This may make it unsuitable for aforementioned devices and may limit its testing to offline simulations with previously recorded data. The RAE-GRU method, on the other hand, may benefit from the reduced complexity of the GRU layers compared to the LSTM, which shall help to minimize the computational and memory requirements. The RAE-GRU method can be seen as a more suitable choice for embedded systems with limited resources. Additionally, the RAE-GRU approach retains the ability to model long-term dependencies in time-series data, ensuring the accuracy and effectiveness of the fault detection process. This approach is suitable for an online operation on an ECU or other embedded device as well.

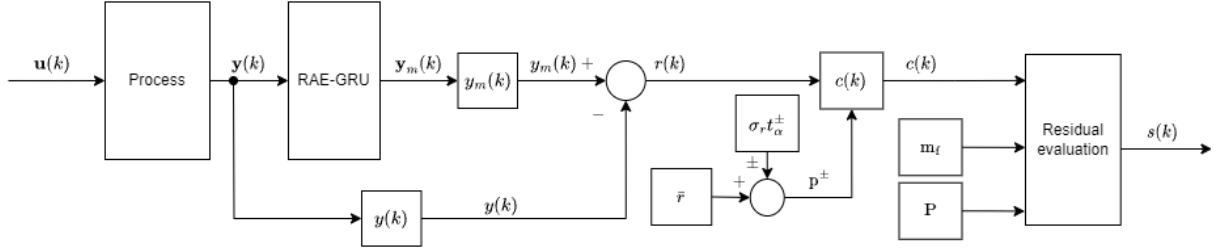


Fig. 5.4. RAE-GRU model-based fault detection scheme

The proposed method (Fig. 5.4), starts with processing the output vector signal, referred to as $\mathbf{y}(k)$, as an input in the recurrent autoencoder model (RAE-GRU):

$$\mathbf{y}(k) = \begin{bmatrix} y(k) \\ y(k-1) \\ \dots \\ y(k-l) \end{bmatrix}, \quad (5.5)$$

where l denotes the number of samples prior to the most recent sample.

The autoencoder produces then a reconstructed output signal sequence, denoted as $\mathbf{y}_m(k)$:

$$\mathbf{y}_m(k) = \begin{bmatrix} y_m(k) \\ y_m(k-1) \\ \dots \\ y_m(k-l) \end{bmatrix}. \quad (5.6)$$

Next, the residuals $r(k)$ are generated as the difference between $y_m(k)$ and $y(k)$. The residuals are then compared against upper and lower thresholds p^\pm , based on the mean value \bar{r} , standard deviation σ_r , and a significance level t_α :

$$p^\pm = \bar{r} \pm t_\alpha^\pm \sigma_r, \quad (5.7)$$

where \bar{r} and σ_r are derived from the data collected under faultless state.

Threshold crossing indicator $c(k)$ is generated using the following conditions:

$$c(k) = \begin{cases} 0 & \text{for } p^+ \geq r(k) \geq p^- \\ 1 & \text{otherwise} \end{cases} . \quad (5.8)$$

Finally, the diagnostic signal $s(k)$ is generated, if the sum of threshold crossing indicator $c(k)$ under predefined time window m_f exceeds the given level P :

$$s(k) = \begin{cases} 0 & \text{for } P \geq \sum_{j=0}^{m_f} c(k-j) \\ 1 & \text{otherwise} \end{cases} . \quad (5.9)$$

5.3 Recurrent neural networks

Over the past decade, RNNs [148] have received significant attention and have been applied to a diverse range of applications, including (but not limited to) signal processing, and anomaly detection [149]. For standard, feed-forward neural networks, the information may flow only in a single direction (Fig. 5.5a). Since such network does not have any mechanism of storing data, the data of previous states of layers is forgotten. Recurrent neural networks are FFNNs adapted to handle sequential data. This is achieved by incorporating a loop in the information flow which allows them to retain the information from previous states of layers as well as new data (Fig. 5.5b). From the practical point of view this property provides the advantage over FFNN that based on provided input data, the RNN is able to distinguish the context of the data. For the FFNN, the order in which the data is fed to the network is irrelevant.

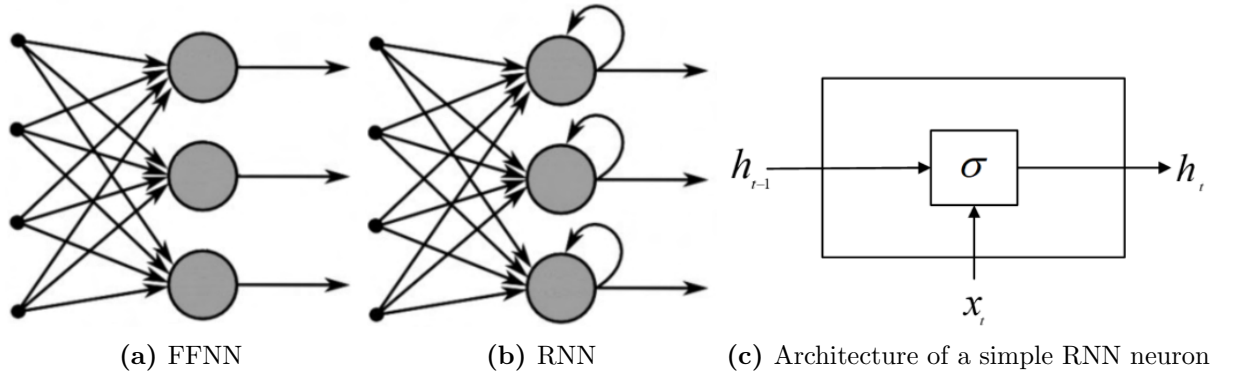


Fig. 5.5. Feed-forward and recurrent neural networks [150, 151]

The output of RRN layer based on a simple RRN neuron (Fig. 5.5c) is computed as follows:

$$\mathbf{h}_t = \sigma_g(\mathbf{W}_h \mathbf{x}_t + \mathbf{R}_h \mathbf{h}_{t-1} + \mathbf{b}_h), \quad (5.10)$$

where σ_g is an activation function; \mathbf{W} and \mathbf{R} are an input weight matrix and a recurrent weight matrix of the h layer; \mathbf{x}_t is an input vector and \mathbf{b} is a bias vector.

Unfortunately, simple RNNs present the so-called vanishing gradient problem [152] that arises during the training of deep neural networks, especially those that use sigmoid or hyperbolic tangent activation functions. In such cases, the gradient of the loss function with respect to the weights of the network can become very small, making it difficult for the network to learn and update its parameters effectively. This occurs because the gradient is propagated backwards

through the layers of the network during backpropagation, and as it passes through each layer, it is multiplied by the weight matrix associated with that layer. If the weight matrix has small values, and the activation function has small derivative values, then the gradient can become vanishingly small as it passes through many layers, making it difficult to learn effective representations. Despite the fact that RNNs can learn long-term dependencies, the training process may be very time-consuming or even fail. To overcome this problem, scientists have proposed new methods such as long short-term memory or newer and simpler gated recurrent unit.

5.3.1 Long Short-Term Memory

Because of self-adaptability, learning ability, and the capability of capturing the dynamics of highly nonlinear systems (such as LIBs), the first selected method was based on a process model trained with the use of an artificial neural network (ANN), more specifically a long short-term memory neural network. The LSTM network is known in the literature as a recurrent neural network that can learn long-term dependencies between time steps of sequence data [153], which in this case can be useful due to the signal drift caused e.g., by a change in temperature and refractive index, as experimentally verified and presented in Fig. 4.22. The main components of such a network are a sequence input layer and an LSTM layer. The architecture of an LSTM layer is shown in Fig. 5.6. This diagram illustrates the flow of a time series \mathbf{X} with \mathbf{C} features (channels) of length \mathbf{S} through an LSTM layer. In the diagram, \mathbf{h}_t , \mathbf{c}_t denote the output (also known as the hidden state) and the cell state at time step t , respectively.

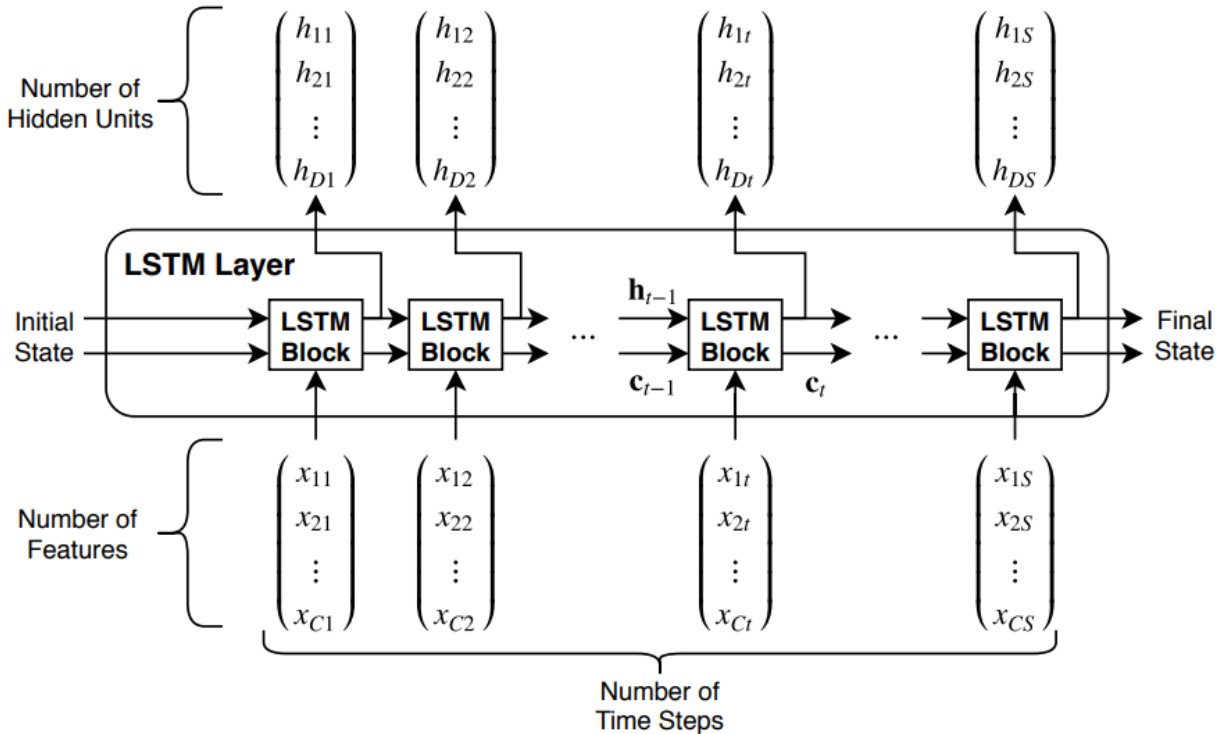


Fig. 5.6. LSTM layer architecture [153]

Initial network state and the sequence's first time step are provided to the first LSTM block to compute the first output and the updated cell state. For a given time step t , the cell state \mathbf{c}_t is derived based on the current state of the network $(\mathbf{c}_{t-1}, \mathbf{h}_{t-1})$ and the next sequence's time step:

$$\mathbf{c}_t = \mathbf{f}_t \odot \mathbf{c}_{t-1} + \mathbf{i}_t \odot \mathbf{g}_t, \quad (5.11)$$

where \odot denotes the element-wise multiplication of vectors. The hidden state \mathbf{h}_t contains the output of the corresponding LSTM layer, and the cell state \mathbf{c}_t contains information learned from the previous time steps:

$$\mathbf{h}_t = \mathbf{o}_t \odot \sigma_c(\mathbf{c}_t), \quad (5.12)$$

where $\sigma_c(\mathbf{c}_t)$ denotes the state activation function.

The learnable weights of an LSTM layer are the input weights \mathbf{W} , the recurrent weights \mathbf{R} , and the bias \mathbf{b} . The matrices \mathbf{W} , \mathbf{R} , and \mathbf{b} are series of interconnected input weights, recurrent weights, and bias of each component, respectively:

$$\mathbf{W} = \begin{bmatrix} \mathbf{W}_i \\ \mathbf{W}_f \\ \mathbf{W}_g \\ \mathbf{W}_o \end{bmatrix}, \mathbf{R} = \begin{bmatrix} \mathbf{R}_i \\ \mathbf{R}_f \\ \mathbf{R}_g \\ \mathbf{R}_o \end{bmatrix}, \mathbf{b} = \begin{bmatrix} \mathbf{b}_i \\ \mathbf{b}_f \\ \mathbf{b}_g \\ \mathbf{b}_o \end{bmatrix}. \quad (5.13)$$

An LSTM layer adds or removes information from the cell state at each time step, which is done using so-called gates, namely input gate

$$\mathbf{i}_t = \sigma_g(\mathbf{W}_i \mathbf{x}_t + \mathbf{R}_i \mathbf{h}_{t-1} + \mathbf{b}_i), \quad (5.14)$$

where \mathbf{x}_t is a variable-length sequence at time step t , forget gate

$$\mathbf{f}_t = \sigma_g(\mathbf{W}_f \mathbf{x}_t + \mathbf{R}_f \mathbf{h}_{t-1} + \mathbf{b}_f), \quad (5.15)$$

cell candidate

$$\mathbf{g}_t = \sigma_c(\mathbf{W}_g \mathbf{x}_t + \mathbf{R}_g \mathbf{h}_{t-1} + \mathbf{b}_g), \quad (5.16)$$

and output gate

$$\mathbf{o}_t = \sigma_g(\mathbf{W}_o \mathbf{x}_t + \mathbf{R}_o \mathbf{h}_{t-1} + \mathbf{b}_o), \quad (5.17)$$

where $\sigma_g(\mathbf{c}_t)$ denotes the gate activation function.

5.3.2 Gated Recurrent Units

The Gated Recurrent Unit (GRU), introduced in 2014 by [154], is a simpler in computation and implementation variant of LSTM network. This is because it employs fewer parameters than LSTM and lacks an output gate. These modifications supply the GRU with unique advantages, such as quicker training times and the ability to handle certain tasks where model simplicity is important aspect.

It consists of update gate (z_t), reset gate (r_t), activation (H_t), and candidate activation (\tilde{H}_t). The update gate is used to control how much historical information and new information needs to be forgotten in the current state:

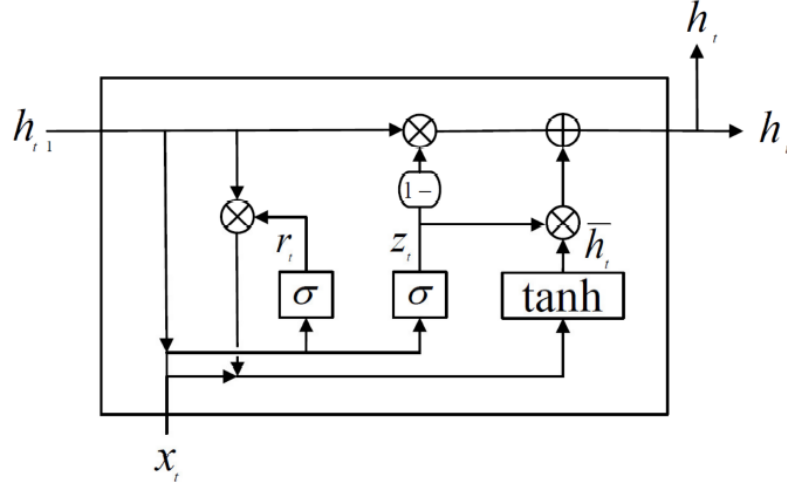


Fig. 5.7. GRU layer architecture [151]

$$\mathbf{z}_t = \sigma_g(\mathbf{W}_z \mathbf{x}_t + \mathbf{R}_z \mathbf{h}_{t-1} + \mathbf{b}_z). \quad (5.18)$$

The reset gate controls how much information is available from the candidate state:

$$\mathbf{r}_t = \sigma_g(\mathbf{W}_r \mathbf{x}_t + \mathbf{R}_r \mathbf{h}_{t-1} + \mathbf{b}_r). \quad (5.19)$$

The candidate activation can be regarded as the new information at the current time:

$$\tilde{\mathbf{H}}_t = \tanh(\mathbf{W}_{\tilde{H}} \mathbf{x}_t + \mathbf{R}_{\tilde{H}} \mathbf{r}_t \odot \mathbf{H}_{t-1} + \mathbf{b}_{\tilde{H}}). \quad (5.20)$$

The activation is generated by the update gate and candidate activation. If a lot of new information is retained, the old information considered will be less, and vice versa:

$$\mathbf{H}_t = \mathbf{z}_t \odot \mathbf{H}_{t-1} + (1 - \mathbf{z}_t) \odot \tilde{\mathbf{H}}_t. \quad (5.21)$$

In this case, the matrices \mathbf{W} , \mathbf{R} , and \mathbf{b} are series of interconnected input weights, recurrent weights, and bias of each component, as follows:

$$\mathbf{W} = \begin{bmatrix} \mathbf{W}_z \\ \mathbf{W}_r \\ \mathbf{W}_{\tilde{H}} \end{bmatrix}, \mathbf{R} = \begin{bmatrix} \mathbf{R}_z \\ \mathbf{R}_r \\ \mathbf{R}_{\tilde{H}} \end{bmatrix}, \mathbf{b} = \begin{bmatrix} \mathbf{b}_z \\ \mathbf{b}_r \\ \mathbf{b}_{\tilde{H}} \end{bmatrix}. \quad (5.22)$$

5.3.3 Autoencoders

Autoencoders are a specific type of feed-forward neural networks where the input is the same as the output. A classic autoencoder consists of three components: encoder, code and decoder. The encoder compresses the input and produces the code, the decoder then reconstructs the input only using this code (Fig. 5.8). The typical autoencoder is trained without supervision to reconstruct the input data as accurately as possible, which can be e.g., used for anomaly detection, text generation, and signal denoising [155]. This is achieved by utilizing a smaller

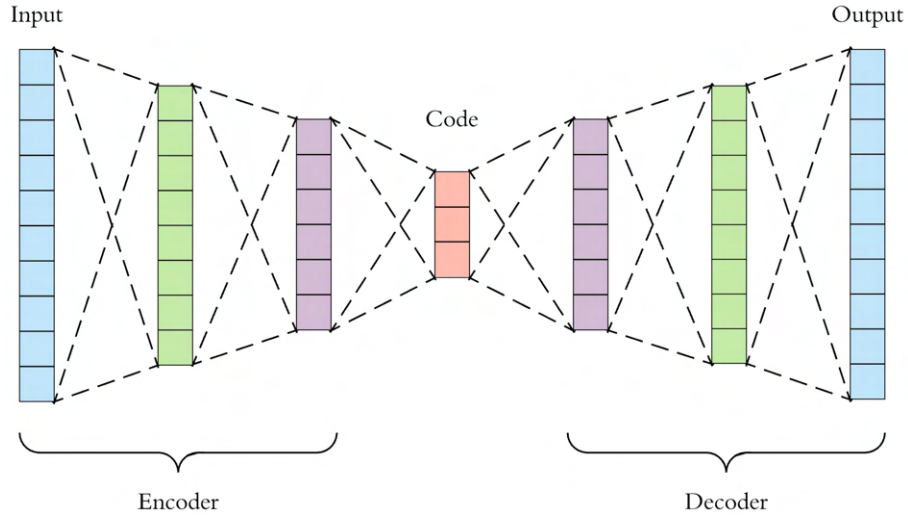


Fig. 5.8. Architecture of a typical autoencoder [156]

number of hidden layers (called as latent representation, context or code) than the number of features [149].

To be able to interface with sequential data, scientists have proposed recurrent autoencoders (RAE) - in the form of Encoder-Decoder [154] or Sequence to Sequence [157]. Their architecture looks very similar to the typical autoencoder and consists of encoder and decoder, where both incorporate RNN layers (Fig. 5.9). The encoder-decoder approach allows having variable-length input and output sequences in contrast to classic RNN solutions.

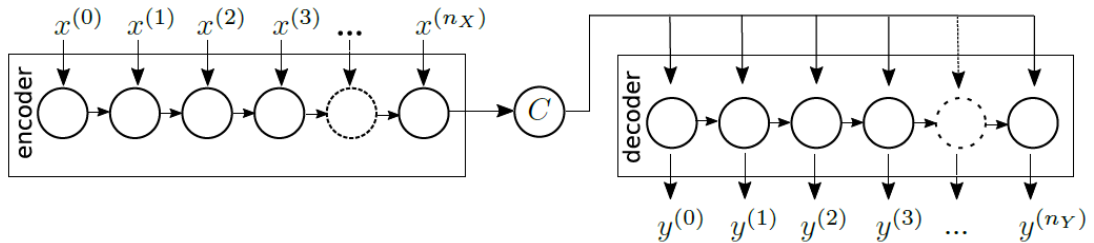


Fig. 5.9. Structure of a recurrent autoencoder [149]

The RAE generates an output sequence \mathbf{Y} :

$$\mathbf{Y} = (y^{(0)}, y^{(1)}, \dots, y^{(n_Y-1)}), \quad (5.23)$$

for given an input sequence \mathbf{X} :

$$\mathbf{X} = (x^{(0)}, x^{(1)}, \dots, x^{(n_X-1)}), \quad (5.24)$$

where n_Y and n_X are the sizes of output and input sequences respectively (both can be of the same or different size). Usually, $\mathbf{X} = \mathbf{Y}$ to force the autoencoder to learn a compact and meaningful representation of the input data. Initially, the input sequence data is encoded by the recurrent neural network encoder, and then the given fixed-size latent representation variable C is decoded by the decoder (usually also RNN).

5.4 Model performance indicators

The evaluation of the process model performance can be conducted in many ways. However, the most frequently applied methods use ex post measures developed for the assessment of the accuracy of forecasts for any time series, regardless of their source of origin. Standard accuracy measures can be employed for assessing process models obtained via any modeling method. To evaluate the performance of the trained deep learning models, different evaluation criteria can be used. Based on the literature research [64, 158], numerous criteria were selected and described in this section.

For the mean absolute error (MAE), mean absolute percentage error (MAPE), mean squared error (MSE), root mean squared error (RMSE), and normalized root mean squared error (nRMSE), the closer the values are to 0, the better the accuracy of the model. Often, when evaluating a model, it is also necessary to consider its complexity. During the creation of neural models, information criteria are used to evaluate the trained models, taking into account their complexity, such as the Akaike's Information Criterion (AIC), the Hannan-Quinn's Criterion (PHI), and Bayesian Information Criterion (BIC).

Mean Absolute Error (MAE)

MAE is a metric used to evaluate the accuracy of predictive models. It quantifies the average magnitude of the errors made by a model in its predictions, irrespective of the direction of the errors. Specifically, MAE is computed as the arithmetic mean of the absolute differences between the predicted values and the corresponding true values in the test dataset. Notably, all the individual differences between the predicted and true values are accorded equal weight when computing the MAE:

$$\text{MAE} = \frac{1}{n_s N_G} \sum_{j=1}^{n_s} \sum_{i=0}^{N_G} |y_{ij} - \hat{y}_{ij}|, \quad (5.25)$$

where n_s represents the number of outputs, y_{ij} is the j -th output of the model observed for the i -th input, \hat{y}_{ij} denotes the predicted value of the j -th output of the model, $N_G = \text{card}(L_G)$ is the amount (cardinality) of the L_G testing dataset.

Mean Absolute Percentage Error (MAPE)

MAPE is a metric used to evaluate the accuracy of model's predictions in percentage terms. It is calculated as the average of the absolute percentage differences between the predicted values \hat{y}_{ij} and the corresponding true values y_{ij} in the test dataset. This definition emphasizes that MAPE measures the average absolute percentage error, and is commonly used in forecasting and time-series analysis:

$$\text{MAPE} = \frac{100\%}{n_s N_G} \sum_{j=1}^{n_s} \sum_{i=0}^{N_G} \left| \frac{y_{ij} - \hat{y}_{ij}}{y_{ij}} \right|. \quad (5.26)$$

Mean Squared Error (MSE)

Mean Squared Error (MSE) is a metric used to quantify the average of the squared errors made by a model in its predictions. More specifically, MSE is calculated as the arithmetic mean of the squared differences between the predicted values \hat{y}_{ij} and the corresponding true values y_{ij}

in the test dataset. This definition emphasizes that MSE captures the average squared difference between the predicted and true values, and is widely used as a measure of the goodness of fit of a model:

$$\text{MSE} = \frac{1}{n_s N_G} \sum_{j=1}^{n_s} \sum_{i=0}^{N_G} (y_{ij} - \hat{y}_{ij})^2. \quad (5.27)$$

Root Mean Squared Error (RMSE)

Root Mean Squared Error (RMSE) is a commonly used metric in the evaluation of predictive models. It is a quadratic scoring rule that provides a measure of the average magnitude of the errors made by a model in its predictions. Specifically, it is computed as the square root of the average of the squared differences between the predicted values \hat{y}_{ij} and the corresponding true values y_{ij} in the test dataset:

$$\text{RMSE} = \frac{1}{n_s} \sum_{j=1}^{n_s} \sqrt{\frac{1}{N_G} \sum_{i=0}^{N_G} (y_{ij} - \hat{y}_{ij})^2}. \quad (5.28)$$

Normalized Root Mean Squared Error (nRMSE)

nRMSE is a metric used to evaluate the performance of predictive models that normalizes the RMSE by dividing it by the range of the target values. This normalization allows for a comparison of the performance of models with different scales of target values. The resulting metric ranges between 0 and 1, with 0 indicating a perfect fit and 1 indicating a complete mismatch between the predicted \hat{y}_{ij} and actual values y_{ij} :

$$\text{nRMSE} = \frac{1}{n_s} \sum_{j=1}^{n_s} \frac{1}{\sigma_{Y_j}} \sqrt{\frac{1}{N_G} \sum_{i=0}^{N_G} (y_{ij} - \hat{y}_{ij})^2}, \quad (5.29)$$

where σ_{Y_j} represents standard deviation of the actual values.

Akaike's Information Criterion (AIC)

AIC is a statistical measure used to compare the goodness of fit of different models, taking into consideration their complexity. The AIC incorporates a penalty term for the number of parameters to account for model complexity. A lower AIC value indicates a better balance between model fit and complexity. When comparing multiple models, the one with the lowest AIC is generally considered to be the best choice.

$$\text{AIC} = N_G \ln(Q_G) + 2h, \quad (5.30)$$

where h is the number of parameters in the model, $Q_G = \{\text{RMSE}, \text{nRMSE}, \dots\}$ is the selected quality measure of the process dynamics representation determined for the test data set.

Hannan-Quinn's Criterion (PHI)

PHI is a criterion used to compare different models. Like the AIC, the PHI includes a penalty term for the number of parameters to account for model complexity. However, it uses a different penalty term, resulting in a more conservative model selection approach. A lower PHI value indicates a better balance between model fit and complexity.

$$\text{HQC} = N_G \ln\left(\frac{Q_G}{N_G}\right) + 2h \ln(\ln(N_G)). \quad (5.31)$$

Bayesian Information Criterion (BIC)

BIC incorporates a penalty term for the number of parameters in the model to avoid overfitting. This penalty term is more severe than that of the Akaike Information Criterion (AIC), making BIC more conservative when it comes to the inclusion of additional variables. In terms of interpretation, a lower BIC value is preferred. The model with the smallest BIC is considered the best because it is the one that minimizes information loss while avoiding unnecessary complexity.

$$\text{BIC} = N_G \ln(Q_G) + h \ln(N_G). \quad (5.32)$$

5.5 Fault detection performance indicators

Evaluation of the fault detection performance is done using a set of different indices. Because the dissertation is focused on fault detection, it is justified to make use of a set of detection-related performance indices proposed by Bartyś et al. [159]. For liquid intrusion and liquid leakage detection purposes, it is sufficient to apply only three fundamental measures:

- False detection rate (r_{fd}):

$$r_{fd} = \frac{\sum_n t_{fd}^n}{t_{from} - t_{on}}, \quad (5.33)$$

where t_{fd}^n is the n th period of the high level of the binary diagnostic signal indicating the existence of a fault in the system between t_{on} and t_{from} .

- True detection rate (r_{td}):

$$r_{td} = \frac{\sum_n t_{td}^n}{t_{hor} - t_{from}}, \quad (5.34)$$

where t_{td}^n is the n th period of the high level of the binary diagnostic signal indicating the existence of a fault in the system between t_{from} and t_{hor} .

- Detection delay time (t_{dt}):

$$t_{dt} = t_{dd} - t_{from}, \quad (5.35)$$

where t_{dd} is the first leading edge of the diagnostic signal at the period of time when a fault exists.

5.6 Summary

This chapter presents the proposed fault detection methods. The first proposed method is a fault detection method using LSTM neural network. This method utilizes a classic model-based process diagnostic approach, where the model is fed with registered process inputs and outputs. Here, two different residual evaluation approaches are proposed. The first is just based on the statistical analysis, employing two moving averages and a fixed threshold for binary diagnostic signal generation. The second is based on a model error modeling methodology for a more robust detection schema, where adaptive upper and lower thresholds are computed. The second fault detection method proposes an alternative process diagnostic approach, wherein an autoencoder neural network model equipped with GRU layers is fed only with the recorded process output signals. This strategy is suggested as a practical solution for real-time monitoring on low-cost embedded devices, such as automotive ECUs.

Furthermore, theoretical background for recurrent neural networks (such as LSTM, GRU, and RAE) including the architecture and functionality overview is provided. Those types of RNNs are identified to be particularly useful for tasks such as anomaly detection for sequence data. As the proposed methods have to be evaluated on a later stage, a set of model-performance indicators as well as fault detection performance indicators are proposed and described.

6. Verification study

This chapter describes the verification study process, whose main goal was to implement and verify the performance of the designed optical liquid detection system and the formulated fault detection methods, namely two schemes of the fault detection method using the LSTM neural network (Fig. 5.2, Fig. 5.3), and the fault detection method using the autoencoder neural network (Fig. 5.4). The chapter is divided into four parts and starts with a description of the verification plan, which provides a general overview of the study and the sequential steps involved. This is followed by a detailed description of the preliminary study that was conducted under laboratory conditions, as well as the comprehensive study that was conducted under road conditions. This iterative approach allowed for the most important aspects of the OLDS to be tested at different stages of its development. Initially, the tests were focused on verifying the minimum viable functionality and the first fault detection method, exposing the system to known and controlled conditions. Based on the obtained results and conclusions drawn, the final version of the OLDS was deployed and exposed to real, road conditions, with data collected over a period of several months. This extensive data acquisition process was followed by the implementation and verification of the second fault detection method, that means the fault detection method using the autoencoder neural network. Lastly, the chapter concludes with a summary of the findings drawn from the verification study process.

6.1 Verification plan

The verification plan presented in Fig. 6.1 provides a structured framework aimed at validating the effectiveness and robustness of the optical liquid detection system, its components, and proposed fault detection methods under controlled laboratory conditions and realistic road conditions. This plan adopts a two-step approach encompassing a preliminary study under laboratory conditions and comprehensive tests under road conditions, thus ensuring a thorough examination of the system’s functionality and fault detection capabilities. Each stage in this study is marked by a series of clear milestones to indicate progress. For both the preliminary and the final study, the verification plan is finalized with a detailed evaluation of the obtained results.

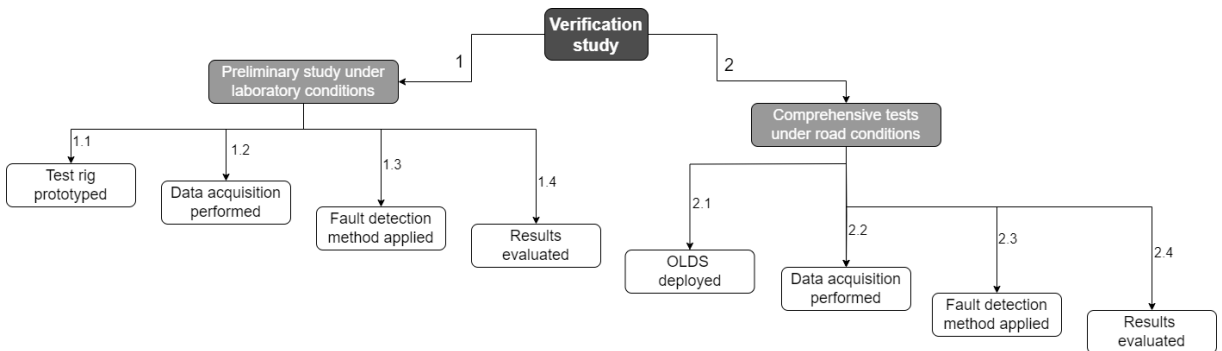


Fig. 6.1. Verification plan

In the preliminary study conducted under laboratory conditions, the first milestone involved the prototyping of a test rig. This phase included the setup of system components such as the fabricated POF sensor, developed hardware and software, measurement devices, and additional devices used for the fault simulation. Once the rig was fully operational, data acquisition was carried out under a controlled environment. This stage involved testing the system's responses under both faultless state and simulated fault scenarios (specifically, water intrusion and oil leakage). The faults were simulated in a controlled manner, using devices such as a peristaltic pump and a magnetic stirrer. The collected datasets provided crucial insights into the system's behavior, exposing the system to constant environmental conditions and variable fault states. Based on registered data, a fault detection method was applied. This process involved the design, parameter selection, training, and testing of a model. Lastly for the preliminary study, the results were thoroughly evaluated, considering both model performance and fault detection performance indicators. The conclusions drawn from this stage provided valuable insights for the next step, i.e., the comprehensive tests conducted under road conditions.

In the comprehensive tests carried out under road conditions, the final version of the OLDS was assembled inside a real battery module's housing and then mounted inside a vehicle, marking the transition to a realistic operating environment. Over the span of six months, data acquisition was performed to account for various road conditions, temperature ranges, and fault states. After applying the fault detection method (which included designing, selecting parameters for, training, and testing a model), the results were evaluated based on the defined performance indicators. The comprehensive tests provided crucial insights into the system's real-world performance and resilience to adverse conditions, leading to a more robust optical liquid detection system.

6.2 Preliminary study under laboratory conditions

The verification study started with a preliminary phase conducted under a controlled laboratory environment. These laboratory conditions were chosen to closely emulate standard ambient settings, with a stable temperature maintained near 25°C and relative humidity oscillating between 40-60%. The intention behind this strategy was to analyze the system's behavior in a neutral environment, not influenced by external temperature variations or other influencing factors. This preliminary study served as a foundation for further comprehensive tests, with the focus on obtaining a clear understanding of the system's behavior under constant conditions, setting the baseline for subsequent, more complex testing scenarios.

6.2.1 Test rig

The development of a test rig was a crucial element in conducting an effective preliminary verification study. It allowed the emulation of both normal and fault conditions in a controlled manner. By employing a test rig (Fig. 6.2), the system's reactions and responses could be examined in a replicable, adjustable, and measurable setting, enabling a thorough and robust verification of the system's capabilities. The test rig was supposed to be able to:

- interface with the fabricated POF sensor,
- interface with the reference polymer optical fiber cable,
- control a magnetic stirrer and a peristaltic pump,
- register the performed measurements and state of external devices.

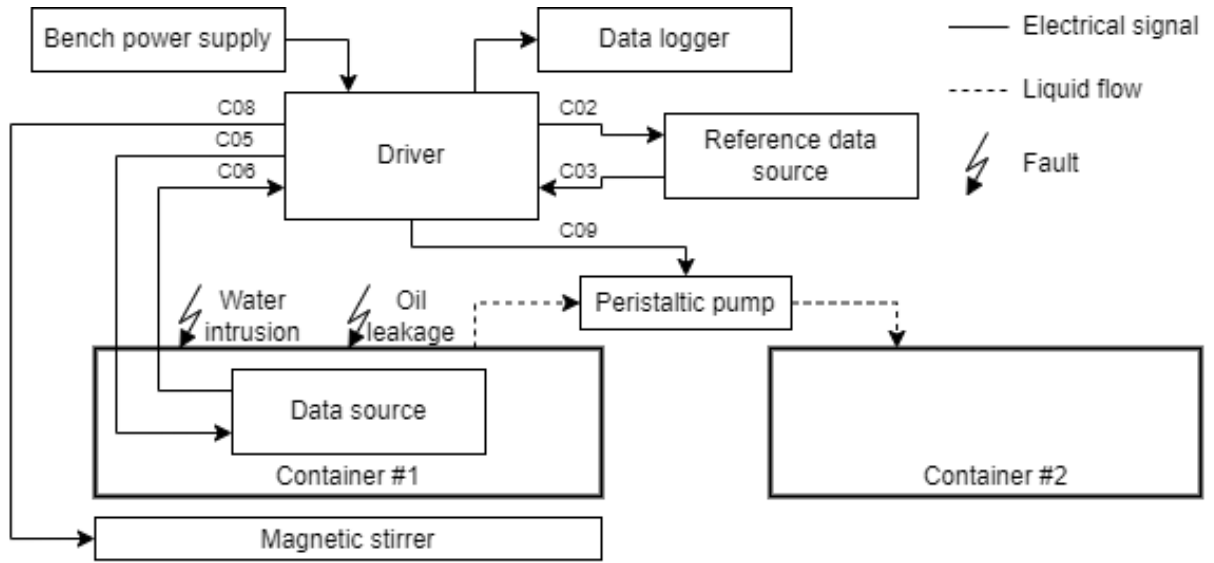


Fig. 6.2. Test rig block diagram

To achieve such functionality, the ECU in its preliminary prototype stage was employed together with laboratory equipment and external devices. The laboratory equipment consisted of a bench power supply (for a consistent and steady power supply), and a digital oscilloscope (for precise, high-resolution measurements). Such equipment (Appendix E) was used to advance the research process and avoid potential hardware-related issues. The output voltage of the bench power supply was set to 12 V, which supplied the main driver. The test rig also consisted of two 500 ml containers. The first container was filled with 300 ml of mineral oil. To simulate different fault conditions, the liquid intrusion was simulated using distilled water dispensed from a syringe. The liquid leakage fault, on the other hand, was simulated using a peristaltic pump that transported the liquid between the two containers. Since water and oil are immiscible, any intruded water would form an oil-water emulsion. If the formed emulsion was quiescent, its particles would settle (based on their densities), separating both liquids over time. To have control over such a physical phenomenon, a magnetic stirrer was employed to occasionally stir both liquids and simulate the vehicle movement. A data source (fabricated evanescent wave absorption polymer optical fiber sensor) was placed inside the container filled with oil. An additional reference data source (polymer optical fiber cable) was employed for conducting supplementary measurements with the purpose of discovering whether the ambient conditions had any influence on the transmitted light over the POF cable. The data recording was realized through serial communication between the ECU and a PC, and an open-source SerialPlot application (Appendix E). An early stage of test rig development process was presented in Fig. 6.3. The figure presents a prototype of the ECU, together with laboratory equipment and a fabricated evanescent wave absorption polymer optical fiber sensor.

From a process diagnostic point of view, there were several process variables (referred to as channels), namely:

- $C02(k)$ - Pulse-Width Modulated (PWM) optical signal to the reference data source (POF cable),
- $C03(k)$ - the returned optical signal of the POF cable,
- $C05(k)$ - PWM optical signal to the data source (POF sensor),
- $C06(k)$ - the returned optical signal of the POF sensor (also referred to as raw measurement),

- $C08(k)$ - controlling signal of the magnetic stirrer (with 0 and 1 values indicating the stirrer turned OFF and ON respectively),
- $C09(k)$ - controlling signal of the peristaltic pump (with 0 and 1 values indicating the peristaltic pump turned OFF and ON respectively).

To establish a connection between the proposed fault detection methods (Fig. 5.2, Fig. 5.3), and the signals registered during the preliminary study under laboratory conditions, the following relationships were defined: $\mathbf{u}(k) = [C05(k), C02(k)]$, $y(k) = C06(k)$. The remaining channels, i.e., $C01(k)$, $C04(k)$, $C07(k)$ were irrelevant as they were not used throughout this study.

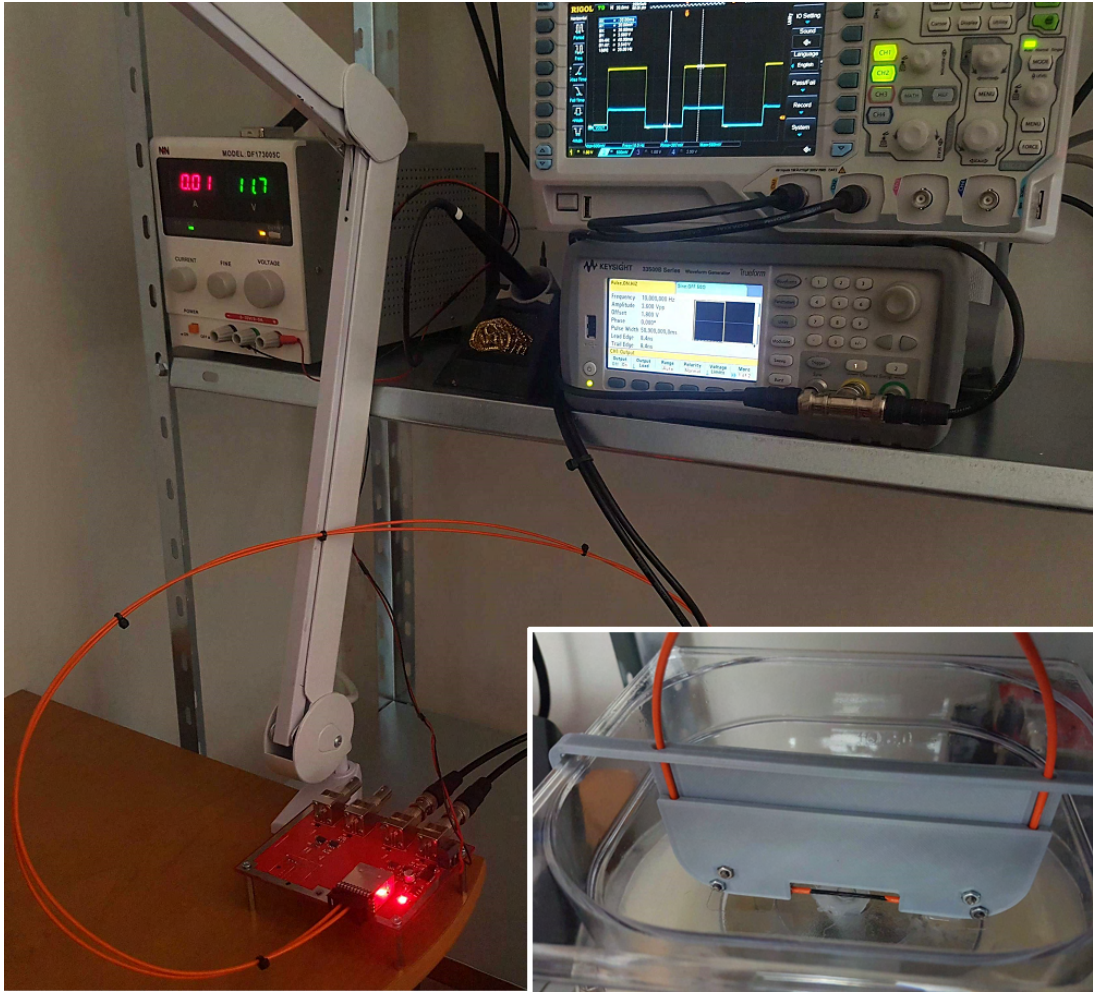


Fig. 6.3. Test rig during its prototyping stage

6.2.2 Data acquisition under laboratory conditions

The process of data acquisition was focused on executing a series of experiments under both faultless and fault states. The principal objective was to collect datasets under different fault states, that could be effectively divided into three different subsets: training, testing, and validation. These subsets were crucial to the establishment of robust models, as each served a unique purpose in the overall process. The training set was used in the development and optimization of the model, the testing set measured the model's performance, and the validation set verified the generated model's effectiveness.

Several experiments with different fault states and system configurations were performed. Each experiment started with system initialization, which was followed by the activation of the data recording application. Depending on the experiment's ID, different activities were performed in order to simulate the desired conditions. During the experiment:

- Q_1 volume of oil could be leaked at time t_1 ,
- Q_1 volume of water could be intruded at time t_1 ,
- the magnetic stirrer could be activated at time t_2 and deactivated at time t_3 .

In the case of oil leakage experiments, the system was brought back to its initial state after each experiment. This ensured that each new experiment started with the main container filled with 300 ml of mineral oil. For the water intrusion faults, only the first experiment began with 0% water concentration. This means that if water was intruded during an experiment, the new resulting water concentration remained for subsequent experiments. This implies that the system initiated subsequent experiments with an already present fault, and over the course of this verification study step, the fault magnitude continually increased.

Using the designed test rig and following the experiment methodology, 25 experiments were carried out in total: 10 experiments for faultless conditions (F0), 5 experiments for oil leakage faults (F1), and 10 experiments for water intrusion faults (F2). Configuration of each experiment was listed in Tab. 6.1. The duration of each experiment was denoted by t_{tot} . In total, 337659 data entries were recorded, which correspond to approx. 55 min of the total duration. The collected data was split into three sets: training data (experiments IDs 1-4, 6-9), testing data (experiments IDs 5 and 10), and verification data (experiments IDs 11-25).

Tab. 6.1. Experiment scenarios

Exp. ID	Data type	State ID	Description	Mag. [%]	Q_1 [ml]	t_1 [s]	t_2 [s]	t_3 [s]	t_{tot} [s]
1	Training	F0	No fault 1	-	-	-	-	-	53
2	Training	F0	No fault 2	-	-	-	-	-	42
3	Training	F0	No fault 3	-	-	-	-	-	30
4	Training	F0	No fault 4	-	-	-	-	-	44
5	Testing	F0	No fault 5	-	-	-	-	-	175
6	Training	F0	No fault stirred 1	-	-	-	12	57	75
7	Training	F0	No fault stirred 2	-	-	-	11	67	82
8	Training	F0	No fault stirred 3	-	-	-	23	67	69
9	Training	F0	No fault stirred 4	-	-	-	-	48	77
10	Testing	F0	No fault stirred 5	-	-	-	7	30	72
11	Verification	F1	Oil leakage 1	100	300	45	-	-	174
12	Verification	F1	Oil leakage 2	100	300	7	-	-	148
13	Verification	F1	Oil leakage 3	50	150	42	-	-	140
14	Verification	F1	Oil leakage 4	100	300	17	-	-	172
15	Verification	F1	Oil leakage 5	100	300	23	-	-	207
16	Verification	F2	Water intrusion 1	9	30	55	15	175	175
17	Verification	F2	Water intrusion 2	14	20	17	0	122	161
18	Verification	F2	Water intrusion 3	14	-	-	17	107	150
19	Verification	F2	Water intrusion 4	14	-	-	0	89	142
20	Verification	F2	Water intrusion 5	14	-	-	4	74	166
21	Verification	F2	Water intrusion 6	21	30	18	0	88	154
22	Verification	F2	Water intrusion 7	21	-	-	19	64	202
23	Verification	F2	Water intrusion 8	21	-	-	24; 69	49; 99	180
24	Verification	F2	Water intrusion 9	30	50	11	0	96	149
25	Verification	F2	Water intrusion 10	30	130	-	19	65	327

In the case of faultless conditions (F0), ten of the planned experiments were divided into two subgroups. For the first five sets (experiment IDs 1-5), the system recorded process variables under quiescent conditions, with no additional activities performed. The next five sets were

recorded with the magnetic stirrer being occasionally activated at the time t_2 and deactivated at the time t_3 , to simulate stirring conditions.

For the oil leakage fault, the magnetic stirrer was not turned at all. Instead, the peristaltic pump was activated at the time t_1 to leak the Q_1 volume of oil, which was to simulate the oil leakage fault. The volume Q_1 was either 150 ml or 300 ml, resulting in different fault magnitudes.

The remaining ten datasets for water intrusion conditions were performed using a variable fault magnitude, where water of the volume Q_1 was intruded at time t_1 . The volume Q_1 ranged from 20 ml to 130 ml throughout the experiments, which ultimately led to rising fault magnitudes, starting with 9%, 14%, 21% and finishing at 30% weight-to-weight water concentration. Additionally, the magnetic stirrer was occasionally activated at the t_2 and deactivated at the t_3 . To improve the visual analysis, $f(k)$ signals were set to 0, 1, 2, 3, and 4 for 0% (faultless state), 9%, 14%, 21%, and 30% water concentration respectively, providing a clear indication of the fault size.

Exemplary output signal $y(k) = C06(k)$ measurements were shown in Fig. 6.4a. The measured signal was a PWM signal, which was presented in details in Fig. 6.4b. This means that the POF sensor's corresponding LED transmitter was switching its state between ON and OFF, in this case with a frequency of 100 Hz. Although the test rig was under faultless state, a variation of the measured signal can be observed. Because the system was exposed to laboratory conditions, the refractive index of the measured oil shall remain constant, especially in such short period as presented in aforementioned figures. Because of that, the recorded signal variation was identified as a noise that resulted e.g. from power supply lines of the ECU that supplied the microcontroller (and its ADC circuits), but also the transimpedance amplifiers that were responsible for controlling LED transmitters and photodiode receivers circuits. Stirring conditions, simulated through a magnetic stirrer, were shown as a blue area as a period where the magnetic stirrer was enabled.

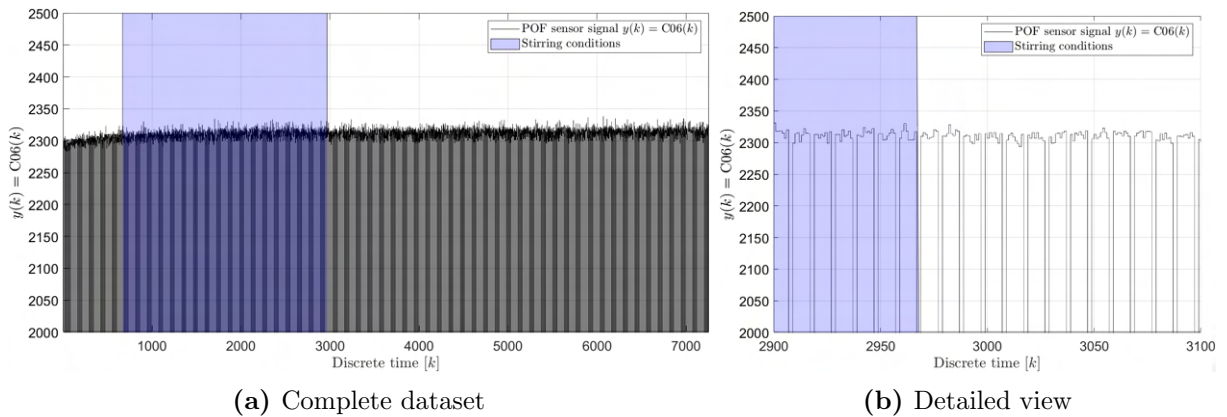


Fig. 6.4. Exemplary measurements $y(k)$ for *No fault stirred 5* dataset

In the case of oil leakage fault, the change of the observed signal can be observed with a notable delay with respect to the $f(k)$ occurrence. The reason behind that was the placement of employed POF sensor (Fig. 6.3). In other words, approximately 150 ml of the oil had to be leaked from the container before the sensing area of the POF sensor was exposed to a different medium. An experiment of such Q_1 oil volume was performed (Fig. 6.5) to investigate a situation where the level of remaining oil was the same as the level at which the employed POF sensor was mounted. By doing so, the POF sensor was partially exposed to oil and air at the same time. In such scenario, the observed rise in $y(k)$ was significantly lower (approximately 2%) than in the case of experiments with Q_1 set to 300 ml, where the oil was leaked completely from the container. In such case, the rise of observed signal $y(k)$ was approximately 25%. Due to

the intrinsic properties of oils, particularly their slower evaporation rate compared to water, the POF sensor would retain a wet state from the residual oil until it completely evaporates or until the remaining droplets would descend from the sensor. Consequently, there would be an initial difference in the POF sensor response, eventually stabilizing and reaching an equilibrium state over time. Such situation was observed for the experiments no. 11, 12, 14, and 15.

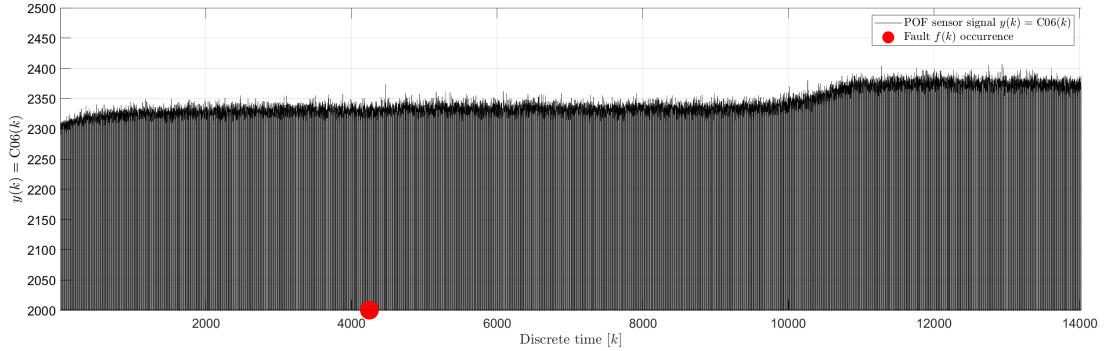
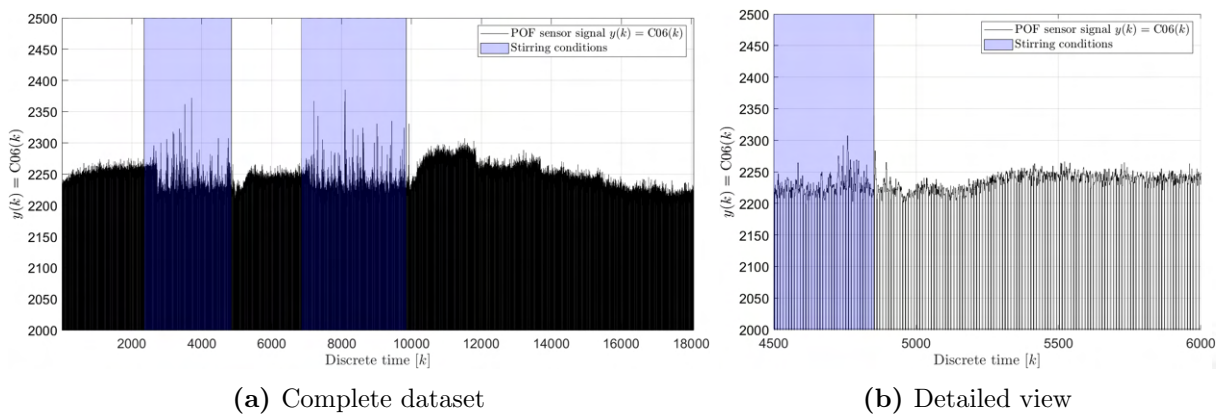


Fig. 6.5. Exemplary measurements $y(k)$ for *Oil leakage 3* dataset

For a water intrusion fault, the specified volume of water Q_1 was intruded at the time t_1 . During this experiment, a magnetic stirrer was occasionally enabled (at the time t_2) and disabled (at the time t_3). The dataset labeled "Water intrusion 8" was the only dataset, for which it was decided to enable and disable the magnetic stirrer twice during the experiment. Observed signal $y(k)$ of this experiment was shown in Fig. 6.6a. This experiment started with already present water intrusion fault $f(k)$ with magnitude of 21%. Together with a detailed view in Fig. 6.6b, it can be observed that variations of the recorded $y(k)$ signal were clearly visible at the moment of stirring the emulsion. They were less visible (or not visible at all) when the emulsion was no longer stirred. For this particular data set and fault magnitude, different behaviors of the formed emulsion were registered after each stirring. In the first case, approximately ten seconds after the magnetic stirrer was disabled, the observed signals $y(k)$ returned to similar values as right before enabling the stirrer. In the second case, much more time was needed to reach the quiescent conditions and similar sensor measurements. This could be related to different strength of the stirring conditions.



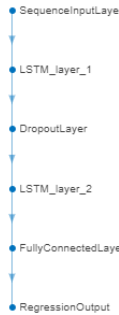
(a) Complete dataset

(b) Detailed view

Fig. 6.6. Exemplary measurements $y(k)$ for *Water intrusion 8* dataset

6.2.3 Elaboration of fault detection schemes for laboratory conditions

According to the verification study, the preliminary study under laboratory conditions was planned to collect datasets for the further evaluation of the fault detection method. This was realized through the first method, i.e., the method using LSTM neural network, which was proposed with two different residuum evaluation schemes (Fig. 5.2 and Fig. 5.3). Both of the proposed schemes employed the same LSTM model. The structure of its corresponding neural network (that was a result of a trial-and-error process) was presented in Fig. 6.7. The neural network was used to model the relationships between input $\mathbf{u}(k) = [C05(k), C02(k)]$, and output $y(k) = C06(k)$ signals.



	Name	Type	Activations	Learnable Properties	Number of Learnables
SequenceInputLayer	1 SequenceInputLayer Sequence input with 2 dimensions	Sequence Input	$2(C) \times 1(B) \times 1(T)$	-	0
LSTM_layer_1	2 LSTM_layer_1 LSTM with 55 hidden units	LSTM	$55(C) \times 1(B) \times 1(T)$	InputWeights 220×2 RecurrentWeights 220×55 Bias 220×1	12760
DropoutLayer	3 DropoutLayer 1% dropout	Dropout	$55(C) \times 1(B) \times 1(T)$	-	0
LSTM_layer_2	4 LSTM_layer_2 LSTM with 55 hidden units	LSTM	$55(C) \times 1(B) \times 1(T)$	InputWeights 220×55 RecurrentWeights 220×55 Bias 220×1	24420
FullyConnectedLayer	5 FullyConnectedLayer 1 fully connected layer	Fully Connected	$1(C) \times 1(B) \times 1(T)$	Weights 1×55 Bias 1×1	56
RegressionOutput	6 RegressionOutput mean-squared-error with response 'Response'	Regression Output	$1(C) \times 1(B) \times 1(T)$	-	0

Fig. 6.7. Structure of LSTM neural network used for fault detection

The network consisted of:

- a sequence input layer that accommodated sequence input data of two dimensions,
- a first LSTM layer with 55 hidden units (12760 learnable parameters, composed of input weights of size 220×2 , recurrent weights of size 220×55 , and biases of size 220×1) with tanh activation function for updating cell and hidden states and sigmoid activation function for gates,
- a dropout layer (to prevent overfitting during training). This layer randomly set 1% of input elements to zero at each update during training time, effectively "dropping out" those units,
- a second LSTM layer, identical in configuration to the first LSTM layer, which consisted of 55 hidden units (24420 learnable parameters, composed of input weights of size 220×55 , recurrent weights of size 220×55 , and biases of size 220×1) with tanh activation function for updating cell and hidden states and sigmoid activation function for gates,
- a fully connected layer with a single output unit, suitable for regression tasks (56 learnable parameters, composed of weights of size 1×55 and a bias of size 1×1). The fully connected layer was important for aggregating the outputs from the previous LSTM layer and producing a single output value,
- a regression output layer with mean squared error as the loss function. This layer was responsible for calculating the error of the network predictions during training, and using this error to update the network's weights.

Such structure was used to generate and train a model using the training set, where 80% of datasets collected under faultless conditions were used (as shown in Tab. 6.1). For the parameter tuning of this model, the adaptive moment estimation (ADAM) method was employed. The gradient decay factor β_1 was set to 0.9, emphasizing the importance of recent gradients. The squared gradient decay factor β_2 was set to 0.999, averaging lengths of 1000 parameter updates.

The epsilon ε value was set to 1E-08 offering numerical stability by preventing any division by zero in the ADAM update rule. The training process began with an initial learning rate of 0.01, determining the step size at each iteration while the model moved towards a minimum of the loss function. Over time, this learning rate dropped by a factor of 0.9 every 10 epochs, helping the model to search more efficiently. The 'l2norm' gradient threshold method was used. Weight updates in the model were based on mini-batches of 409600 samples in each iteration. The generated model was tested using the testing set (data collected under experiments 5 and 10), for which a set of model performance indicators was calculated to evaluate its performance. The trained model showed the performance in predicting outcomes with an MSE of 9.2245E-05 and MAPE of 0.7874%, indicating modest deviations from actual values. AIC indicated -9.2512 in terms of complexity and fit. Values of \bar{r} and σ_r were calculated as -0.0075 and 0.0060 respectively.

Figure 6.8 presents detailed views of the exemplary normalized observed and generated signals, for faultless state (a), oil leakage state (b), and water intrusion state (c).

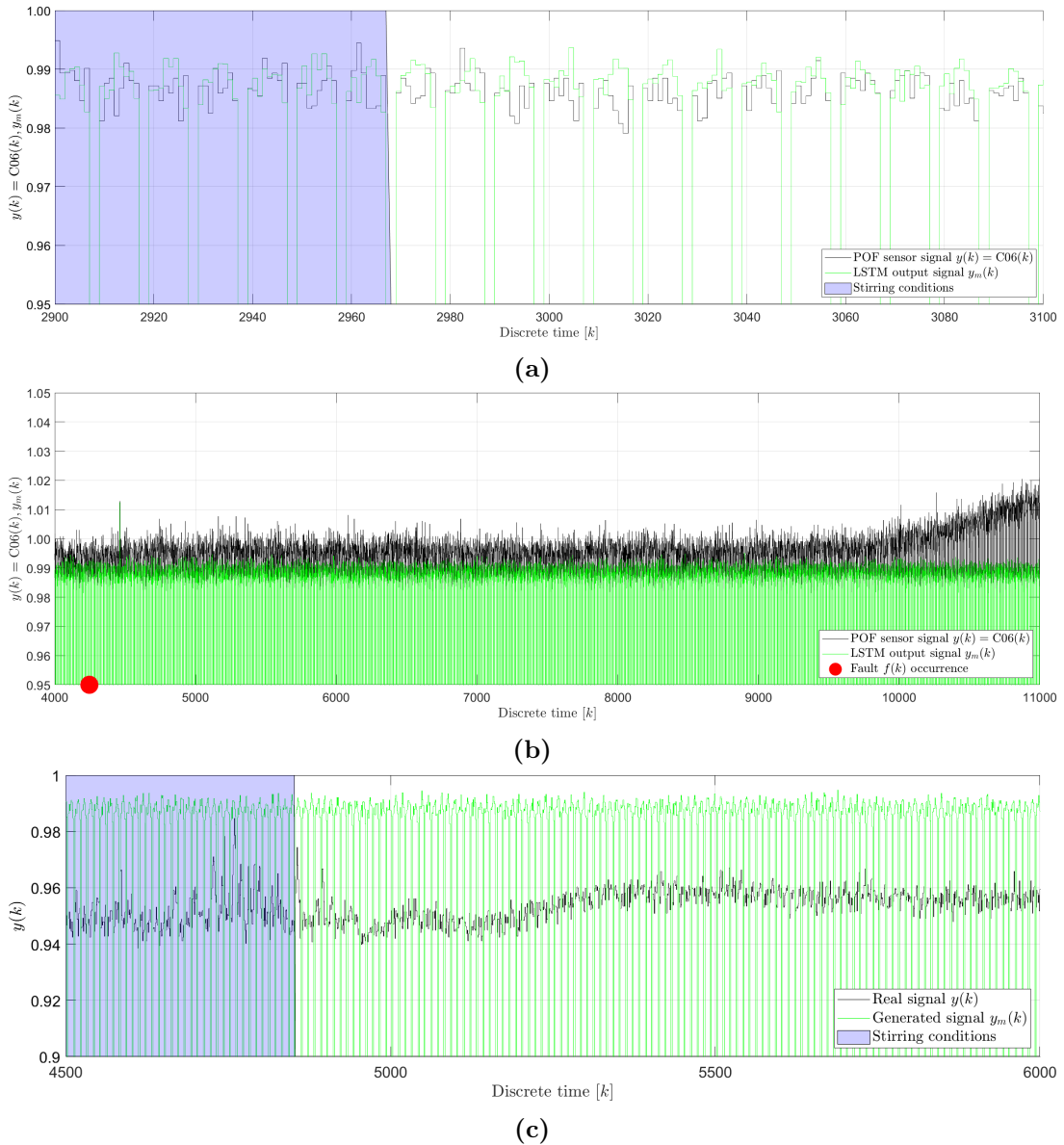


Fig. 6.8. Exemplary POF sensor and LSTM model output signals for: (a) *No Fault stirred 5* dataset (b) *Oil leakage 3* dataset (c) *Water intrusion 8* dataset.

The detailed views clearly present that the model has successfully replicated the variable frequency of the POF sensor signal $y(k)$. It can be also observed that the level of LSTM model output signal $y_m(k)$ remains similar even in the case of fault occurrence. For the oil leakage fault, the $y(k)$ rises with respect to $y_m(k)$, while in the case of the water intrusion fault, the $y(k)$ falls with respect to $y_m(k)$.

Figure 6.9 presents the generated residuum for the faultless state (a), the oil leakage fault (b), and the water intrusion fault (c).

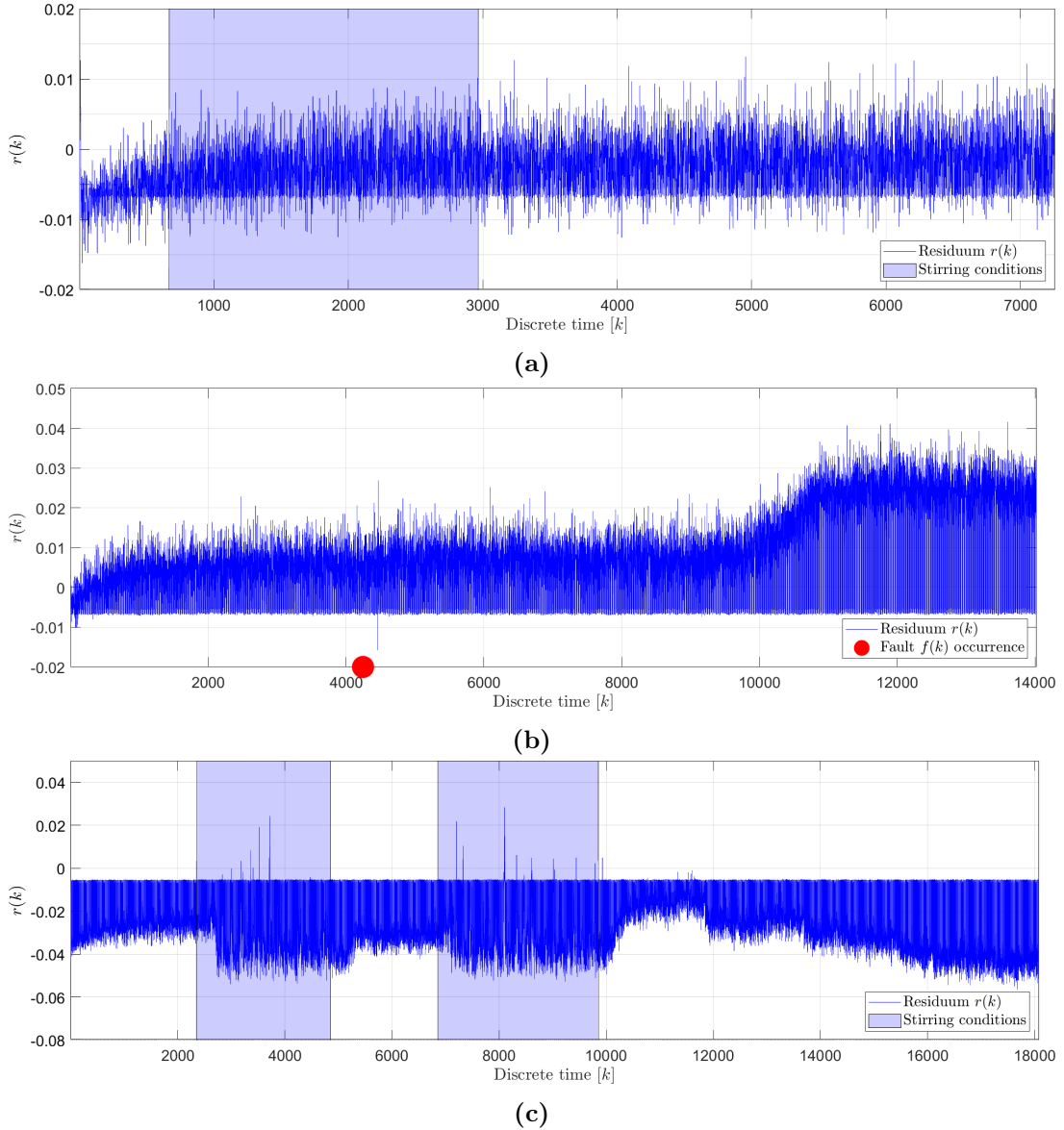


Fig. 6.9. Exemplary residua generated for: (a) *No Fault stirred 5* dataset (b) *Oil leakage 3* dataset (c) *Water intrusion 8* dataset.

It can be observed that for the faultless state, the magnetic stirrer state did not have any influence on the generated residuum $r(k)$. For the oil leakage fault, the first deviations were observed moments after the fault occurred. For this dataset, the magnitude of fault was 50%. Because of that, the sensing area has not been fully exposed to interact with the air, which resulted in a different sensor response than if the oil leaked completely. The presented dataset of water intrusion fault indicates that the fault was visible mostly under stirring conditions, or

during the short time after stirring. This was because water droplets of the formed emulsion were settling over time. If the magnitude of this fault was not high enough, then the sensing area would not be completely covered by the water. Such a type of fault can be dangerous for the lithium-ion battery pack, as the intruded water may not be detected unless the vehicle starts moving.

The applied fault detection method was realized using the same LSTM model and therefore, the same residuum generation approach. However, the residuum evaluation was realized through two different schemes. The first, simpler, was based on statistical analysis (Fig. 5.2). This method required three parameters in advance to be set, namely moving average window sizes n_1 , n_2 , and a fixed fault threshold p . Through the trial-and-error procedure, the following parameters were chosen: $n_1 = 300$, $n_2 = 150$, and a fixed fault threshold $p = 0.0015$ (Eq. 5.2).

The second, more complex yet more robust scheme, utilized model error modeling methodology (Fig. 5.3). This particular technique employed an additional TDNN model, which structure consisted of:

- a sequence input layer that accommodated sequence input data of two dimensions,
- a time delay layer, which applied time delays up to 50 time steps back,
- a dropout layer (to prevent overfitting during training). This layer randomly set 1% of input elements to zero at each update during training time, effectively "dropping out" those units,
- a hidden layer, that contained 20 neurons (with a tanh activation function),
- an output layer, that output the final predicted values (with a linear activation function).

The presented neural network was used to model the relationships between input signal $\mathbf{u}(k) = [C05(k), C02(k)]$, and output one $y_e(k) = r(k)$. To train and test such TDNN model, the testing set of the LSTM model was split into new training and testing subsets with ratios of 80% and 20% respectively. The training of the TDNN was carried out using the Levenberg-Marquardt algorithm, with the number of epochs equal to 55, initial value of regularization factor $\mu = 0.001$, decrease ratio of $\mu = 0.1$, and increase ratio of $\mu = 10$. In this case, the MSE indicator was calculated as 3.1404E-05. According to this scheme, to calculate the adaptive thresholds (Eq. 5.3) this technique required mean \bar{r} and standard deviation σ_r values derived from the generated residuum $r(k)$ under the faultless state. The method required one additional parameter that should be set in advance, namely the significance level t_α^\pm . This scheme of the fault detection method using LSTM recurrent neural networks was applied using the following values: $\bar{r} = -0.0075$, $\sigma_r = 0.0060$, $t_\alpha^+ = 2.3$, $t_\alpha^- = 0.05$.

6.2.4 Fault detection results for experiments under laboratory conditions

The exemplary results of the simple fault detection scheme were presented in Fig. 6.10, where selected data from experiments no. 13 (*Oil leakage 3*, Fig. 6.10a) and no. 23 (*Water intrusion 8*, Fig. 6.10b) were provided. The figures present the difference between $\bar{r}_1(k)$ and $\bar{r}_2(k)$ (as per Eq. 5.2). Moreover, indications of stirring conditions, as well as the fault $f(k)$ occurrence, were provided (if they were present for a given experiment). Although this residuum evaluation scheme is based on moving averages which by definition introduced delays in the fault detection, this computational undemanding method allowed to detect both oil leakage well as water intrusion faults. The visualized results of every performed experiment can be found in Appendix C.

In the case of oil leakage, it can be observed that the diagnostic signal $s(k)$ was triggered approximately 0.5 s after the fault $f(k)$ was simulated, although further positive values were registered approximately 60 s later. In this specific case, the magnitude of fault was set to 50%, which resulted in the exposure of the POF sensor's sensing area to different mediums (air and oil). After the medium reached its equilibrium state, no further anomalies were registered.

This residuum evaluation scheme was found to be more effective for water intrusion faults, especially at their early stages, where rapid changes occur due to the presence of water droplets inside the container. This was because water differs in its refractive index from oil significantly. Such an approach does also filter out long-term drifts caused e.g. by the ambient temperature (which influences the light emitted by POF transmitters or the refractive index of oil). Furthermore, the collected data indicated that this residuum evaluation scheme was the most effective under stirring conditions. Once the formed oil-water emulsion reached its equilibrium state and quiescent conditions, faults were harder to detect as the water fell below the POF sensor's sensing area.

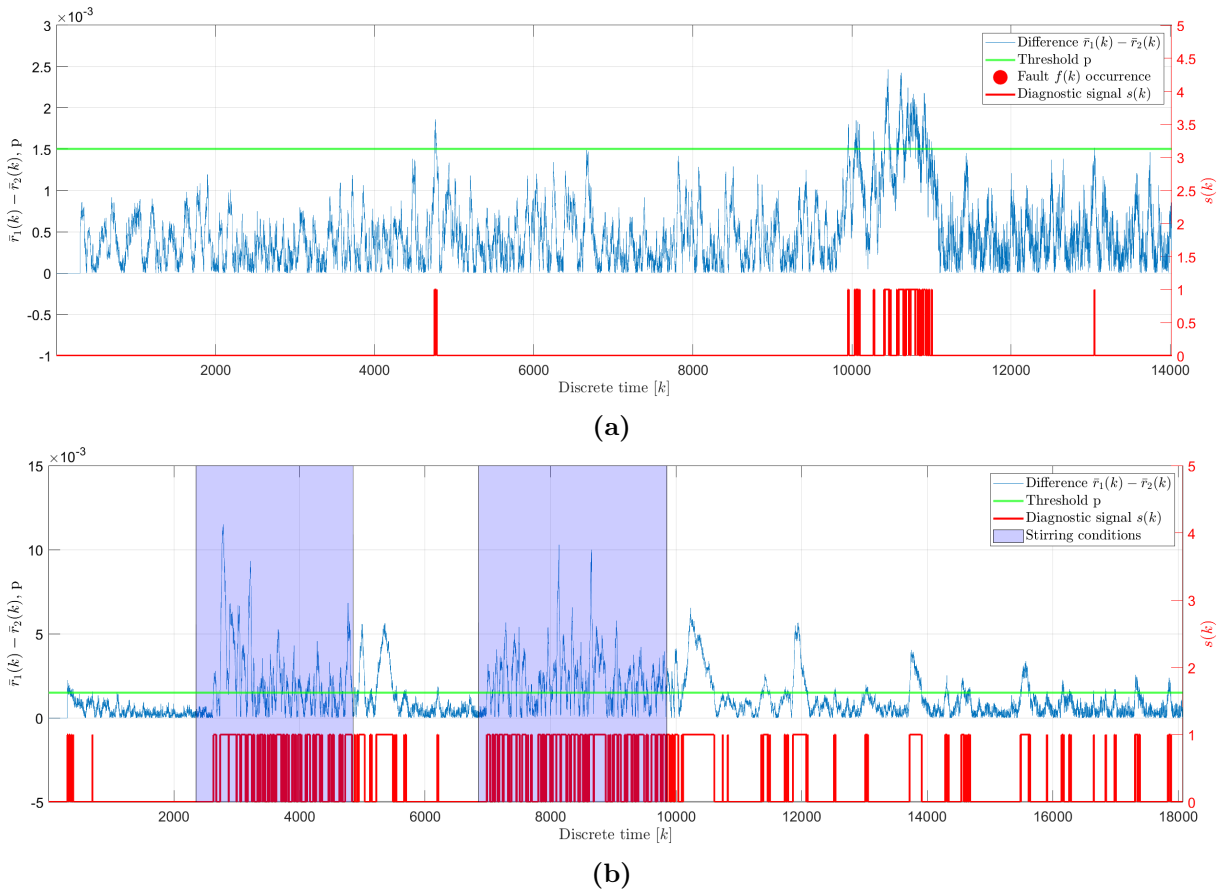


Fig. 6.10. Exemplary results obtained using simple fault detection scheme for: (a) *Oil leakage 3* dataset (b) *Water intrusion 8* dataset.

The results of the robust fault detection scheme for the same datasets were shown in Fig. 6.11. Similarly as for the previous residuum evaluation scheme, indications of the stirring conditions and fault occurrences $f(k)$ were provided. In comparison to the simple fault detection scheme, this approach calculated adaptive upper and lower thresholds (as per Eq. 5.3). Besides noticeably higher performance, a large variation of the diagnostic signal can be observed. This was because:

- the polymer optical fiber sensor was provided with the PWM-driven light source,
- the LSTM model was trained to represent this behavior and it reports faultless state in between PWM cycles (even under stirring conditions),
- the residuum evaluation using adaptive thresholds given by Eq. (5.3) does not consider low states in between PWM cycles, and therefore, the diagnostic signal $s(k)$ fluctuated between 0 and 1.

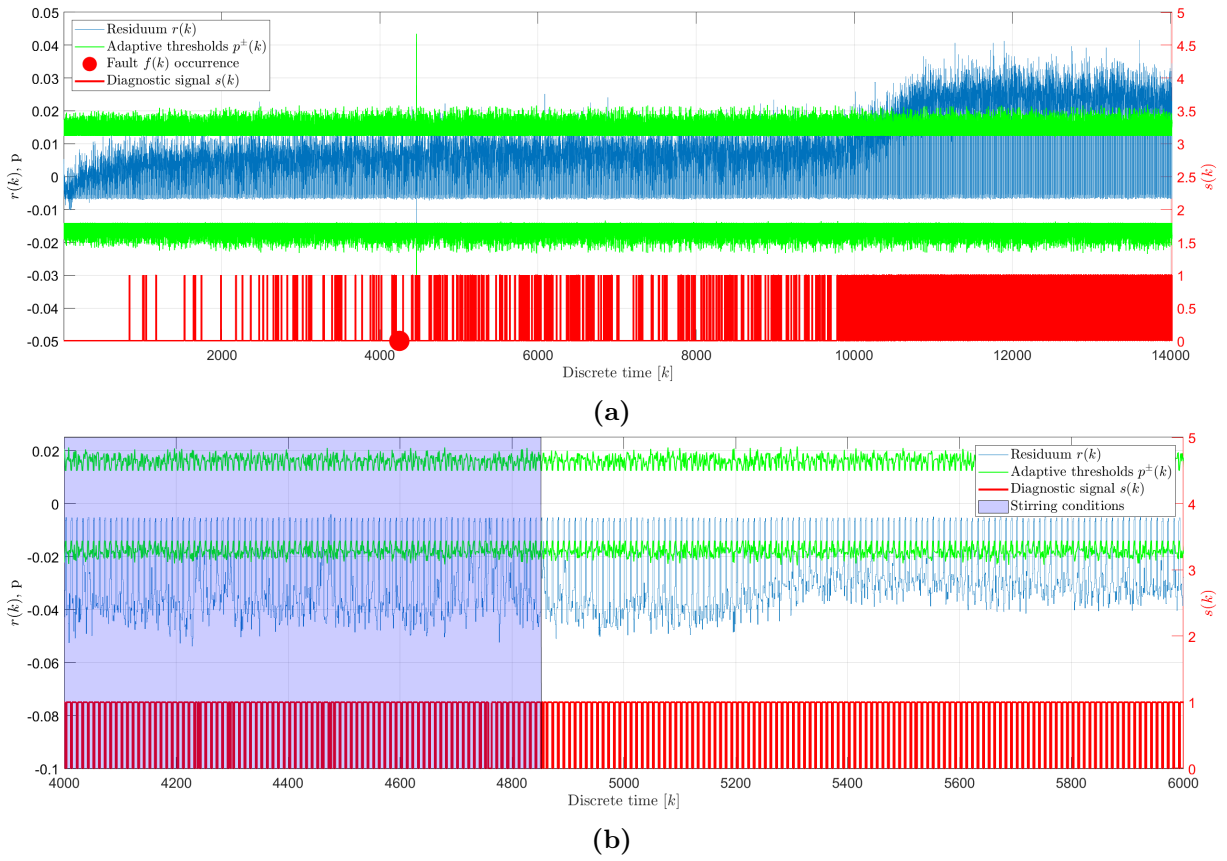


Fig. 6.11. Exemplary results obtained using robust fault detection scheme for: (a) *Oil leakage 3* dataset (b) *Water intrusion 8* dataset.

The performance of both approaches (Fig. 5.2 and Fig. 5.3) was evaluated using indices (Eq. 5.33-5.34) previously described in Section 5.5. Additionally for the water intrusion fault, where under the stirring conditions the formed emulsion could become a nonstable suspension of small water droplets in oil, a third index r'_{td} was proposed. This index was derived similarly to r_{td} (Eq. 5.34), but only under stirring conditions. The indices were calculated for the first and the second fault detection schemes and listed in Tab. 6.2 together with fault magnitude. The obtained results indicate that the highest performance by means of r_{td} and r'_{td} was achieved using a model error modeling methodology. In the case of water intrusion fault, the true detection rates of the second approach were significantly higher than indices obtained for the first scheme. For datasets with fault magnitudes of 9%, 14%, 21%, and 30%, indices obtained for the robust fault detection scheme were higher on average of 21%, 92%, 181%, and 208% respectively. In the case of true detection rate indices under stirring conditions, the difference was notably lower due to the higher performance of the first method. For datasets with fault magnitudes of 9%, 14%, 21%, and 30%, r'_{td} index for the second approach was higher on average of 21%, 24%, 47%, and 36% respectively. A significant positive correlation was found between the magnitude of faults and the performance of both approaches, especially under stirring conditions. Oil leakage detection based on the robust fault detection scheme provided higher true detection rate indices on average by 34% for 50% leakage and as much as five times higher indices for 100% leakage. The only false detection rate r_{fd} (Eq. 5.33) for the simple fault detection scheme was measured for oil leakage faults and was merely about 1%. It should be noted that for water intrusion faults there was only the first dataset, for which the false detection index could be measured. The oil for the remaining F1 datasets was intruded with water and the formed emulsion had at least 9%

Tab. 6.2. Fault detection performance measures

Experiment ID	Dataset description	r_{fd}		r_{fd}		r_{fd}'		Fault magnitude
		Scheme I	Scheme II	Scheme I	Scheme II	Scheme I	Scheme II	
5	F0 - 5	-	-	0.000	0.019	-	-	-
10	F0 (stirred) - 5	-	-	0.000	0.000	-	-	-
11	F1 - 1	0.375	0.405	0.000	0.001	-	-	100%
12	F1 - 2	0.372	0.466	0.000	0.003	-	-	100%
13	F1 - 3	0.047	0.305	0.000	0.013	-	-	50%
14	F1 - 4	0.411	0.551	0.011	0.096	-	-	100%
15	F1 - 5	0.362	0.614	0.013	0.059	-	-	100%
16	F2 - 1	0.034	0.007	0.000	0.002	0.034	0.007	9%
17	F2 - 2	0.124	0.010	-	-	0.148	0.014	14%
18	F2 - 3	0.143	0.198	-	-	0.206	0.152	14%
19	F2 - 4	0.154	0.603	-	-	0.224	0.553	14%
20	F2 - 5	0.125	0.573	-	-	0.219	0.467	21%
21	F2 - 6	0.388	0.753	-	-	0.509	0.751	21%
22	F2 - 7	0.154	0.632	-	-	0.541	0.728	21%
23	F2 - 8	0.291	0.736	-	-	0.568	0.763	21%
24	F2 - 9	0.556	0.689	-	-	0.649	0.708	30%
25	F2 - 10	0.150	0.784	-	-	0.452	0.790	30%

water concentration. For the second approach, the highest r_{fd} of was measured for *Oil leakage 4* and was almost 10%.

The obtained results emphasized the importance of the quality of data that are fed to neural models. For EV battery packs with a direct-liquid cooling battery thermal management system, it is important to apply an appropriate sensor placement to obtain useful data. For oil leakage, the sensors shall be placed in an upper part of the battery pack so the sensor can report a change in fluid type as quickly as possible. Furthermore, the battery pack shall be designed to have additional sensors placed in sections, where the water intrusion is most likely to occur or to detect. For example, additional sensors could be placed in the lower parts to effectively sense water intrusion, as the water droplets would settle there when the formed emulsion is quiescent. Another example would be to place water sensors near the heat exchanger, where liquid leakage or intrusion is likely to occur (e.g. due to different thermal coefficients of the used materials).

Due to the characteristics of these faults, they were categorized as abrupt (oil leakage) and intermittent (water intrusion). If the volume of intruded water is not enough to cover sensing devices during quiescent conditions, the fault would appear mainly during the vehicle's movement (or in the case of research performed under laboratory conditions - during the stirring conditions). Both of the proposed approaches had the same LSTM process model and differed in the residuum evaluation. The simple residuum evaluation scheme utilized a statistical analysis, based on short-term and long-term moving averages. This method presented a limited performance for faults of lower magnitudes, but increased performance for abrupt changes and stirring conditions. The robust residuum evaluation scheme utilized a TDNN model. Although more complicated and computationally demanding, this method performed notably better for all cases, and the difference in its performance between quiescent and stirring conditions was significantly lower. However, the generated diagnostic signal presented signal variations of frequency similar to the frequency of provided input signals $C03(k)$, $C05(k)$. To increase the method's performance even further, an additional diagnostic signal state timeout should have been used to filter out the low states of the $C06(k)$ signal. The presented detection method was provided with datasets that cover only a fraction of factors that affect system measurements. On a daily basis, EVs are exposed to elevated operating temperatures, vibrations, component aging, etc. The next step is to obtain datasets affected by those factors, e.g. under road conditions.

6.3 Comprehensive tests under road conditions

The primary objective of exposing the final version of the optical liquid detection system to road conditions was to broaden the spectrum of factors influencing the system and to generate new datasets for the development of the new fault detection method (Fig. 5.4). During the on-road testing phase, the system was exposed to a wide array of real-world scenarios, including elevated operating temperatures and vibrations. This holistic testing strategy ensured a higher degree of practicality and effectiveness. Furthermore, the tests were conducted over an extended period spanning several months. This extended duration added another layer of complexity, e.g. by introducing component aging effects and a wide temperature range. These effects had a non-negligible influence on the measurements, making the data interpretation and processing more demanding.

Furthermore, the vehicle was operated in a "business-as-usual" manner throughout the testing phase. This approach involved daily routines that a typical vehicle might experience, including traveling to and from the office and utilizing highways and local roads. The testing phase did not use any specific driving patterns, further simulating real-world scenarios. The tests were conducted in the Silesian region of Poland. The combination of various road types and consistent geographical location served to enrich the data, facilitating the development of more robust and adaptable systems.

This chapter presents different stages of the tests performed under road conditions. It starts with a detailed description of the final OLDS version. This is followed by the overview of the performed data acquisition process where the experiment methodology was presented and the data collected under faultless and fault states was analyzed. Subsequently, the implementation phase of the secondary fault detection method (Fig. 5.4) was described, presenting the generation, training, and testing process of the RAE-GRU model. All of this leads to the results, where the fault detection method is evaluated using a set of model performance indicators and corresponding conclusions.

6.3.1 Test rig for experiments in road conditions

The recorded datasets are needed to be used for offline training and testing the formulated model-based fault detection methods. To be able to handle those factors and effectively record corresponding datasets, a new system (Fig. 6.12, Fig. 6.13) derived from the architecture presented in Fig. 4.2 was prototyped. It was decided to use an evanescent wave absorption polymer optical fiber sensor with just one sensing area. Furthermore, the derived system architecture presents one additional (optional) device, called a BMS simulator. Although beyond the scope of this dissertation and designed for future works in advance, the BMS simulator is a device that is meant to be responsible for executing the diagnostics methods based on provided data from the ECU, and forwarding it further to the data recorder. During the current research, the BMS simulator device was not present and the serial communication was forwarded directly between the ECU and the Data recorder.

During the road conditions tests the developed OLDS with the so-called high voltage section filled with 16500 ml of mineral oil (Fig. 6.13 - 1) was employed to gather extensive data over an extended period of time. The system was cautiously installed in the trunk of an automobile to ensure stability throughout the duration of the tests, mitigating the risk of data skewness due to any unwanted movement. The system was designed to gather and record datasets with the frequency of 100 Hz, where each individual data frame encapsulated fields as it was presented in Tab 4.3. The study was conducted over several months (specifically from December 2022 to May 2023), highlighting the reliability and durability of the device in maintaining its function and effectiveness over time during a continuous and long-term data collection process. The design

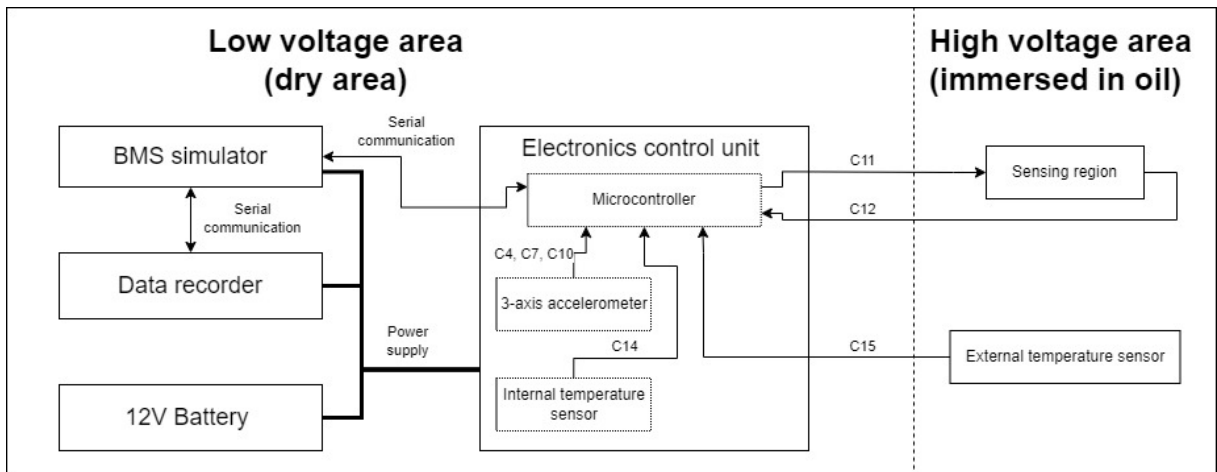


Fig. 6.12. Block diagram of a simplified battery module utilizing an optical liquid detection system during in-field tests

of the OLDS incorporated both internal and external thermistors to provide comprehensive temperature measurements. The internal thermistor was permanently positioned inside the ECU, ensuring a stable recording of the electronics' thermal environment. In contrast, the external thermistor was submerged in oil (Fig. 6.13 - 3), mirroring the arrangement of the polymer optical fiber sensor. The POF sensor itself (Fig. 6.13 - 2) was excited with a PWM optical signal and provided its measurements to the ECU. Since the heat capacity is strongly related to the total volume of used liquid, such an arrangement yielded a well-rounded understanding of the POF sensor's operational conditions. To ensure comprehensive and representative data, each dataset was collected over periods ranging from a few hours up to 60 hours in duration. This methodology was adopted to record the potential daily temperature variation, allowing an assessment of the influence of thermal fluctuation on the measurements. To record vibrations that the OLDS was exposed to during such comprehensive tests, a 3-axis accelerometer was employed which provided its acceleration measurements along the x, y, and z-axes.

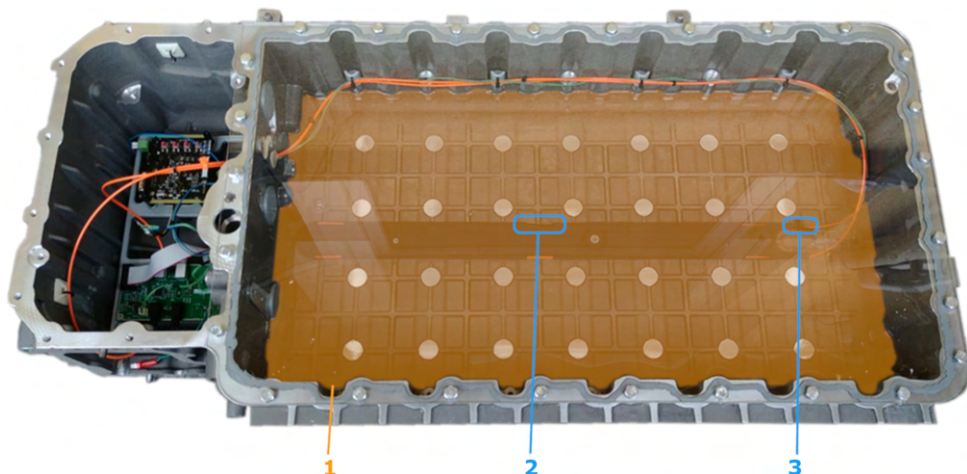


Fig. 6.13. Optical liquid detection system used during the tests under road conditions

From a process diagnostic point of view, there were several process variables (channels) to handle internal and external devices, namely:

- $C04(k)$, $C07(k)$, $C10(k)$ - accelerations measured along x, y, and z-axes respectively (using MEMS accelerometer with $\pm 8g$ range, sensitivity scale factor of $8192 \frac{LSB}{g}$, and temperature sensitivity of $\pm 0.026 \frac{\%}{C}$ [160]),
- $C11(k)$ - PWM optical signal provided to the POF sensor,
- $C12(k)$ - the returned optical signal from the POF sensor,
- $C14(k)$ - resistance of the internal thermistor,
- $C15(k)$ - resistance of the external thermistor.

To establish a connection between the final fault detection methods (Fig. 5.4), and the aforementioned channels, the following relationships for the process input $\mathbf{u}(k)$ and output $\mathbf{y}(k)$ signals were defined:

$$\mathbf{u}(k) = \begin{bmatrix} C11(k) \\ C11(k-1) \\ \dots \\ C11(k-l) \end{bmatrix}, \quad (6.1) \quad \mathbf{y}(k) = \begin{bmatrix} C12(k) \\ C12(k-1) \\ \dots \\ C12(k-l) \end{bmatrix}. \quad (6.2)$$

The remaining channels, i.e., $C01(k)$ - $C03(k)$, $C05(k)$, $C06(k)$, $C08(k)$, $C09(k)$, $C13(k)$, were irrelevant for the sake of this verification study.

Figure 6.14 presents the final optical liquid detection system securely installed within the trunk of a vehicle that was used during this verification study. To ensure the stability of the OLDS, flexible ropes have been used for its attachment. These ropes allow for the system to remain steady and in place during the vehicle's operation, eliminating the potential for dislocation due to vehicle movement.



Fig. 6.14. Optical liquid detection system installed inside the vehicle

6.3.2 Data acquisition under road conditions

The aforementioned approach also ensured that each dataset was not only extensive in its temporal scope but also inclusive of the varying ambient conditions, thus providing a holistic perspective of the system's performance and responsiveness under road conditions. Despite the extensive duration of each dataset, it's important to note that the vehicle was primarily stationary throughout the day, with only intermittent periods of motion, generally in the range of several dozen minutes. For the majority of the time, the car was parked, resulting in a static environment (by means of orientation and vibrations). Such an approach provided a unique study context where data was collected across both stationary and moving states, exposing the optical liquid detection system to close to the real conditions, under different technical states:

- Faultless state (F0) - the container was filled with non-conductive liquid (16500 ml).
- Oil leakage fault (F1) - after having F0 experiment finished, this fault was simulated by inducing an oil leakage of a volume Q_1 . The resulting scenario simulates a leak in the system and its effects on the OLDS.
- Water intrusion fault (F2) - after the completion of the F1 experiment, the water intrusion fault was injected (with variable fault magnitudes). Once intruded, the volume of intruded water remained for further experiment scenarios and accumulated with each consecutive water intrusion occurrence.

A parametric summary of the recorded dataset was presented in Tab. 6.3. In total, 21 experiments were carried out: 7 experiments for faultless conditions (F0), 5 experiments for oil leakage fault (F1), and 9 experiments for water intrusion fault (F2). Every collected dataset has been graphically visualized and presented in Appendix D. The Q_1 parameter indicates the magnitude (in milliliters) of simulated faults. It was constant for the oil leakage fault, but variable for the water intrusion fault. The time horizon of each dataset (in minutes) is described by t_1 . The value of t_2 represents the total time that the vehicle was in motion. This time was derived during the data post-processing based on the logged accelerometer readings. Among the datasets, one dataset (F0, no. 6) was recorded without any movement of the vehicle. F0 is the only state, where datasets were numbered starting with 0. This is because the very first dataset (no. 0) might present unusual behavior (by means of recorded temperatures) as the system was moved from the room to the vehicle.

In the case of oil leakage, the volume Q_1 was set to 15000 ml to emulate a condition where the sensor, under quiescent circumstances, is fully submerged in oil. However, as the vehicle initiates movement, the sensing region becomes prone to exposure to air, especially during vehicular turns. This is when the oil, under the influence of centrifugal force, alters its distribution within the container. Such leakage volume was chosen due to the fact that only one POF sensor was employed and that this POF sensor was placed at the very bottom of the HPB80 container. Significant volume of oil had to be leaked before the polymer optical fiber sensor would be exposed to a different medium during vehicle movement.

For the water intrusion fault, different fault magnitudes were introduced to observe the system's response under varying degrees of fault severity. Initially, the fault magnitude was set to the minimum value of 50 ml, corresponding to an approximate weight-to-weight concentration of 0.3%. This initial setup provided a baseline scenario for minimal water intrusion. Subsequently, the fault magnitude was accumulated in a step-wise manner. The first increment brought the fault magnitude to 150 ml, followed by a further increase to the final fault magnitude of 300 ml. These increments allowed for a progressive examination of the system's performance and responsiveness under increasingly severe water intrusion conditions.

Tab. 6.3. Experiment scenarios

Exp. ID	Data type	State ID	Description	Mag. [%]	Q_1 [ml]	t_1 [min]	t_2 [min]
1	Verification	F0	No fault 0	-	-	2596	104
2	Verification	F0	No fault 1	-	-	1873	127
3	Verification	F0	No fault 2	-	-	3468	274
4	Testing	F0	No fault 3	-	-	3623	176
5	Training	F0	No fault 4	-	-	1061	70
6	Training	F0	No fault 5	-	-	907	51
7	Verification	F0	No fault 6	-	-	562	-
8	Verification	F1	Oil leakage 1	90	15000	1692	51
9	Verification	F1	Oil leakage 2	90	15000	211	15
10	Verification	F1	Oil leakage 3	90	15000	726	27
11	Verification	F1	Oil leakage 4	90	15000	1932	89
12	Verification	F1	Oil leakage 5	90	15000	1299	11
13	Verification	F2	Water intrusion 1	0.3	50	684	65
14	Verification	F2	Water intrusion 2	0.3	50	860	10
15	Verification	F2	Water intrusion 3	0.9	150	344	24
16	Verification	F2	Water intrusion 4	0.9	150	1098	91
17	Verification	F2	Water intrusion 5	1.8	300	122	10
18	Verification	F2	Water intrusion 6	1.8	300	31	27
19	Verification	F2	Water intrusion 7	1.8	300	62	26
20	Verification	F2	Water intrusion 8	1.8	300	221	21
21	Verification	F2	Water intrusion 9	1.8	300	42	32

In total, 140532540 data entries were recorded, which correspond to approx. 390 hours of the total duration. The collected data was split into three sets: training data (experiments IDs 5 and 6), testing data (experiment ID no. 6), and verification data (remaining experiments).

An exemplary dataset was visualized in Fig. 6.15. The dataset presents observed signals of the evanescent wave absorption polymer optical fiber sensor $C12(k)$ versus the temperature of the oil $C15(k)$ (Fig. 6.15a), and versus registered accelerations caused by the movement of the vehicle $C04(k)$, $C07(k)$, $C10(k)$ (Fig. 6.15b) under the faultless state (F0).

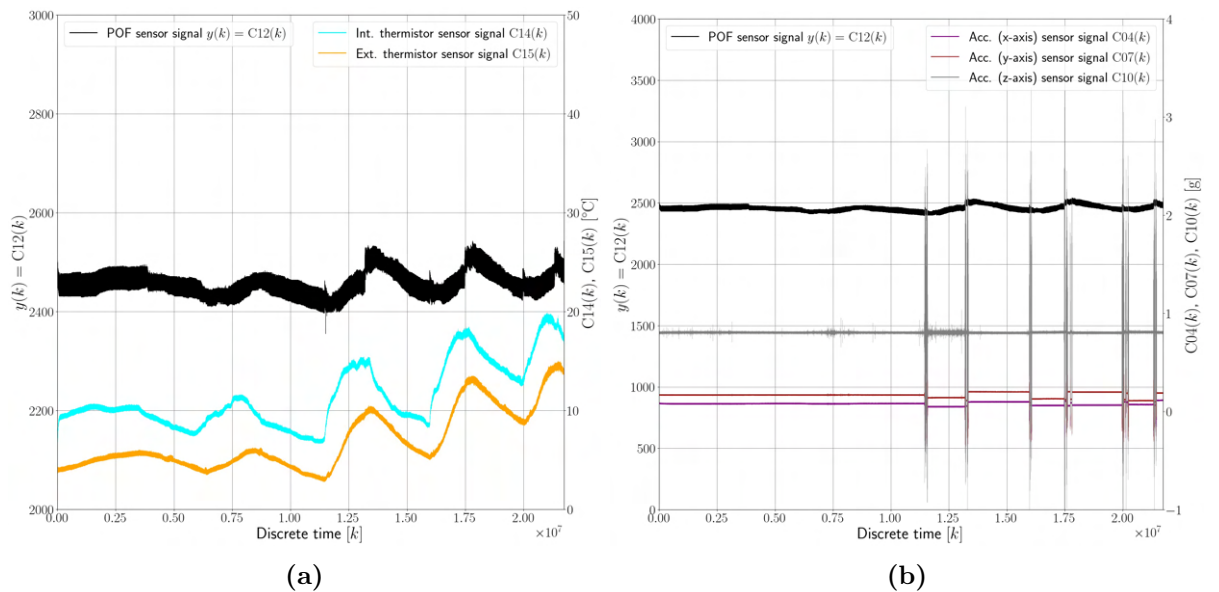


Fig. 6.15. Exemplary measurements $y(k)$ for experiment no. 4 (F0 state) versus (a) temperature (b) accelerations

This particular dataset, with a time horizon of 3623 minutes (approximately 60 hours), revealed the response of the sensor due not only to daily changes in ambient temperature, but also to the movement of the vehicle. Although climatic chamber tests were performed in the past, during those tests only the sensor was susceptible to elevated temperatures. During road conditions tests, on the other hand, both the sensor and the ECU were susceptible to such conditions. The internal thermistor C14(k) of the ECU reported a minimum and a maximum temperature of 5°C, and 20°C respectively. The external thermistor C15(k) (submerged in oil) reported a minimum and a maximum temperature of 3°C, and 15°C respectively. A temperature variation in the range of 10–15°C has already resulted in a variation of the POF sensor’s response by $\pm 4\%$. Additional temperature rises could be observed once the vehicle started moving. This was associated with the additional systems of the car being turned on, such as the heating system which increased the overall temperature inside the car. Even though impacts in the order of 2–3 g could be observed, they did not cause any significant signal variation. This indicates that the optical coupling between the polymer optical fiber sensors and the corresponding LED transmitter and photodiode receiver was robust against vibrations of this order.

The dataset representing the oil leakage fault (F1), presented in Fig. 6.16, covers a time horizon of 1692 minutes (approximately 28 hours) and illustrates the sensor’s response versus temperature (Fig. 6.16a) and measured accelerations (Fig. 6.16b) to conditions wherein 90% of oil had leaked prior to the experiment’s initiation.

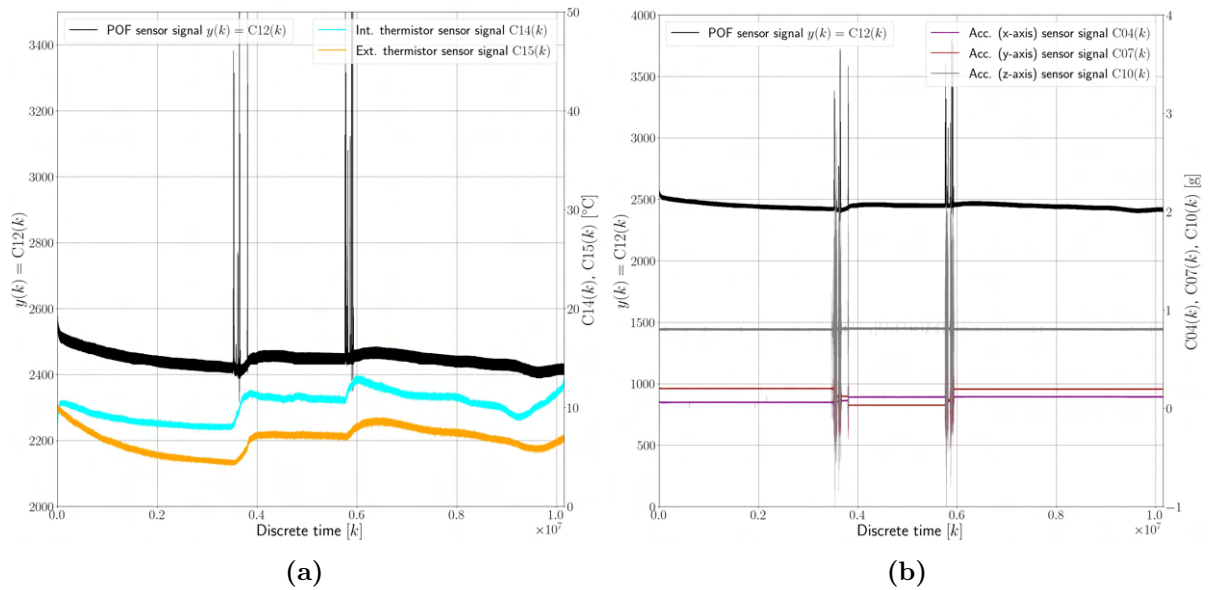


Fig. 6.16. Exemplary measurements $y(k)$ for experiment no. 8 (F1 state) versus (a) temperature (b) accelerations

Unlike the faultless state, where temperature changes were the dominant influencing factors, the sensor’s response under the F1 condition displayed a notable signal variation (of up to 50%). Such change primarily manifested during vehicle turns. In periods of inactivity or static conditions, the system seemed to return to the faultless state (F0). However, during vehicle turns, the distribution of oil within the container was altered, causing the POF sensor to no longer be submerged in oil. This state reversed under static conditions, as the oil re-covered the sensing region.

A dataset demonstrating the water intrusion fault (F2) was shown in Fig. 6.17 with respect to measured temperatures (Fig. 6.17a) and accelerations (Fig. 6.17b). This dataset, unusually, represents a time horizon of only 42 minutes, which was to show the response of the sensor with

greater resolution, under conditions of the oil-water emulsion formed due to water intrusion fault and during varying accelerations caused by the vehicle's movement. The dataset presents a signal variation up to 20%, which is considerably less than what was seen in the case of oil leakage. This is attributed to the different refractive indices that the sensors was exposed to. Regardless of specific maneuvers such as turns, caused by the sensor's exposure to water droplets was registered when the vehicle was in motion. This requirement for motion results from the absence of forced circulation in the system. The vehicle's movement served to disperse and reveal any present water droplets within the system, creating a detectable variation. Without any form of active liquid flow, such as a pump (which could not be included due to component availability at that time), the vehicle's movement was vital for exposing the presence of water droplets with such low fault magnitudes. After the vehicle stopped, the signal variation remained visible for a certain duration until the water droplets settled. Once settled, the system falsely appeared to be in a faultless state again. It was because the volume of intruded water was insufficient to cover the sensing area entirely. This represents a challenging aspect of detecting water intrusion (at its early stage), as the fault may be easily overlooked if the vehicle remains in static conditions, and the volume of intruded water is not high enough to reach the sensor.

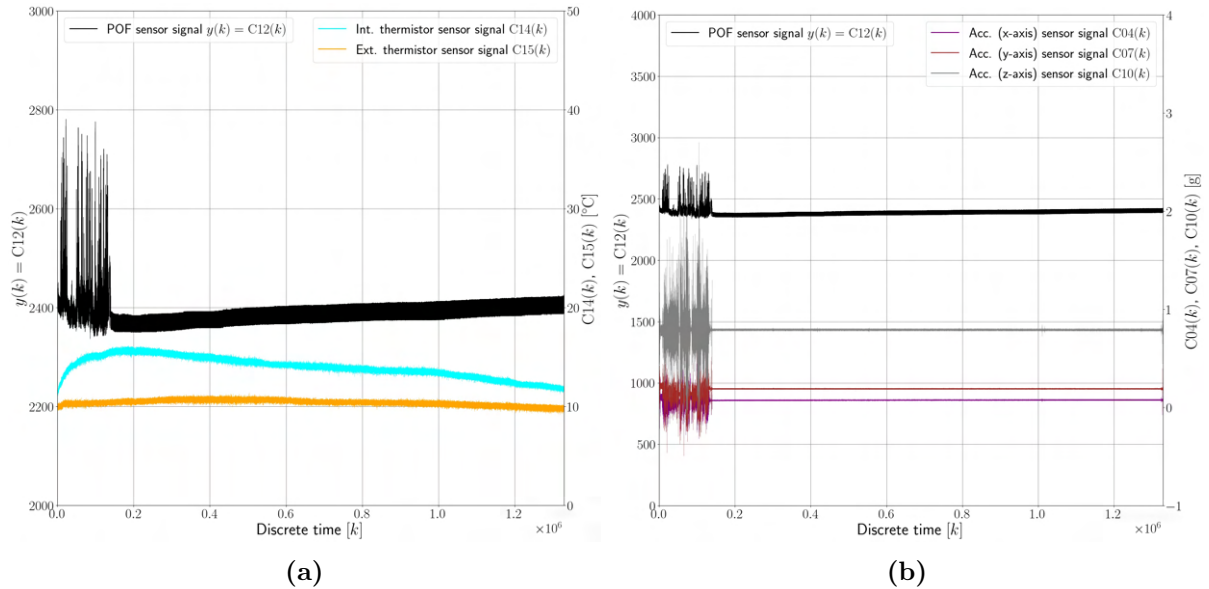


Fig. 6.17. Exemplary measurements $y(k)$ for experiment no. 21 (F2 state) versus (a) temperature (b) accelerations

To gain a comprehensive understanding of the recorded data, all of the datasets were aggregated based on their state and represented as histograms. This format offers a summary of the data distribution across different states under varying ambient conditions. Figure 6.18 presents the POF sensor's measured signals $y(k)$ distribution across different fault states, including oil leakage (Fig. 6.18a), and water intrusion (Fig. 6.18b). Datasets registered for the faultless state presented variations between the values of 2158 and 2942, with a majority of data clustering around 2450. Such signal variations were identified to be attributed to changing ambient conditions (especially ambient temperature). The datasets were collected over an extensive period, spanning several weeks through winter and spring. This acquisition period was interspersed with various recording times throughout the day, sometimes including full day-night cycles, and at other times capturing only specific phases such as daytime or evening. Combined with the diverse temperature ranges encountered over weeks, the distribution of recorded signals does not align with any distinct pattern in terms of the number of data entries at any specific signal

value. Furthermore, the total number of recorded data frames (F0, F1, and F2) is in the order of hundreds of millions, highlighting the extensive duration of the verification study.

In the case of oil leakage, the raw signal strongly exceeded the range of the corresponding signal under the faultless state, although the majority of the recorded signals fell into the same sets as for F0. This, combined with the chart analysis, indicates that the oil leakage fault was not commonly visible throughout each dataset recorded under the oil leakage fault. For the water intrusion fault, on the other hand, the raw signal range was similar to the range of the faultless state. The signal distribution fits the normal distribution, although some minor right skewness can be observed. This could indicate that similarly to oil leakage, this fault could be distinguished mostly under some specific circumstances (e.g., vehicle movement as concluded during chart analysis).

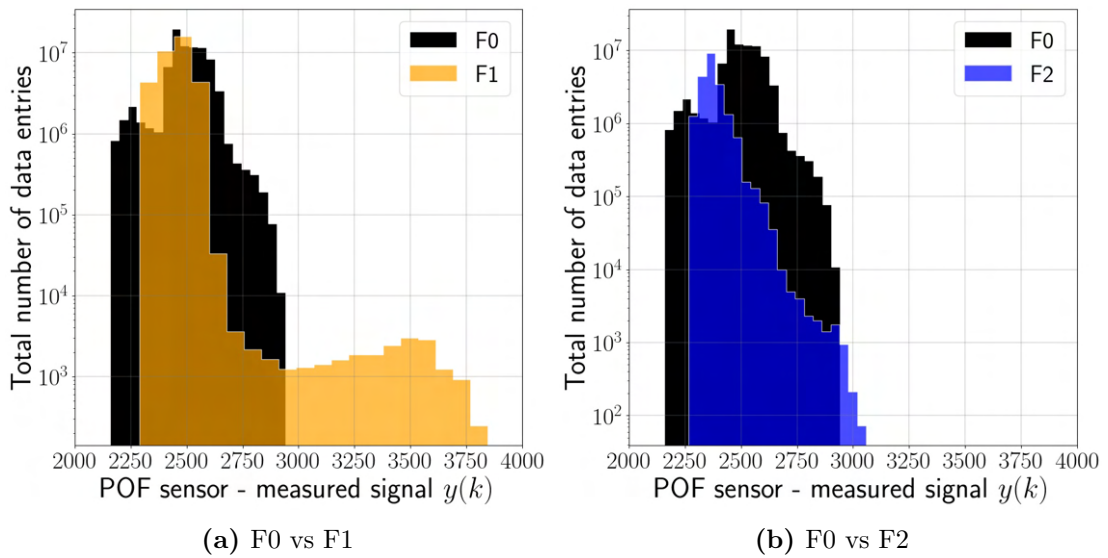


Fig. 6.18. POF sensor's measured signal $y(k)$ distribution across different states

Statistical metrics regarding the collected datasets for every state have been calculated and presented in Tab. 6.4. Across all states, the mean and median were very similar, suggesting that the distributions might be symmetrical, with no significant skewness. The standard deviation was the highest in the faultless state (F0), and lower for the oil leakage (F1) and water intrusion (F2) states, which could be caused by the larger volume of data gathered under F0 state than for F1 and F2 states. Differences between the 25% and 75% quartiles for each state were consistent with the standard deviation findings, suggesting a larger spread in the faultless state, and tighter spreads for the F1 and F2 conditions. As noted before, the oil leakage state showed a wider range between the minimum and maximum values compared to the other states.

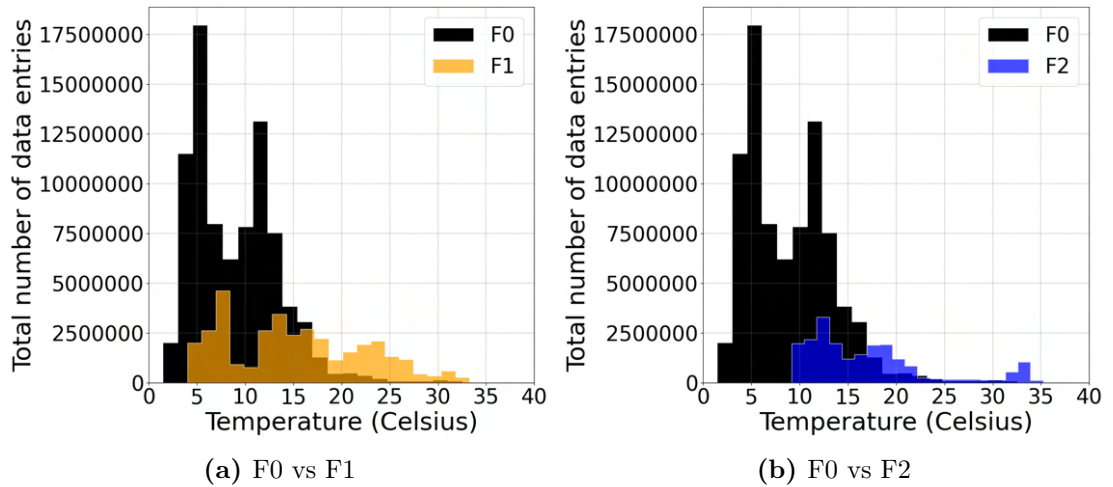
Figure 6.19 presents the aggregated datasets as histograms of recorded signals in relation to the temperature of the oil. Overall, these histograms provide a visual summary of the POF sensor's measured signal $y(k)$ distribution against oil temperature, aiding in understanding the sensor's behavior under various fault conditions and ambient temperatures. As mentioned before, the data collection took place during the winter and spring months, specifically from December 2022 to May 2023. Throughout this period, under faultless conditions, the oil temperature ranged between a minimum of 1,5°C and a maximum of 32°C.

For the oil leakage fault, the tests were conducted after the completion of the faultless state experiments, with the oil temperature in these tests ranging between 4°C and 32°C. This temperature range closely corresponds to the range of the faultless state (Fig. 6.19a). The water intrusion fault state presents a slightly different distribution, which was shown in Fig. 6.19b.

Tab. 6.4. Statistical metrics (POF sensor's output)

Statistic	Faultless State (F0)	Oil Leakage (F1)	Water Intrusion (F2)
Count	8.455404×10^7	3.517700×10^7	2.080150×10^7
Mean	2.495865×10^3	2.452798×10^3	2.371601×10^3
Median	2.495000×10^3	2.455000×10^3	2.363000×10^3
Std	1.035656×10^2	6.690992×10^1	5.136483×10^1
Min	2.158000×10^3	2.289000×10^3	2.266000×10^3
25%	2.447000×10^3	2.423000×10^3	2.343000×10^3
50%	2.495000×10^3	2.455000×10^3	2.363000×10^3
75%	2.560000×10^3	2.496000×10^3	2.390000×10^3
Max	2.942000×10^3	3.846000×10^3	3.058000×10^3

The temperature during these experiments ranged between 9°C and 35°C. Despite the maximum temperature recorded during the F1 and F2 states being just a few degrees higher than that in the case of the F0 state, the number of collected data entries above 20°C was significantly larger for both the oil leakage and water intrusion fault states. Provided that the sensor's response is notably influenced by temperature, the execution of these experiments presented significant challenges due to variations in weather conditions. Ensuring similar temperature conditions across all three experiments — thereby maintaining consistency in the datasets — required careful alignment and timing, which increased the difficulty of the data collection process.

**Fig. 6.19.** Signal distribution (oil temperature) of collected datasets

6.3.3 Elaboration of fault detection approach for road conditions

In the verification study (Fig. 6.1), comprehensive tests under road conditions were planned to collect data for the further evaluation of the fault detection method using autoencoder neural networks (Fig. 5.4). As shown in Chapters 5.2 and 6.3.1, the method utilizes signal $\mathbf{y}(k)$ (Eq. 6.2). The proposed method was applied with the number of samples prior to the most recent sample l set to four (chosen empirically), which results with the following relationships:

$$\mathbf{y}_m(k) = f_{RAE}(\mathbf{y}(k)) = f_{RAE}\left(\begin{bmatrix} \text{C12}(k) \\ \text{C12}(k-1) \\ \text{C12}(k-2) \\ \text{C12}(k-3) \\ \text{C12}(k-4) \end{bmatrix}\right). \quad (6.3)$$

where f_{RAE} represents the relationship approximated by the recurrent autoencoder network proposed in Chapter 5.3.3.

In summary, this approach utilized past and current POF sensor readings to learn a representation of input data in a lower-dimensional space (3 dimensions as per GRU layer). The aim was to train the network such that it could successfully reconstruct the original input data from this lower-dimensional representation, which could be used for anomaly detection. Any significant deviation in the reconstruction error (residuum) could be indicative of anomaly i.e., caused by faults. The final network structure of the applied RAE-GRU model is presented in Fig. 6.20. Analysis of the recorded signals revealed that under the faultless state, the signal variation was observable mainly in the long term, and any abrupt change could indicate a fault. Because of that, executing the fault detection method with the same frequency as the data sampling frequency (100 Hz) was identified as unnecessary. Therefore, an additional step was added, i.e., the signal decimation with the decimation factor of 500. The purpose of signal decimation was to decrease the sample rate from 100 Hz to 0.2 Hz. This was realized through a lowpass Chebyshev Type I Infinite Impulse Response (IIR) filter of order 8. Such filter was chosen due to its ripple characteristics in the passband, which allowed it to effectively retain crucial signal components while attenuating higher frequencies.

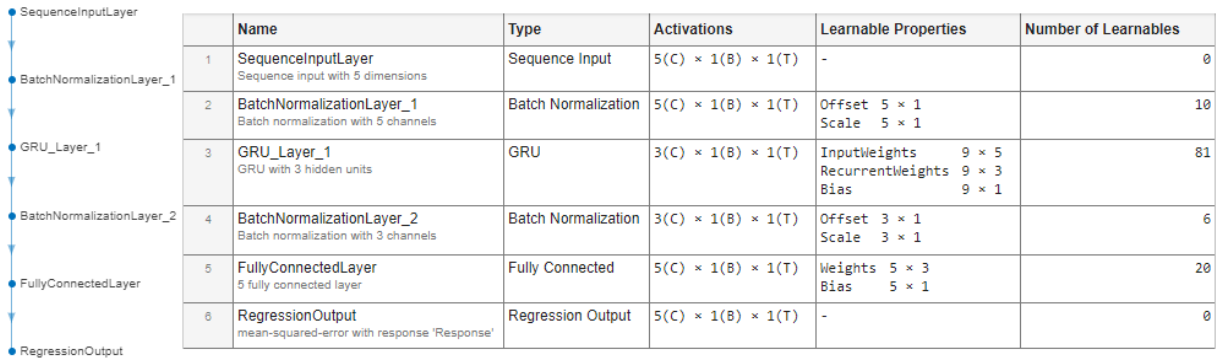


Fig. 6.20. The final structure of autoencoder neural network used for fault detection

The network consisted of:

- a sequence input layer that accommodated sequence input data of five dimensions,
- a first batch normalization layer (10 learnable parameters, composed of offset of size 5x1 and scale of size 5x1) that was used to normalize the features in the batch of input, ensuring zero mean and unit variance,
- the first and only GRU layer (81 learnable parameters, composed of input weights of size 9x5, recurrent weights of size 9x3, and biases of size 9x1) with tanh and sigmoid activation functions for updating state and gates correspondingly. The number of input features was set to five. In order to force the autoencoder to learn a meaningful representation of the input data, the number of GRU hidden units was set to three,
- the second batch normalization layer (6 learnable parameters) responsible for the normalization of GRU layer outputs,

- a fully connected layer with five output units, suitable for regression tasks (20 learnable parameters, composed of weights of size 5x3 and a bias of size 5x1). The fully connected layer was important for the reconstruction of the sequence signals,
- a regression output layer with mean squared error as the loss function, for calculating the network predictions' error during training, and using it to update the network's weights.

To obtain the final structure of RAE-GRU various network architectures were explored. The modifications included the changing of the number of GRU layers (either one or two) together with the number of their corresponding hidden layers. Tab. 6.5 presents the selected, most promising configurations together with corresponding model performance indices (calculated using Eq. 5.25 - 5.32). The model was trained using 2 out of 7 datasets recorded under faultless state (experiments no. 5 and 6, as per Tab. 6.3), that constitute approximately of 14% of the total F0 data entries. Those datasets were selected because on the one hand, they contain measurements from the lower and middle sections of the $y(k)$ signal range, but on the other hand, their data correspond to the mid-range of registered oil temperatures. The trained model was tested using dataset no. 3 (Appendix D).

During the training phase, the ADAM optimization algorithm was utilized, similarly as in the case of the fault detection method using LSTM neural networks. While the majority of the parameters remained the same, the training process began with an initial learning rate of 0.096. This rate exhibited a decremental pattern. Over time, this learning rate dropped by a factor of 0.99 every 50 epochs. Given the substantial volume of data, weight adjustments within the model were based on mini-batches comprising $1.00E+11$ samples during each iteration.

Tab. 6.5. Model performance indicators for various GRU structures

Model ID	GRU_Layer_1	GRU_Layer_2	MAE	MAPE	MSE	RMSE	nRMSE	AIC	PHI	MDL/BIC
1	1	3	1.91	1.84	5.83	2.41	0.12	204.00	-463803.94	1089.35
2	5	3	1.88	1.81	5.26	2.29	0.11	564.00	-462951.33	3011.73
3	10	3	0.83	0.80	1.32	1.15	0.06	1284.00	-461246.11	6856.49
4	1	5	0.68	0.66	0.80	0.90	0.04	352.00	-463453.43	1879.66
5	3	5	2.78	2.68	9.21	3.03	0.14	532.00	-463027.12	2840.85
6	5	5	1.84	1.77	3.94	1.99	0.09	760.00	-462487.13	4058.36
7	10	5	0.59	0.57	0.67	0.82	0.04	1460.00	-460829.28	7796.32
8	3	-	1.03	0.99	1.70	1.30	0.06	234.00	-463732.89	1249.55
9	5	-	1.46	1.41	3.39	1.84	0.08	430.00	-463268.69	2296.18
...										
10	10	-	2.24	2.16	5.63	2.37	0.11	1130.00	-461610.84	6034.14

Following the principle that simpler models are generally less prone to overfitting, and are more generalizable to unseen data, model ID no. 8 was selected. The selected model showed reasonably good performance in predicting outcomes with a mean average error of 1.028 and mean average percentage error of 0.992%, indicating modest deviations from actual values. The root mean squared error and mean squared error were slightly larger, suggesting larger errors were penalized. The normalized root mean squared error revealed that the model's error was about 6.2 of the range of the target variable, suggesting room for improvement. Akaike's Information Criterion and Bayesian Information Criterion indicated a well-balanced model in terms of complexity. For example, model no. 3 presented a better performance by means of MAE - RSME indicators, yet its AIC was more than five times higher, suggesting more complexity than necessary. This highlights the trade-off between model accuracy and complexity, and the importance of considering multiple evaluation metrics when selecting the most appropriate model. Among the obtained model performance indicators, model no. 1 was identified as a comparable alternative to model no. 3, mostly because of its lower complexity (AIC of 204). However, model no. 3 was chosen because of its lower MAPE value, which did not exceed 1.0%.

The distribution of the generated residuum $r(k)$ for the testing set is presented in Fig. 6.21. The residuum spans a range from -5 to 5. Such a range is indicative of the model's capability to capture both underestimations and overestimations of the actual values. Upon closer examination, it can be observed that the distribution exhibits characteristics typical of a normal distribution with negative skewness. This skewness suggests that there are more negative residua than positive ones, meaning the model has a tendency to overestimate more frequently than it underestimates.

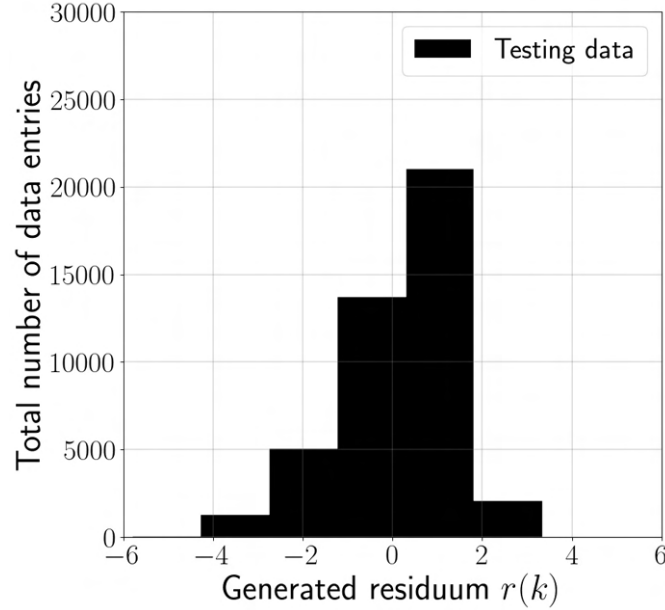


Fig. 6.21. Distribution of generated residuum $r(k)$ for testing set

Figure 6.22 presents exemplary polymer optical fiber sensor and recurrent autoencoder GRU model output signals for exemplary states. The figure represents testing and verification data (as indicated in Tab. 6.3), including testing data collected under the experiment no. 4 for the faultless state (Fig. 6.22a), and verification data collected for the liquid leakage and liquid intrusion states. Figure 6.22b presents data for experiment no. 8 (F1 state). Figure 6.22c presents data for experiment no. 21 (F2 state). Additionally, the charts present periods under which the vehicle was in motion. This was realized through blue areas, covering corresponding periods of the vehicle in motion states. The motion state was derived during a post-processing phase from the registered acceleration values measured from the employed accelerometer signals $C04(k)$, $C07(k)$, and $C10(k)$. The RAE-GRU model output signals $y_m(k)$ correspond to the observed polymer optical fiber sensor signals $y(k) = C12(k)$, although some signal offset can be visible. Such deviations are present, especially in the case of water intrusion state, i.e., Fig. 6.22c. Moreover, under both liquid leakage and water intrusion states, the fluctuations that occur during the vehicle's movement due to the presence of the faults were reconstructed by the RAE-GRU model as well - although with reduced amplitude.

The generated residuum $r(k)$ are presented in Fig. 6.23, including the faultless state (Fig. 6.23a), the oil leakage fault (Fig. 6.23b), and the water intrusion fault (Fig. 6.23c). For the faultless state, a small correlation between vehicle activity and the generated residuum can be observed. In the case of both faults, the generated residuum are close to 0 when the vehicle is not in motion. Once the vehicle starts moving, a variation in the generated residuum appears. A difference in signal magnitude was caused by different fluids that the polymer optical fiber sensor was exposed to. For oil leakage fault, the sensor was occasionally exposed to air. In such

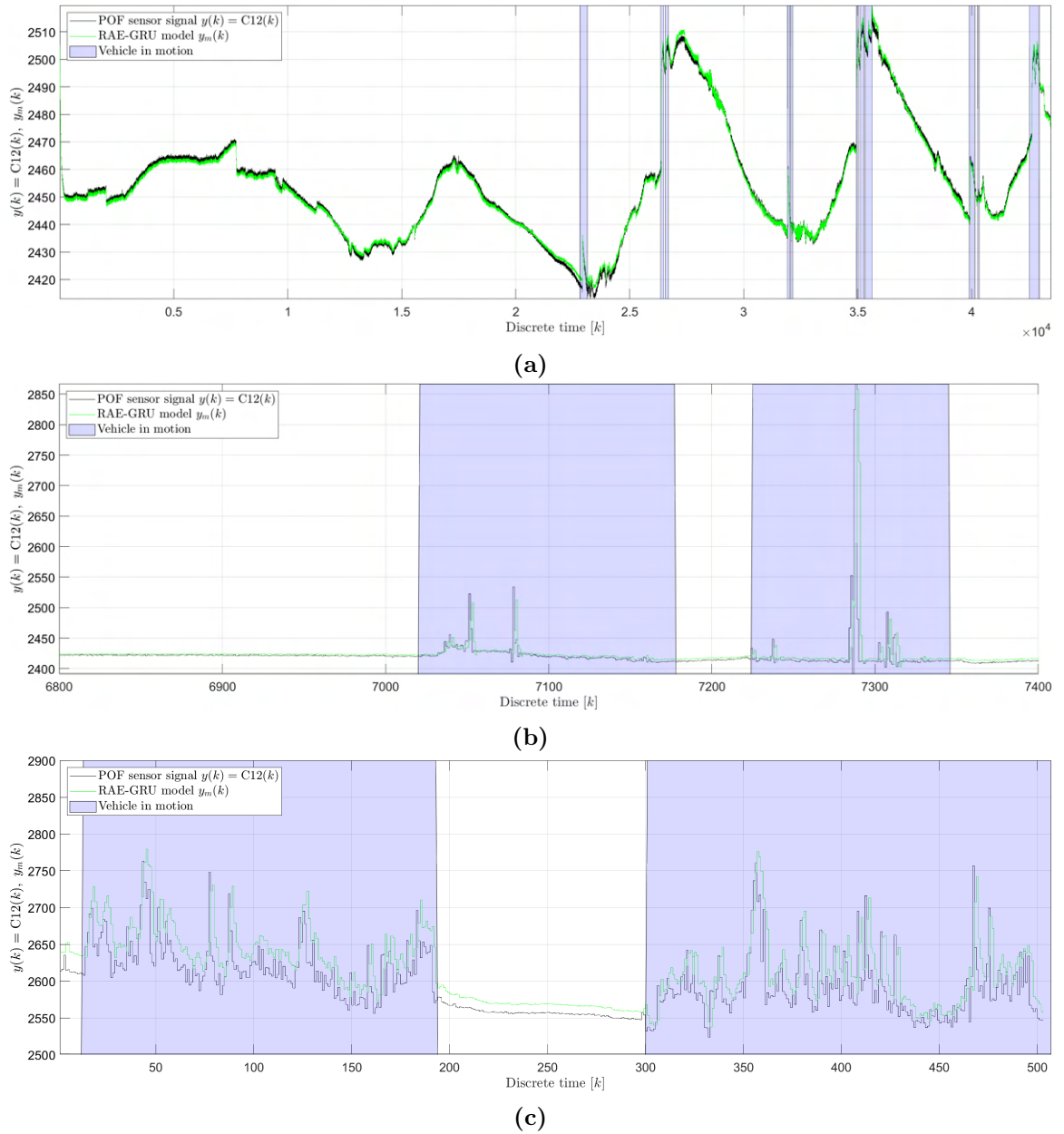


Fig. 6.22. Exemplary POF sensor and REA-GRU model output signals for: (a) *No Fault 3* dataset (b) *Oil leakage 1* dataset (c) *Water intrusion 9* dataset.

cases, the signal amplitude was as much as ten times higher than in the case of water intrusion fault, where the POF sensor was exposed to the water-oil emulsion.

The method requires two statistical measures (Eq. 5.7), namely \bar{r} and σ_r , together with three pre-defined parameters, i.e. t_α , m_f , and t_s . \bar{r} , σ_r , and t_α are used to generate upper p^+ and lower p^- thresholds. The first two measures were derived during the statistical analysis of the generated residuum from the testing dataset. \bar{r} and σ_r were set to 0.133478 and 1.425754 respectively. The significance level t_α was empirically set to 24. Using a similar approach, the parameters associated with the diagnostic signal generation (m_f , P) were set to 3 and 5 respectively. This means, that the final diagnostic signal is set if the generated residuum exceeds the thresholds at least 5 times within 2 minutes (P equal to 24 results in 120 seconds, as the time interval between residual data samples after the decimation is 5 seconds).

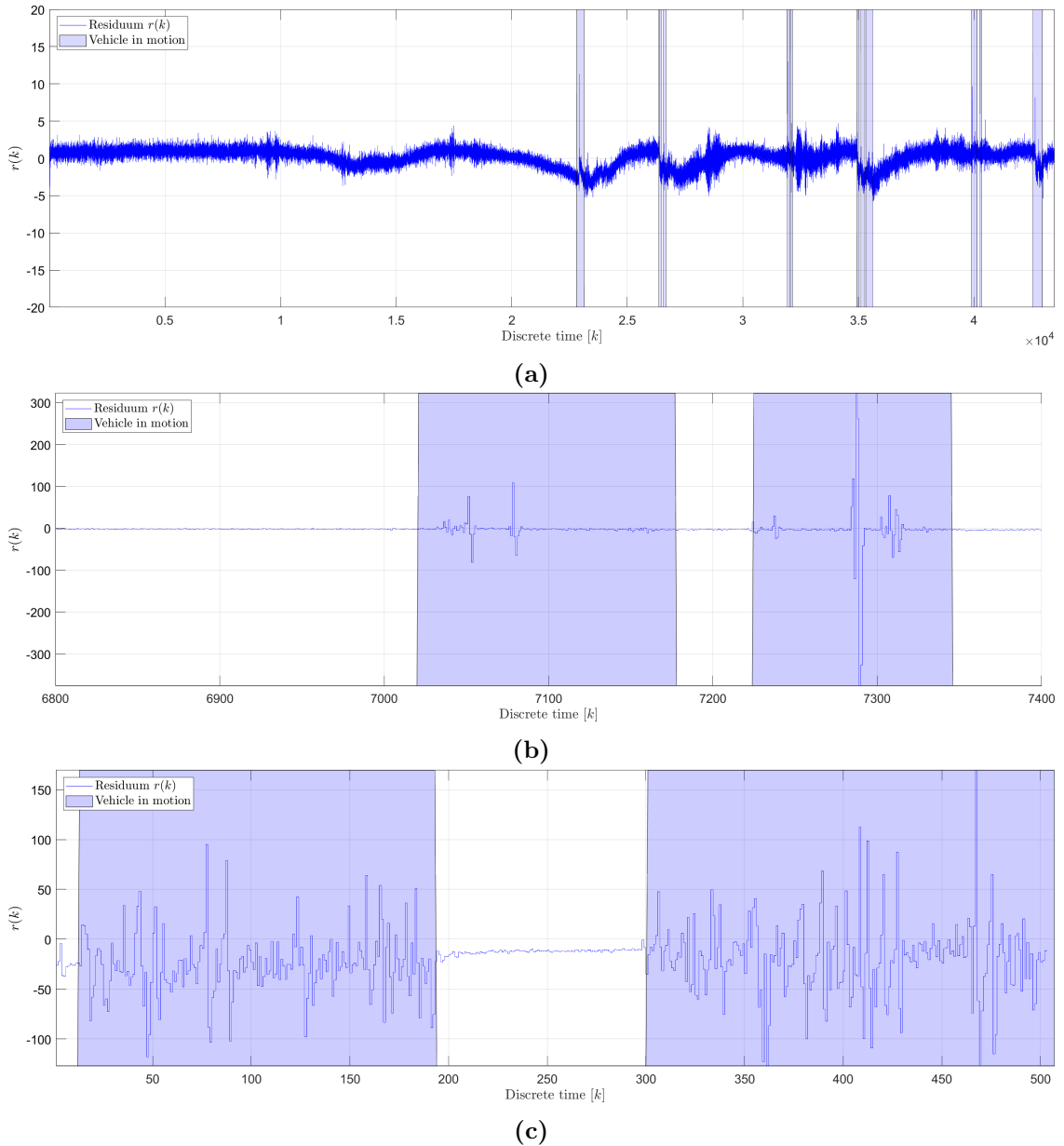


Fig. 6.23. Exemplary residuum generated for: (a) *No Fault 3* dataset (b) *Oil leakage 1* dataset (c) *Water intrusion 9* dataset.

6.3.4 Fault detection results for experiments under road conditions

The exemplary results of the fault detection method using autoencoder neural networks (Fig. 5.4) are presented in Fig. 6.24. Results show that the upper and lower thresholds were set appropriately, as the generated residuals do not exceed them under the faultless state. It can be also observed that regardless of the vehicle motion state, the fault magnitude was not high enough and no variation of the POF sensor's signal $y(k)$ could be visible. Once the vehicle starts moving, the observed signal $y(k)$ and its corresponding residuum $r(k)$ start fluctuating and the fault detection method detects faults for both states. Because the fault reveals itself mostly under vehicle motion, the assessment of method performance using the traditional performance indices r_{td} and t_{dt} (Eq. 5.33 and 5.34) turned out to be unreliable, and it was decided to derive new indices r'_{td} and t'_{dt} , similarly like for laboratory conditions, where the method performance was

evaluated during the stirring conditions. The motion state was derived based on the accelerometer measurements, which were also recorded for every collected dataset. Because the indices r_{td} , t_{dt} were evaluated during the vehicle's motion, and the collected datasets, in many cases, incorporated more than just one of such period. Values of the false and true detection rates and detection delay times were calculated for each motion state and then averaged \bar{r}'_{td} and \bar{t}'_{dt} for a given dataset. The total summary of the evaluation is given in Tab. 6.6.

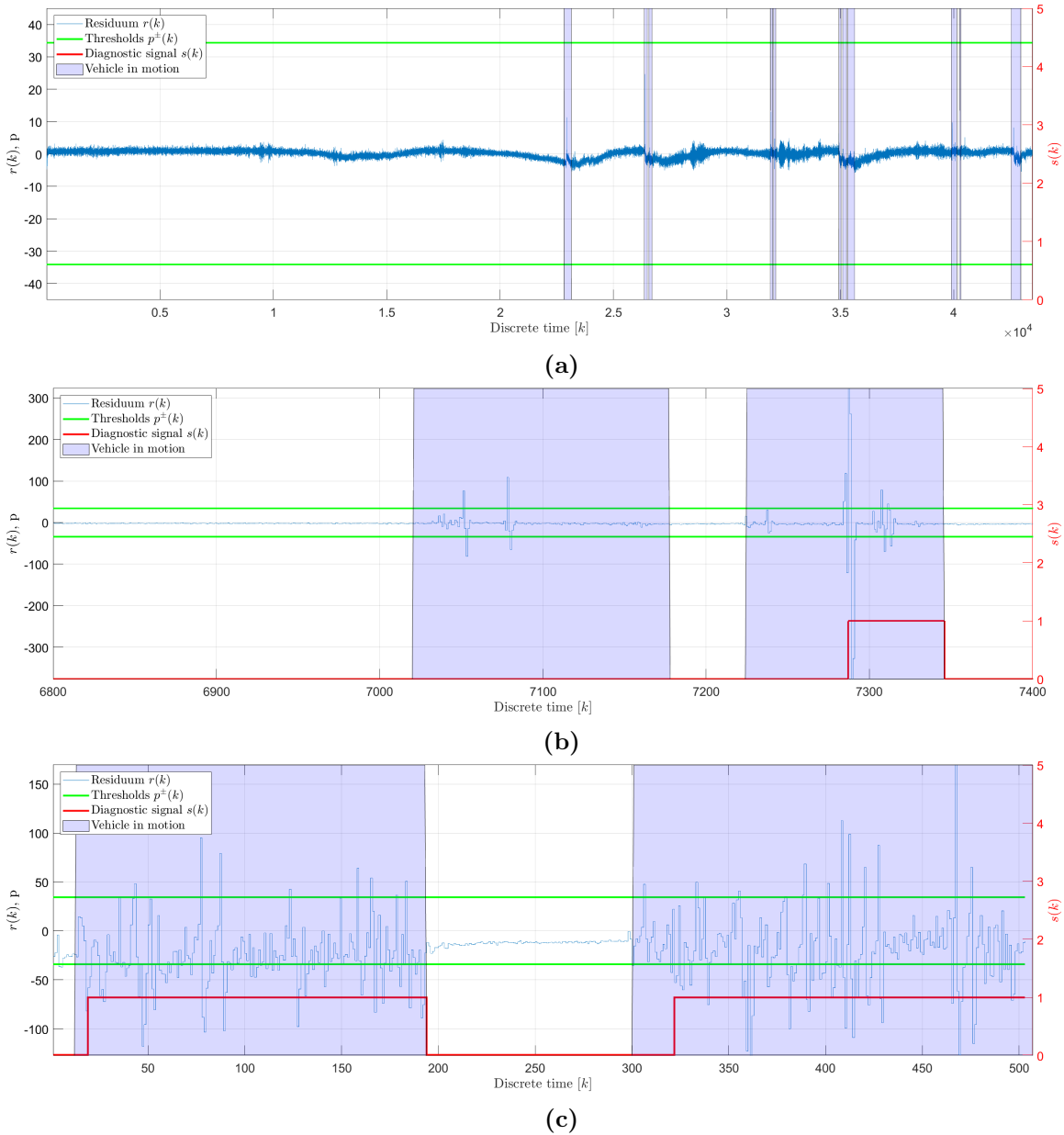


Fig. 6.24. Exemplary results for: (a) *No Fault 3* dataset (A) *Oil leakage 1* dataset (B) *Water intrusion 9* dataset.

Taking into account the results presented in this table, one can observe that the fault detection method based on RAE-GRU model does not report any false positives (expressed as \bar{r}_{fd}) under conditions of the F0 state. Additionally, detection delay time \bar{t}_{dt} is not applicable in these instances, given the absence of any fault. The measure of \bar{r}_{fd} consistently remains zero across all considered datasets, signifying no incorrect fault detections. This finding is particularly sig-

Tab. 6.6. Performance measures for fault detection method corresponding to Fig. 5.4

Exp. ID	State ID	Dataset description	\bar{r}_{fd}	\bar{r}'_{td}	\bar{t}'_{dt} [s]	Mag. [%]
1	F0	No fault 0	0.000	-	-	-
2	F0	No fault 1	0.000	-	-	-
3	F0	No fault 2	0.000	-	-	-
4	F0	No fault 3	0.000	-	-	-
5	F0	No fault 4	-	-	-	-
6	F0	No fault 5	-	-	-	-
7	F0	No fault 6	0.000	-	-	-
8	F1	Oil leakage 1	0.000	0.609	133	90
9	F1	Oil leakage 2	0.000	0.972	25	90
10	F1	Oil leakage 3	0.000	0.797	160	90
11	F1	Oil leakage 4	0.000	0.800	170	90
12	F1	Oil leakage 5	0.000	0.678	53	90
13	F2	Water intrusion 1	0.000	0.000	-	0.3
14	F2	Water intrusion 2	0.000	0.000	-	0.3
15	F2	Water intrusion 3	0.000	0.000	-	0.9
16	F2	Water intrusion 4	0.000	0.086	2100	0.9
17	F2	Water intrusion 5	0.000	0.796	48	1.8
18	F2	Water intrusion 6	0.000	0.969	50	1.8
19	F2	Water intrusion 7	0.000	0.882	185	1.8
20	F2	Water intrusion 8	0.000	0.889	140	1.8
21	F2	Water intrusion 9	0.000	0.931	68	1.8

nificant in the context of the automotive industry, where false positive detection of faults may trigger unnecessary service actions and additional effort on vehicle drivers. For the developed optical liquid detection system, the proposed method of calculation of indices \bar{r}'_{td} and \bar{t}'_{dt} appear to offer a more detailed interpretation of its operational performance.

Under the oil leakage state, the fault detection method demonstrated the ability to identify the presence of faults with the vehicle being in motion, with an average \bar{r}'_{td} of 77.1%. The maximum value for \bar{r}'_{td} was achieved during experiment no. 2 and was 97.2%. On the other hand, the minimum \bar{r}'_{td} value was reported for experiment no. 1 and was 60.9%. During the vehicle motion, the detection method successfully identified faults with an average \bar{t}'_{dt} of 108.2 seconds. The minimum \bar{t}'_{dt} was achieved during experiment no. 9 and was 25 seconds. The maximum value for \bar{t}'_{dt} was registered for experiment no. 11 and was 170 seconds. It can be observed that the average detection delay time \bar{t}'_{dt} met the required 300 seconds (Section 4.1.2) for this state ID. Taking into account the true detection rate under motion \bar{r}'_{td} , the fault detection method successfully met the required 80% for experiments no. 9 and 11.

For the water intrusion fault state, the detection performance presented a notable variation among the collected datasets. The first and the second experiments performed under the F2 state assumed that the weight-to-weight concentration of the formed oil-water emulsion was only 0.3%. It can be observed that for such a low fault magnitude, the fault detection method was unable to generate the diagnostic signal $s(k)$. The subsequent two experiments were performed under three times higher total volume of intruded water (150 ml), providing 0.9% concentration. As given in Tab. 6.6, the fault was detected by the end of the experiment (after approximately

52 minutes). This resulted in a low \bar{r}'_{td} which was nearly 9%. The best performance measures were achieved when the water concentration reached 1.8%, i.e., 300ml of intruded water. Under such fault magnitude, the fault detection method presented \bar{r}'_{td} on average of 89%. Taking into account non-functional requirements, four out of five experiments performed under F2 state and fault magnitude of 1.8% met both the required 80% \bar{r}'_{td} and 300 seconds for \bar{r}'_{td} . The experiment no. 17 presented \bar{r}'_{td} value of 79.6%, which was the minimum achieved \bar{r}'_{td} value. The maximum value was reported for experiment no. 18 and was as much as 96.9%. Interestingly, the average \bar{r}'_{td} for water intrusion state with 1.8% fault magnitude was reported as 98 seconds. It was 10% lower than in the case of the oil leakage fault. This difference can be attributed to the underlying mechanics of the respective faults. Specifically, oil leakage detection necessitates the movement of oil within the container, typically caused by forces exerted during vehicle turns. On the other hand, water intrusion is sensitive to any form of vehicle movement, which initiates the circulation of water droplets within the container.

To provide a more detailed insight into the results, the r'_{td} and t'_{dt} indices were calculated for every consecutive motion state that the vehicle was susceptible to under the tests. The visualized results of every performed experiment together with indicated vehicle motion states can be found in Appendix D. Table 6.7 lists detection delay time calculated for vehicle-in-motion conditions \bar{t}'_{dt} , while Tab. 6.8 presents the true detection indices under the same conditions \bar{r}'_{td} . Both tables present corresponding indices calculated for each subsequent vehicle-in-motion state. It can be observed that the number of cycles was not the same for every experiment, which emphasizes the real conditions and the lack of driving patterns during the carried experiments.

Tab. 6.7. Detection delay time t'_{dt} under vehicle motion

Dataset description	t'_{dt} for subsequent vehicle-in-motion states [s]									
	1	2	3	4	5	6	7	8	9	10
Oil leakage 1	-	310	30	85	105					
Oil leakage 2	25									
Oil leakage 3	160	160								
Oil leakage 4	55	50	70	225	85	20	225	105	640	225
Oil leakage 5	75	50	35	50						
Water intrusion 1	-	-	-							
Water intrusion 2	-	-								
Water intrusion 3	-	-	-							
Water intrusion 4	-	-	2100							
Water intrusion 5	70	5s	70							
Water intrusion 6	50									
Water intrusion 7	185									
Water intrusion 8	140									
Water intrusion 9	30	105								

More detailed data revealed that in the case of the oil leakage fault, the proposed fault detection method has successfully detected the fault presence under 21 out of 22 periods when the vehicle was in motion. The detection delay varied significantly, ranging from 20 s to as much as 640 s. Calculated r'_{td} varied in the range of 33.8% up to 97.2%. For the water intrusion fault, once the w-w concentration reached 1.8%, the method detected fault presence every time the vehicle was in motion. Under those conditions, the detection delay index ranged from as low as 5 s (minimum time interval due to data decimation), to as much as 185 s. True detection rate index presented the performance in the range of 79.6% to 96.0%.

Tab. 6.8. True detection rate r'_{td} under vehicle motion

Dataset description	r'_{td} for subsequent vehicle-in-motion states									
	1	2	3	4	5	6	7	8	9	10
Oil leakage 1	0.000	0.527	0.760	0.760	0.883	0.876				
Oil leakage 2	0.972									
Oil leakage 3	0.759	0.834								
Oil leakage 4	0.917	0.882	0.932	0.793	0.653	0.840	0.918	0.840	0.883	0.338
Oil leakage 5	0.595	0.600	0.720	0.796						
Water intrusion 1	0.000	0.000	0.000							
Water intrusion 2	0.000	0.000								
Water intrusion 3	0.000	0.000	0.000							
Water intrusion 4	0.000	0.000	0.257							
Water intrusion 5	0.714	0.960	0.714							
Water intrusion 6	0.969									
Water intrusion 7	0.882									
Water intrusion 8	0.889									
Water intrusion 9	0.967	0.896								

The results indicate that the developed polymer optical fiber sensor can be used for the detection of both water intrusion and oil leakage faults. The extensive and comprehensive tests that were carried out have proven the designed and prototyped OLDS to be robust enough for the purposes of this dissertation. Taking into account relatively small values of the generated residuum $r(k)$ (in the order of 1-2% of the observed POF sensor's signal $y(k)$) for the faultless state it can be concluded, that the RAE-GRU model of the proposed method has successfully learned long-term dependencies that the system experienced during road conditions. The formulated residuum evaluation approach resulted in zero false detection alarms across all datasets that were recorded during the comprehensive tests. The obtained results indicate that the performance of the proposed fault detection method is correlated with the fault magnitude. Furthermore, because of the absence of components facilitating forced liquid flow, the performance of the fault detection method was related to the vehicle's motion. Due to the construction of the container, the sensor was mounted at the base of the container on small ribs. This placement could lead to limitations in the system's sensitivity under certain conditions. In the case of water intrusion, the fault magnitude must be substantial enough for water to reach the sensor under quiescent conditions. If the volume of the intruding water is insufficient, it may accumulate beneath the sensor, making the system unaware of the fault until the vehicle is in motion and the water droplets of the formed oil-water emulsion begin to circulate.

6.4 Summary

This chapter covered the verification study of the three distinct model-based fault detection approaches related to Fig. 5.2, 5.3, and 5.4 that were dedicated for the developed optical liquid detection system. The methods were evaluated offline, that means with the recorded datasets that were collected under laboratory conditions (fault detection method using LSTM neural networks) as well as road conditions (fault detection method using autoencoder neural networks).

Under laboratory conditions, the study emphasized the significance of data quality and sensor placement in neural models for EV battery packs with a direct-liquid cooling battery thermal management system. Liquid leakage and liquid intrusion which are the subject of the following dissertation present fundamental differences. The liquid leakage is understood as leakage of the coolant (oil), for which placement of the sensor in the upper part of the container would be highly

beneficial. On the other hand, the liquid intrusion fault is understood as an intrusion of water. Because of density differences, the formed emulsion would separate both liquids under so-called quiescent conditions, making the placement of the sensor in the lower part of the container more beneficial for the sake of water detection. This limitation caused the experiments to simulate one of the faults with a relatively high magnitude, as the employed sensor was not placed appropriately for both of the faults at the same time.

A key point of the preliminary study under laboratory conditions was the use of an LSTM neural network, proposed in two distinct residuum evaluation schema. Its final neural network structure employed 6 layers (with two LSTM layers) and as many as 37200 total learnable parameters. Despite the satisfactory performance of such a model structure in the generated residua, the complexity of the network raised concerns regarding its practicality for integration into the automotive ECUs. Because of that, two fault detection approaches were explored (Fig. 5.2 and Fig. 5.3), that utilized the same LSTM-based neural model for residual generation but differed in the residual evaluation technique. One utilized a simple statistical analysis based on short-term and long-term moving averages. The other leveraged a TDNN model for robust residual evaluation. While the simple residual evaluation scheme performed better under the faultless state, situations of abrupt changes, and stirring conditions, it had limited effectiveness for minor fault magnitudes. The second scheme, however more complex, performed better in all test cases and proved more consistent across all fault states. Because of the absence of a locking mechanism, the generated residuals $r(k)$ frequently descended below the adaptive thresholds, as a consequence of $y(k)$ being a PWM signal. Based on the insights gained from this verification study, several conclusions were drawn towards further, comprehensive tests under road conditions. These included the need to reduce the complexity of the neural network and the techniques for residual evaluation, not employing a PWM signal as an input for the POF sensor, the importance of having a mechanism to monitor the movement state, and the recommendation to position the POF sensor as low as possible inside the final system.

The final version of the optical liquid detection system took advantage of the results obtained during the preliminary study. The prototyped OLDS was equipped with various components, allowing the system to handle road conditions, communicate with data acquisition devices, and monitor ambient and oil temperatures together with vehicle movement state. The OLDS was exposed to road conditions, under which new datasets were extensively collected for all three states F0, F1, and F2. The aim of reducing the neural network's complexity resulted in a new fault detection method that employed autoencoder and GRU neural networks (Fig. 5.4). The final neural network structure was a result of a trial-and-error process, during which multiple architectures were considered. Ultimately, the structure employed 6 layers (with a single GRU layer) and only 117 learnable parameters. The new fault detection method was verified offline using the collected datasets. In the case of faultless state F0, the method demonstrated perfect performance, providing no false positives, which is critical in avoiding unnecessary maintenance and driver inconvenience. Under experiments with simulated oil leakage, the system successfully identified faults when the vehicle was in motion with the average true detection rate r'_{td} of 77.1% and average detection delay time t'_{dt} of 108 seconds. In the case of water intrusion fault, the detection performance exhibited noticeable variability across the collected datasets. The system was unable to consistently identify faults until a 1.8% weight-to-weight concentration of the water-oil emulsion was reached. Once this threshold was achieved, the detection performance improved significantly, reaching average r'_{td} and t'_{dt} of 89% and 98 seconds correspondingly.

7. Dissertation summary

The thesis addresses the problem of electric vehicles' battery pack faults that could initiate a chain reaction and propagate into more severe faults, ultimately leading to the most serious faults such as thermal propagation and explosion. In particular, the thesis is associated with an electric car battery leakage detection system in the context of liquid leakage and liquid intrusion detection for battery packs with an immersion cooling strategy. The proposed system, together with developed model-based fault detection methods, not only reduces the risks of the occurrence of thermal propagation but is also identified as a more robust solution to state-of-the-art devices, as the liquid detection is done using optical signals, therefore no electricity is used inside the hazardous, high-voltage areas. The fault detection is enhanced with artificial intelligence and machine learning - such model-based fault detection methods rely on a process model with the use of computational intelligence that accurately represents the normal operation of the system. Through continuous monitoring and comparison of real-time operational data against this model, the algorithm can detect deviations that would signal potential anomalies and faults. The research was initiated in the Dräxlmaier Group, as the result of the most recent electromobility trends associated with legal and technical aspects, such as thermal propagation-related regulations and battery thermal management systems, that are evolving into sophisticated solutions based on immersive cooling approach.

The goal of this doctoral dissertation was to develop a liquid leakage and intrusion detection system for immersion-cooled electric vehicle lithium-ion battery packs. The research started with a state-of-the-art analysis, which targeted modern battery pack systems, their thermal management systems, faults, diagnosis methods and algorithms, and the patents associated with liquid leakage and intrusion detection systems. Such an overview was followed by research on polymer optical fiber sensors, their sensing and manufacturing techniques, and application overview in automotive and aerial industries. The literature research led to the conception of a liquid leakage and liquid intrusion detection system. Based on the formed functional and non-functional requirements, the system was prototyped. The prototyping phase was an extensive design and implementation process, that required comprehensive knowledge, particularly in the fields of mechanical engineering including mechatronics (embedded hardware and software) as well as fiber optic techniques. The initial version of the OLDS was exposed to water intrusion and oil leakage faults under laboratory conditions to formulate the first version of the fault detection method. Based on the obtained results, the final OLDS was prototyped and then subjected to the same faults, but under the road conditions. The collected datasets were used to define the final fault detection method, which performance was evaluated using a different set of metrics. The verification study highlighted the most prominent advantages of the system, such as being able to detect two different types of fault using the developed polymer optical fiber sensor and model-based fault detection approach, and also marked some of its flaws, such as the importance of sensor placement inside the battery pack system, which shall be only done at the early phase of the battery pack design.

The thesis addressed many concerns of modern battery pack systems in the fields of mechanical engineering and artificial intelligence. According to the author's opinion, the most important contributions of this doctoral dissertation include:

- A novel approach to monitor liquid leakage and intrusion, which are critical mechanical engineering challenges for ensuring the reliability and performance of battery packs, by the successful adaptation and application of polymer optical fiber sensing techniques.
- Comprehensive solution that goes beyond traditional mechanical engineering boundaries, showcasing an interdisciplinary approach to adapt existing optical sensing techniques to solve mechanical engineering challenges, thereby advancing the safety and reliability of electric vehicle battery packs.
- The formal description of robust and effective approaches for model-based fault detection within the battery pack system. The proposed fault detection methods will improve the overall safety and performance of electric vehicles by reducing the risks of thermal propagation and other faults.
- The prototyping phase of the liquid leakage and intrusion detection system, along with the extensive testing under both laboratory and road conditions, that demonstrate the practical applicability of the research in the context of battery pack systems, providing valuable insights into the system's performance and highlighting the strengths and weaknesses of the proposed solution.
- The ongoing implementation of the proposed liquid leakage and intrusion detection system within the Dräxlmaier Group, in collaboration with the very first customer. This phase underlines the practical significance and industry relevance of the research, marking a transition from theoretical findings to real-world applications, ensuring the system meets both industry standards and specific client requirements.

7.1 Main conclusions

The research carried out during the thesis has led to the following conclusions:

- The scientific community expresses concerns that industry attention has been disproportionately devoted to cost reduction and enhancing the energy output of individual battery cells, instead of the development of battery thermal management systems.
- Due to the high power outputs, electrical vehicle battery packs present vulnerability to a range of faults, with this study identifying accelerated degradation and thermal runaway as the most severe among them. Liquid leakage and water intrusion have been highlighted as potential triggers, which could escalate into a chain reaction, that could ultimately lead to the thermal runaway.
- The implementation of liquid detection sensing devices within battery packs is an uncommon practice among OEMs. In instances where such incorporation does occur, the sensors employed are generally of an electrical nature, utilizing either conductometry or capacitive principles. This dissertation introduces an innovative approach, employing polymer optical fiber evanescent wave absorption sensors, which deviate from these traditional methods.
- Polymer optical fiber sensors have already been used in the automotive industry, although not in the context of battery pack systems. Their application has been primarily seen in areas such as pedestrian protection systems and power window jam protection systems. The literature research has shown that the aerial industry has also recognized the potential benefits of polymer optical fiber sensing, despite the challenging and safety-critical nature of its environment. This attests to the growing interest in this technology across various fields, indicating its potential for wider implementation in the future.
- The developed and prototyped optical liquid detection system has been effectively utilized to record a substantial amount of data under road conditions. The system's robustness

was substantiated through its consistent performance across a spectrum of temperatures and for extended durations, varying from a matter of hours to several days (for a single dataset). This represented a significant challenge, given the requirement to collect data for three different states: faultless (F0), oil leakage (F1), and water intrusion (F2).

- Fluctuating weather conditions necessitated a concise data collection process, ensuring that the system was subjected to comparable ambient temperatures across the three states. This was to avoid the situation of having data associated with the faultless state being more susceptible to lower temperatures compared to the oil leakage and water intrusion states.
- The data collection process yielded a substantial dataset, with a total number of entries reaching into hundreds of millions. This impressive quantity, accumulated through data logging at a frequency of 100 Hz, underscores the significant time investment dedicated to data collection. Given that the prototype system is not the finalized version, any instance of system failure could necessitate a repetition of the process. This would consequently introduce a potential threat to the planned timeline of the dissertation. Thus, the reliability of the prototyped system and its successful operation through the research process should be emphasized.
- A central element of this study was the incorporation of artificial intelligence and machine learning techniques to formulate fault detection methods tailored for the optical liquid detection system. Two different methodologies were proposed to realize this goal. The initial method (used during the preliminary study) leveraged LSTM neural networks and employed two different residual evaluation schemes. Recognizing the significance of optimizing computational efficiency, particularly in real-world automotive applications, a subsequent model was proposed for the final verification study performed under road conditions. This was the fault detection method using autoencoder neural networks, specifically designed to reduce the system's complexity without compromising its performance.
- The verification study conducted under laboratory conditions, along with the executed temperature stress tests, indicated the potential to reduce the number of features input into the model. Consequently, the final fault detection method using autoencoder neural network operated using decimated sensor readings from current and past data samples. This makes this method a predictive fault detection approach, which is fed with historical data that was susceptible to variation caused e.g. by temperature changes. This data allows the RAE-GRU model to learn the long-term temperature dependencies, enhancing the accuracy and reliability of fault detection.
- The fault detection method using LSTM neural networks was based on an LSTM model, which structure employed 6 layers (including two LSTM layers), with a total of 37200 learnable parameters. The subsequent, fault detection method using autoencoder neural networks, incorporated an RAE-GRU model that employed 6 layers as well (with one GRU layer), but which total number of learnable parameters was only 117 parameters. This progression from a more complex LSTM model to a simplified autoencoder showcases the dynamic potential of artificial intelligence in developing robust yet efficient fault detection systems.
- The evaluation of the final fault detection method revealed that the method provided no false detection indices (regardless of the vehicle's movement state). This is important, especially in the context of an automotive industry where both the cost of false positives and the safety implications of missed faults carry significant weight.
- Although it was possible to acquire a bottom part of a housing of the commercial battery pack system (HPB80), it was not possible to acquire the remaining parts of the system, especially the parts of the battery thermal management system, as they are manufactured

and sourced from different companies. This caused the system to lack the functionality of forced coolant circulation. In the context of this doctoral dissertation, this caused the simulated faults to be visible mainly during the vehicle's movement, as the goal of the verification study was to verify the OLDS and formulated methods against faults of lower magnitudes, to be able to report faults as early as possible. This is especially important for the water intrusion fault, where the water might gather inside the system during long periods, e.g. due to damage to the heat exchanger.

- For the developed optical liquid detection system and selected magnitudes of simulated faults, the proposed indices, namely r'_{td} and t'_{dt} , appear to offer a more detailed interpretation of the operational performance. For the oil leakage fault (F1), the method presented \bar{r}'_{td} of 77.12% on average for all datasets. Although the magnitude of generated residuals was lower in the case of water intrusion fault, the method presented a higher performance with \bar{r}'_{td} of 90.86% once the weight-to-weight concentration of water and oil reached 1.8%.
- An important outcome of this study was the impact of sensor placement on the performance of the detection system. Current positioning constraints potentially undermine system sensitivity under certain conditions, particularly when dealing with lower-magnitude faults. This observation underscores the need for future research and system optimization, focusing on sensor placement strategies. Properly optimized, this placement could enhance the system's ability to detect both water intrusion and oil leakage faults, regardless of the vehicle's state of motion, thereby increasing the safety and reliability of battery pack systems.
- A notable difference in fault detection delay times has been identified among F1 and F2 states. The reason for that is the different responses of the optical liquid detection system and the utilized polymer optical fiber sensor - by means of generated residual magnitude and residual variation versus vehicle movement. This observation might be important for the sake of further algorithm improvement toward the fault diagnosis method.
- This research serves as the first comprehensive study exploring this application, providing valuable insights into the challenges and opportunities inherent in this novel optical liquid detection system approach. As such, it establishes a solid benchmark against which future work in this area can be compared. The methodologies developed, the data collected, and the insights gained from this study could provide a roadmap for researchers and engineers working on similar problems, thereby making a significant contribution to the field.

7.2 Future works

Some important remarks to be considered to increase the system's technology readiness level in future research are as follows:

- **Improving sensor placement:** The research has highlighted the significant impact of sensor placement on the performance of the fault detection system. Future work could focus on optimizing sensor positioning within the battery pack to enhance sensitivity under various conditions. Studies could be undertaken to identify the optimal sensor locations for detecting both water intrusion and oil leakage faults, regardless of the vehicle's state of motion.
- **Expansion of test conditions:** This dissertation has evaluated the developed methods under both laboratory and road conditions. Future studies could consider other test environments, including more extreme weather conditions or varying driving scenarios, to further validate the performance and robustness of the system.

- **Integration with battery pack system:** A logical next step would be to integrate the fault detection system with other components of the battery pack, such as a battery management system and a battery thermal management system. Performing subsequent verification studies using the real system would allow the battery pack to maintain the forced liquid flow, increasing the effectiveness of the employed fault detection method during vehicle inactivity. This integration would also involve dealing with computational constraints and real-time processing requirements, presenting an exciting challenge for future research.
- **Sensor development and innovation:** This dissertation has showcased the significant potential of polymer optical fiber sensors in electric vehicle battery pack systems and emphasized the importance of further exploration within and beyond the mechanical engineering domain. The innovative integration of these sensors necessitates additional research dedicated to developing more sensitive, reliable, and robust POF sensors tailored to the specific demands of the application. Moreover, the achievements detailed herein suggest a broader inquiry into advanced sensing techniques for fault detection, isolation, and identification, demonstrating the potential of harnessing novel technologies in this domain.
- **Cross-disciplinary exploration and future research directions:** The success and implications of this work underscore the benefits of a multidisciplinary approach to addressing such intricate challenges. Prospective research initiatives could encompass domains such as mechanical engineering, optics, material science, electrical engineering, computer science, and artificial intelligence, aiming to elevate the performance and adaptability of sensing systems. Within the realm of artificial intelligence, there is a potential for the integration of other techniques. The investigation of other AI models might further optimize the real-time data processing and decision-making capacities of these systems. Thus, the influence of this dissertation penetrates various scientific disciplines, offering a rich source of inspiration for future advancements and collaborations.

7.3 Implementation in the industry

The journey towards implementing the project in the industry has been marked by significant milestones, despite the technology not being fully realized. With an estimated technology readiness level of 5 (which indicates that the technology has been validated in a relevant environment), the company has recognized the potential of the project and has decided to continue its development, providing the budget and more resources from other departments. This section outlines the key achievements to date and emphasizes the importance of engaging with decision-makers and directors in facilitating the project's progress within the industry.

The project's milestones include the filing of two patent applications with the UK's Intellectual Property Office. The first patent application, an EU patent, was filed on December 10, 2020 (titled "Optical liquid detection sensor device", application number: GB2019513.7), and is currently published (publication number: GB2602001 [24]). The second patent application, filed on March 9, 2022 (titled "Optical liquid detection system", application number: GB2203308.8 [25]) is a worldwide patent and is still awaiting publication. The sole authorship of both patent applications is attributed to the author of this dissertation, and they have been assigned to the Dräxlmaier Group. These applications provide legal protection for the project's intellectual property and demonstrate the initial potential.

The technology demonstrator (preliminary version of the system described in Section 4.2.3) was presented to the CTO of the company, resulting in additional funding and valuable connections with the directors of other engineering departments, opening the door to potential customers. The success of this event triggered a series of meetings with the director of the

battery department and on December 20, 2022, the technology demonstrator was presented to the first potential customer (one of the OEMs), initiating a crucial dialogue that can lead to the official system development. Such cooperation must be established as the system has to be tailored for a specific BEV. In March 2023, the technology was presented during a monthly board meeting attended by the CTO and directors from various departments. This presentation served to highlight the current progress and to have a discussion (regarding further steps and client-oriented goals) with key decision-makers within the organization. Engaging with key decision-makers and directors is pivotal for the successful integration of the project into the industry. Their support and endorsement can play a crucial role in the project's development and eventual implementation. Decision-makers have the authority to allocate resources, such as funding and personnel, that are necessary for the project to progress. Moreover, they have the ability to influence other stakeholders, which can have a significant impact on the project's success. As of September 2023, the technology is actively under implementation, with the primary focus shifted toward enhancing the reproducibility of the polymer optical fiber sensor. Ensuring consistent and reliable production of the sensor is critical for its successful large-scale integration into electric vehicle systems.

In conclusion, the project's progress thus far has been marked by significant milestones and achievements, despite not being fully implemented. The research and development conducted during the course of the thesis served as a catalyst for launching an internal project (and possibly a project in collaboration with a customer). The work presented in the thesis not only provided a strong foundation for the technology but also enabled the company to gain interest from potential clients and secure funding for further development. By showcasing the technology's potential and its readiness for real-world applications, the research and development efforts played a crucial role in bridging the gap between academic research and industry implementation.

Bibliography

- [1] International Energy Agency, “Global EV outlook 2023,” tech. rep., International Energy Agency, Paris, France, 2023.
- [2] International Energy Agency, “Global EV outlook 2019,” tech. rep., International Energy Agency, Paris, France, 2019.
- [3] International Energy Agency, “Global EV outlook 2022,” tech. rep., International Energy Agency, Paris, France, 2022.
- [4] International Energy Agency, “Global EV outlook 2020,” tech. rep., International Energy Agency, Paris, France, 2020.
- [5] W. Chao, Z. Chunbo, G. Yunwang, and Z. Yongping, “A review on fault mechanism and diagnosis approach for Li-Ion batteries,” *Journal of Nanomaterials*, vol. 15, 2015.
- [6] Sony, “Lithium-Ion rechargeable battery technical information -US18650VTC6,” 2015. Rev. 0.2.
- [7] M.-K. Tran and M. Fowler, “A review of Lithium-Ion battery fault diagnostic algorithms: Current progress and future challenges,” *Algorithms*, vol. 13, no. 3, 2020.
- [8] L. Schindele, D. Schütz, F. Heber, P. Sailer, L. H. Gaël, and N. Müller, “Future e-mobility and the change in system requirements,” *ELIV 2019*, 2019.
- [9] Porsche, “Sophisticated thermal management, up to 800-volt system voltage.” Accessed: 01.08.2023 <https://media.porsche.com/mediakit/taycan/en/porsche-taycan/die-batterie>, 2023.
- [10] Dräxlmaier Group, “Website.” Accessed: 01.08.2023 <https://www.draexlmaier.com/en/>, 2023.
- [11] J. Klink, R. Benger, J. Grabow, N. Orazov, A. Hebenbrock, H.-P. Beck, and U. Nylén, “Comparison of model-based and sensor-based detection of thermal runaway in Li-Ion battery modules for automotive application,” *Batteries*, vol. 8, 04 2022.
- [12] UN Global Technical Regulation, “Proposal for Amendment 4 to UN GTR No. 4 (WHDC).” Accessed: 10.03.2023 https://unece.org/sites/default/files/2021-06/ECE_TRANS_WP.29_2021_79E.pdf, 2021.
- [13] Amphenol, “BAF147 water detection sensor,” 2019.
- [14] Porsche, “The battery: Sophisticated thermal management, 800-volt system voltage.” Accessed: 12.07.2020 <https://newsroom.porsche.com/en/products/taycan/battery-18557.html>, 2020.
- [15] Medium, “Website.” Accessed: 26.09.2020 <https://medium.com/@FaradayFuture/fully-submerged-battery-pack-af4fda493923>, 2020.

- [16] C. Roe, X. Feng, G. White, R. Li, H. Wang, X. Rui, C. Li, F. Zhang, V. Null, M. Parkes, Y. Patel, Y. Wang, H. Wang, M. Ouyang, G. Offer, and B. Wu, "Immersion cooling for Lithium-Ion batteries – a review," *Journal of Power Sources*, vol. 525, p. 231094, 03 2022.
- [17] Motor1, "McLaren reveals speedtail electric secrets." Accessed: 08.01.2022 <https://uk.motor1.com/news/419393/mclaren-reveals-speedtail-electric-secrets/>, 2020.
- [18] Mercedes-AMG, "World premiere of the first performance hybrid from mercedes-amg." Accessed: 07.01.2022 <https://www.mercedes-amg.com/en/world-of-amg/news/press-information/mercedes-amg-gt-63-s-e-performance.html>, 2022.
- [19] Porsche, "Porsche taycan." Accessed: 01.08.2023 <https://www.porsche.com/international/models/taycan/taycan-models/taycan/>, 2023.
- [20] L. Lu, X. Han, L. Jianqiu, J. Hua, and M. Ouyang, "A review on the key issues for Lithium-Ion battery management in electric vehicles," *Journal of Power Sources*, vol. 226, pp. 272–288, 03 2013.
- [21] HT Auto, "Audi recalls its first electric car for battery fire risk." Accessed: 19.06.2023 HyundaiKona{EV}facescoolantleakissue;over800modelsaffected, 2019.
- [22] Fortune, "Audi recalls its first electric car for battery fire risk." Accessed: 19.06.2023 <https://fortune.com/2019/06/10/audi-electric-car-recall/>, 2019.
- [23] USA Today, "Electric vehicle fires in florida flooding: What happened?." Accessed: 19.06.2023 <https://eu.usatoday.com/story/money/cars/2022/10/26/electric-vehicle-fires-florida-flooding-what-happened/10553207002/>, 2022.
- [24] G. Wójcik, "Optical liquid detection sensor device," U.K. Patent GB2602001A, 01 2021.
- [25] G. Wójcik, "Optical liquid detection system," U.K. Patent GB2203308, 03 2022.
- [26] International Organization for Standardization, "Website ISO 26262-1:2011 road vehicles - functional safety." Accessed: 19.07.2020 <https://www.iso.org/standard/43464.html>, 2020.
- [27] Y.-L. Ding, Z. Cano, A. Yu, J. Lu, and C. Z., "Automotive Li-Ion batteries: Current status and future perspectives," *Electrochemical Energy Reviews*, pp. 1–28, 2019.
- [28] Y. Miao, P. Hynan, A. Von Jouanne, and A. Yokochi, "Current Li-Ion battery technologies in electric vehicles and opportunities for advancements," *Energies*, vol. 12, no. 6, pp. 1–20, 2019.
- [29] J. Choi and D. Aurbach, "Promise and reality of post-Li-Ion batteries with high energy densities," *Nature Reviews Materials*, vol. 1, 2016.
- [30] T. Y. Chian, W. L. J. Wei, E. L. M. Ze, L. Z. Ren, Y. E. Ping, N. Z. Abu Bakar, M. Faizal, and S. Sivakumar, "A review on recent progress of batteries for electric vehicles," *International Journal of Applied Engineering Research*, vol. 14, no. 24, pp. 4441–4461, 2019.
- [31] ISO 6469:3(E), "Electrically propelled road vehicles. Safety specifications. Part 3: Electrical safety," standard, International Organization for Standardization, Geneva, CH, Dec. 2011.
- [32] J. Alvarez, M. Sachenbacher, D. Ostermeier, H. Stadlbauer, U. Hummitzsch, and A. Alexeev, "D6.1 analysis of the state of the art on BMS," tech. rep., Everlasting, 2017.

- [33] M. Zwicker, M. Moghadam, W. Zhang, and C. Nielsen, "Automotive battery pack manufacturing -a review of battery to tab joining," *Journal of Advanced Joining Processes*, vol. 1, 2020.
- [34] L. David Roper, "Website." Accessed: 04.10.2020 <http://www.roperld.com/science/TeslaModelS.htm>, 2020.
- [35] Green Car Congress, "A closer look at Audi's new R8 e-tron EV and battery." Accessed: 04.10.2020 <https://www.greencarcongress.com/2015/06/20150612-r8etron.html>, 2015.
- [36] T. Bandhauer, S. Garimella, and T. Fuller, "A critical review of thermal issues in Lithium-Ion batteries," *Journal of The Electrochemical Society*, vol. 158, p. R1, 01 2011.
- [37] D. H. Jeon, "Numerical modeling of Lithium-Ion battery for predicting thermal behavior in a cylindrical cell," *Current Applied Physics*, vol. 14, 01 2013.
- [38] G. Xia, L. Cao, and G. Bi, "A review on battery thermal management in electric vehicle application," *Journal of Power Sources*, vol. 367, pp. 90–105, 11 2017.
- [39] Z. Rao and S. Wang, "A review of power battery thermal energy management," *Renewable & Sustainable Energy Reviews - RENEW SUSTAIN ENERGY REV*, vol. 15, 12 2011.
- [40] STMicroelectronics, "Automotive battery management system (BMS)." Accessed: 04.10.2020 <https://www.st.com/en/applications/electro-mobility/automotive-battery-management-system-bms.html>, 2020.
- [41] STMicroelectronics, "Spc58 e line mcus." Accessed: 04.10.2020 <https://www.st.com/en/automotive-microcontrollers/spc58-e-line-mcus.html>, 2020.
- [42] Texas Instruments, "Tms570ls0432." Accessed: 04.10.2020 <https://www.ti.com/product/TMS570LS0432>, 2020.
- [43] Wired, "EVs fire up pyroswitches to cut risk of shock after a crash." Accessed: 04.10.2020 <https://www.wired.com/story/evs-fire-pyroswitches-cut-risk-shock-crash/>, 2019.
- [44] Green Car Reports, "Busting 7 of the most common myths about electric cars." Accessed: 04.10.2020 https://www.greencarreports.com/news/1122838_busting-7-of-the-most-common-myths-about-electric-cars, 2019.
- [45] D. Ouyang, M. Chen, J. Liu, R. Wei, J. Weng, and J. Wang, "Investigation of a commercial Lithium-Ion battery under overcharge/over-discharge failure conditions," *RSC Advances*, vol. 8, pp. 33414–33424, 09 2018.
- [46] Y. Liu and J. Xie, "Failure study of commercial LiFePO₄ cells in overcharge conditions using electrochemical impedance spectroscopy," *Journal of the Electrochemical Society*, vol. 162, pp. A2208–A2217, 01 2015.
- [47] B. Mao, H. Chen, Z. Cui, W. Tang qin, and Q. Wang, "Failure mechanism of the Lithium-ion battery during nail penetration," *International Journal of Heat and Mass Transfer*, vol. 122, pp. 1103–1115, 07 2018.
- [48] D. Lyu, B. Ren, and S. Li, "Failure modes and mechanisms for rechargeable lithium-based batteries: a state-of-the-art review," *Acta Mechanica*, vol. 230, 03 2019.

- [49] F. Larsson, P. Andersson, P. Blomqvist, and B.-E. Mellander, “Toxic fluoride gas emissions from Lithium-Ion battery fires,” *Scientific Reports*, vol. 7, 12 2017.
- [50] J. Xu, R. Deshpande, J. Pan, Y.-T. Cheng, and V. Battaglia, “Electrode side reactions, capacity loss and mechanical degradation in Lithium-Ion batteries,” *Journal of The Electrochemical Society*, vol. 162, pp. 2026–2035, 01 2015.
- [51] L. Kanevskii and V. Dubasova, “Degradation of Lithium-Ion batteries and how to fight it: A review,” *Russian Journal Of Electrochemistry*, vol. 41, pp. 1–16, 03 2005.
- [52] S. Wilke, B. Schweitzer, S. A. Khateeb Razack, and S. Al-Hallaj, “Preventing thermal runaway propagation in Lithium-Ion battery packs using a phase change composite material: An experimental study,” *Journal of Power Sources*, vol. 340, pp. 51–59, 02 2017.
- [53] S. Ma, M. Jiang, P. Tao, C. Song, J. Wu, J. Wang, T. Deng, and W. Shang, “Temperature effect and thermal impact in Lithium-Ion batteries: A review,” *Progress in Natural Science: Materials International*, vol. 28, 11 2018.
- [54] N. Galushkin, N. Yazvinskaya, and D. Galushkin, “Mechanism of thermal runaway in Lithium-Ion cells,” *Journal of The Electrochemical Society*, vol. 165, pp. A1303–A1308, 01 2018.
- [55] R. Xiong, Q. Yu, and W. Shen, “Review on sensors fault diagnosis and fault-tolerant techniques for Lithium-Ion batteries in electric vehicles,” pp. 406–410, 05 2018.
- [56] M.-K. Tran and M. Fowler, “Sensor fault detection and isolation for degrading Lithium-Ion batteries in electric vehicles using parameter estimation with recursive least squares,” *Batteries*, vol. 6, p. 1, 12 2019.
- [57] L. Yao, Z. Wang, and J. Ma, “Fault detection of the connection of Lithium-Ion power batteries based on entropy for electric vehicles,” *Journal of Power Sources*, vol. 293, 10 2015.
- [58] Fisher Engineering, Inc., “Victorian big battery fire: July 30, 2021.” Accessed: 18.06.2023 <https://victorianbigbattery.com.au/wp-content/uploads/2022/12/VBB-Fire-Independent-Report-of-Technical-Findings.pdf>, 2021.
- [59] PV Magazine, “Fire at victorian big battery now under control.” Accessed: 18.06.2023 <https://www.pv-magazine-australia.com/2021/08/02/fire-at-victorian-big-battery-now-under-control/>, 2021.
- [60] Z. Liu, Q. Ahmed, G. Rizzoni, and h. Hongwen, “Fault detection and isolation for Lithium-Ion battery system using structural analysis and sequential residual generation,” *ASME 2014 Dynamic Systems and Control Conference, DSCC 2014*, vol. 2, 10 2014.
- [61] Electric Vehicle Subcommittee, “Electric vehicle safety global technical regulation - protection against water,” tech. rep., Japan Automobile Manufacturers Association, China, 2019.
- [62] C. Xu, M. Ouyang, L. Lu, X. Liu, S. Wang, and X. Feng, “Preliminary study on the mechanism of Lithium-Ion battery pack under water immersion,” *ECS Transactions*, vol. 77, pp. 209–216, 07 2017.
- [63] C. Hendricks, N. Williard, S. Mathew, and M. Pecht, “A failure modes, mechanisms, and effects analysis (fimea) of Lithium-Ion batteries,” *Journal of Power Sources*, vol. 297, pp. 113–120, 11 2015.

- [64] J. Korbicz, Z. Kowalczyk, J. M. Kościelny, and W. Cholewa, *Fault diagnosis. Models, artificial intelligence, applications*. Berlin/Heidelberg: Springer, 2004.
- [65] R. Isermann, *Fault Diagnosis Systems*. Darmstadt, Germany: Springer, 2006.
- [66] J. Lee, O. Nam, and B. Cho, “Li-Ion battery soc estimation method based on the reduced order extended kalman filtering,” *Journal of Power Sources - J POWER SOURCES*, vol. 174, pp. 9–15, 11 2007.
- [67] H. Hongwen, Z. Liu, and Y. Hua, “Adaptive extended kalman filter based fault detection and isolation for a Lithium-Ion battery pack,” *Energy Procedia*, vol. 75, pp. 1950–1955, 08 2015.
- [68] Z. Liu and H. Hongwen, “Sensor fault detection and isolation for a Lithium-Ion battery pack in electric vehicles using adaptive extended kalman filter,” *Applied Energy*, vol. 185, 11 2015.
- [69] Z. Liu and H. Hongwen, “Model-based sensor fault diagnosis of a Lithium-Ion battery in electric vehicles,” *Energies*, vol. 8, pp. 6509–6527, 07 2015.
- [70] R. Xiong, Q. Yu, W. Shen, C. Lin, and F. Sun, “A sensor fault diagnosis method for a Lithium-Ion battery pack in electric vehicles,” *IEEE Transactions on Power Electronics*, vol. PP, pp. 1–1, 01 2019.
- [71] A. Singh, A. Izadian, and S. Anwar, “Fault diagnosis of Li-Ion batteries using multiple-model adaptive estimation,” pp. 3524–3529, 11 2013.
- [72] A. Sidhu, A. Izadian, and S. Anwar, “Adaptive nonlinear model-based fault diagnosis of Li-Ion batteries,” *IEEE Transactions on Industrial Electronics*, vol. 62, pp. 1002–1011, 02 2015.
- [73] X. Feng, Y. Pan, X. He, L. Wang, and M. Ouyang, “Detecting the internal short circuit in large-format Lithium-Ion battery using model-based fault-diagnosis algorithm,” *Journal of Energy Storage*, vol. 18, pp. 26–39, 08 2018.
- [74] W. Gao, Y. Zheng, M. Ouyang, L. Jianqiu, X. Lai, and X. Hu, “Micro-short circuit diagnosis for series-connected Lithium-Ion battery packs using mean-difference model,” *IEEE Transactions on Industrial Electronics*, vol. PP, pp. 1–1, 05 2018.
- [75] S. Alavi, M. Samadi, and M. Saif, “Plating mechanism detection in Lithium-Ion batteries, by using a particle-filtering based estimation technique,” pp. 4356–4361, 06 2013.
- [76] W. Chen, W. Chen, M. Saif, M.-F. Li, and H. Wu, “Simultaneous fault isolation and estimation of Lithium-Ion batteries via synthesized design of luenberger and learning observers,” *Control Systems Technology, IEEE Transactions on*, vol. 22, pp. 290–298, 01 2014.
- [77] S. Dey, Z. Abdollahi Biron, S. Tatipamula, N. Das, S. Mohon, B. Ayalew, and P. Pisu, “On-board thermal fault diagnosis of Lithium-Ion batteries for hybrid electric vehicle application,” vol. 48, 07 2015.
- [78] S. Dey, Z. Abdollahi Biron, S. Tatipamula, N. Das, S. Mohon, B. Ayalew, and P. Pisu, “Model-based real-time thermal fault diagnosis of Lithium-Ion batteries,” *Control Engineering Practice*, vol. 56, 08 2016.

- [79] S. Dey, H. Perez, and S. Moura, "Model-based battery thermal fault diagnostics: Algorithms, analysis, and experiments," *IEEE Transactions on Control Systems Technology*, vol. XX, 12 2017.
- [80] J. Xu, J. Wang, L. Shiyang, and B. Cao, "A method to simultaneously detect the current sensor fault and estimate the state of energy for batteries in electric vehicles," *Sensors*, vol. 16, p. 1328, 08 2016.
- [81] S. Dey, S. Mohon, P. Pisu, and B. Ayalew, "Sensor fault detection, isolation, and estimation in Lithium-Ion batteries," *IEEE Transactions on Control Systems Technology*, vol. 99, pp. 1–9, 03 2016.
- [82] J. Marcicki, S. Onori, and G. Rizzoni, "Nonlinear fault detection and isolation for a Lithium-Ion battery management system," vol. 1, 01 2010.
- [83] W. Lombardi, M. Zarudniev, S. Lesecq, and S. Bacquet, "Sensors fault diagnosis for a BMS," pp. 952–957, 06 2014.
- [84] X. Kong, Y. Zheng, M. Ouyang, L. Lu, L. Jianqiu, and Z. Zhang, "Fault diagnosis and quantitative analysis of micro-short circuits for Lithium-Ion batteries in battery packs," *Journal of Power Sources*, vol. 395, pp. 358–368, 08 2018.
- [85] B. Xia, Y. Shang, T. Nguyen, and C. Mi, "A correlation based fault detection method for short circuits in battery packs," *Journal of Power Sources*, vol. 337, pp. 1–10, 01 2017.
- [86] Y. Kang, B. Duan, Z. Zhou, Y. Shang, and C. Zhang, "A multi-fault diagnostic method based on an interleaved voltage measurement topology for series connected battery packs," *Journal of Power Sources*, vol. 417, pp. 132–144, 03 2019.
- [87] J. Xiong, H. Banvait, L. Li, Y. Chen, J. Xie, Y. Liu, M. Wu, and J. Chen, "Failure detection for over-discharged Li-ion batteries," *2012 IEEE International Electric Vehicle Conference, IEVC 2012*, 03 2012.
- [88] V. Muddappa and S. Anwar, "Electrochemical model based fault diagnosis of Li-Ion battery using fuzzy logic," *ASME International Mechanical Engineering Congress and Exposition, Proceedings (IMECE)*, vol. 4, 11 2014.
- [89] Y. Zhao, P. Liu, Z. Wang, L. Zhang, and J. Hong, "Fault and defect diagnosis of battery for electric vehicles based on big data analysis methods," *Applied Energy*, 06 2017.
- [90] A. Samanta, S. Chowdhuri, and S. Williamson, "Machine learning-based data-driven fault detection/diagnosis of Lithium-Ion battery: A critical review," *Electronics*, vol. 10, p. 1309, 05 2021.
- [91] J. Hong, Z. Wang, and Y. Yao, "Fault prognosis of battery system based on accurate voltage abnormality prognosis using long short-term memory neural networks," *Applied Energy*, vol. 251, 10 2019.
- [92] Y. Li, C. Zou, M. Bercibar, E. Nanini-Maury, J. Chan, P. Van den Bossche, J. Van Mierlo, and N. Omar, "Random forest regression for online capacity estimation of Lithium-Ion batteries," *Applied Energy*, vol. 232, pp. 197–210, 09 2018.
- [93] L. Yao, Z. Fang, Y. Xiao, J.-J. Hou, and Z. Fu, "An intelligent fault diagnosis method for lithium battery systems based on grid search support vector machine," *Energy*, vol. 214, p. 118866, 01 2021.

- [94] P. Ortiz, J. Valladolid, C. Garcia, G. Novillo, and F. Berrezueta, "Analysis of machine learning techniques for the intelligent diagnosis of Ni-MH battery cells," pp. 1–6, 11 2018.
- [95] D. Yang, X. Zhang, R. Pan, Y. Wang, and Z. Chen, "A novel gaussian process regression model for state-of-health estimation of Lithium-Ion battery using charging curve," *Journal of Power Sources*, vol. 384, pp. 387–395, 04 2018.
- [96] P. Tagade, K. Hariharan, S. Ramachandran, A. Khandelwal, A. Naha, S. Kolake, and S. Han, "Deep gaussian process regression for Lithium-Ion battery health prognosis and degradation mode diagnosis," *Journal of Power Sources*, vol. 445, p. 227281, 01 2020.
- [97] M. Fasahat and M. Manthouri, "State of charge estimation of Lithium-Ion batteries using hybrid autoencoder and long short term memory neural networks," *Journal of Power Sources*, vol. 469, p. 228375, 09 2020.
- [98] P. Vincent, H. Larochelle, I. Lajoie, Y. Bengio, and P.-A. Manzagol, "Stacked denoising autoencoders: Learning useful representations in a deep network with a local denoising criterion," *Journal of Machine Learning Research*, vol. 11, pp. 3371–3408, 12 2010.
- [99] United States Patent and Trademark Office, "Us patent full-text database boolean search." Accessed: 17.07.2021 <https://patft.uspto.gov/netahhtml/PTO/search-bool.html>, 2021.
- [100] Y. Furuya, S. Ogasawara, H. Inoue, S. Nagata, and T. Syoji, "Battery pack," U.S. Patent US20140154531A1, 04 2018.
- [101] K. Yanagi, "Battery pack tray," U.S. Patent US20140014428A1, 03 2015.
- [102] "Fail safe serviceable high voltage battery pack," U.S. Patent US20110014501A1, 10 2015.
- [103] D. G. Duff, J. C. Weintraub, and G. Arcenio, "Method of controlling battery pack humidity utilizing an active reactivation system," U.S. Patent US8247097B1, 08 2012.
- [104] D. G. Duff, J. C. Weintraub, and G. Arcenio, "Battery pack dehumidifier with active reactivation system," U.S. Patent US20120315517A1, 05 2015.
- [105] E. Farha, H. Addanki, K. Kearney, and C. Kuo, "Electronics umbrella for electrified vehicle battery packs," U.S. Patent US10333118B2, 01 2019.
- [106] L. Young-Bin, "Battery pack," U.S. Patent US20120194004A1, 11 2016.
- [107] Y. Jianfeng, "Damage detection and warning system of a battery pack," U.S. Patent US20190198946A1, 02 2021.
- [108] Y. Kazuhiro, "Liquid leakage detector, liquid transport apparatus and method of detecting liquid leakage," U.S. Patent US20120038912A1, 03 2015.
- [109] W. Key, "Fuel dispenser leak detector," U.S. Patent US5514920A, 12 1993.
- [110] Y. Congming, T. Zhiming, and L. Xiang, "Battery pack system and liquid leakage detection method thereof," U.S. Patent US20130183552A1, 09 2015.
- [111] H. Tatekazu, S. Futoshi, and O. Yohey, "Liquid leakage sensor and liquid leakage detecting system," U.S. Patent US20050162280A1, 01 2007.
- [112] R. Ali, Z. Kambiez, and P. Staton, "Leak detector using optical fiber," Japanese Patent JP2013250281A, 09 2015.

- [113] K. Sung-kyu, “Battery module including flexible printed circuit board sensing liquid,” Korean Patent KR20210037459A, 09 2015.
- [114] G. Offer, Y. Patel, A. Hales, L. Bravo Diaz, and M. Marzook, “Cool metric for Lithium-Ion batteries could spur progress,” *Nature*, vol. 582, pp. 485–487, 06 2020.
- [115] M. M. Werneck and R. C. S. B. Allil, *Plastic Optical Fiber Sensors: Science, Technology and Applications*. Boca Raton, Florida: CRC Press Inc., 2020.
- [116] MOST Cooperation, “Website.” Accessed: 02.05.2020 <https://www.mostcooperation.com/>, 2020.
- [117] Mitsubishi Chemical, “Website.” Accessed: 08.05.2020 <https://www.pofeska.com/pofeskae/product/02/index.html>, 2020.
- [118] L. Bilro, N. Alberto, J. Pinto, and R. Nogueira, “Optical sensors based on plastic fibers,” *Sensors (Basel, Switzerland)*, vol. 12, pp. 12184–207, 12 2012.
- [119] A. Sharma, J. Gupta, and S. Ishika, “Fiber optic evanescent wave absorption-based sensors: A detailed review of advancements in the last decade (2007-18),” *Optik*, vol. 183, 02 2019.
- [120] FBGS International, “Website.” Accessed: 30.07.2021 <https://fbgs.com/>, 2021.
- [121] A. Onoufriou, K. Kalli, and G. Kohnke, “Fiber bragg gratings: Fundamentals and applications in telecommunications and sensing,” *Physics Today - PHYS TODAY*, vol. 53, 05 2000.
- [122] D. Webb, “Fibre bragg grating sensors in polymer optical fibres,” *Measurement Science and Technology*, vol. 26, 09 2015.
- [123] S. Wang, D. Zhang, Y. Xu, S. Sun, and X. Sun, “Refractive index sensor based on double side-polished U-shaped plastic optical fiber,” *Sensors*, vol. 20, p. 5253, 09 2020.
- [124] J. Shin and P. Jaehee, “Plastic optical fiber refractive index sensor employing an in-line submillimeter hole,” *Photonics Technology Letters, IEEE*, vol. 25, pp. 1882–1884, 10 2013.
- [125] F. De-Jun, L. Guan-Xiu, L. Xi-Lu, J. Ming-Shun, and S. Qing-Mei, “Refractive index sensor based on plastic optical fiber with tapered structure,” *Applied optics*, vol. 53, pp. 2007–2011, 04 2014.
- [126] F. Sequeira, N. Cennamo, A. Rudnitskaya, R. Nogueira, L. Zeni, and L. Bilro, “D-shaped POF sensors for refractive index sensing-the importance of surface roughness,” *Sensors*, vol. 19, p. 2476, 05 2019.
- [127] O. Ziemann, J. Krauser, P. E. Zamzow, and W. Daum, *POF Handbook*. Berlin: Springer, 2008.
- [128] M. Miedreich and H. Schober, “Pedestrian protection system, featuring fiber optic sensor,” *ATZ Worldwide*, vol. 107, no. 3, pp. 15–19, 2005.
- [129] G. Kodl, “A new optical waveguide pressure sensor using evanescent field,” pp. 1943 – 1946 Vol.2, 07 2004.
- [130] P. Lallana, G. Aldabaldetrekua, A. López, D. Montero, G. Durana, J. Mateo, M. A. Losada, J. Zubia, and C. Vázquez, “Sensing applications in aircrafts using polymer optical fibres,” *Sensors*, vol. 21, p. 3605, 05 2021.

- [131] W. Zhang, D. Webb, M. Carpenter, and C. Williams, "Measuring water activity of aviation fuel using a polymer optical fiber bragg grating," *Proceedings of SPIE - The International Society for Optical Engineering*, vol. 9157, 06 2014.
- [132] G. Durana, M. Kirchhof, M. Lubber, I. Ocáriz, H. Poisel, J. Zubia, and C. Vázquez, "Use of a novel fiber optical strain sensor for monitoring the vertical deflection of an aircraft flap," *IEEE Sensors Journal*, vol. 9, 11 2009.
- [133] Green Car Congress, "Mercedes-AMG reveals performance hybrid and battery-electric AMG derivative strategy." Accessed: 29.01.2023 <https://www.greencarcongress.com/2021/03/20210331-amg.html>, 2021.
- [134] Hasan Yavuz, "Serialplot. small and simple software for plotting data from serial port in realtime.." Accessed: 30.10.2021 <https://github.com/hy0zd/serialplot>, 2022.
- [135] Adafruit Industries , "Thermistor guide datasheet by adafruit industries LLC.." Accessed: 01.02.2023 <https://www.digikey.de/htmldatasheets/production/2104050/0/0/1/thermistor-guide.html>, 2023.
- [136] G. Wójcik and P. Przystalka, "Experimental investigation of factors influencing the transmission capabilities of a low cost, side-polished evanescent wave absorption plastic optical fiber sensors," *Procedia Structural Integrity*, vol. 37, pp. 179–186, 02 2022.
- [137] Bones Electronics Co Ltd., "Website." Accessed: 14.04.2021 http://www.bones-electronics.com/html_products/Automobile-Polymer-Optical-Fiber-200.html, 2021.
- [138] Dok.kern-sohn.com, "Website." Accessed: 18.08.2021 <https://dok.kern-sohn.com/manuals/files/English/orf-ba-e-1911.pdf>, 2021.
- [139] J. He, W. Liu, and Y. Huang, "Simultaneous determination of glass transition temperatures of several polymers," *PloS one*, vol. 11, p. e0151454, 03 2016.
- [140] S. Khodier, "Refractive index of standard oils as a function of wavelength and temperature," *Optics and Laser Technology - OPT LASER TECHNOL*, vol. 34, pp. 125–128, 03 2002.
- [141] W. Cholewa and W. Moczulski, *Diagnostyka techniczna maszyn. Pomiar i analiza sygnałów*. Gliwice: Wydawnictwo Politechniki Śląskiej, 1993.
- [142] E. F. Schubert, *Light Emitting Diodes. Second edition*. New York: Cambridge university press, 2006.
- [143] U. Elele, A. Nekahi, A. Arshad, and I. Fofana, "Towards online ageing detection in transformer oil: A review," *Sensors*, vol. 22, p. 25, 10 2022.
- [144] V. Bećirović, V. Helac, B. Arslanagic, and H. Samic, "Effects on leds during the accelerated ageing test," pp. 1–6, 03 2019.
- [145] Y. Shao and S.-C. Lin, "Using a time delay neural network approach to diagnose the out-of-control signals for a multivariate normal process with variance shifts," *Mathematics*, vol. 7, p. 959, 10 2019.
- [146] K. Patan, *Artificial Neural Networks for the Modelling and Fault Diagnosis of Technical Processes*. Springer, 01 2008.

- [147] M. Sznura and P. Przystalka, "Development of a power and communication bus using HIL and computational intelligence," *Applied Sciences*, vol. 11, 09 2021.
- [148] D. Rumelhart, G. Hinton, and R. Williams, "Learning representations by back propagating errors," *Nature*, vol. 323, pp. 533–536, 10 1986.
- [149] R. Susik, "Recurrent autoencoder with sequence-aware encoding," pp. 47–57, 06 2021.
- [150] BuiltIn, "A guide to recurrent neural networks: Understanding RNN and LSTM networks." Accessed: 02.05.2023 <https://builtin.com/data-science/recurrent-neural-networks-and-lstm>, 2023.
- [151] K. Park, Y. Jung, K. Kim, and S. Park, "Determination of deep learning model and optimum length of training data in the river with large fluctuations in flow rates," *Water*, vol. 12, p. 3537, 12 2020.
- [152] Y. Bengio, P. Simard, and P. Frasconi, "Learning long-term dependencies with gradient descent is difficult," *IEEE transactions on neural networks / a publication of the IEEE Neural Networks Council*, vol. 5, pp. 157–66, 02 1994.
- [153] S. Hochreiter and J. Schmidhuber, "Long short-term memory," *Neural computation*, vol. 9, pp. 1735–80, 12 1997.
- [154] K. Cho, B. Merriënboer, C. Gulcehre, F. Bougares, H. Schwenk, and Y. Bengio, "Learning phrase representations using RNN encoder-decoder for statistical machine translation," 06 2014.
- [155] The MathWorks, Inc., "Autoencoders." Accessed: 02.05.2022 <https://www.mathworks.com/discovery/autoencoder.html>, 2023.
- [156] Medium, "Applied deep learning - part 3: Autoencoders." Accessed: 13.07.2023 <https://towardsdatascience.com/applied-deep-learning-part-3-autoencoders-1c083af4d798>, 2017.
- [157] Y. Su, Y. Zhao, C. Niu, R. Liu, W. Sun, and D. Pei, "Robust anomaly detection for multivariate time series through stochastic recurrent neural network," pp. 2828–2837, 07 2019.
- [158] W. Duch, J. Korbicz, L. Rutkowski, and R. Tadeusiewicz, *Sieci neuronowe*. Warszawa: Akademicka Oficyna Wydawnicza EXIT, 2000.
- [159] M. Bartyś, R. Patton, M. Syfert, S. de las Heras, and J. Quevedo, "Introduction to the damatics actuator FDI benchmark study, control engineering practice, (invited special issue paper), 14: 577-596, 2006. [doi: 10.1016/j.conengprac.2005.06.015]," *Control Engineering Practice*, vol. 14, pp. 577–596, 06 2006.
- [160] TDK Invensense, "MPU-9250." Accessed: 02.08.2023 <https://invensense.tdk.com/products/motion-tracking/9-axis/mpu-9250/>, 2020.
- [161] International Energy Agency, "Website." Accessed: 07.07.2020 <https://www.iea.org/reports/innovation-gaps>, 2020.
- [162] Refractometer.pl, "Website." Accessed: 12.04.2021 <http://www.refractometer.pl/refraction-datasheet-sucrose>, 2021.

Electric car battery leakage detection system

PhD thesis - summary

Author: MSc, Eng. Grzegorz Wójcik

Dissertation advisor: PhD, DSc, Eng. Piotr Przystałka, Associate Professor

Industry supervisor: PhD, Eng. Wojciech Sebzda

Silesian University of Technology, Faculty of Mechanical Engineering

Dräxлмаier Group

The rapid growth of the battery electric vehicles (BEVs) market has brought lithium-ion battery packs (LIBs) to the forefront due to their superior power and energy density properties. However, these benefits come with inherent safety challenges. LIBs operate within a narrow safety window and are highly susceptible to environmental factors, operating conditions, and manufacturing inconsistencies. Because of that, modern battery packs utilize Battery Management Systems (BMS) and Battery Thermal Management (BTM) systems to prevent the battery cells from damaging or aging too quickly.

Battery faults, both external and internal, pose significant risks, including overheating, accelerated degradation, and the potentially catastrophic thermal runaway, that could be initiated even by smaller faults, propagating further into a chain reaction of cascaded failures. Such smaller faults could be in the form of intruded water, which gathers in the battery pack due to e.g., damage to the heat exchanger, potentially causing corrosion and short circuits in the high voltage areas. BMS and BTM designs are thus crucial to ensure system safety and longevity, particularly under high current demand scenarios in EVs. The state-of-the-art solutions utilize either conductometric or capacitive electronic circuits (depending on chosen BTM approach), which present some major drawbacks if employed inside the high-voltage areas of the battery pack.

Aiming to address these challenges, this doctoral dissertation focuses on the development of an electric car battery leakage detection system, which is seen as a liquid leakage and intrusion detection system for immersion-cooled EV LIBs. Utilizing optical rather than electrical signals in high-voltage areas, this novel approach is designed to improve the safety of EV battery packs by adding a new fault detection mechanism, enhanced by computational intelligence and machine learning, and mitigating some of the drawbacks of the current solutions.

The work carried out to achieve this goal resulted in the design of an Optical Liquid Detection System (OLDS), a solution necessitating extensive research and development in several domains, including mechanical engineering, hardware, software, and optical. This comprehensive effort resulted in the fabrication of an evanescent wave absorption polymer optical fiber sensor and the development of custom mechatronics system and its software. This led to the prototype of a tailored hardware and software platform used to collect datasets with the system exposed to laboratory and road conditions under faultless and fault states (liquid leakage, water intrusion) in an iterative way. Based on the recorded datasets, a set of model-based detection methods using LSTM and RAE-GRU neural networks was proposed, formulated, and then verified offline. The performance of methods was evaluated using the recorded datasets under faultless states and under simulated fault states through specific model performance indicators as well as detection performance indicators.

The results of this dissertation provide a significant contribution to the safety and reliability of EV lithium-ion battery packs. The optical liquid detection system, coupled with the developed model-based fault detection methods based on computational intelligence approaches such as shallow and deep neural networks, promises to substantially decrease risks associated with liquid intrusion or leakage in battery packs, contributing to the wider adoption and customer acceptance of electric vehicles. Future work could further refine these methods and extend their applicability to an even broader range of conditions.

System wykrywania nieszczelności akumulatorów stosowanych w samochodach elektrycznych

Rozprawa doktorska - streszczenie

Autor: mgr inż. Grzegorz Wójcik
Promotor: dr hab. inż. Piotr Przystałka, prof. PŚ
Opiekun z przemysłu: dr inż. Wojciech Sebzda
Politechnika Śląska, Wydział Mechaniczny Technologiczny
Dräxlmaier Group

Gwałtowny wzrost rynku pojazdów elektrycznych spowodował, że ze względu na coraz wyższe wymagania dotyczące mocy i gęstości energii pakiety akumulatorów litowo-jonowych znalazły się w centrum uwagi. Rzutuje to jednak na szereg konsekwencji związanych z bezpieczeństwem ich eksploatacji. Akumulatory te powinny być eksploatowane w wąskim przedziale temperaturowym. Są one podatne na czynniki środowiskowe, warunki pracy i błędy produkcyjne. Z tego powodu nowoczesne pakiety akumulatorowe wykorzystują systemy zarządzania baterią (ang. Battery Management System, BMS) i termiczne systemy zarządzania (ang. Battery Thermal Management System, BTMS) w celu zapobieżenia uszkodzeniom lub zbyt szybkiemu starzeniu się ogniw akumulatorowych.

Uszkodzenia akumulatorów, zarówno na poziomie pakietu i modułów jak i pojedynczych ogniw, stanowią poważne ryzyko i mogą skutkować np. przegrzewaniem czy przyspieszoną degradacją ogniw. Mogą również prowadzić do katastrof w skutek zainicjowania reakcji łańcuchowej, prowadzącej do utraty stabilności termicznej pakietu akumulatorowego. Taka reakcja może zostać spowodowana nawet pozornie niewielkim uszkodzeniem, które może z biegiem czasu propagować i uszkadzać inne ogniwa. Takie niewielkie uszkodzenia mogą przyjmować różną formę, np. wtargnięcie wody, która gromadzi się w pakiecie akumulatorowym, np. w skutek uszkodzonego wymiennika ciepła, i może powodować korozję oraz zwarcia w obszarach o wysokim napięciu. Właściwe projektowanie układów BMS i BTMS jest więc kluczowe dla zapewnienia bezpieczeństwa i trwałości systemu, zwłaszcza w kontekście pakietów akumulatorowych o wysokich wymogach dotyczących natężenia prądu ładowania i rozładowania. W celu wykrywania obecności wody, aktualnie stosowane są głównie elektryczne czujniki konduktometryczne i pojemnościowe (w zależności od zastosowanego BTMS), które wykazują pewne wady ze względu na stosowanie niskonapięciowych sygnałów elektrycznych w obszarach wysokonapięciowych.

Wychodząc na przeciw powyższym wyzwaniom niniejsza praca doktorska skupia się na opracowaniu systemu wykrywania nieszczelności dla samochodowych pakietów akumulatorowych z chłodzeniem zanurzeniowym. Ze względu na specyfikę chłodzenia zanurzeniowego, nieszczelność jest rozumiana w znaczeniu wycieku czynnika chłodzącego oraz wtargnięcia wody. W pracy wykorzystano tor optyczny w miejscach wysokonapięciowych, niwelując wady takie jak ekspozycja niskonapięciowych układów na wyładowania elektrostatyczne oraz zakłócenia elektromagnetyczne.

Zaprojektowanie i wykonanie prototypu takiego systemu wymagało obszernych, interdyscyplinarnych prac badawczo-rozwojowych, ze względu na konieczność opracowania dedykowanej warstwy mechanicznej, sprzętowej, programowej oraz czujników światłowodowych. Prace te doprowadziły do wytworzenia polimerowego światłowodowego czujnika absorpcji fali zanikającej oraz opracowania dedykowanej platformy sprzętowej służącej do rejestrowania danych w warunkach laboratoryjnych oraz drogowych dla systemu w stanie pełnej zdadności oraz przy celowo wprowadzonych uszkodzeniach (wyciek oleju, wtargnięcie wody). Na podstawie zgromadzonych danych przeprowadzono ich analizę, której wynikiem było sformułowanie zestawu metod detekcji uszkodzeń opartych na modelu (z sieciami LSTM, RAE-GRU), a następnie ich weryfikacja. Działanie metod było oceniane na podstawie zarejestrowanych zestawów danych w stanie pełnej zdadności i podczas zasymulowanych stanów z rozważanymi uszkodzeniami za pomocą konkretnych wskaźników jakości i złożoności modelu, jak również wskaźników sprawności detekcji.

Wyniki rozprawy doktorskiej stanowią istotny wkład w bezpieczeństwo i niezawodność litowo-jonowych pakietów akumulatorowych pojazdów elektrycznych. System optycznego wykrywania cieczy, w połączeniu z opracowanymi metodami detekcji uszkodzeń opartymi na modelach, zmniejsza ryzyka związane z wtargnięciem cieczy lub wyciekiem czynnika chłodzącego, przyczyniając się do poprawy bezpieczeństwa i spełnienia przyszłych regulacji dotyczących pojazdów elektrycznych, w szczególności regulacji dotyczących zjawiska utraty stabilności termicznej.

Appendices

A. Elementary terms and definitions

Battery pack

A battery pack is a mechanical assembly comprising battery cells and retaining frames or trays, and possibly components for battery management [31].

Traction battery

A traction battery is a collection of all battery packs that are electrically connected for the supply of electric power to the electric drive and to the conductively connected auxiliary electrical system, if any [31]. Electrical vehicles discussed in this dissertation consist of only one battery pack, therefore the term traction battery is used interchangeably with the term battery pack.

Technology readiness level

Scale, which goes from the concept stage to scaling up the technology solution [161]:

1. Initial idea: basic principles have been defined.
2. Application formulated: concept and application of solution have been formulated.
3. Concept needs validation: solution needs to be prototyped and applied.
4. Early prototype: prototype proven in test conditions.
5. Large prototype: components proven in conditions to be deployed.
6. Full prototype at scale: prototype proven at scale in conditions to be deployed.
7. Pre-commercial demonstration: solution working in expected conditions.
8. First-of-a-kind commercial: commercial demonstration, full-scale deployment in final form.
9. Commercial operation in relevant environment: solution is commercially available, needs evolutionary improvement to stay competitive.
10. Integration at scale: solution is commercial but needs further integration efforts. Proof of stability: predictable growth.

Low voltage

Low voltage, also referred as voltage class A. Classification of an electric component or circuit with a maximum working voltage of less than 30 V A.C. (RMS) or 60 V D.C. [31].

High voltage

High voltage, also referred as voltage class B. Classification of an electric component or circuit with a maximum working voltage between 30 V A.C. (RMS) and 1000 V A.C. (RMS) or between 60 V D.C. and 1500 V D.C. [31].

Fault

Unpermitted deviation of at least one characteristic property of the system [65].

Failure

Permanent interruption of a system's ability to perform a required function under specified operating conditions [65].

Malfunction

Intermittent irregularity in fulfillment of a system's desired functions [65].

Error

The deviation between a computed value (of an output variable) and the true, specified, or theoretically correct value [65].

Disturbance

An unknown (and uncontrolled) input acting on a system [65].

Perturbation

An input acting on a system which results in a temporary departure from steady state [65].

Residuum

Fault indicator, based on deviations between measurements and model equation-based calculation [65].

Symptom

Change of an observable quantity from normal behavior [65].

Fault Detection

Determination of faults present in a system and time of detection [65].

Fault Isolation

Determination of kind, location, and time of detection of a fault by evaluating symptoms. Follows fault detection [65].

Fault Identification

Determination of size and time-variant behavior of a fault. Follows fault isolation [65].

B. Tables

Tab. B.1. Refractive index of sucrose solutions [162]

concentration % w/w	Refractive index	concentration % w/w	Refractive index
0.00	1.3330	44.00	1.4078
2.00	1.3359	46.00	1.4118
4.00	1.3388	48.00	1.4159
6.00	1.3418	50.00	1.4201
8.00	1.3448	52.00	1.4243
10.00	1.3478	54.00	1.4286
12.00	1.3509	56.00	1.4330
14.00	1.3541	58.00	1.4374
16.00	1.3573	60.00	1.4419
18.00	1.3606	62.00	1.4465
20.00	1.3639	64.00	1.4511
22.00	1.3672	66.00	1.4558
24.00	1.3706	68.00	1.4606
26.00	1.3741	70.00	1.4654
28.00	1.3776	72.00	1.4703
30.00	1.3812	74.00	1.4753
32.00	1.3848	76.00	1.4803
34.00	1.3885	78.00	1.4854
36.00	1.3922	80.00	1.4958
38.00	1.3960	82.00	1.4958
40.00	1.3999	84.00	1.5010
42.00	1.4038	N/A	N/A

C. Preliminary study under laboratory conditions - datasets

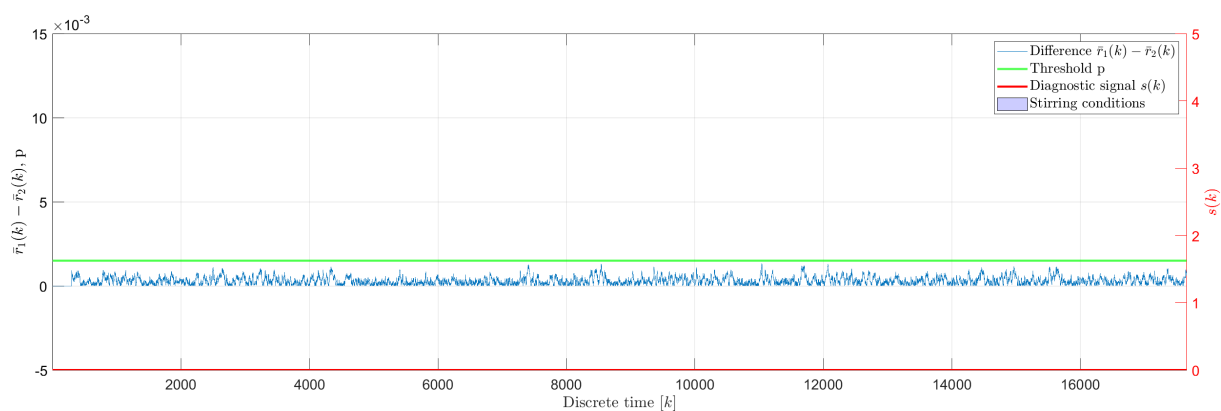


Fig. C.1. No fault 5 - scheme 1 - binary diagnostic signal $s(k)$

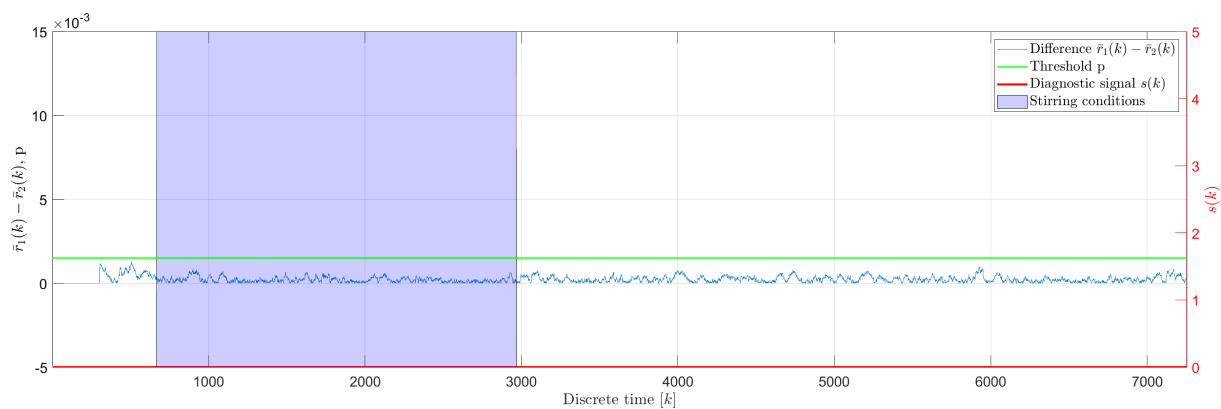


Fig. C.2. No fault 5 stirred - scheme 1 - binary diagnostic signal $s(k)$

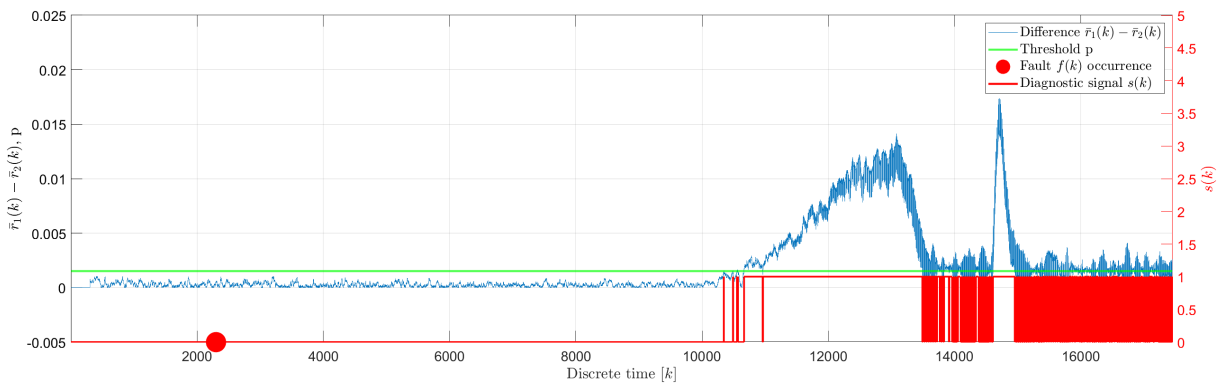


Fig. C.3. Oil leakage 1 - scheme 1 - binary diagnostic signal $s(k)$

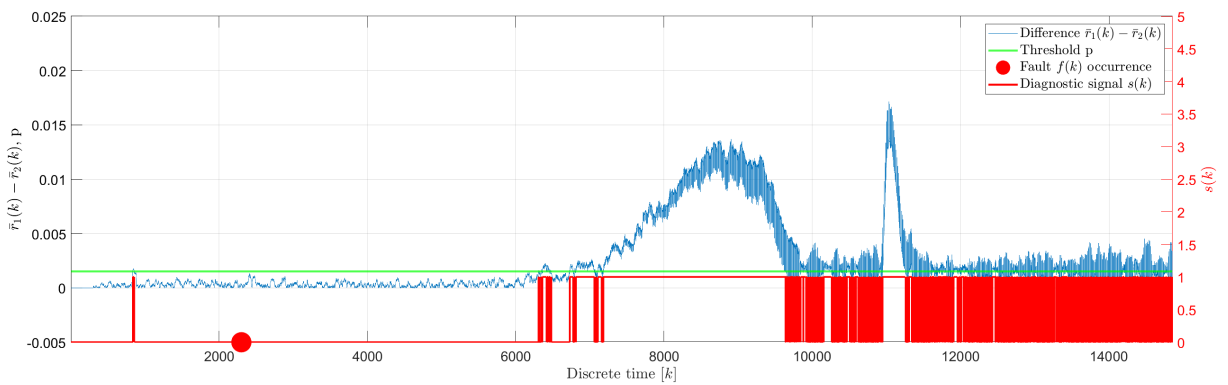


Fig. C.4. Oil leakage 2 - scheme 1 - binary diagnostic signal $s(k)$

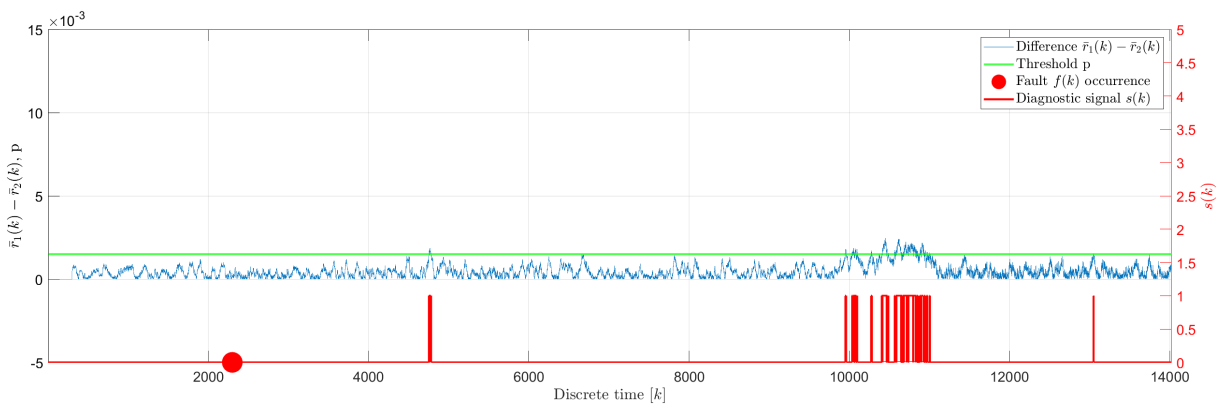


Fig. C.5. Oil leakage 3 - scheme 1 - binary diagnostic signal $s(k)$

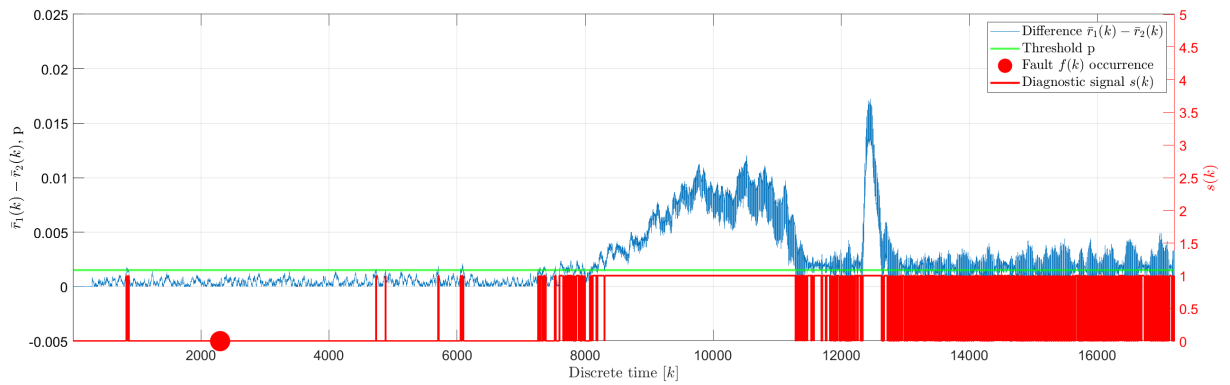


Fig. C.6. Oil leakage 4 - scheme 1 - binary diagnostic signal $s(k)$

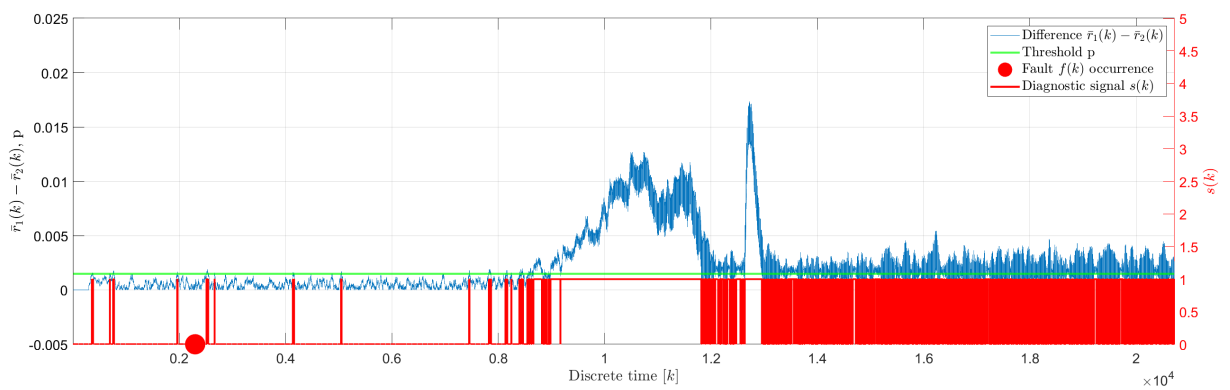


Fig. C.7. Oil leakage 5 - scheme 1 - binary diagnostic signal $s(k)$

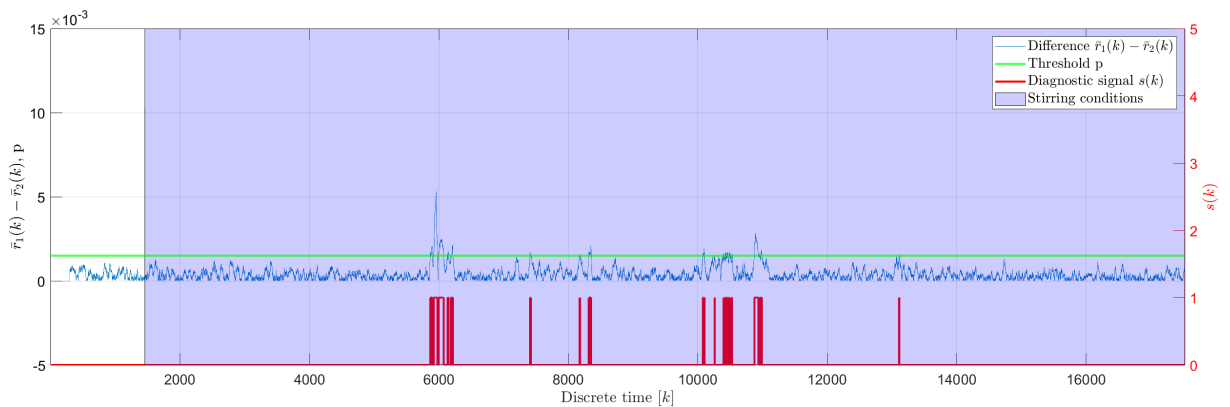


Fig. C.8. Water intrusion 1 - scheme 1 - binary diagnostic signal $s(k)$

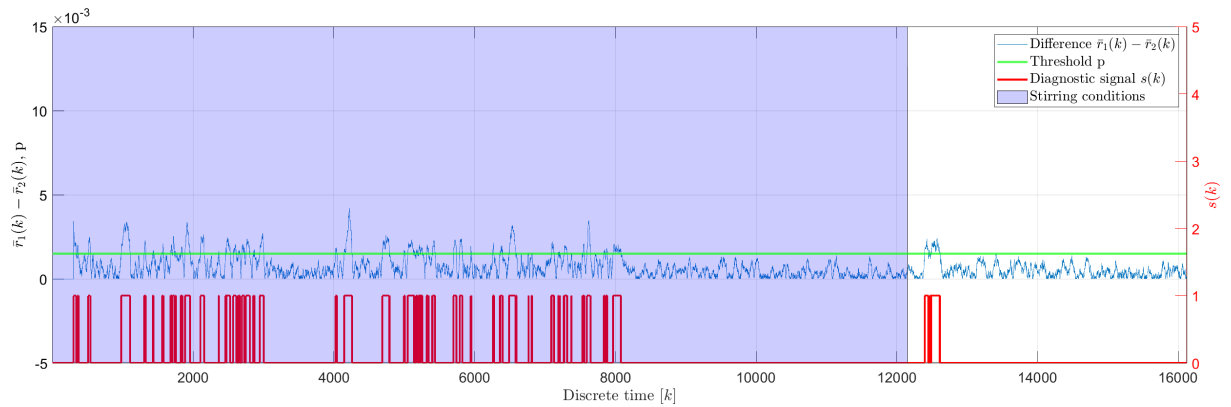


Fig. C.9. Water intrusion 2 - scheme 1 - binary diagnostic signal $s(k)$

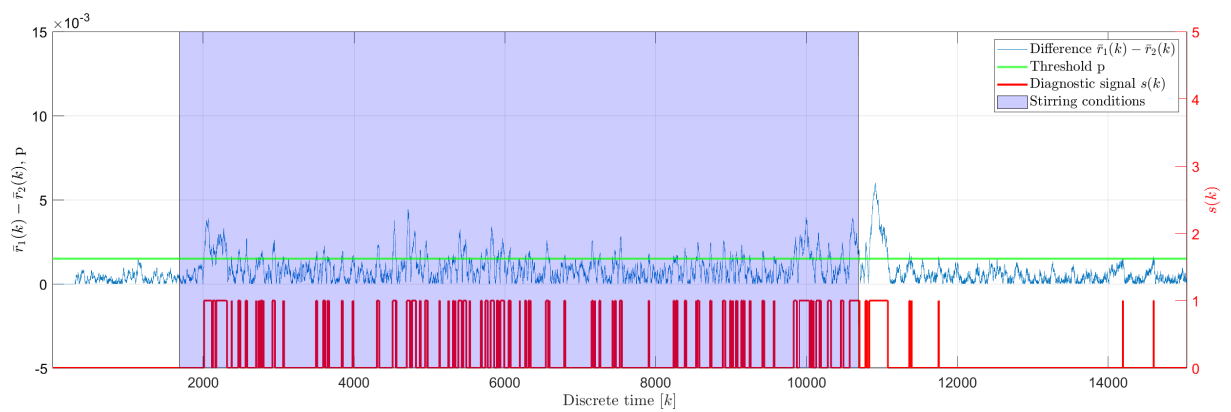


Fig. C.10. Water intrusion 3 - scheme 1 - binary diagnostic signal $s(k)$

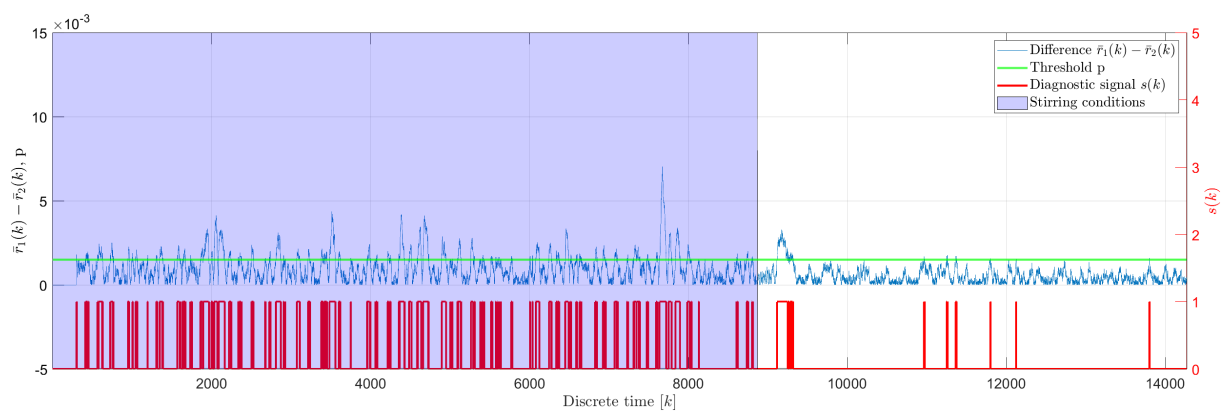


Fig. C.11. Water intrusion 4 - scheme 1 - binary diagnostic signal $s(k)$

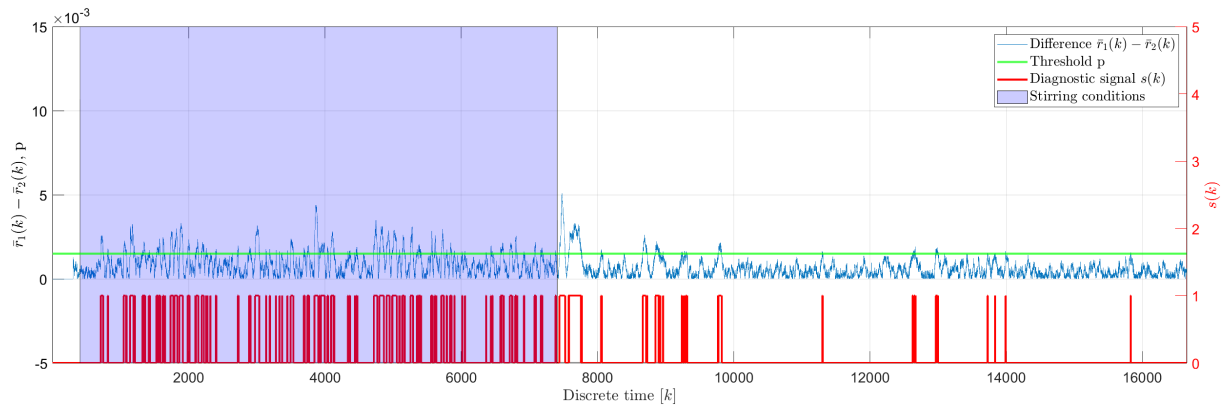


Fig. C.12. Water intrusion 5 - scheme 1 - binary diagnostic signal $s(k)$

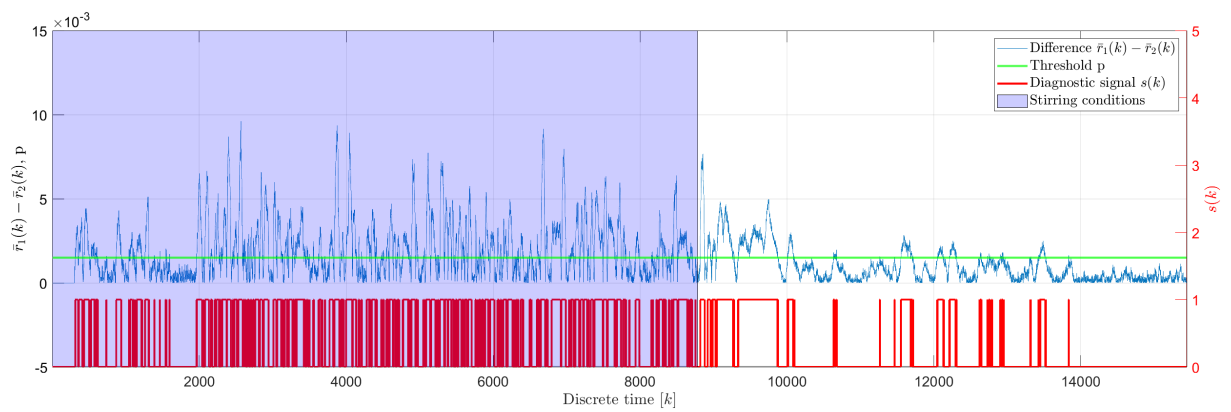


Fig. C.13. Water intrusion 6 - scheme 1 - binary diagnostic signal $s(k)$

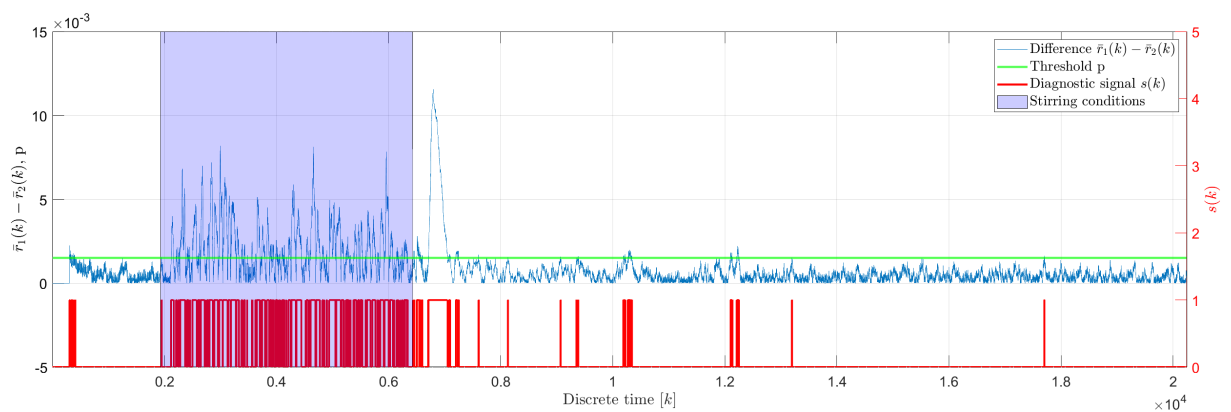


Fig. C.14. Water intrusion 7 - scheme 1 - binary diagnostic signal $s(k)$

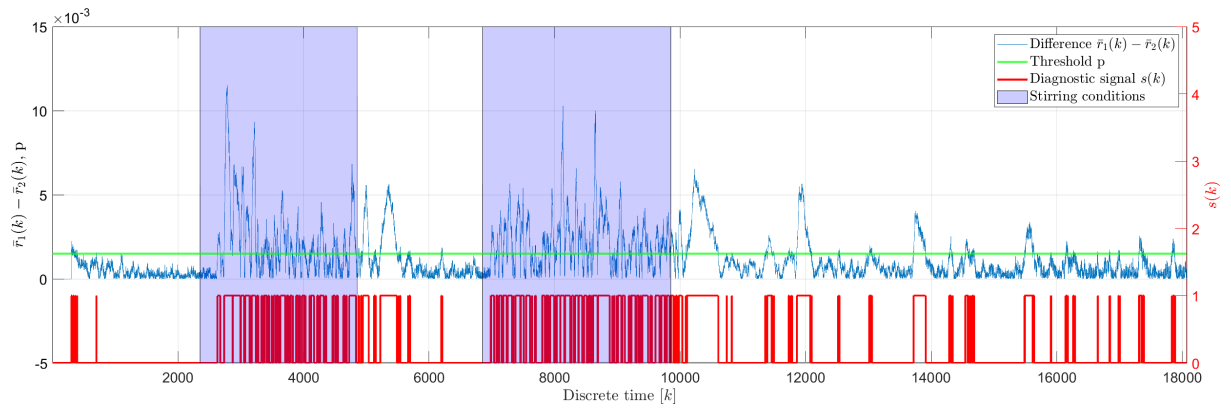


Fig. C.15. Water intrusion 8 - scheme 1 - binary diagnostic signal $s(k)$

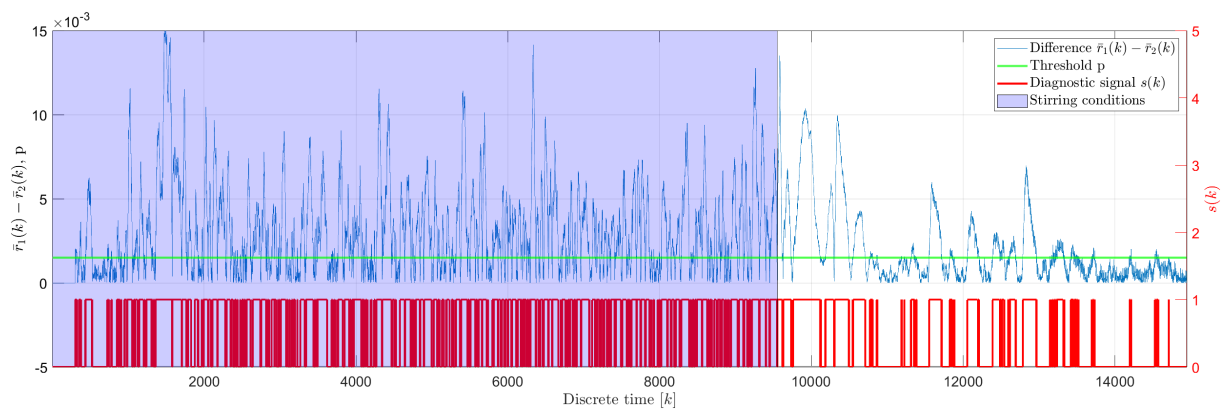


Fig. C.16. Water intrusion 9 - scheme 1 - binary diagnostic signal $s(k)$

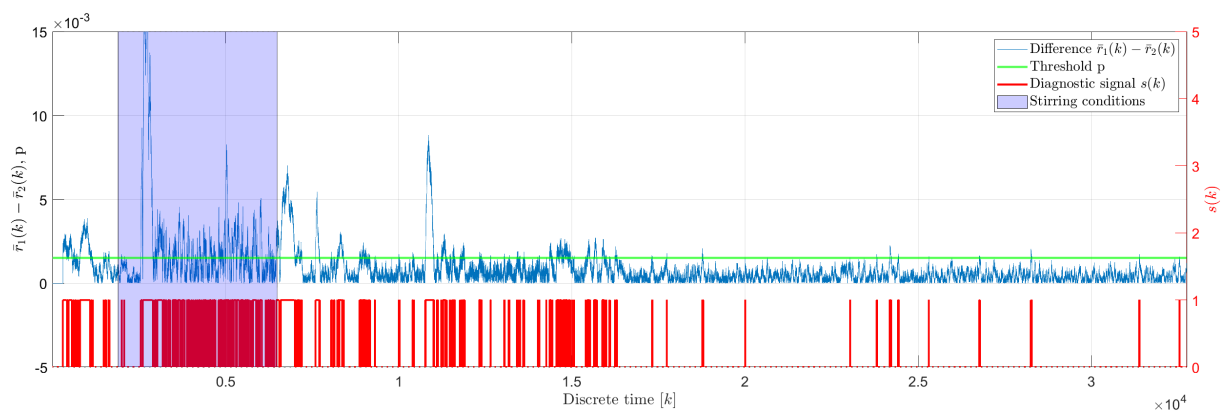


Fig. C.17. Water intrusion 10 - scheme 1 - binary diagnostic signal $s(k)$

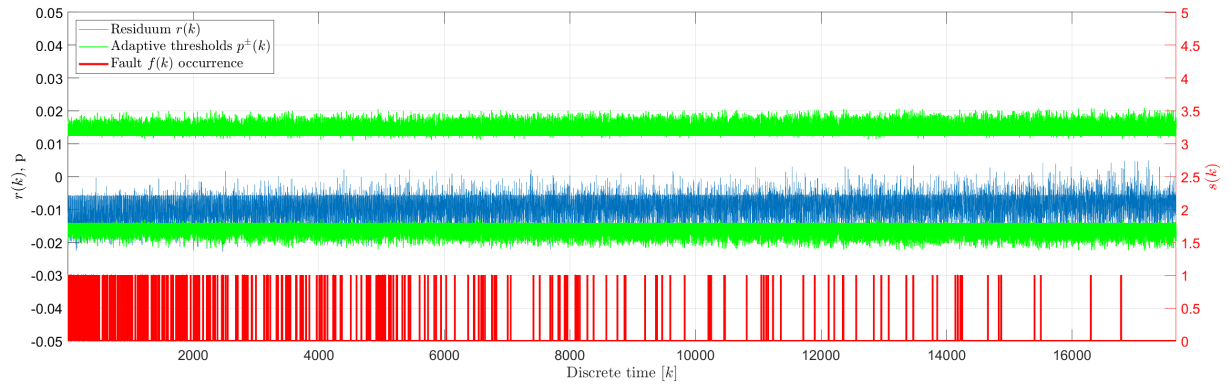


Fig. C.18. No fault 5 - scheme 2 - binary diagnostic signal $s(k)$

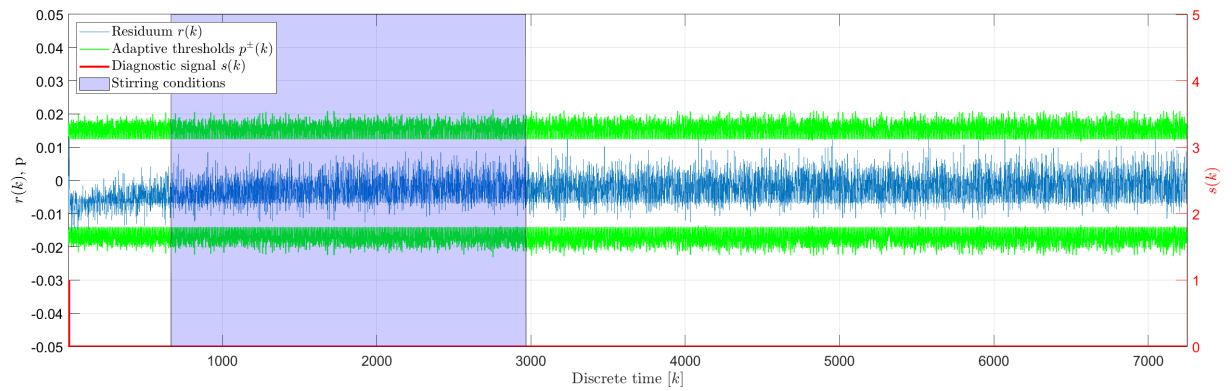


Fig. C.19. No fault 5 stirred - scheme 2 - binary diagnostic signal $s(k)$

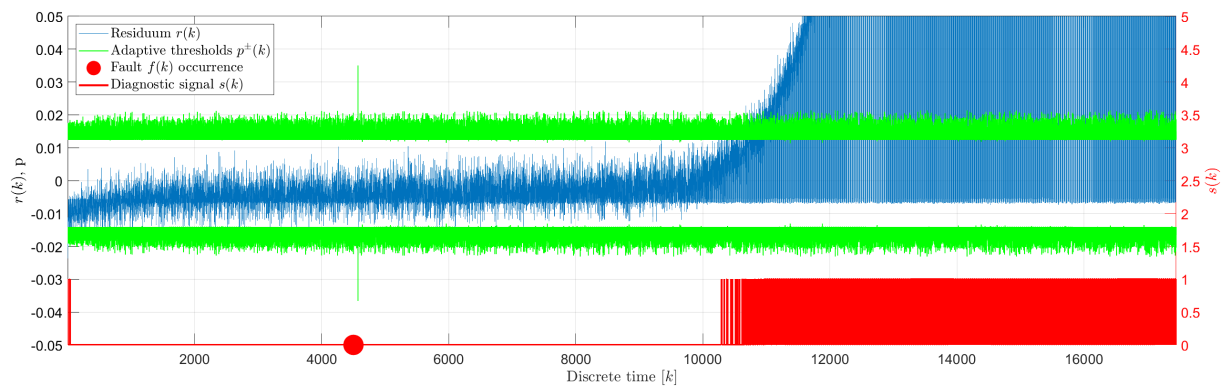


Fig. C.20. Oil leakage 1 - scheme 2 - binary diagnostic signal $s(k)$

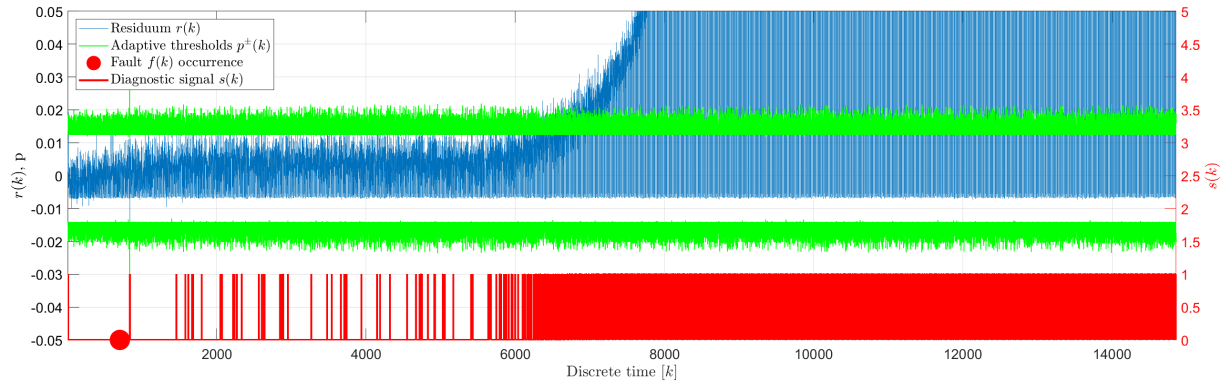


Fig. C.21. Oil leakage 2 - scheme 2 - binary diagnostic signal $s(k)$

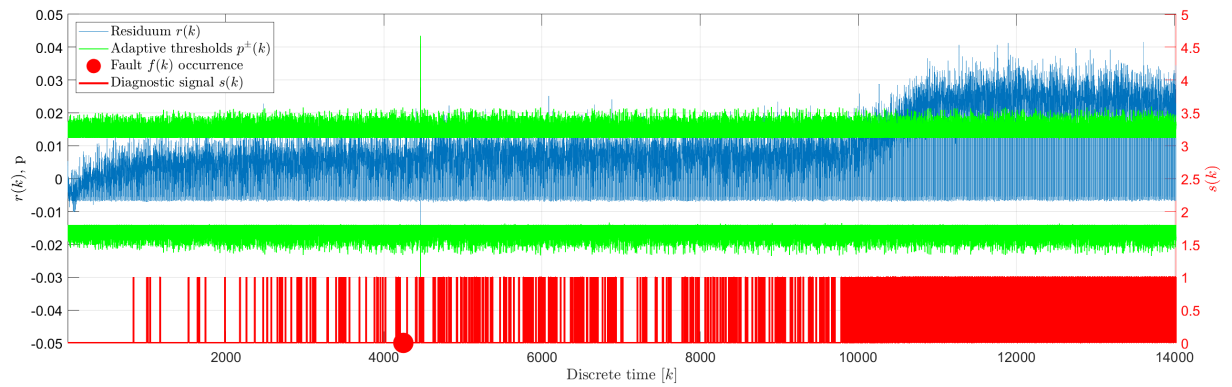


Fig. C.22. Oil leakage 3 - scheme 2 - binary diagnostic signal $s(k)$

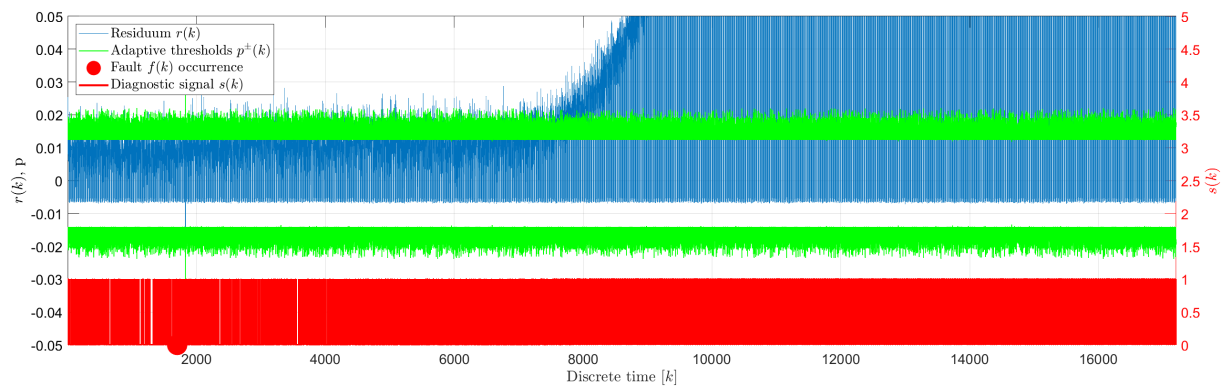


Fig. C.23. Oil leakage 4 - scheme 2 - binary diagnostic signal $s(k)$

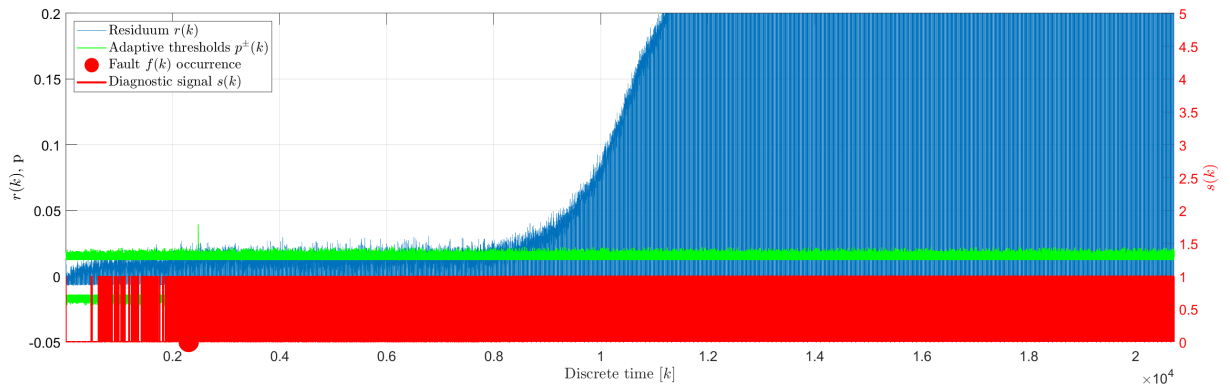


Fig. C.24. Oil leakage 5 - scheme 2 - binary diagnostic signal $s(k)$

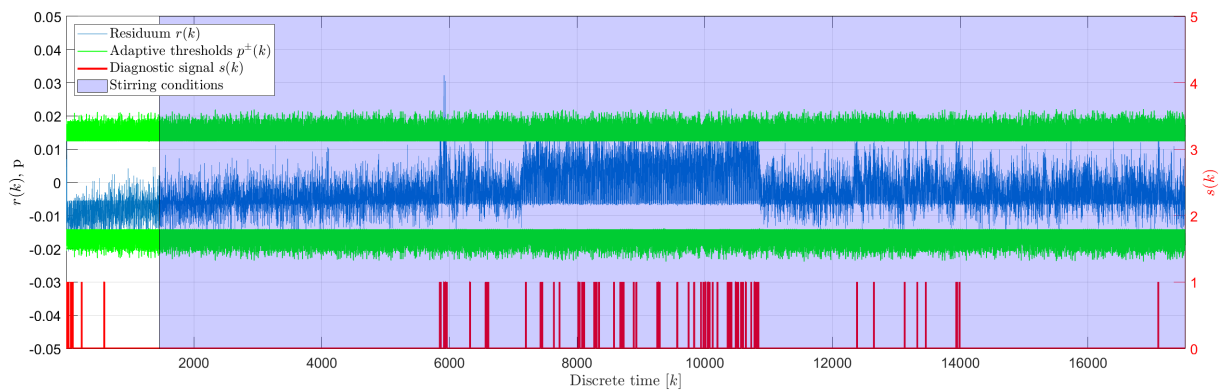


Fig. C.25. Water intrusion 1 - scheme 2 - binary diagnostic signal $s(k)$

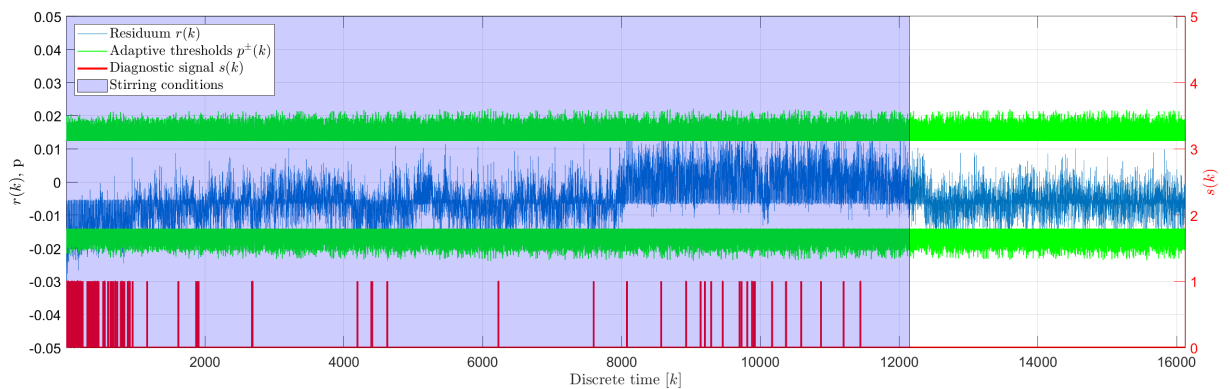


Fig. C.26. Water intrusion 2 - scheme 2 - binary diagnostic signal $s(k)$

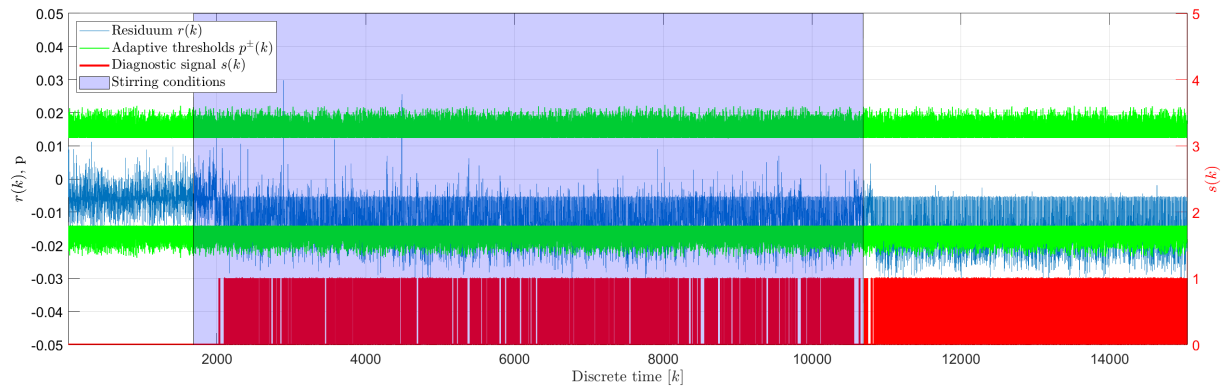


Fig. C.27. Water intrusion 3 - scheme 2 - binary diagnostic signal $s(k)$

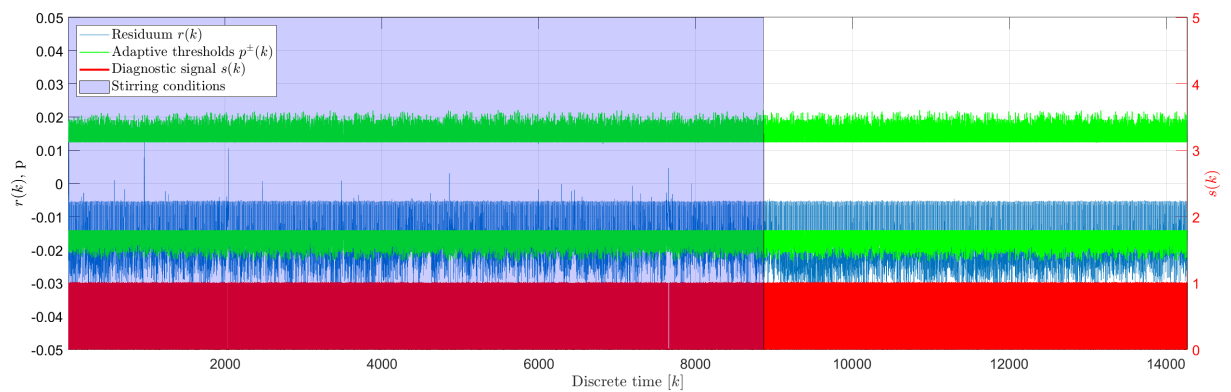


Fig. C.28. Water intrusion 4 - scheme 2 - binary diagnostic signal $s(k)$

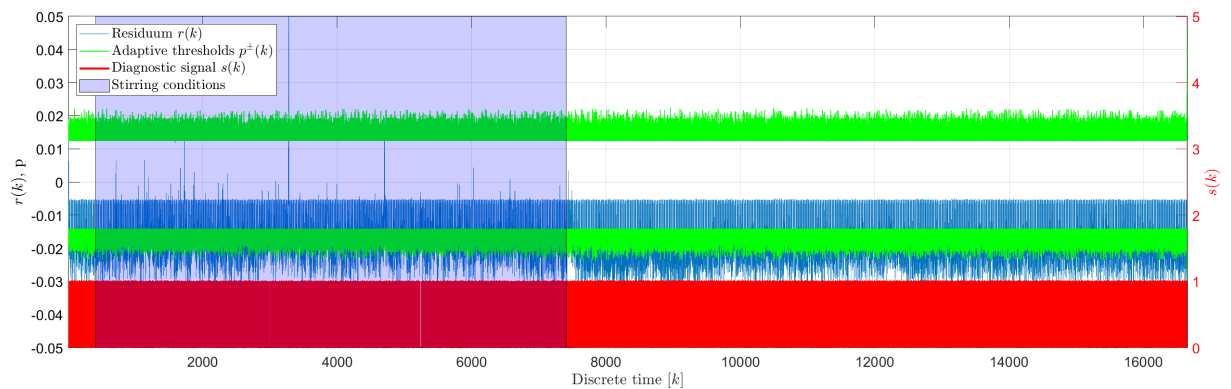


Fig. C.29. Water intrusion 5 - scheme 2 - binary diagnostic signal $s(k)$

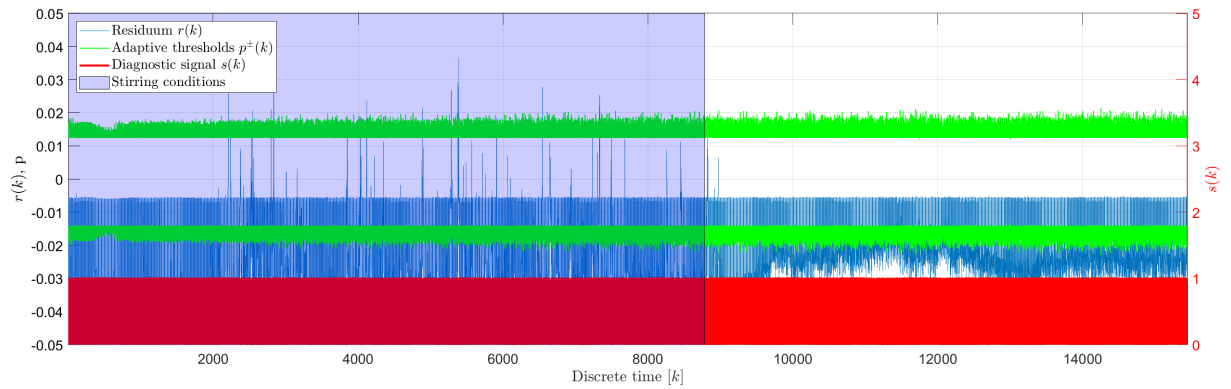


Fig. C.30. Water intrusion 6 - scheme 2 - binary diagnostic signal $s(k)$

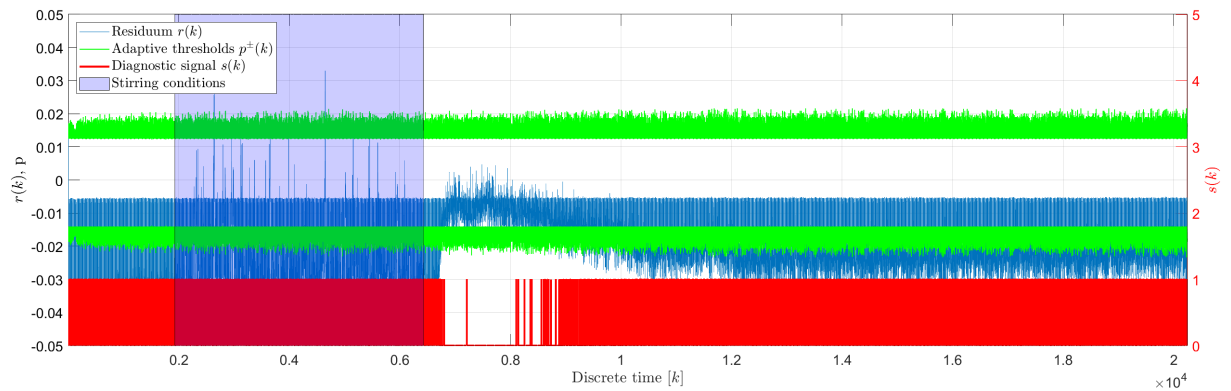


Fig. C.31. Water intrusion 7 - scheme 2 - binary diagnostic signal $s(k)$

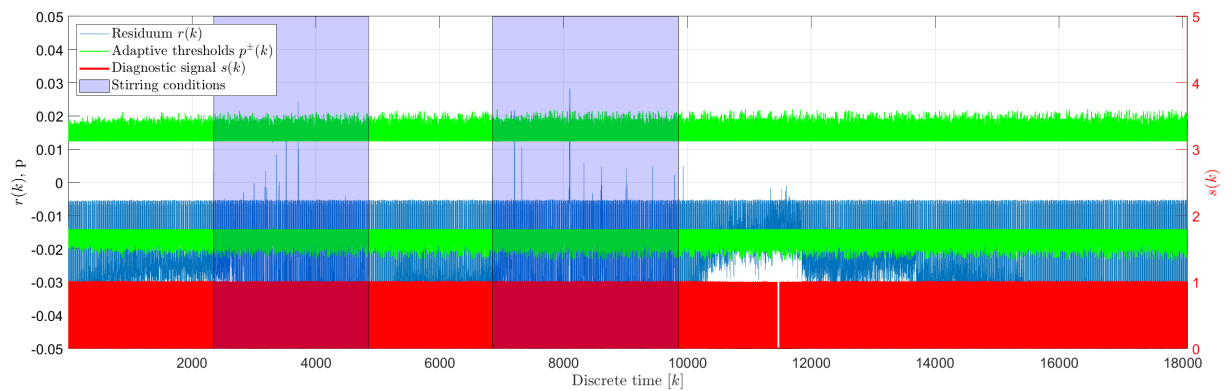


Fig. C.32. Water intrusion 8 - scheme 2 - binary diagnostic signal $s(k)$

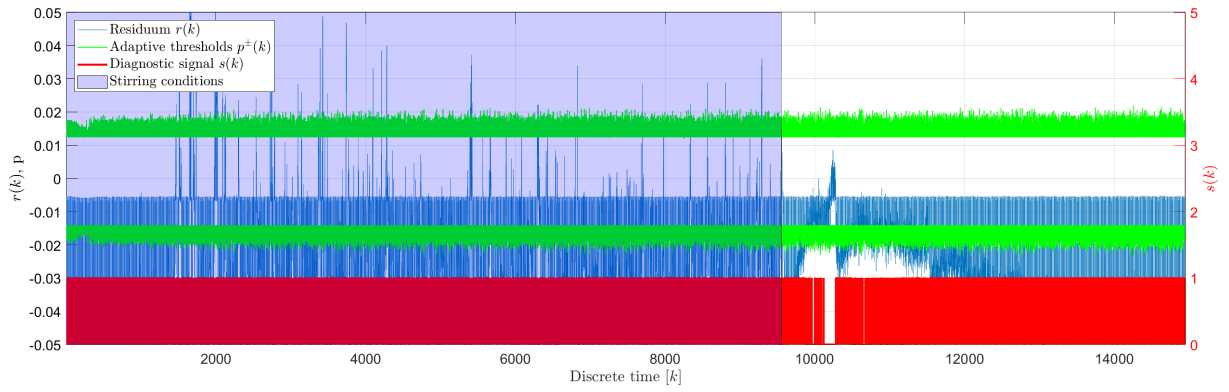


Fig. C.33. Water intrusion 9 - scheme 2 - binary diagnostic signal $s(k)$

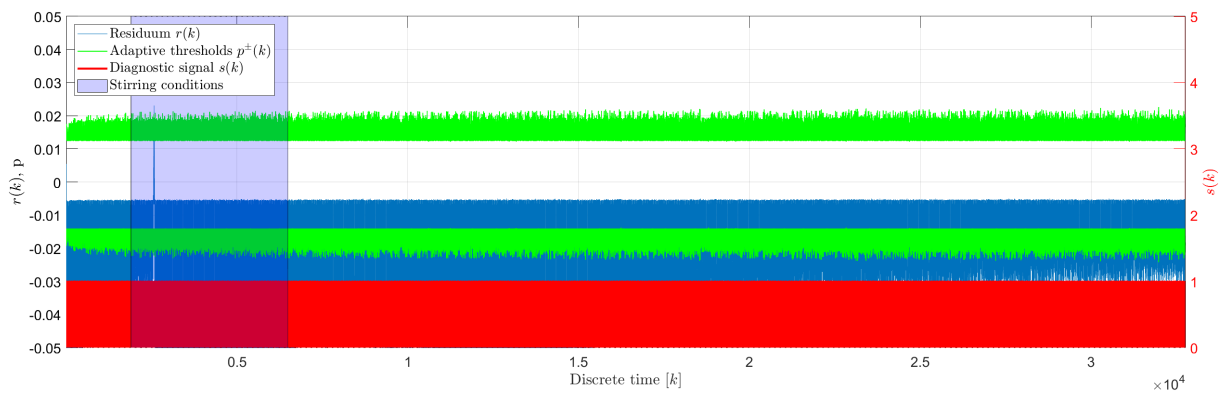


Fig. C.34. Water intrusion 10 - scheme 2 - binary diagnostic signal $s(k)$

D. Comprehensive tests under road conditions - datasets

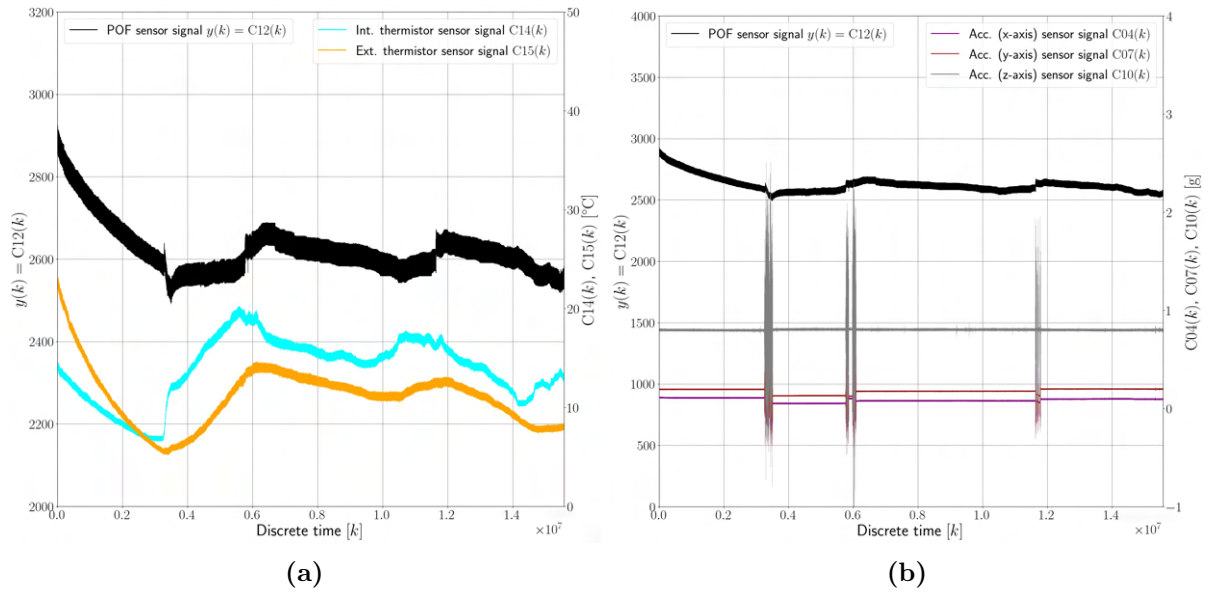


Fig. D.1. No fault 0 - observed POF sensor signal $y(k)$ versus: a) temperature, b) accelerations

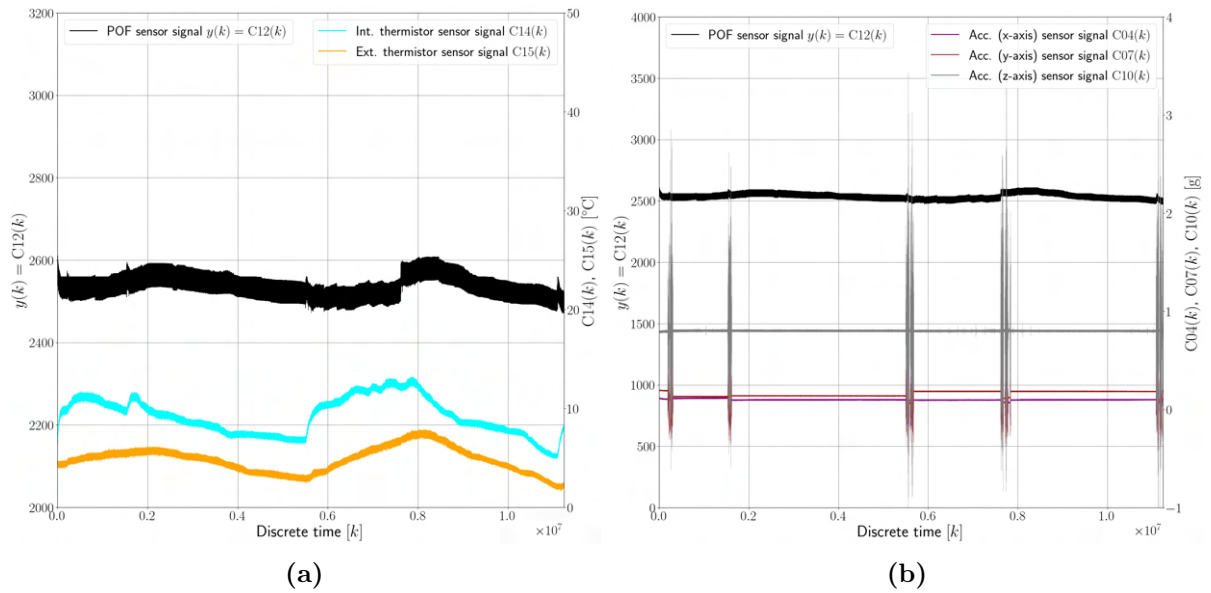


Fig. D.2. No fault 1 - observed POF sensor signal $y(k)$ versus: a) temperature, b) accelerations

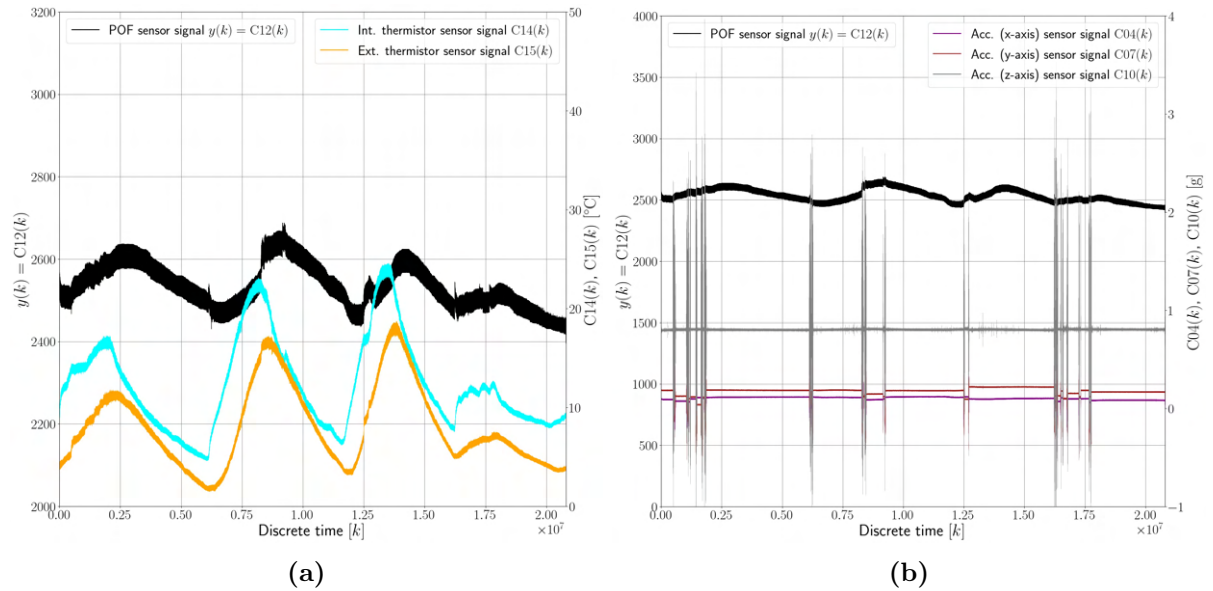


Fig. D.3. No fault 2 - observed POF sensor signal $y(k)$ versus: a) temperature, b) accelerations

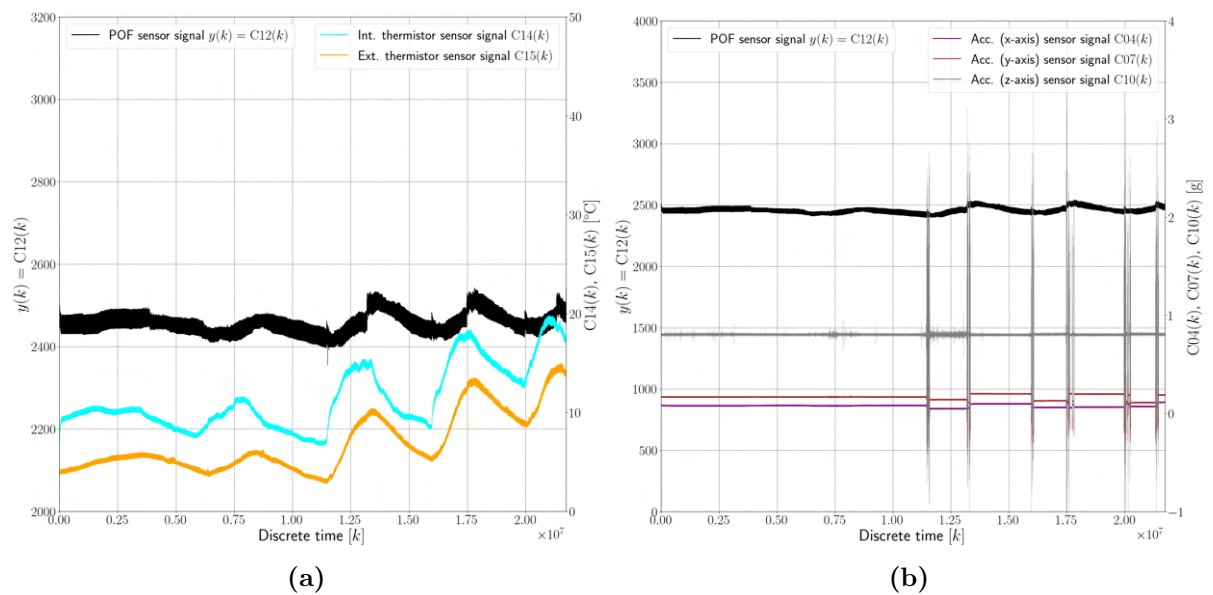


Fig. D.4. No fault 3 - observed POF sensor signal $y(k)$ versus: a) temperature, b) accelerations

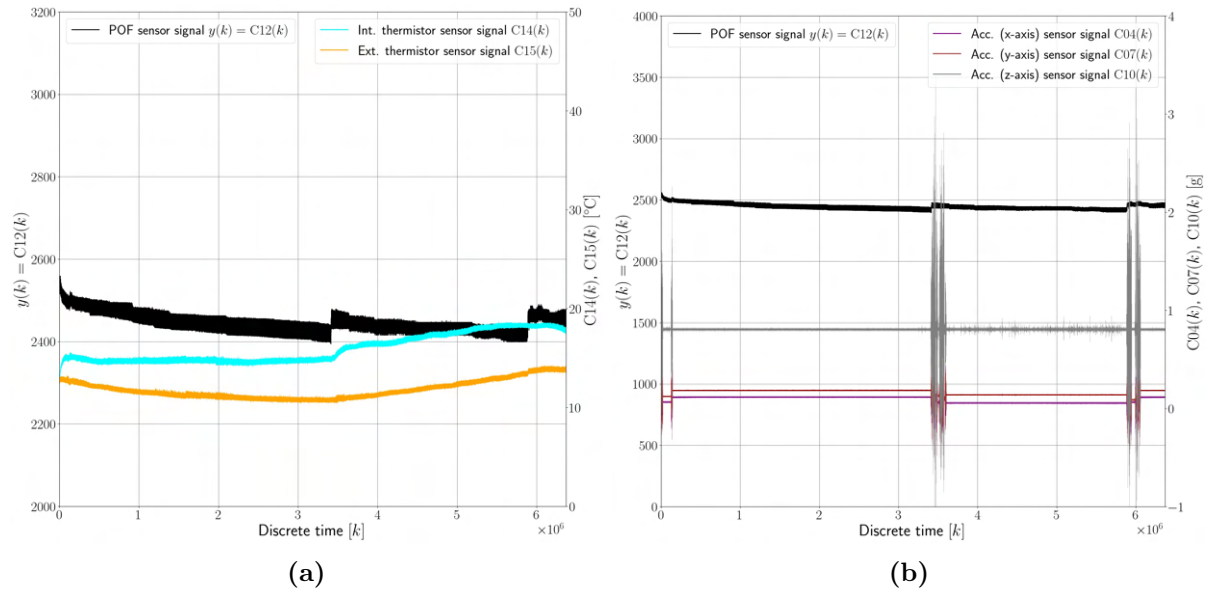


Fig. D.5. No fault 4 - observed POF sensor signal $y(k)$ versus: a) temperature, b) accelerations

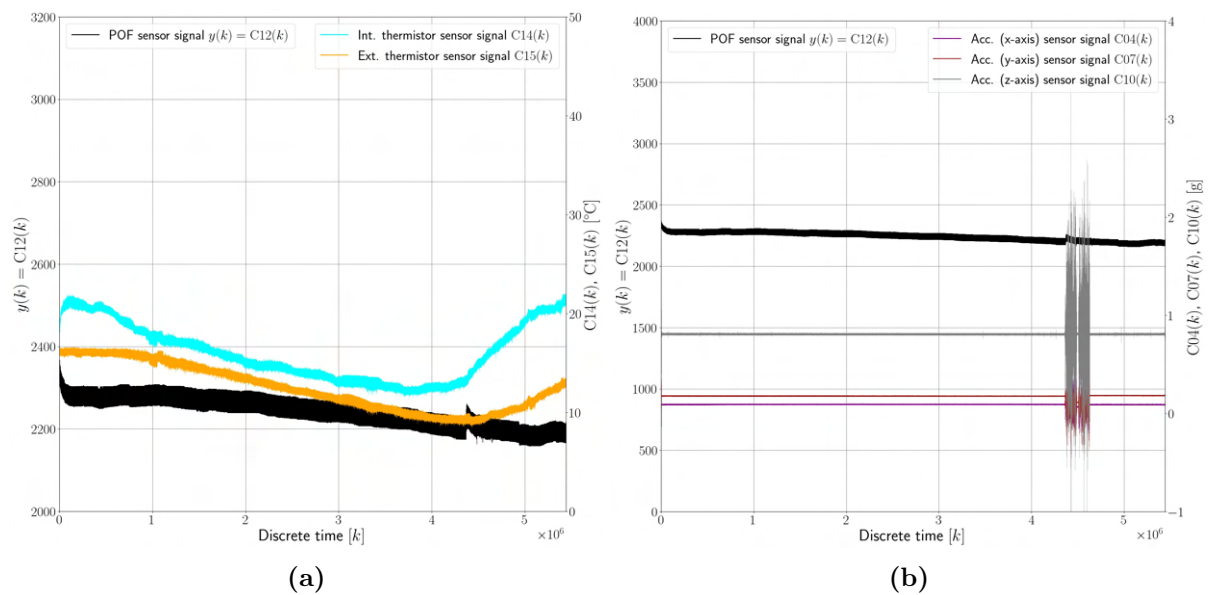


Fig. D.6. No fault 5 - observed POF sensor signal $y(k)$ versus: a) temperature, b) accelerations

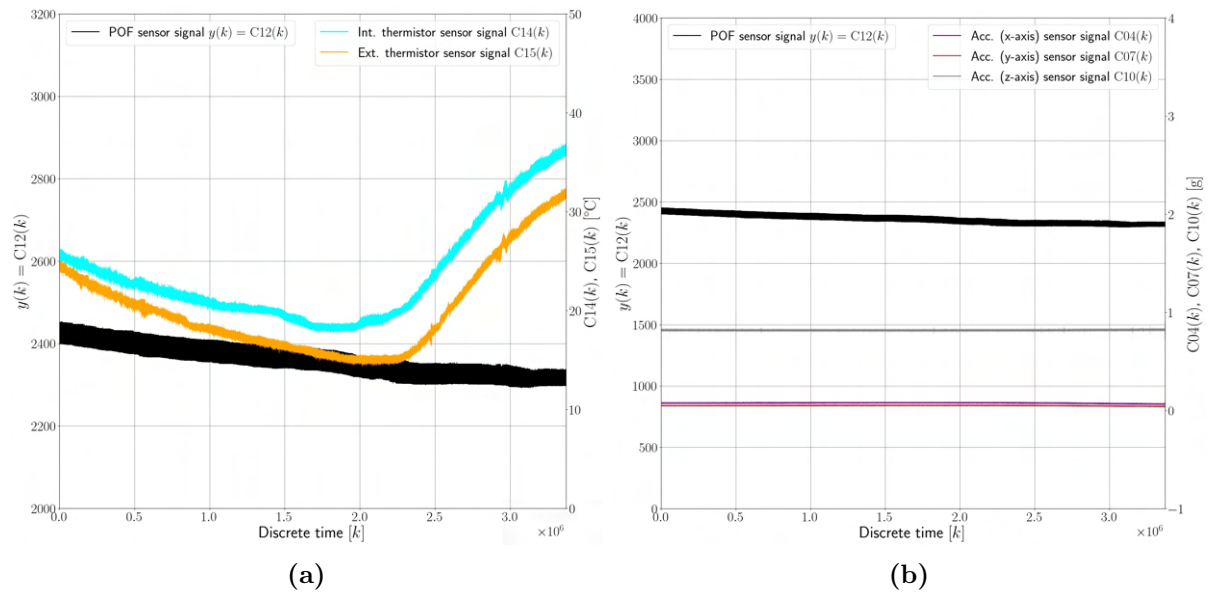


Fig. D.7. No fault 6 - observed POF sensor signal $y(k)$ versus: a) temperature, b) accelerations

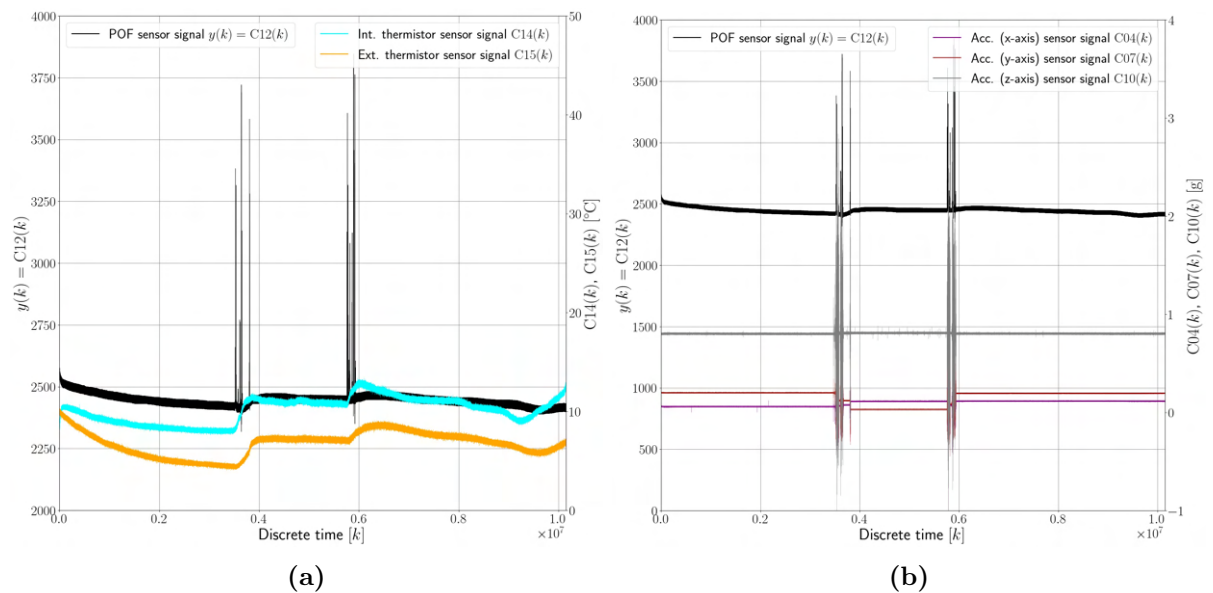


Fig. D.8. Oil leakage 1 - observed POF sensor signal $y(k)$ versus: a) temperature, b) accelerations

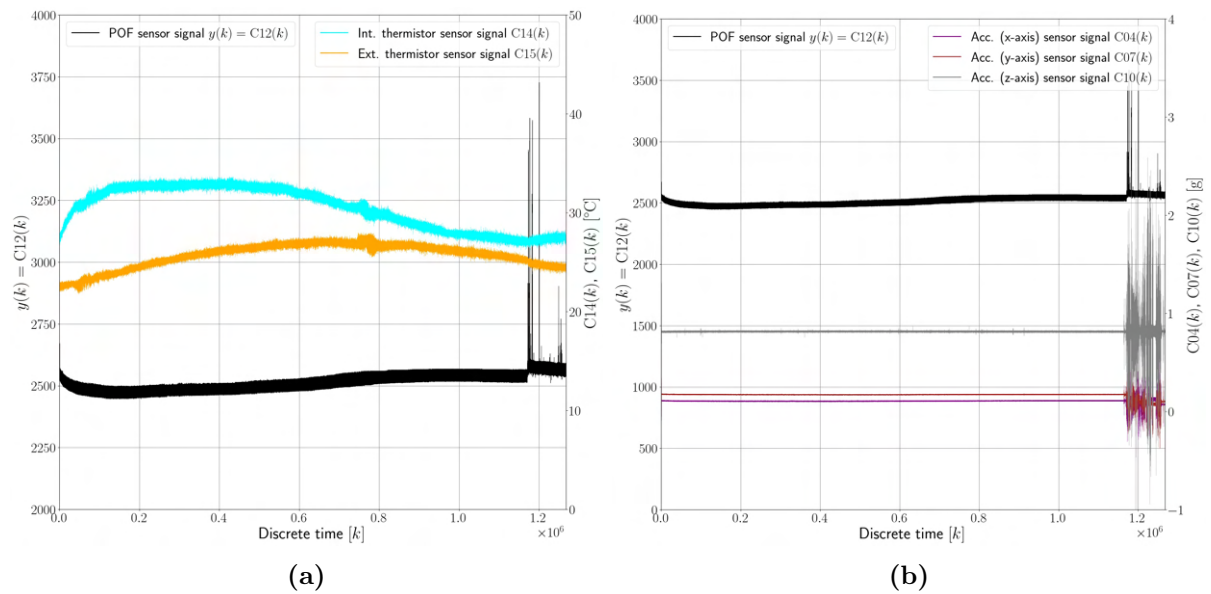


Fig. D.9. Oil leakage 2 - observed POF sensor signal $y(k)$ versus: a) temperature, b) accelerations

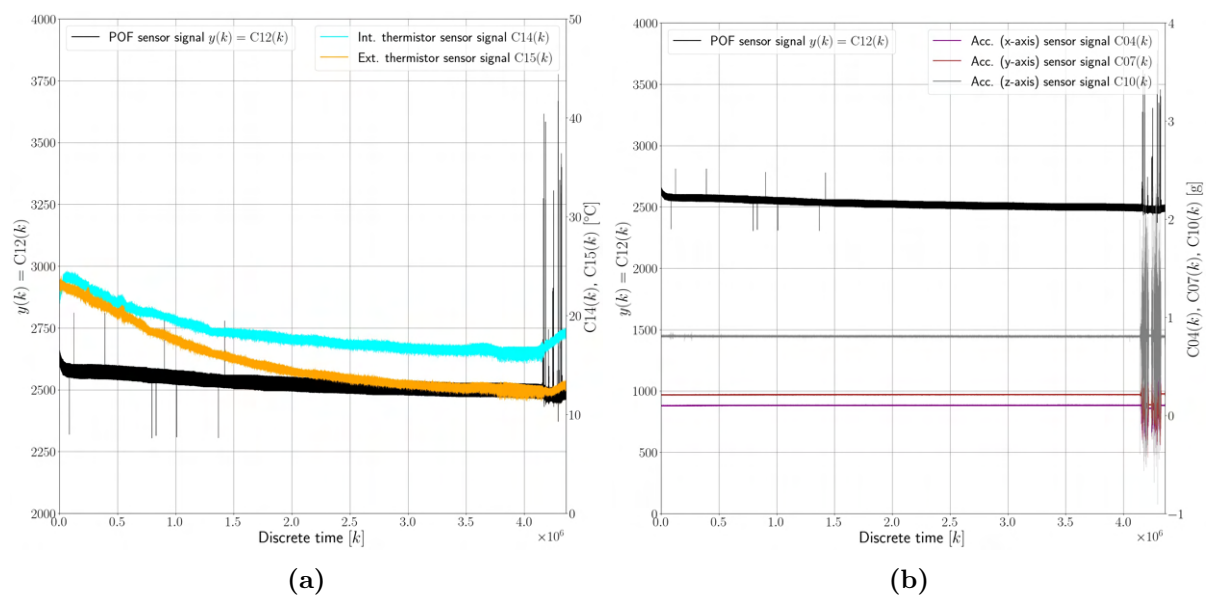


Fig. D.10. Oil leakage 3 - observed POF sensor signal $y(k)$ versus: a) temperature, b) accelerations

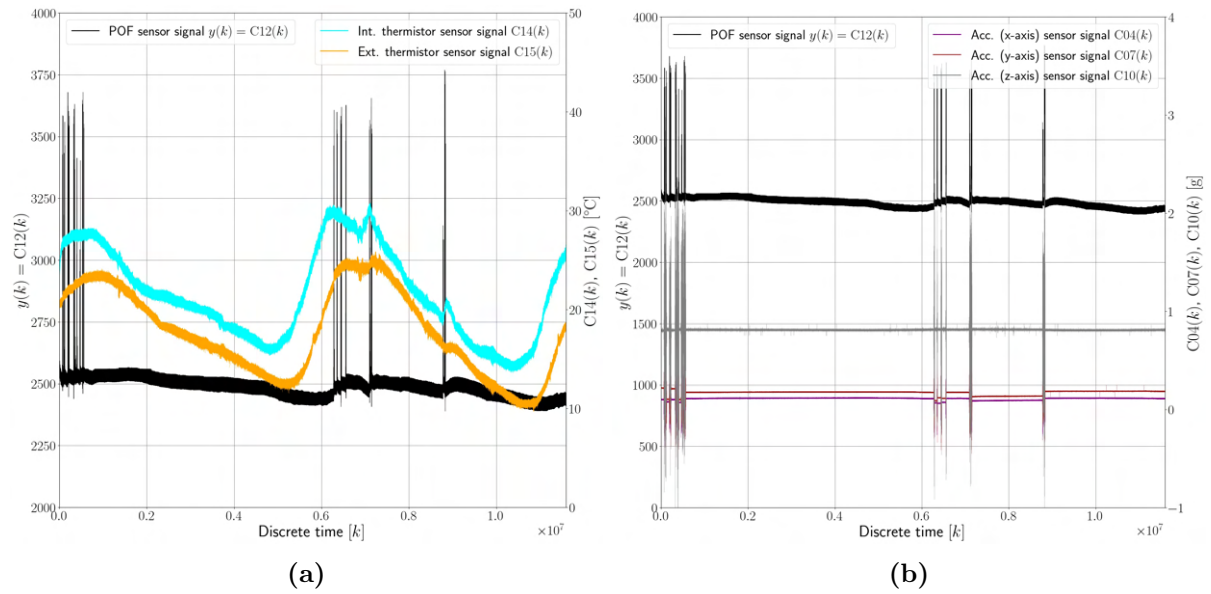


Fig. D.11. Oil leakage 4 - observed POF sensor signal $y(k)$ versus: a) temperature, b) accelerations

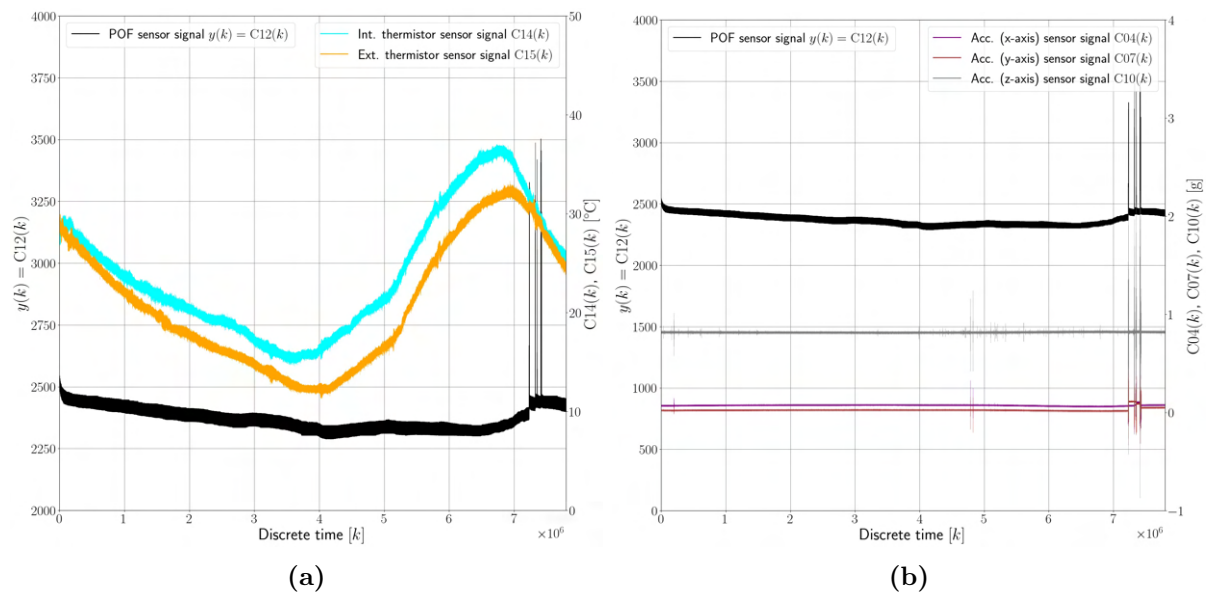


Fig. D.12. Oil leakage 5 - observed POF sensor signal $y(k)$ versus: a) temperature, b) accelerations

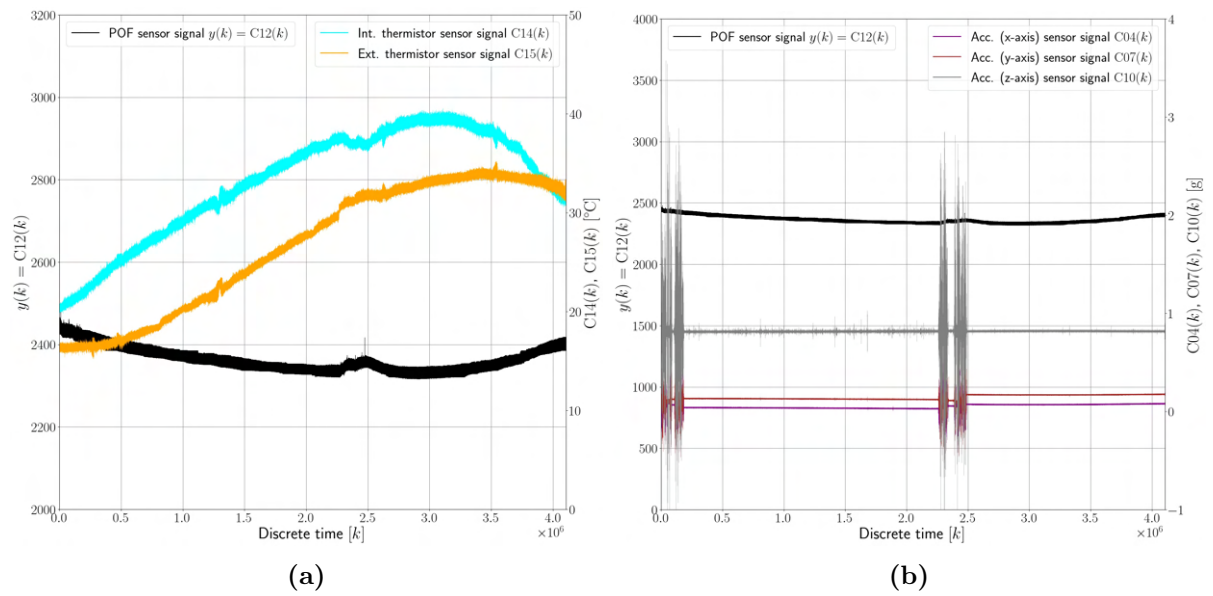


Fig. D.13. Water intrusion 1 - observed POF sensor signal $y(k)$ versus: a) temperature, b) accelerations

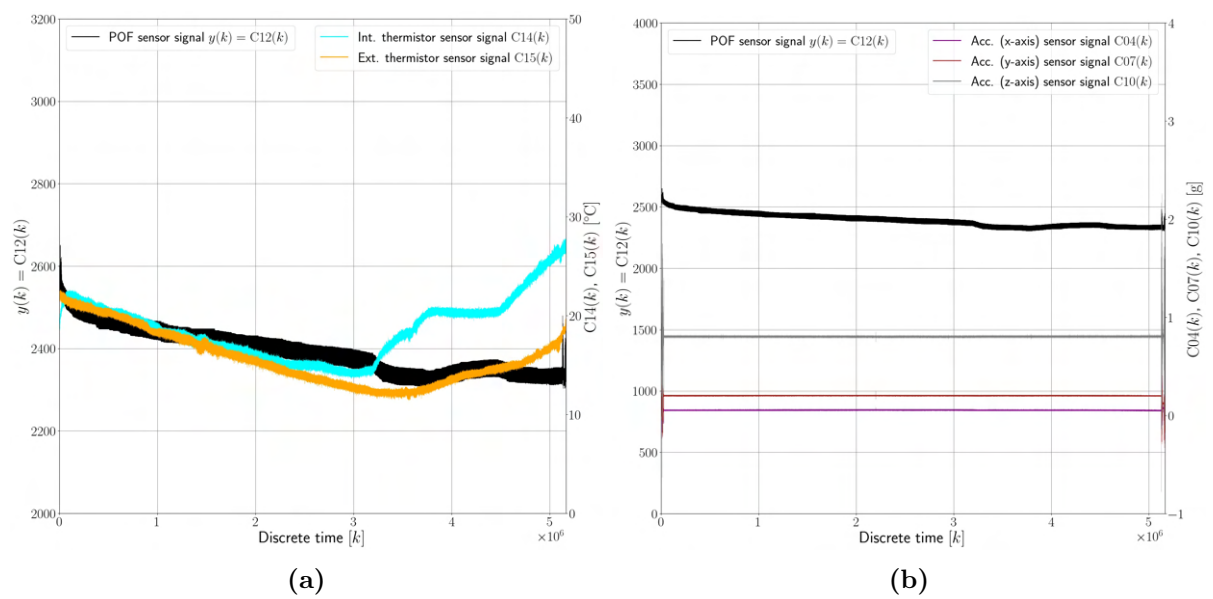


Fig. D.14. Water intrusion 2 - observed POF sensor signal $y(k)$ versus: a) temperature, b) accelerations

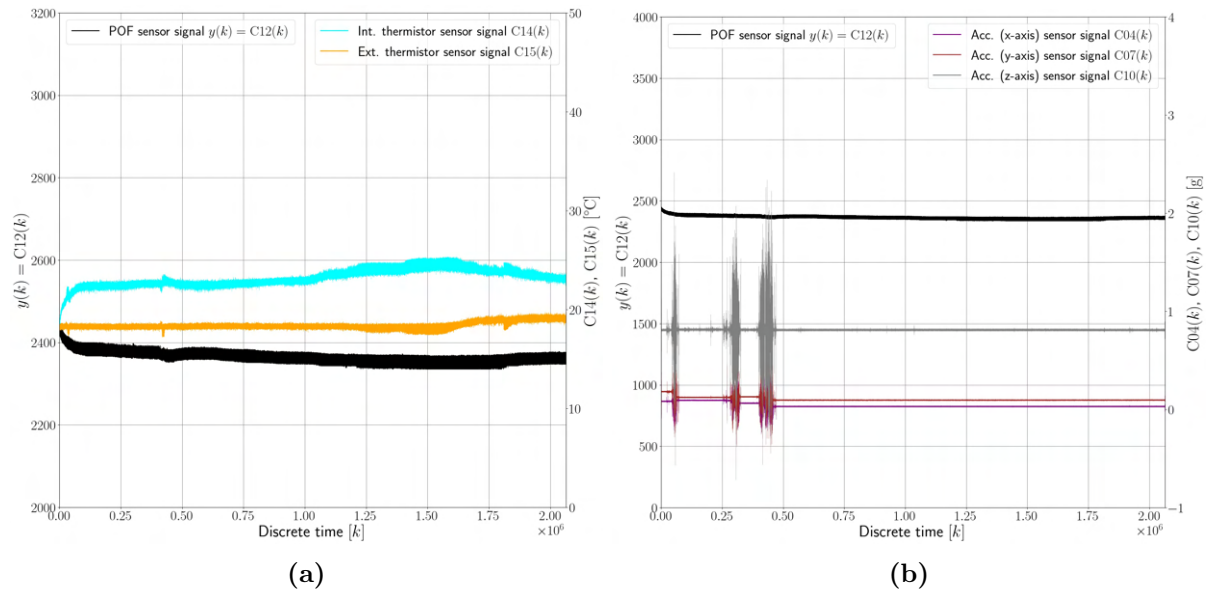


Fig. D.15. Water intrusion 3 - observed POF sensor signal $y(k)$ versus: a) temperature, b) accelerations

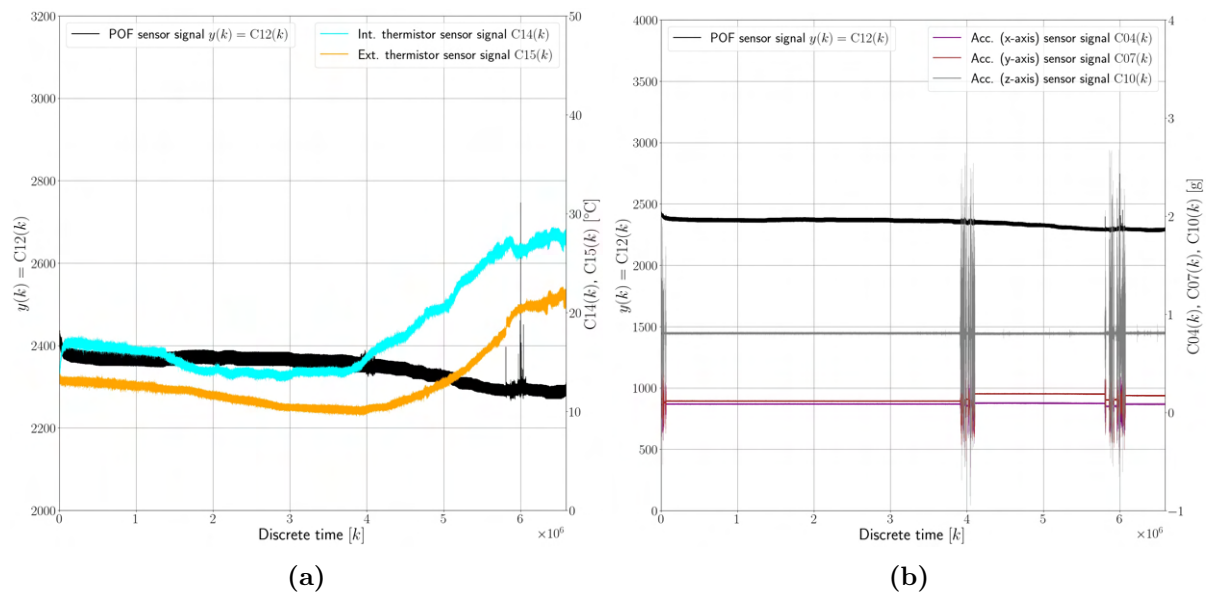


Fig. D.16. Water intrusion 4 - observed POF sensor signal $y(k)$ versus: a) temperature, b) accelerations

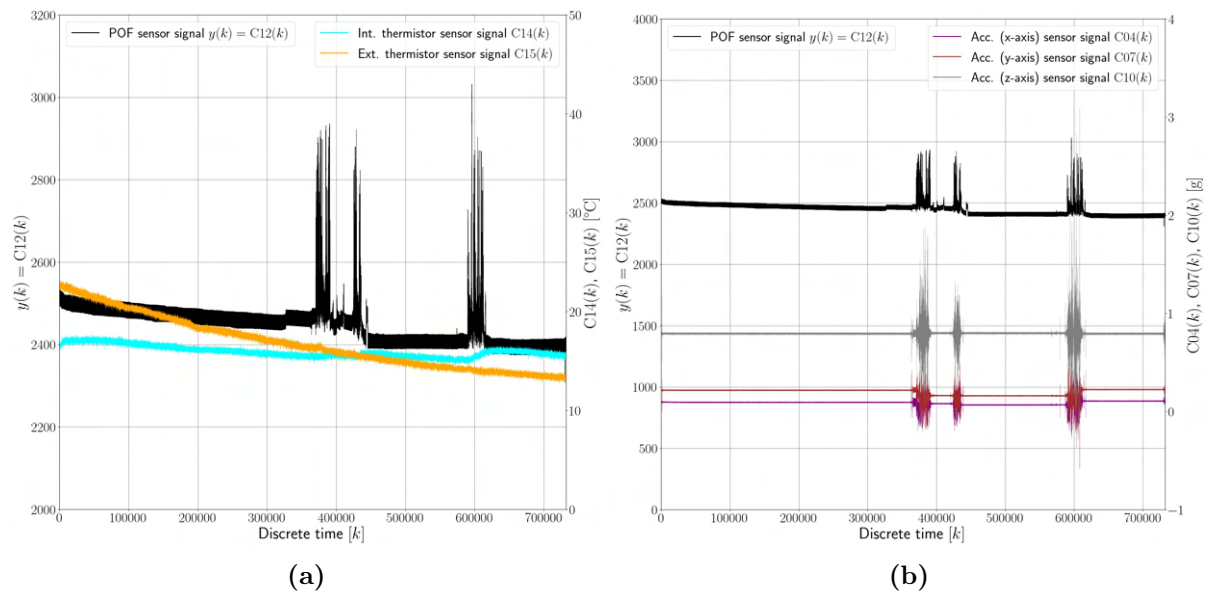


Fig. D.17. Water intrusion 5 - observed POF sensor signal $y(k)$ versus: a) temperature, b) accelerations

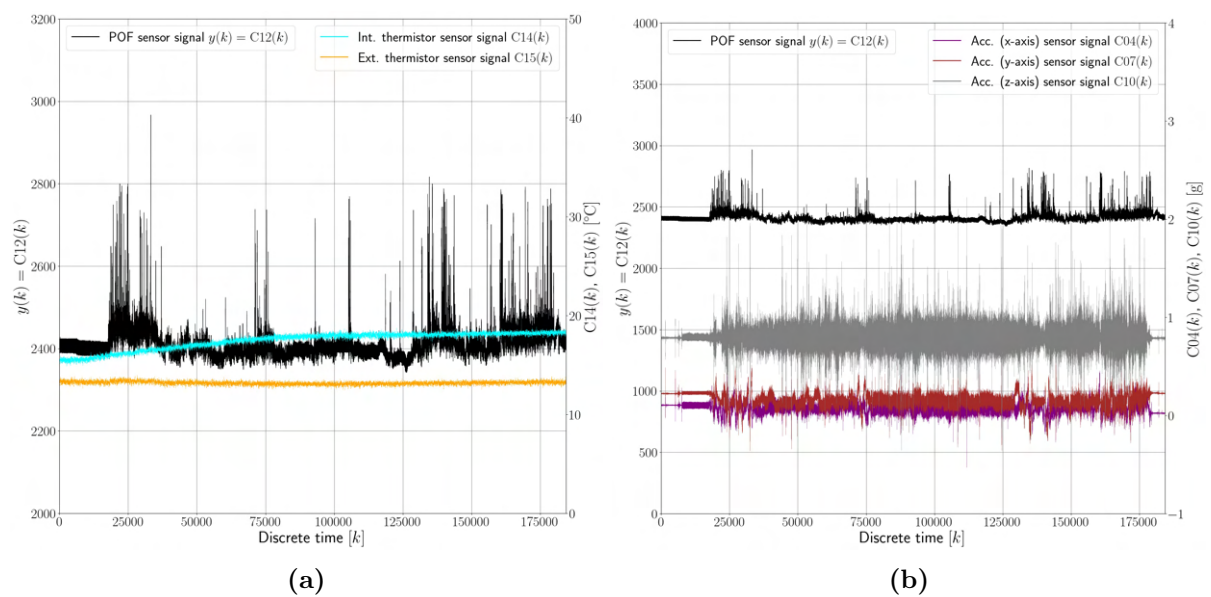


Fig. D.18. Water intrusion 6 - observed POF sensor signal $y(k)$ versus: a) temperature, b) accelerations

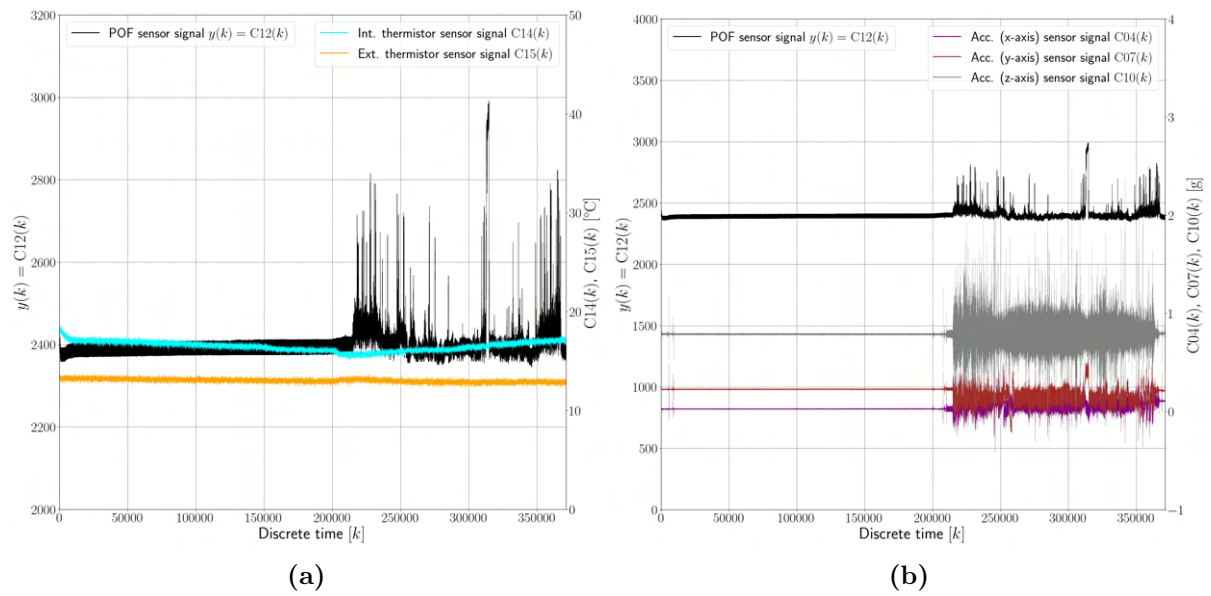


Fig. D.19. Water intrusion 7 - observed POF sensor signal $y(k)$ versus: a) temperature, b) accelerations

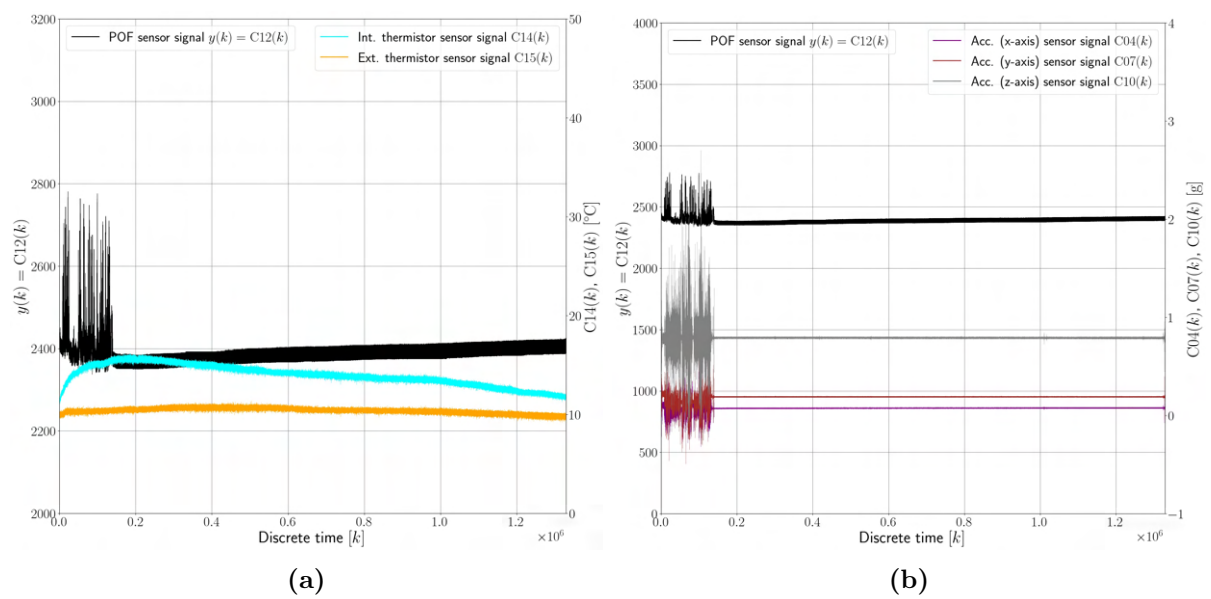


Fig. D.20. Water intrusion 8 - observed POF sensor signal $y(k)$ versus: a) temperature, b) accelerations

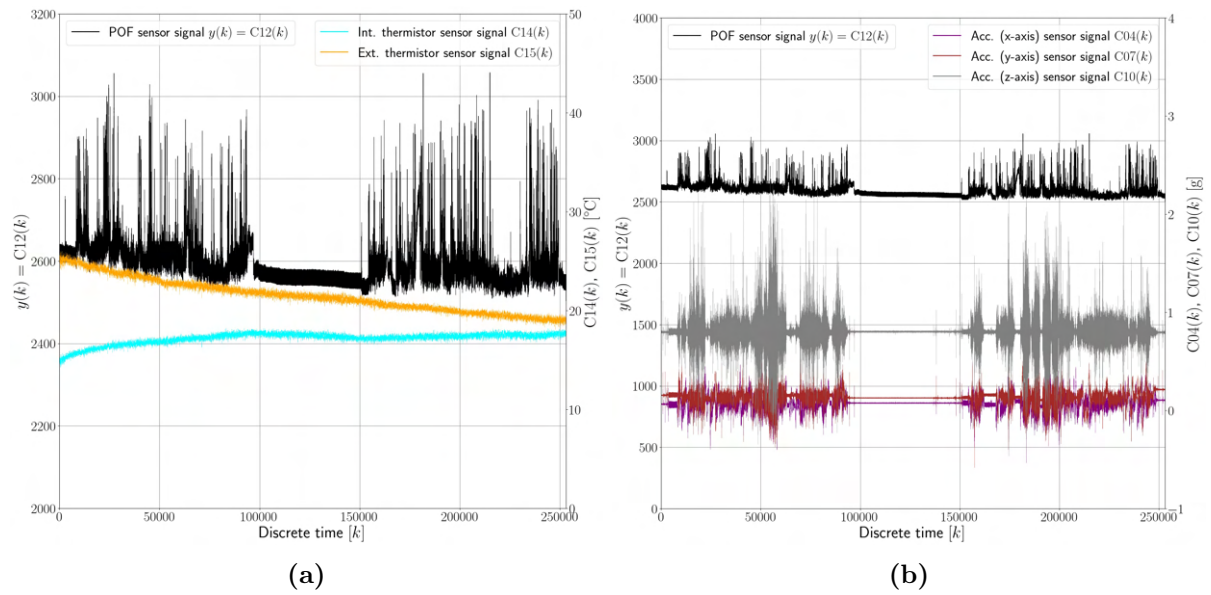


Fig. D.21. Water intrusion 9 - observed POF sensor signal $y(k)$ versus: a) temperature, b) accelerations

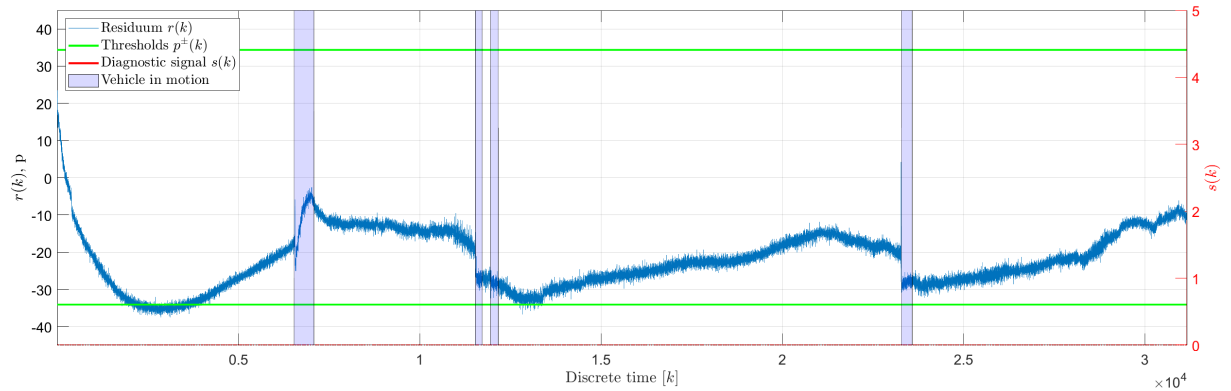


Fig. D.22. No fault 0 - binary diagnostic signal $s(k)$

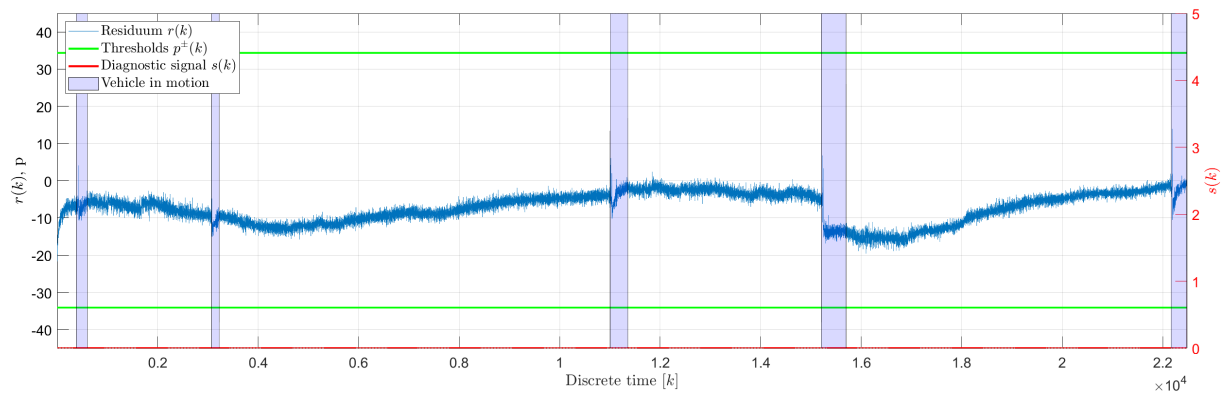


Fig. D.23. No fault 1 - binary diagnostic signal $s(k)$

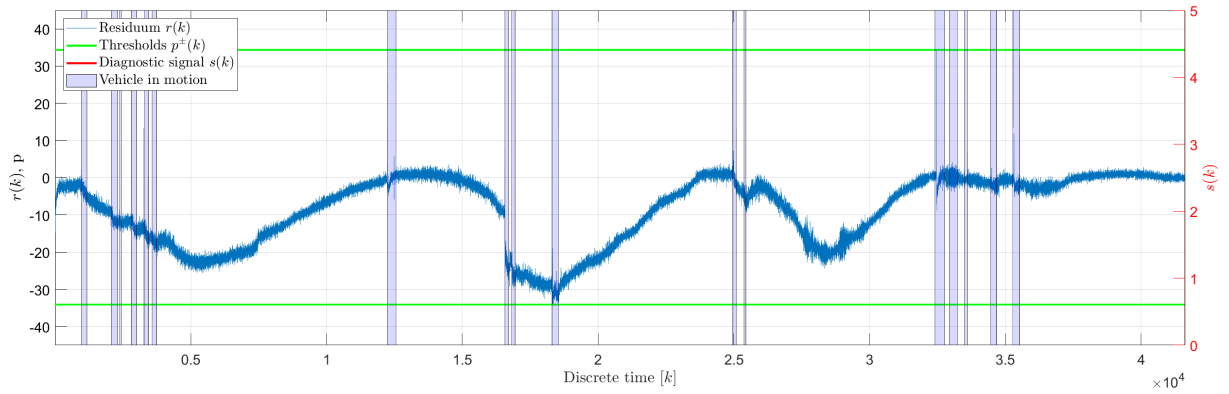


Fig. D.24. No fault 2 - binary diagnostic signal $s(k)$

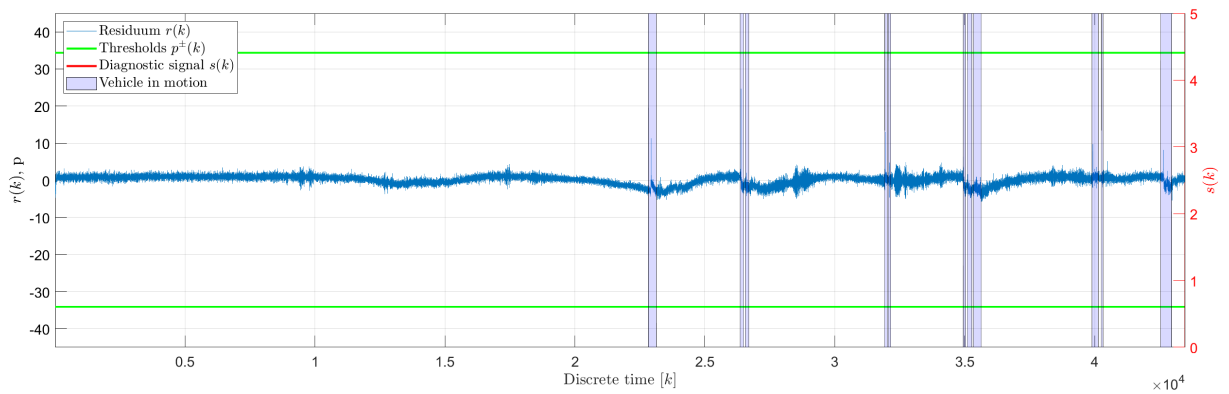


Fig. D.25. No fault 3 - binary diagnostic signal $s(k)$

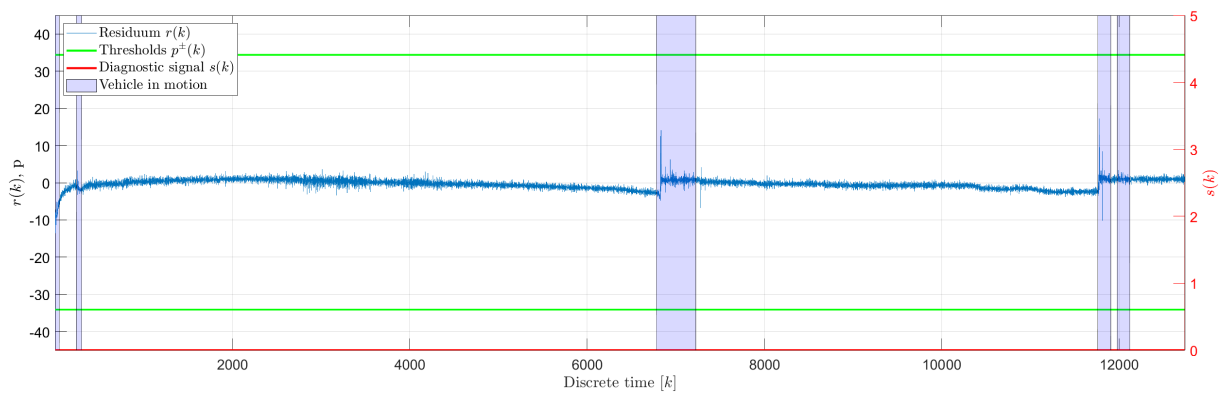


Fig. D.26. No fault 4 - binary diagnostic signal $s(k)$

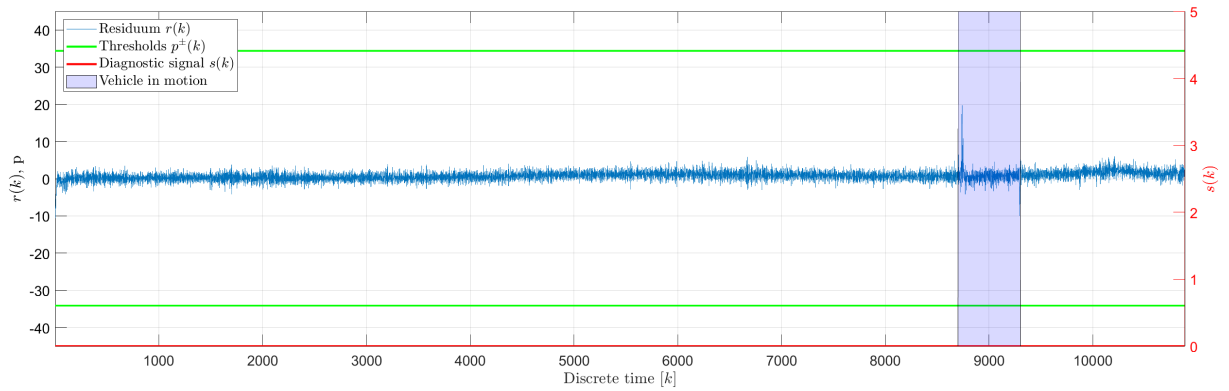


Fig. D.27. No fault 5 - binary diagnostic signal $s(k)$

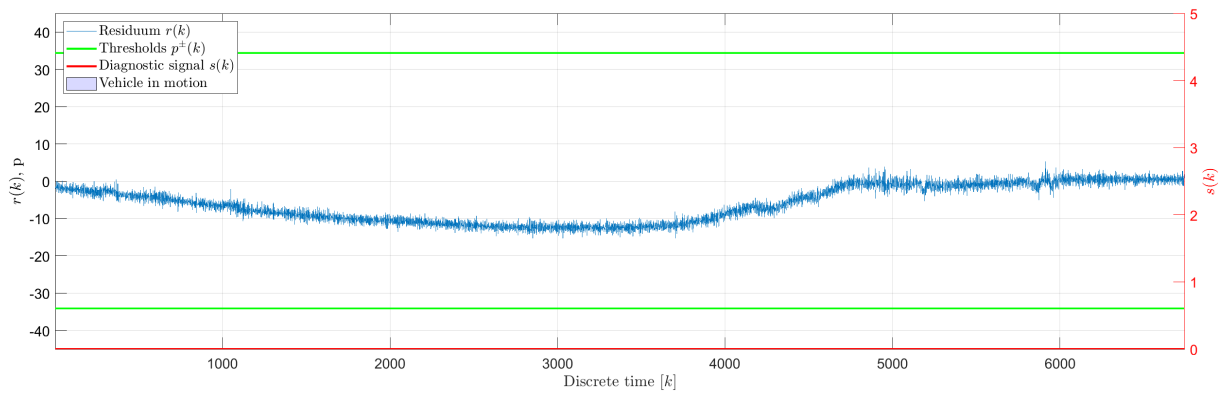


Fig. D.28. No fault 6 - binary diagnostic signal $s(k)$

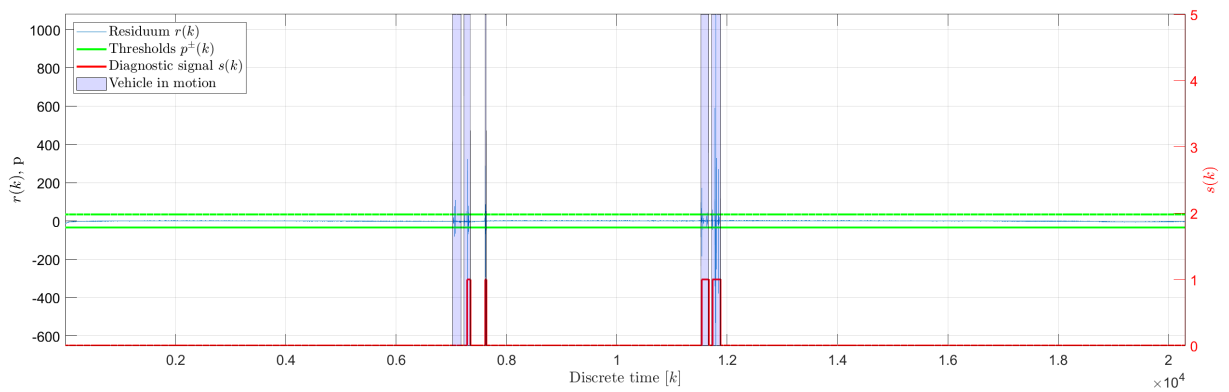


Fig. D.29. Oil leakage 1 - binary diagnostic signal $s(k)$

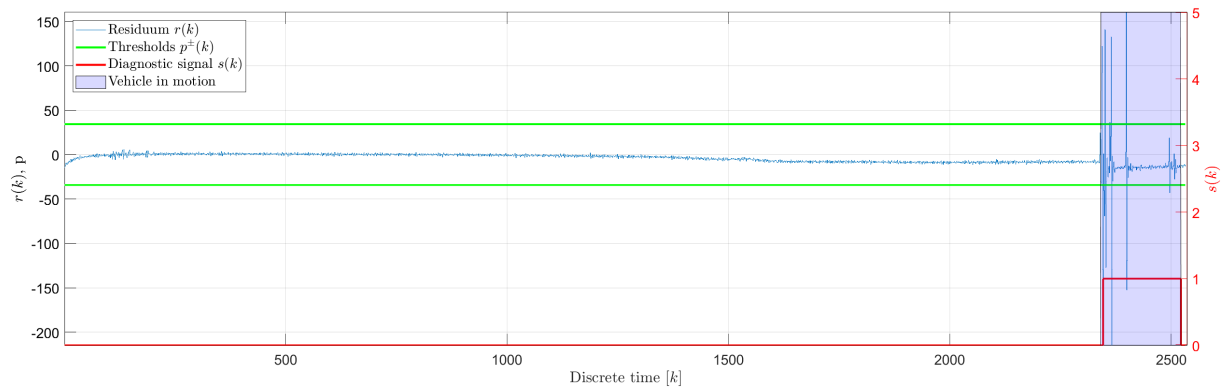


Fig. D.30. Oil leakage 2 - binary diagnostic signal $s(k)$

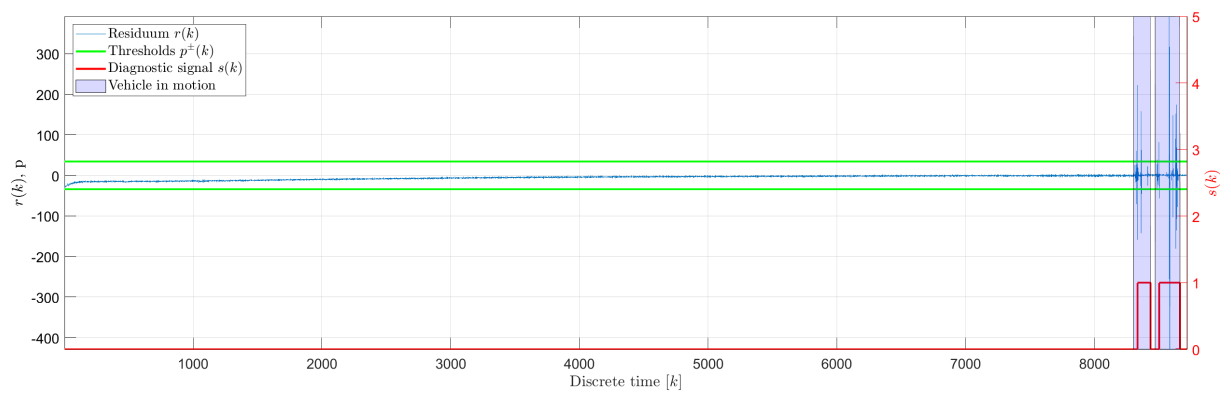


Fig. D.31. Oil leakage 3 - binary diagnostic signal $s(k)$

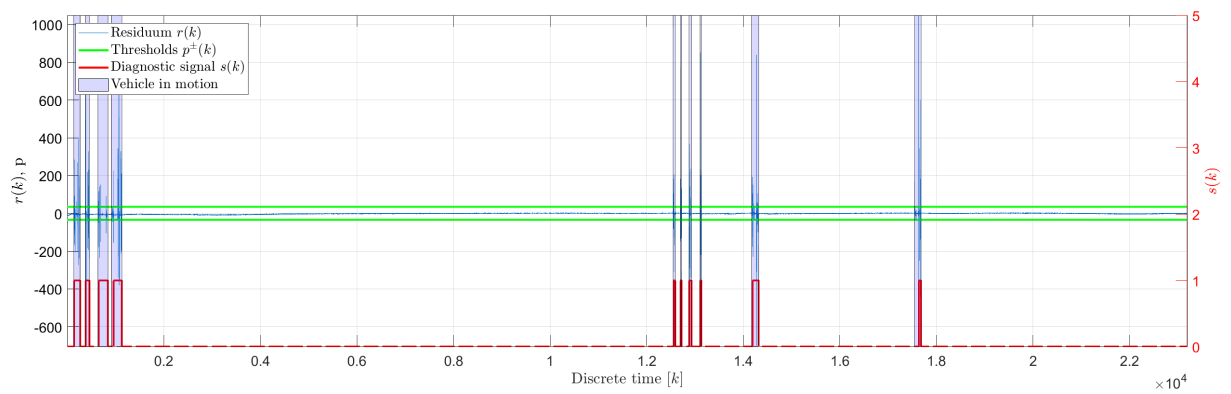


Fig. D.32. Oil leakage 4 - binary diagnostic signal $s(k)$

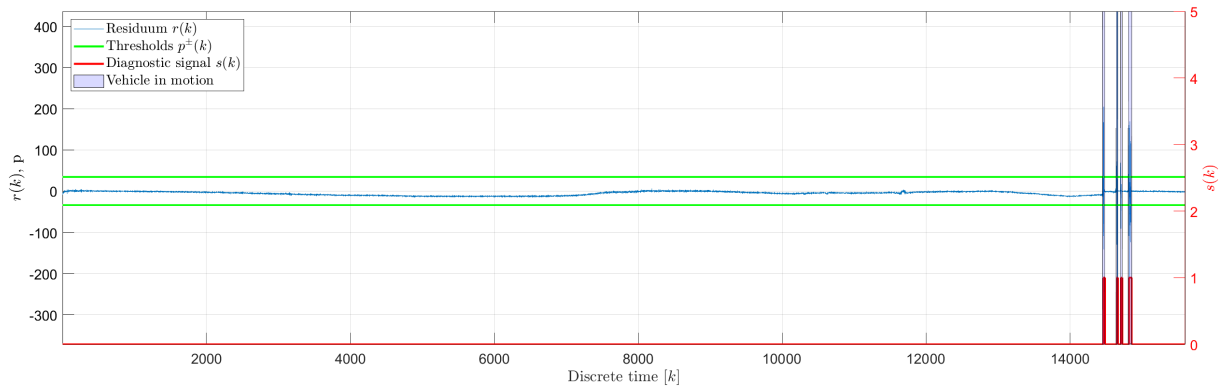


Fig. D.33. Oil leakage 5 - binary diagnostic signal $s(k)$

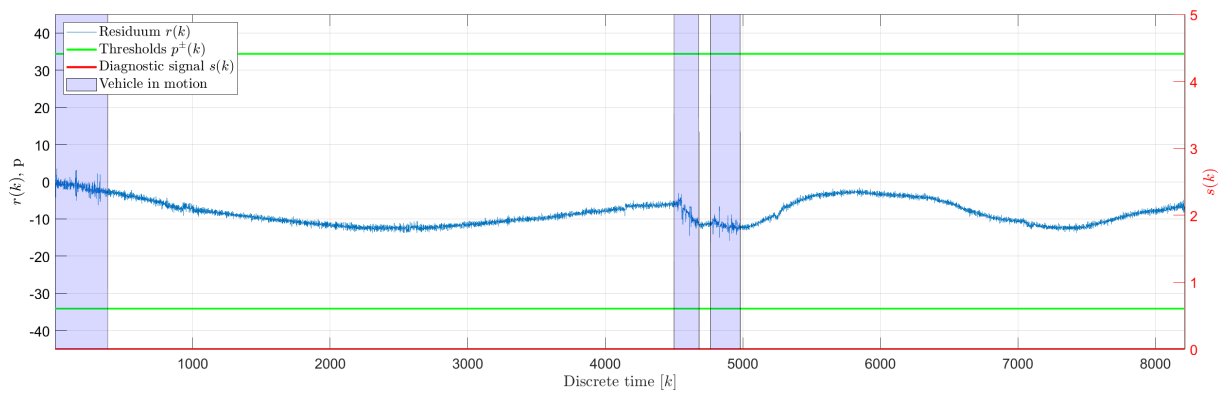


Fig. D.34. Water intrusion 1 - binary diagnostic signal $s(k)$

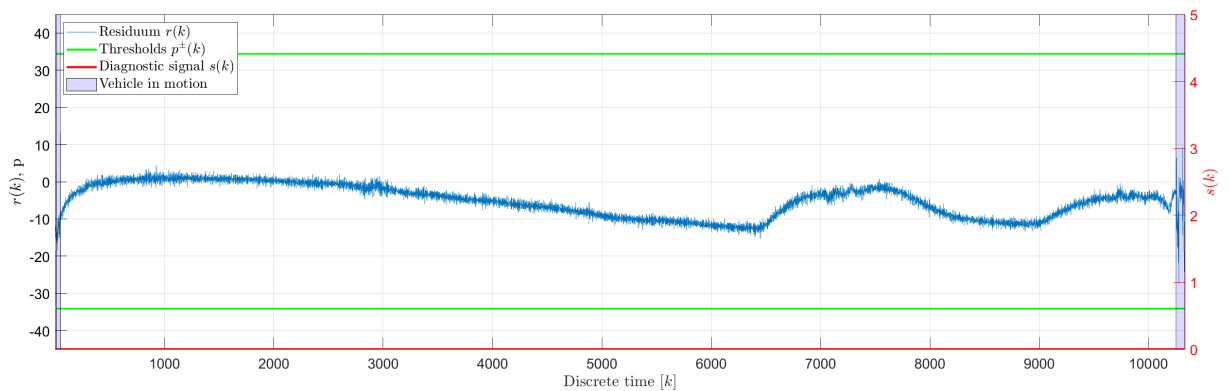


Fig. D.35. Water intrusion 2 - binary diagnostic signal $s(k)$

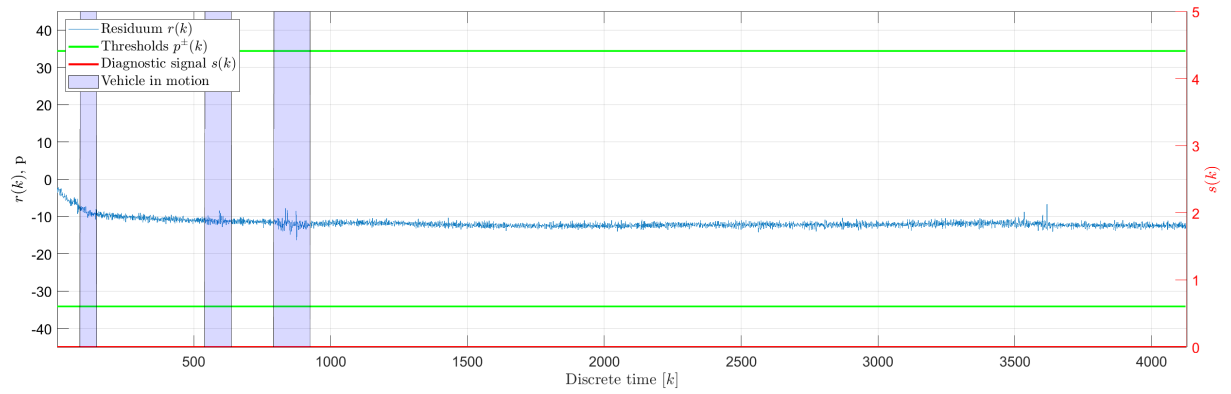


Fig. D.36. Water intrusion 3 - binary diagnostic signal $s(k)$

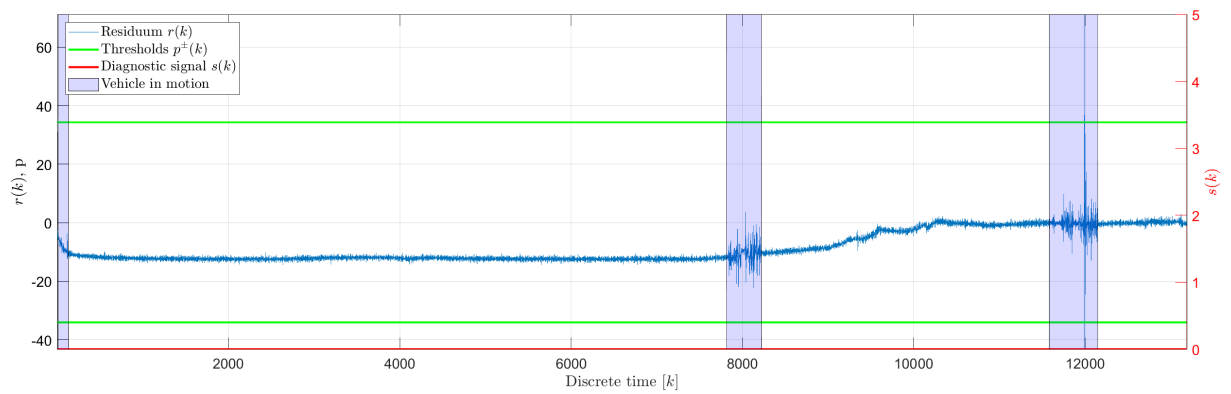


Fig. D.37. Water intrusion 4 - binary diagnostic signal $s(k)$

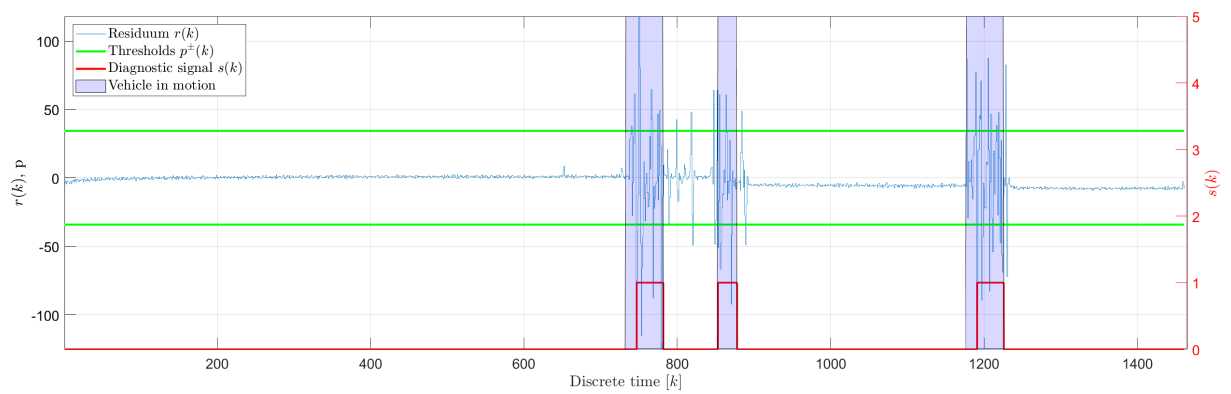


Fig. D.38. Water intrusion 5 - binary diagnostic signal $s(k)$

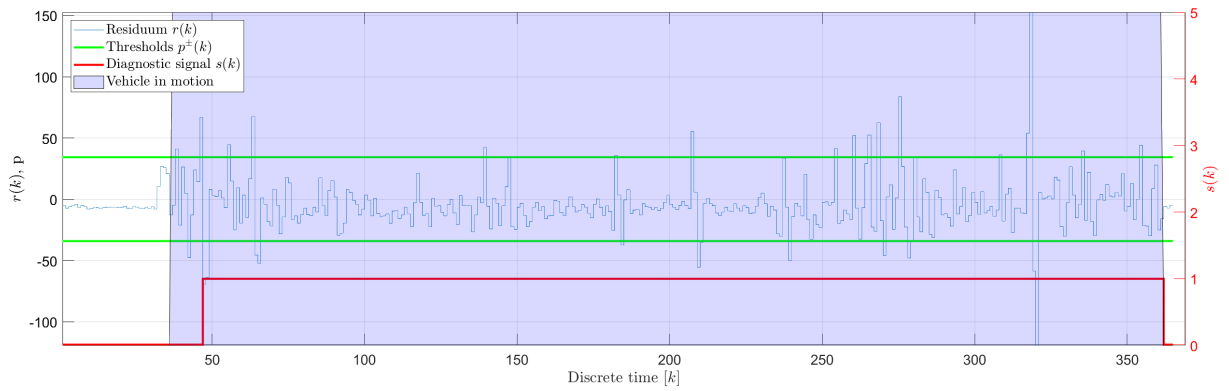


Fig. D.39. Water intrusion 6 - binary diagnostic signal $s(k)$

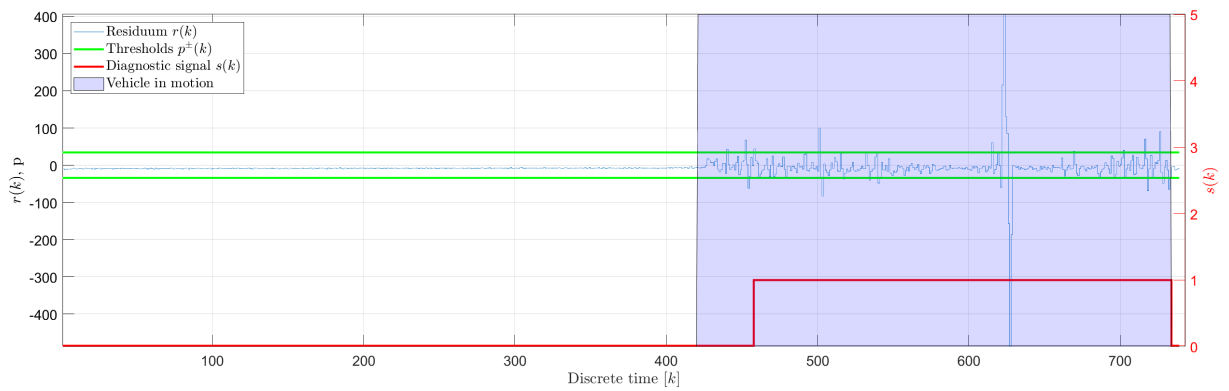


Fig. D.40. Water intrusion 7 - binary diagnostic signal $s(k)$

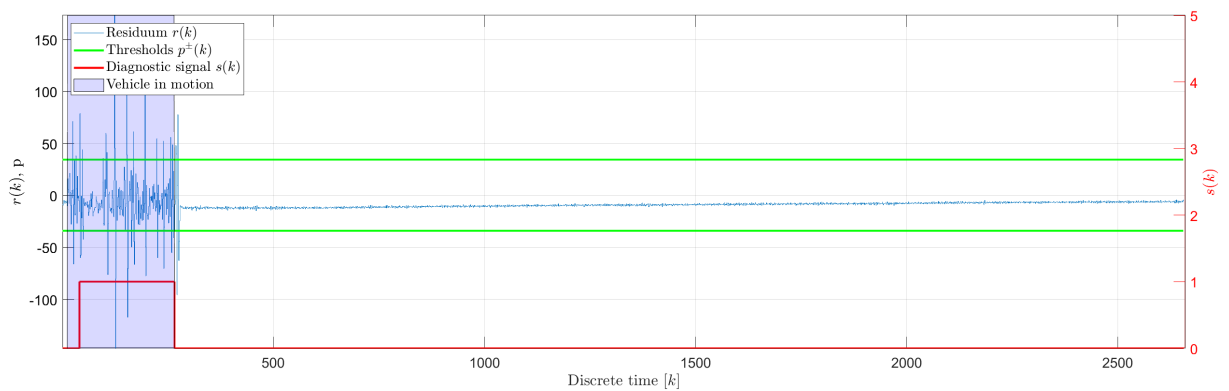


Fig. D.41. Water intrusion 8 - binary diagnostic signal $s(k)$

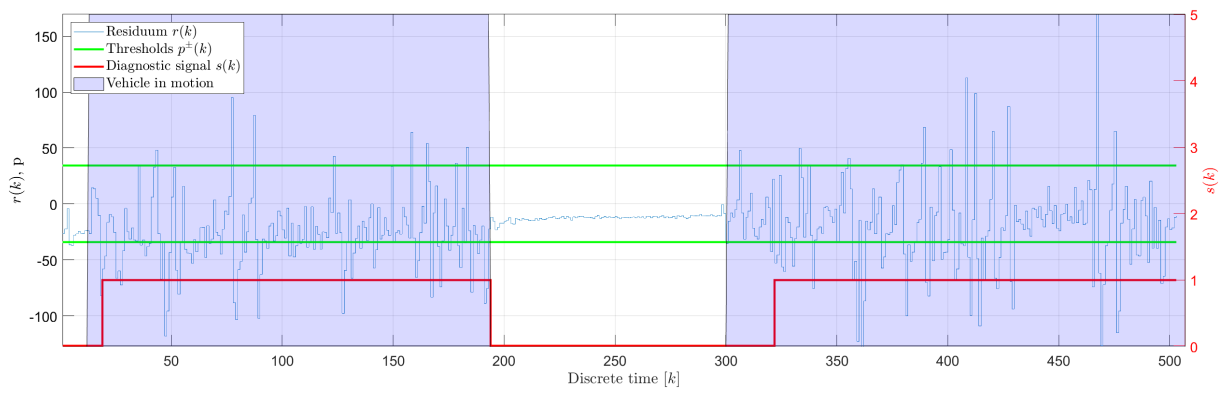


Fig. D.42. Water intrusion 9 - binary diagnostic signal $s(k)$

E. Used hardware and software

The majority of the research was carried out on a personal computer with Windows 10.

The algorithms were developed and verified using **MATLAB R2023a** (9.14.0.2239454) 64-bit licensed under the Academic License (master license: 31464320, the author's PC: 40876907) (<https://www.mathworks.com/products/matlab.html>). Other MATLAB Toolboxes included:

- **Deep Learning Toolbox**, version 14.6,
- **Embedded Coder**, version 7.10;
- **MATLAB Coder**, version 5.6;
- **Signal Processing Toolbox**, version 9.2;
- **Simulink**, version 10.7.

Printed Circuit Boards (PCB) were designed using the **Altium Designer 22.0.2** (Build 36) licensed under the Academic License.

Firmware was written using the **STM32 Cube IDE 1.7.0** (Build 10852_20210715_0634 (UTC)) offered under an industry-standard open license.

The prototyping phase was assisted by an **Original Prusa i3 MK3S** 3D printer with an instrumental error of 0.1mm and **PrusaSlicer 2.5.2** licensed under GNU Affero General Public License v3.0.

Additional software used while writing the thesis included:

- **Diagrams.net** 14.8.0 (formerly Draw.IO), free software even for commercial purposes, <https://www.diagrams.net>.
- **GIMP** 2.10.30 licensed under GNU General Public License v. 3.0, <https://www.gimp.org/>,
- **Microsoft Visual Studio Code** licensed under MIT License, with with **Python** v2023.8.0 and **Jupyter** v2023.4.1011241018 extensions <https://code.visualstudio.com/>.
- **TeXstudio** 2.12.22 licensed under GNU General Public License v. 2.0, <http://texstudio.sourceforge.net>.
- **SerialPlot** licensed under GNU General Public License v. 3.0, <https://github.com/hy0zd/serialplot>.

Most important laboratory equipment used throughout the dissertation:

- Bench direct current power supply - **NDN DF173005C**:
 - Output voltage: 0-30 V.
 - Output current: 0-5 A.
 - Voltage measurement accuracy: $\pm 1\% + 2$ digits, current measurement accuracy: $\pm 2\% + 2$ digits.
 - Ripples and noise: $CV \leq 1$ mVrms (5 Hz - 1 MHz), $CC \leq 2$ mArms.
- Digital oscilloscope - **Rigol DS1054Z**:
 - 50MHz bandwidth, 4 channels.
 - Maximum sample rate 1 GSa/s.
 - Vertical scale from 1 mV/div to 10 V/div.
 - Memory depth 24 Mpts.
- Digital refractometer - **Kern ORF-E**:
 - Measuring capacity: 1.3330 nD - 1.4098 nD.
 - Measurement accuracy: 0.0003 nD.

-
- Measurement division: 0.0001 nD.
 - Temperature range: 0°C - 40°C.
 - Automatic temperature compensation: 5°C - 40°C.
 - FFF/FDM 3D printer - **Original Prusa i3 MK3S:**
 - Build Volume: 25 × 21 × 21 cm.
 - Layer height: 0.05 – 0.35 mm.
 - Filament diameter: 1.75 mm.
 - Max travel speed: 200+ mm/s.
 - Max nozzle temperature: 300°C.
 - Max heatbed temperature: 120°C.
 - Optical microscope - **SKU: SM-3TZZ-FRL-3M-3PL:**
 - Head: 45 degree inclined 360 degree swiveling trinocular.
 - Eyepiece: 30 mm super widefield high-eyepoint WF10X/20 and WF20X/10.
 - Objective: 0.7-4.5X.
 - Barlow Lens: 0.5X and 2.0X.
 - Zoom Range: 51:1.
 - Maximum Field of View: 2 – 1/2" (65 mm).
 - Minimum Field of View: 3/16" (4.75 mm).
 - Diopter Adjustment: +/- 5 dp.
 - Interpupillary Distance: 2 – 3/16" - 2 – 15/16" (55-75 mm).
 - Working Distance: 8" (200mm).
 - Microscope camera - **Aptina MT9T001:**
 - Sensor: Aptina MT9T001.
 - Sensor Type: CMOS.
 - Sensor Size: 6.55 × 4.92 mm.
 - Pixel Size: 3.2.
 - Resolution: 3.1 MP.
 - Frame Rate: 8 @ 2048 × 1536, 22 @ 1024 × 768, 43 @ 680 × 510.
 - Sensitivity: 1.0 V/lux-sec.
 - Computer set for calculations - **Specifications:**
 - Processor: 16 cores, ranging from 4.2 GHz to 5.7 GHz.
 - Memory: DR5, 128GB, 6000MHz, CL36.
 - Graphics Card: 24 GB RAM, 16384 stream processors, 512 tensor cores, core clocking at 2610 MHz.
 - SSD: 4 TB M.2 2280 PCI-E x4 Gen4 NVMe.
 - Operating System: 64 Bit.
 - Computer for edge computing - **Data processing and compression module.**
 - VGA Graphics card - **PNY Quadro RTX 5000 16GB.**
 - Notebook for other works - **Lenovo ThinkBook 15 G2 ARE 20VG0008PB.**

